NORMAL MODE ANALYSIS OF SINGLE BUNCH, CHARGE DENSITY DEPENDENT BEHAVIOR IN ELECTRON/POSITRON BEAMS

A Dissertation

Presented to the Faculty of the Graduate School

of Cornell University

in Partial Fulfillment of the Requirements for the Degree of

Doctor of Philosophy

by

Michael Ehrlichman

May 2013

NORMAL MODE ANALYSIS OF SINGLE BUNCH, CHARGE DENSITY

DEPENDENT BEHAVIOR IN ELECTRON/POSITRON BEAMS

Michael Ehrlichman, Ph.D.

Cornell University 2013

Accelerator science in coming years will be increasingly dependent upon high single-bunch charges and/or small emittances. Under these conditions, single-particle dynamics are not a sufficient description of beam behavior and interactions between the beam particles must be taken into account. One such interaction is when collisions between the particles that compose a bunch perturb the motion of the colliding particles significantly and frequently enough to impact the beam dynamics. Multiple, small-angle, collisions blow up the emittance of the bunch and are referred to as intrabeam scattering (IBS). Here are documented the theoretical and experimental studies of IBS in storage rings undertaken as part of the CesrTA program.

Under the conditions where IBS becomes dominant, other multi-particle effects can also appear. The additional effects we investigate include potential well distortion, coherent current-dependent tune shift, and direct space charge.

CesrTA design and analysis is conducted in a normal mode coordinates environment which allows for natural handling of coupling. To that end, we develop a 6D normal modes decomposition of the linear beam optics.

Multi-particle effects are also important for Energy Recovery Linear Accelerators (ERLs). Because the beam circulates for only a short period of time in an ERL, the beam lifetime imposed by Touschek scattering is not significant. However, the particles scattered out of the bunch can generate a radiation hazard where they collide with the beam pipe. We re-derive Piwinski's original Touschek scattering equation to check its validity when applied to ERL beams, then repurpose the formula to generate a profile of where scattered particles are generated and where they are lost.

The results presented here advance our understanding of charge-dependent behavior in the sorts of high charge-density accelerators that will be implemented in coming years.

BIOGRAPHICAL SKETCH

Michael Ehrlichman obtained his Bachelor of Science in Physics from the University of Minnesota Institute of Technology in the Spring of 2007. He graduated Magna Cum Laude with a thesis titled "Design Studies for the Proposed CESR Accelerator Test Facility". He received a double major in Philosophy. Michael began his graduate career at Cornell University in June of 2007. He presented his Ph.D. defense March 14th, 2013.

This doctoral thesis is dedicated to my wife Yiou (Scarlett) Zuo.

ACKNOWLEDGMENTS

but I have made much use of the excellent resources they make easily accessible online. In particular, the material written by Andrzej Wolski has been helpful my progression to a doctorate.

Finally, I would like to thank the open source development community. The tools they develop are an integral component of the world's research infrastructure. In particular, I would like to thank the developers of `gnuplot`, `Paint.NET`, `Scientific Linux`, `Ubuntu`, `Debian`, `Inkscape`, `vim`, `Xfig`, `OpenSSH`, `OpenVPN`, and of course, LaTeX.

TABLE OF CONTENTS

LIST OF TABLES

LIST OF FIGURES

PREFACE

This document presents the results of theoretical and experimental investigations of current dependent effects in the types of bunched electron/positron beams that will be utilized in the next generation of advanced particle accelerators. The charge-dependent behavior of single bunch beams dominated by intrabeam scattering is investigated using CesrTA, and design studies are conducted to determine where Touschek particles are lost in the Cornell Energy Recovery Linear Accelerator.

The first chapter is a brief introduction which discusses the importance of accelerators in high technology and scientific research. Some of the challenges involved in developing the next generation of accelerators are discussed.

In the second chapter, the IBS investigations conducted at CesrTA are presented. CesrTA lattice design and analysis of beam dynamics is conducted in a normal mode coordinates environment which allows for a natural handling of coupling. To that end, this chapter begins by deriving a demonstration storage ring from first principles. Starting with the Hamiltonian of a charged particle in a magnetic field, we derive the transfer matrices necessary to assemble a simple storage ring. A tilted quadrupole is introduced to create a storage ring with coupling between the horizontal, vertical, and longitudinal motion.

After discussing the difficulties encountered when analyzing particle motion in the demonstration storage ring, we derive a formalism for decomposing the particle motion into the eigen modes of the magnetic lattice. The derivation starts with Wolski's eigen mode formalism found in [58], and extends it to a 6-dimensional normal mode formalism. This 6-dimensional normal mode formalism can be viewed as an extension of the 4-dimensional normal mode formalism developed by Sagan and Rubin in [41].

An important advantage of the normal mode formalism is that it allows beam sizes that can be measured in the laboratory to be properly calculated in coupled machines.

This is particularly important when predicting beam size measurements in CesrTA. Due to dispersion in the RF cavities, bunches in CesrTA are tilted in the xz plane and the usual formulas for calculating beam size do not apply.

The normal mode formalism is then applied to the demonstration storage ring, where it is shown that quantities such as particle action and beam emittance (phase space volume occupied by the ensemble of particles) regain their significance in a normal modes coordinate system.

The thesis then discusses the Σ-matrix-based IBS formalism developed by Kubo and Oide [21]. This is a generalization of Bjorken & Mtingwa's formalism [5] and naturally handles coupled motion. Particular attention is paid to the Coulomb Logarithm. One of the main results of our investigations at CesrTA is that the proper tail-cut should be applied when calculating IBS growth rates in electron/positron storage rings.

Piwinski's original IBS formalism [30] is re-derived such that its Coulomb Logarithm factor can be treated in the same manner as in Kubo's formalism. It is shown that all three formalisms give similar results when applied to CesrTA, provided the Coulomb Logarithm is treated consistently

A Monte Carlo IBS simulation based on Takizuka & Abe's binary collision model for non-relativistic plasmas [48] is developed. The main advantage of the Monte Carlo simulation is that it is independent of any coupling formalism and takes nonlinearities of the guide field into account.

In addition to intrabeam scattering, potential well distortion and coherent tune shift are observed in CesrTA. A theoretical model for potential well distortion is described and coherent tune shift measurements are presented.

Having developed and presented the theory necessary to describe current-dependent beam sizes in CesrTA, we present data on IBS-dominated beams obtained during the April 2012 and December 2012 CesrTA machine studies. An interesting anomaly in

our data is a blow up in the vertical beam size at high current that does not fit with our models. Incoherent tune shift due to direct space charge is presented as a possible explanation of the blow up.

The last chapter of this thesis presents work done on Touschek Scattering in Energy Recovery Linear Accelerators (ERLs). Piwinski's original Touschek formula [32] is re-derived to check its validity when applied to ERLs. We find that Piwinski's Touschek formula is accurate to first order in energy spread, $\frac{1}{\gamma_0^2}$, and divergence. The formula is then re-purposed to determine the locations in the ERL where Touschek particles are generated and lost. These loss profiles guide the placement of collimators in the ERL design.

CHAPTER 1

INTRODUCTION

Particle accelerators are a broad class of high technology electromagnetic devices that produce, accelerate, store, and transport beams of leptons, hadrons, or ions to very high velocities. Particle accelerators are ubiquitous in scientific research, high tech industry and medicine. There are roughly 26,000 accelerators operating world wide.

Depending on application, the velocities attained in an accelerator may be quite low. An industrial use of particle accelerators is ion implantation. Beams of ions, such as boron, arsenic, or oxygen, are accelerated to about 0.5% the speed of light and are used to dope semiconductors. Ion implantation is an important step in the manufacture of silicon-on-insulator (SOI) microprocessors. A similar process is be used to harden steel tools with nitrogen, improving tool lifetime by 60% [50].

In medicine, particle therapy bombards tumors inside the body with ionizing beams of electrons, protons, or ions. The energy and species of the particle determine the depth at which the radiation is delivered. Figure 1.1 compares this depth for various particles. Particle beam therapy is a very high precision technique and can be used to treat tumors where damage to the surrounding tissue must be avoided [56]. An accelerator for proton therapy typically consists of an ion source, a cyclotron to accelerate the particles, and a transport line to deliver the beam to the patients.

Another medical application of accelerators is the production of radiopharmaceuticals. Radiopharmaceuticals are compounds that are both biologically active and radioactive. They are usually designed to localize in certain parts of the body. For example, they may localize in regions where glucose uptake, and therefore metabolism, is high. This can be useful for identifying cancer metastasis. The location of radiopharmaceuticals in
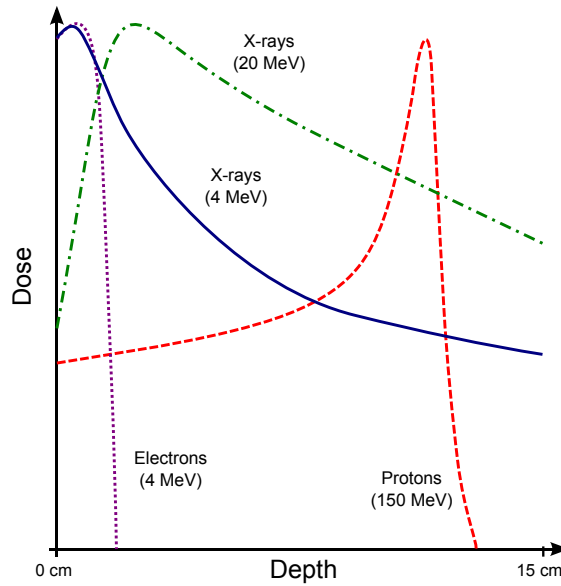
Figure 1.1: Radiation dose delivered versus depth for various forms of particle therapy. Image source: [54].

the body can be determined by looking for the positron radiation they emit [55]. Similarly, radiopharmaceuticals can be designed to release radiation that destroys diseased tissues. Many of the radioisotopes used in medicine are produced in accelerators such as the Brookhaven Linac Isotope Producer at Brookhaven National Laboratory (BNL).

About 100 accelerators worldwide are operated for scientific research. These can be divided into to two broad categories: colliders and light sources.

Colliders include the Large Hadron Collider (LHC) at CERN in Geneva, Switzerland, the Relativistic Heavy Ion Collider (RHIC) at BNL in New York, and the Beijing Electron Positron Collider (BEPC) in Beijing, China. These machines accelerate particles to very high energy, 99.995% the speed of light and higher, and collide them head on. These collisions generate exotic states of matter that tell us about the the early universe and help us define the standard model. The standard model is a particle-based classification scheme for the data obtained in high energy physics experiments. It describes the particles and interactions that make up the world around us and also those
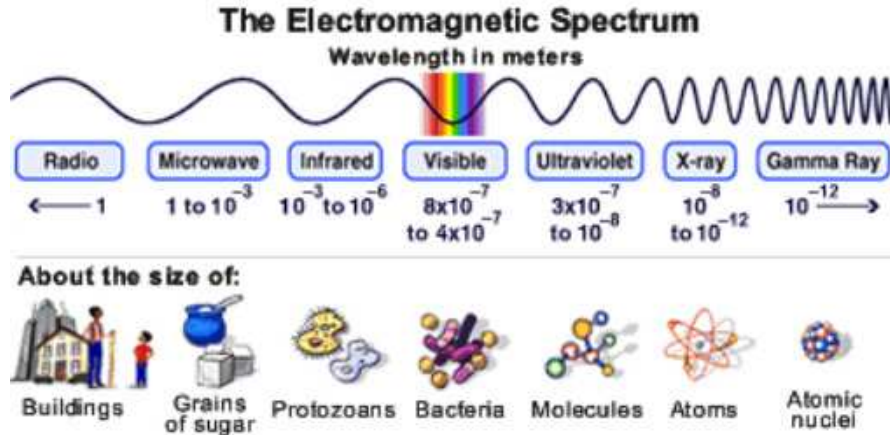
Figure 1.2: Chart of the electromagnetic spectrum. Accelerator-based light sources span the far infrared through gamma rays. Image source [26].

that made up the very early universe. The recent discovery of the Higgs boson, which explains why particles have inertial mass, is the result of accelerator-based collision experiments.

Light sources are a broad class of accelerators dedicated to producing intense, precise pulses of photons. They are unique in their ability to generate intense light pulses over a wide range of photon energies. Shown in Fig. 1.2 is the electromagnetic spectrum. Generally speaking, the wavelength of the light being used to investigate an object determines the size of the features that can be resolved. Probing the arrangement of atoms in a crystal requires light in the x-ray region of the electromagnetic spectrum, which has a wavelength of about 10^{-10} meters. However, such light is blind to the details of a nucleus. Nuclear studies require light with a wavelength smaller than about 10^{-14} meters.

Accelerator-based light sources work on the principle that a charged particle emits electromagnetic radiation when it is accelerated. This is the same principle behind radio transmission and the reason metals glow red when heated. In an accelerator-based light source, electrons are accelerated to very high energy and injected into a storage
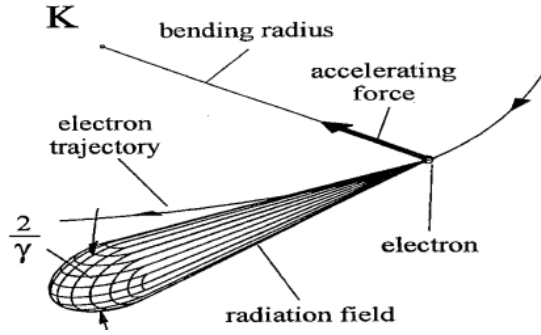
Figure 1.3: A charged particle beam emits a cone of radiation when bent by a dipole magnet. Image source [57].
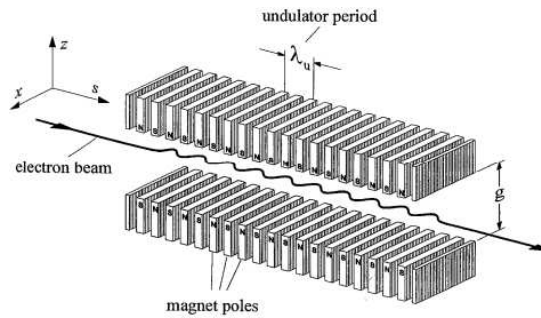
Figure 1.4: In an undulator, a series of bends causes the particle beam to emit an intense pulse of light. Image source [57].

ring where they circulate for several 10s of minutes. Storage rings are typically several hundred meters in circumference. The storage ring contains strong dipole fields that accelerate the beam perpendicular to its trajectory. As depicted in Fig. 1.3, this acceleration generates a strong radiation field in the forward direction. Accelerator-based light sources are particularly useful because the opening angle of the radiation varies inversely with the beam energy. The light emitted by a charged particle beam is concentrated into a very narrow cone. The opening angle of the radiation in a 5 GeV electron beam is about $0.005°$.

An undulator, depicted in Fig. 1.4, is a specialized device used in a light source that consists of a series of bend magnets of alternating gradient. The series of bends causes the beam to accelerate back and forth very quickly and emit an intense pulse of light.

4
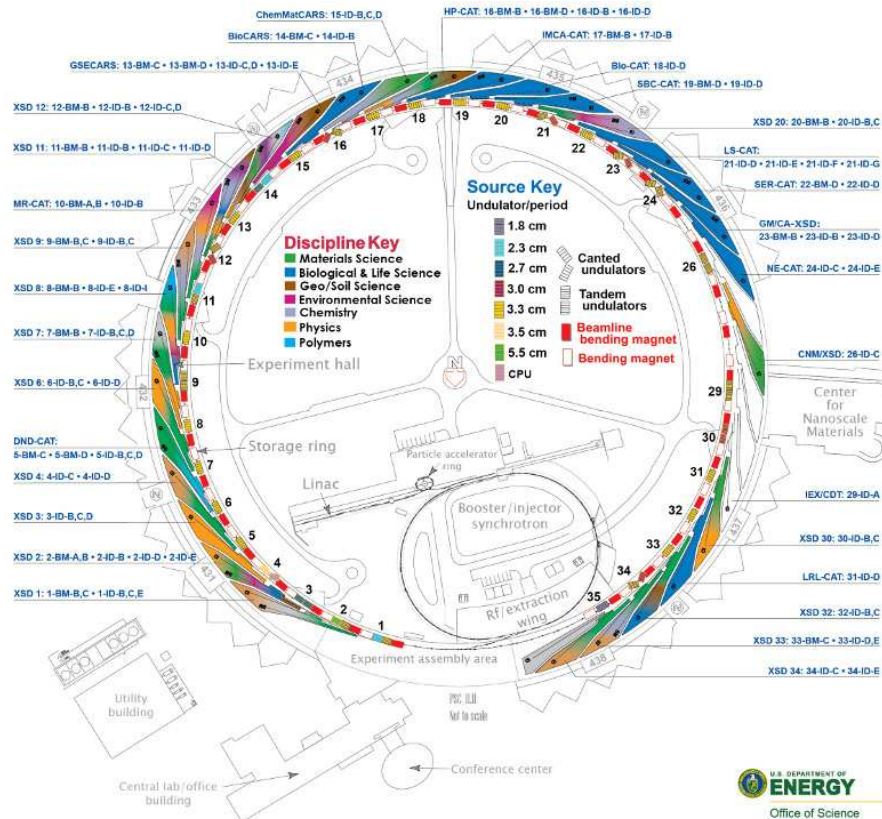
Figure 1.5: Layout of the Advanced Photon Source showing the various experimental stations. Electrons are accelerated in the linac and booster synchrotron, then injected into the storage ring where they are used to generate light.

Undulators can be tailored to deliver the exact type of light needed for an experiment. The wavelength of light from an undulator is determined by the undulator period λ_u, the strength of the bend magnets, and the energy of the beam. The bandwidth and intensity of the light is determined by the number of periods. Shown in Fig. 1.5 is the layout of the Advanced Photon Source (APS) located at Argonne National Lab in Illinois. The type of light delivered and setup of the experimental station are determined by the application. Applications include materials science, biology & life science, geology, chemistry, and condensed matter physics.

From 1939 to 2009, about one-third of Physics Nobel Prizes have incorporated data from accelerator-based experiments [7]. Accelerators are also important in other fields.
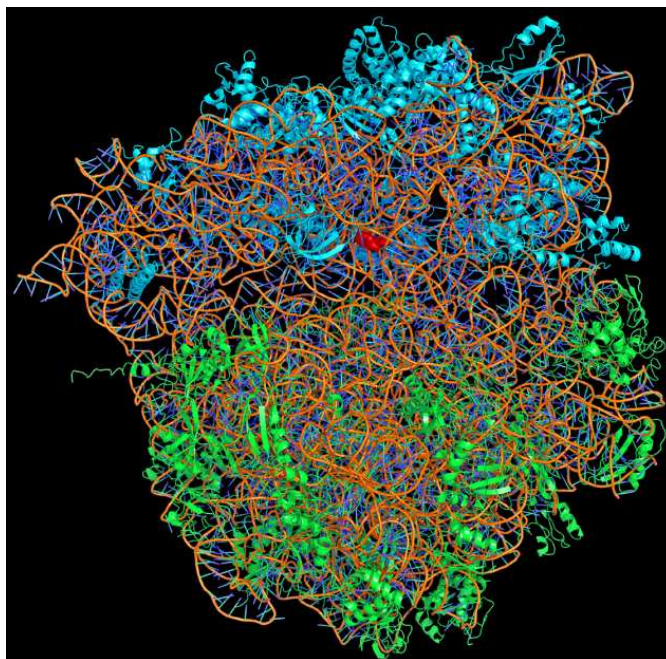
Figure 1.6: Structure of a bacterial ribosome as determined by accelerator-based x-ray crystallography. The ribosome contains more than 2800 nucleotides and about 33 protein molecules. The locations of over 84,000 non-hydrogen atoms have been identified [43].

Nobel Prizes in Chemistry were awarded for accelerator-based research in 1998, 2003, and 2009. The 2009 Nobel Prize in Chemistry was awarded for determining the structure and function of the ribosome using accelerator-based x-ray crystallography. The ribosome, depicted in Fig. 1.6, is the primary site of biological protein synthesis in the cell.

The next generation of advanced particle accelerators are being developed to support continued advances across a wide range of disciplines. Discoveries at the LHC over the next several years will hopefully tell us in which direction to take high energy physics. One possible direction is that of high-precision collision experiments. To that end, the International Linear Collider (ILC) and Compact Linear Collider (CLIC) are being developed. These machines are designed to enable higher precision measurements of the discoveries at LHC. New light sources, such as Cornell's Energy Recovery Linac (ERL)

and Ultimate Storage Rings (USRs) aim to deliver brighter, shorter pulse length light pulses over a wide range of wavelengths.

The aim of the research presented in this thesis is to understanding the charge-dependent beam physics phenomena that arise when electron and positron beams are pushed to very high charge densities. These effects will be increasingly important in future accelerators. In a low current accelerator, the beam can be modeled as an ensemble of non-interacting particles. As the density of particles in the beam increases, the particles begin interacting with each other and the beam is no longer well-described as an ensemble of non-interacting particles. The interactions can be one-particle to one-particle, as in intrabeam scattering. The interactions can also be many to one, as in direct space charge, or the particles can interact with each other through the beam chamber, as in impedance effects.

Our primary goal is to understand intrabeam scattering (IBS). This is where collisions among the particles that compose the bunch transfer momentum between the particles in such a way that the total amplitude of their oscillations increases. However, other collective effects may arise in beams where intrabeam scattering is important. Those other effects include impedance effects and direct space charge. Because particle motion in CesrTA is coupled, these studies are done in terms of the normal modes of the beam.

CHAPTER 2

INTRABEAM SCATTERING STUDIES AT CESRTA

Intrabeam scattering has been studied in detail at p and $\bar{p}$ [24, 25, 31], and heavy ion colliding beam machines [14]. In such machines, IBS slowly increases the phase space volume occupied by the beam (emittance) and imposes a luminosity lifetime. Studies of IBS in ion beams have been conducted at the Relativistic Heavy Ion Collider (RHIC) at Brookhaven National Lab [14]. There, good agreement was found between IBS theory and experiment. Lattices which reduce IBS growth by minimizing the dispersion invariant $\mathcal{H}_a = \gamma_a \eta_a^2 + 2\alpha_a \eta_a \eta_a' + \beta_a \eta_a'^2$ have been implemented at RHIC and are used regularly for colliding-beam experiments [13]. For beams of protons and anti-protons, good agreement between theory and measurements was found at the Tevatron [24].

Electron and positron beams in rings come to equilibrium much more rapidly than hadron beams, hence IBS in lepton rings manifests itself differently. Lepton machines have strong radiation damping, and the equilibrium emittance is determined by a balance between radiation damping and quantum excitation. Typical damping times are on the order of tens of milliseconds. The quantized nature of IBS contributes a random motion to the scattered particles, which tends to increase the emittance (phase space volume occupied by the beam). The random excitation of the IBS equilibrates with radiation damping to determine the beam size. The result is a current-dependent emittance.

Single, large-angle scattering events that can kick particles outside the core of the bunch and contribute to particle loss or beam halo are relatively rare. Multiple, small-angle, scattering events are more common. The former are commonly referred to as Touschek scattering, and the latter as intrabeam scattering. The emphasis in this chapter is intrabeam scattering.

IBS in electron beams has been studied at the Accelerator Test Facility (ATF) at KEK [2], where detailed measurements of the current dependence of bunch energy spread and length are in good agreement with theory. Measurements of the transverse dimensions at ATF, however, are not as complete.

One of the goals of the CesrTA IBS investigation is to improve on the ATF results by including detailed measurements of the bunch charge dependence of the transverse beam sizes. CesrTA has independently powered quadrupoles and the capability to store larger single-bunch charges. This flexibility allows for measurements in a greater variety of conditions. In this chapter, we describe the CesrTA IBS experiments, and compare the results to both analytic theory and Monte Carlo simulations. Some of the results shown here were first presented at the 2012 International Particle Accelerator Conference [11]. The presentation here provides a more complete description and theoretical framework for the results.

CesrTA is a re-purposing of the Cornell Electron Storage Ring (CESR) as a test accelerator for future storage rings designs [29]. CesrTA is a wiggler-dominated storage ring, with 90% of the synchrotron radiation produced by twelve 1.9 T superconducting damping wigglers. Some parameters for CesrTA are given in Table 2.1. Design and analysis of CesrTA is done using the `Bmad` relativistic charged beam simulation library [37]. Design a-mode (horizontal-like), single particle geometric emittance ϵ_a is 2.7 nm-rad. The minimum measured b-mode (vertical-like) emittance ϵ_b at the time of these measurements is about 20 pm-rad and is dominated by magnet misalignments and the effectiveness of our emittance tuning procedure. The flexibility of the CesrTA optics allows precise control of b-mode emittance above that minimum. We are able to vary b-mode emittance by using closed coupling bumps to introduce a localized vertical dispersion in the damping wigglers. In this way, vertical emittance can be increased by an

Table 2.1: Machine parameters for IBS measurements.

Beam Energy (GeV)	2.085
Circumference (m)	768
RF Frequency (MHz)	449.765
Horizontal Tune (Q_x)	14.624
Vertical Tune (Q_y)	9.590
Synchrotron Tune (Q_z)	-0.065
Transverse Damping Time (ms)	56.6

order of magnitude without affecting the global optics. The bunch length is determined by the RF accelerating voltage. With a voltage of 6 MV, the bunch length is about 10.5 mm. Measurements were made with bunch charges ranging from 1.6×10^9 to 1.6×10^{11} particles/bunch (0.10 mA to 10.0 mA).

CesrTA is instrumented for precision bunch size measurements in all three dimensions.

Vertical beam size measurements are made by imaging x-rays from a hard bend magnet through a pinhole onto a vertical diode detector array [35]. The measurements are turn-by-turn, but the average of the fits of 1024 turns is taken as the measurement.

Horizontal beam size measurements are made with a visible synchrotron light interferometer [52]. The interferometer is used to image visible synchrotron radiation on a charge-coupled device (CCD) that is exposed over about 400 turns at high current and about 40000 turns at low current. Bunch length measurements are done with a streak camera, making use of visible light in the synchrotron radiation spectrum from a bending magnet [17].

Validation of the beam size instrumentation includes checking for intensity dependent systematics using filters, and size systematics by varying source-point betatron-

functions. The horizontal beam size monitor undergoes direct calibration with a source of known size [52].

2.1 Overview of Modeling Environment

The primary tool used for CesrTA design and modeling is the `Bmad` relativistic charged beam simulation library [38]. `Bmad` is suite of modules that enable the development of codes for designing and simulating charged particle accelerators and X-Ray beam lines.

Physics conventions, such as coordinate system, used in this thesis follow those outlined in the `Bmad` manual [38].

The code I have contributed to `Bmad` includes calculation of intrabeam scattering growth rates, Touschek scattering rates, potential well distortion, eigen mode decomposition of transfer matrices, and simulation of a digital tune tracker, which is a phase-lock loop instrument used to resonantly excite oscillations in a particle beam. I have also made performance enhancements to the symplectic lie tracking module for wigglers and the module for tracking particles through higher order multipoles. These enhancements consist of simplifying and rearranging the math operations to enable the compiler to more efficiently vectorize the code.

2.2 Canonical Coordinates

Following the `Bmad` coordinate convention, the phase space coordinate of a particle relative to the reference particle is,

$$\vec{x}(s) = (x(s), p_x(s), y(s), p_y(s), z(s), p_z(s)), \tag{2.1}$$

11

where s refers to position along the length of the machine. x and y refer to horizontal and vertical coordinate and p_x and p_y refer to horizontal and vertical momentum. z is time-like and p_z refers to the total momentum of the particle. Both are defined in detail below.

The transverse momenta are normalized by the reference particle momentum P_0,

$$p_x = \frac{P_x}{P_0} \tag{2.2}$$

$$p_y = \frac{P_y}{P_0}. \tag{2.3}$$

The reference particle momentum is related to the design energy of the machine, $P_0 = \beta(s) E_0/c$. The z coordinate is defined as the time $t(s)$ that a particle arrives at a particular location s in the machine,

$$z(s) = -\beta(s) c (t(s) - t_0(s)) \tag{2.4}$$

$$\equiv -\beta(s) c \Delta t(s), \tag{2.5}$$

where $\beta(s)$ is the velocity of the particle at position s and $t_0(s)$ is the time at which the reference particle arrived at s. A particle with a positive z arrives at s before the reference particle, and a particle with a negative z arrives at s after the reference particle. The longitudinal momentum coordinate is defined as,

$$p_z = \frac{P - P_0}{P_0}, \tag{2.6}$$

where P is the total momentum of the particle,

$$P^2 = P_x^2 + P_y^2 + P_s^2. \tag{2.7}$$

Note that P is not the longitudinal momentum of the particle.

Within the paraxial approximation where $p_x, p_y << 1$,

$$x' = \frac{dx}{ds} \approx \frac{p_x}{1 + p_z}(1 + gx)$$
$$y' = \frac{dy}{ds} \approx \frac{p_y}{1 + p_z}(1 + gx) \tag{2.8}$$

where $g = 1/\rho$ and ρ is the radius of curvature. Typically, g is non-zero only when the particle is travelling through a bend magnet.

$\vec{x} = (x(s), p_x(s), y(s), p_y(s), z(s), p_z(s))$ is a $2n$, with $n = 3$, canonical coordinate system. (x, p_x), (y, p_y), and (z, p_z) are canonically conjugate coordinate pairs. x, y, and z are the generalized coordinates (the q_i's in the usual Hamiltonian notation). p_x, p_y, and p_z are the generalized momenta. Trajectories in $\mathbf{x}$ can be described by a Hamiltonian.

The coordinate system $\mathbf{x}$ described here is s-dependent. The z and p_z coordinates tell us about the arrival time of particles at a particular location s. They do not tell us about the longitudinal distribution of the particles. The longitudinal distribution is necessary when calculating intra-bunch effects, when it is important to know the relative spatial coordinates of the particles. In Sec. 2.9.2, where Monte Carlo IBS simulation is discussed, the time-dependent Hamiltonian is used to develop a map from the s-dependent coordinate system to a time-dependent coordinate system.

2.3 Hamiltonian Formalism

The s-dependent Hamiltonian for a particle traveling in the positive s direction through a canonical vector potential $\vec{A}$ and electric potential ϕ is,

$$
H_s =
$$

$$
- \left(1 + \frac{x}{\rho}\right) \sqrt{\left((1 + p_z) - \frac{q\psi}{cP_0}\right)^2 - \left(p_x - \frac{qA_x}{P_0}\right)^2 - \left(p_y - \frac{qA_y}{P_0}\right)^2}
$$

$$
+ \frac{1}{\beta_0} \sqrt{(1 + p_z)^2 + \frac{m^2c^2}{P_0^2}} - \frac{q}{P_0}A_s, \quad (2.9)
$$

P_0 is the reference particle momentum, ρ is the horizontal bending radius for the reference particle, q is the particle charge, ψ is the electric potential, c is the speed of light, and m is the particle mass. The second term in the Hamiltonian appears because we defined z relative to z_0. $(A_x, A_y, A_s) = \vec{A}$ is the magnetic vector potential. The Hamiltonian for a particle travelling in the negative s direction is

$$
H_{-s} =
$$

$$
\left(1 + \frac{x}{\rho}\right) \sqrt{\left((1 + p_z) - \frac{q\psi}{cP_0}\right)^2 - \left(p_x - \frac{qA_x}{P_0}\right)^2 - \left(p_y - \frac{qA_y}{P_0}\right)^2}
$$

$$
+ \frac{1}{\beta_0} \sqrt{(1 + p_z)^2 + \frac{m^2c^2}{P_0^2}} - \frac{q}{P_0}A_s. \quad (2.10)
$$

The equations of motion are obtained by applying the Hamilton equations [34],

$$
\frac{d\vec{x}}{ds} = \mathbf{S}\frac{\partial H}{\partial \vec{x}}, \quad (2.11)
$$

where,

$$\mathbf{S} = \begin{pmatrix} 0 & 1 & 0 & 0 & 0 & 0 \\ -1 & 0 & 0 & 0 & 0 & 0 \\ 0 & 0 & 0 & 1 & 0 & 0 \\ 0 & 0 & -1 & 0 & 0 & 0 \\ 0 & 0 & 0 & 0 & 0 & 1 \\ 0 & 0 & 0 & 0 & -1 & 0 \end{pmatrix}, \tag{2.12}$$

and $\vec{x}$ was defined in Eqn. (2.1). The transformation from from one location s_i to another location s_{i+1} is given by,

$$\vec{x}(s_{i+1}) = \vec{x}(s) + \mathbf{S}\frac{\partial H}{\partial \vec{x}}(s_{i+1} - s_i). \tag{2.13}$$

Solutions to the equations of motions can usually be found for many common accelerator components by linearizing Eqn. (2.13).

Knowing the electromagnetic field potentials ψ and $\vec{A}$ and bending radius of a magnetic component, one can quickly go from the Hamiltonian to the equations of motion. Lie algebra techniques can be applied to the Hamiltonian to integrate symplectically while taking into account arbitrary number of non-linear terms. This can be useful when tracking through highly non-linear elements such as damping wigglers.

In the following sections, we will derive from the Hamiltonian the transfer matrices necessary to construct a simple demonstration storage ring. The storage ring will consist of quadrupoles, bend magnets, and drift sections. We will also introduce a simple longitudinal focusing element and a tilted quadrupole. The purpose of this storage ring is to demonstrate coupled particle motion. The symplecticity of the Hamiltonian will be used to derive an eigen modes decomposition of the demonstration storage ring. This decomposition will allow us to recover concepts such as particle action and beam emittance.

The eigen decomposition will later be extended to a normal mode decomposition, from which we can obtain additional information about coupled motion in the beam. We will also obtain a method for calculating the projected beam sizes in a coupled machine.

2.3.1 Equations of Motion Through a Quadrupole

Consider a particle travelling through a quadrupole. Ignoring fringe fields, the field of a magnetic multipole has only x and y components and only the A_s component of the vector potential is non-zero. Outside of a bend magnet, ρ^{-1} is zero and the magnetic vector potential is given by

$$\vec{A}_s = \Re\left(\sum_{\nu=1}^{\infty} \Psi_\nu \left(x - \iota y \right)^\nu \right),$$ (2.14)

where Ψ_ν is the strength of the multipole of order ν. For a dipole, only Ψ_1 is non-zero, for a quadrupole, only Ψ_2 is non-zero, and so on.

Evaluating Eqn. (2.14) for a quadrupole, where $\Psi_2 \neq 0$, yields,

$$\begin{aligned} A_s &= \Re\left(\Psi_2 \left(x - \iota y \right)^2 \right) \\ &= \Re\left(\Psi_2 \left(x^2 - y^2 - 2\iota xy \right) \right) \\ &= 2\Psi_2 \left(x^2 - y^2 \right). \end{aligned}$$ (2.15)

To check Eqn. (2.15), we calculate its curl. In the curvilinear coordinate system of

$\hat{x}$, $\hat{y}$, $\hat{s}$, the curl of **A** is [47],

$$
\begin{aligned}
\vec{B} &= \nabla \times \vec{A} \\
&= \left(\frac{\partial A_s}{\partial y} - \frac{1}{1 + \rho^{-1}x} \frac{\partial A_y}{\partial s} \right) \hat{x} + \\
&\quad \left(\frac{1}{1 + \rho^{-1}x} \frac{\partial A_x}{\partial s} - \frac{1}{1 + \rho^{-1}x} \frac{\partial}{\partial x} \left(1 + \rho^{-1}x \right) A_s \right) \hat{y} + \\
&\quad \left(\frac{\partial A_y}{\partial x} - \frac{\partial A_x}{\partial y} \right) \hat{s} \\
&= \frac{\partial A_s}{\partial y} \hat{x} - \frac{\partial A_s}{\partial x} \hat{y} \\
&= \Psi_2 \left(y\hat{x} - x\hat{y} \right),
\end{aligned}
\tag{2.16}
$$

which is indeed the magnetic field inside a quadrupole.

The electric potential ψ is zero inside a quadrupole and the magnetic vector potential is given by (2.15). Furthermore, g is zero because we are not inside a bend. We can now write down the Hamiltonian for a particle moving through a quadrupole,

$$
H_{s,\text{quad}} = - \sqrt{ \left(1 + p_z \right)^2 - p_x^2 - p_y^2 } + \frac{1}{\beta_0} \sqrt{ \left(1 + p_z \right)^2 + \frac{m^2 c^2}{P_0^2} } - \frac{k_1}{2} \left(x^2 - y^2 \right),
$$

$$
\tag{2.17}
$$

where we have defined $\dfrac{k_1}{2} = \dfrac{q\Psi_2}{P_0}$.

The equations of motion for this Hamiltonian are,

$$\frac{dx}{ds} = \frac{\partial H_{s,\text{quad}}}{\partial p_x} = \frac{p_x}{p_s}$$

$$\frac{dp_x}{ds} = -\frac{\partial H_{s,\text{quad}}}{\partial x} = -k_1 x$$

$$\frac{dy}{ds} = \frac{\partial H_{s,\text{quad}}}{\partial p_y} = \frac{p_y}{p_s}$$

$$\frac{dp_y}{ds} = -\frac{\partial H_{s,\text{quad}}}{\partial y} = k_1 y$$

$$\frac{dz}{ds} = \frac{\partial H_{s,\text{quad}}}{\partial p_z} = -\frac{1 + p_z}{p_s} + \frac{1}{\beta_0} \frac{1 + p_z}{\sqrt{(1 + p_z)^2 + \frac{m^2 c^2}{P_0^2}}}$$

$$\frac{dp_z}{ds} = -\frac{\partial H_{s,\text{quad}}}{\partial z} = 0 \tag{2.18}$$

where,

$$p_s = \sqrt{(1 + p_z)^2 - p_x^2 - p_y^2}, \tag{2.19}$$

has been defined to simplify the notation.

In the paraxial approximation, where $p_x, p_y \ll 1$, and assuming $m^2 c^2 / P_0^2 \ll 1$, the simplified Hamiltonian is

$$H_{s,\text{quad}} \approx \frac{p_x^2 + p_y^2}{2 (1 + p_z)} + \frac{k_1}{2} \left(x^2 - y^2 \right) \tag{2.20}$$

and the equations of motion become,

$$\frac{dx}{ds} = \frac{p_x}{1 + p_z} \qquad\qquad \frac{dp_x}{ds} = -k_1 x$$

$$\frac{dy}{ds} = \frac{p_y}{1 + p_z} \qquad\qquad \frac{dp_y}{ds} = k_1 y$$

$$\frac{dz}{ds} = 0 \qquad\qquad\qquad \frac{dp_z}{ds} = 0$$

$$\tag{2.21}$$

For the case of a quadrupole, general solutions can be found for the equations of motion. The equation for (x, p_x) can be converted into a single second order differential

18

equation, and so can those for (y, p_y). Clearly, z and p_z are constant. The trajectory of a particle through a horizontally focusing $(k_1' > 0)$ quadrupole is,

$$x(s) = x_0 \cos\left(\sqrt{|k_1'|}\, s\right) + \frac{p_{x0}}{\sqrt{|k_1'|}} \sin\left(\sqrt{|k_1'|}\, s\right)$$

$$y(s) = y_0 \cosh\left(\sqrt{|k_1'|}\, s\right) + \frac{p_{y0}}{\sqrt{|k_1'|}} \sinh\left(\sqrt{|k_1'|}\, s\right). \qquad (2.22)$$

For a quadrupole that is vertically focusing $(k_1' < 0)$,

$$x(s) = x_0 \cosh\left(\sqrt{|k_1'|}\, s\right) + \frac{p_{x0}}{\sqrt{|k_1'|}} \sinh\left(\sqrt{|k_1'|}\, s\right)$$

$$y(s) = y_0 \cos\left(\sqrt{|k_1'|}\, s\right) + \frac{p_{y0}}{\sqrt{|k_1'|}} \sin\left(\sqrt{|k_1'|}\, s\right). \qquad (2.23)$$

Equations (2.22) and (2.23) are valid at any location inside a quadrupole. If a particle with initial coordinates $(x_0, p_{x0}, y_0, p_{y0})$ is at the entrance end of a quadrupole of length L, its coordinates at the exit end are found by evaluating Eqn. (2.22) and (2.23) at $s = L$.

2.3.2 Transfer Matrix of a Quadrupole

The form of Eqs. (2.22) and (2.23) invites a transfer matrix representation. We define the focusing parameter K of a quadrupole with strength k_1' and length L as $K = \sqrt{k_1'}\, L$.

The transfer matrix for a horizontally focusing (vertically defocusing) quadrupole is,

$$\mathbf{M}_{QF} =$$

$$\begin{pmatrix} \cos(K) & \frac{1}{\sqrt{|k|}}\sin(K) & 0 & 0 & 0 & 0 \\ -\sqrt{|k|}\sin(K) & \cos(K) & 0 & 0 & 0 & 0 \\ 0 & 0 & \cosh(K) & \frac{1}{\sqrt{|k|}}\sinh(K) & 0 & 0 \\ 0 & 0 & \sqrt{|k|}\sinh(K) & \cosh(K) & 0 & 0 \\ 0 & 0 & 0 & 0 & 1 & 0 \\ 0 & 0 & 0 & 0 & 0 & 1 \end{pmatrix}. \quad (2.24)$$

By similar means, the transfer matrix for a horizontally defocusing (vertically focusing) quadrupole is obtained,

$$\mathbf{M}_{QD} =$$

$$\begin{pmatrix} \cosh(K) & \frac{1}{\sqrt{|k|}}\sinh(K) & 0 & 0 & 0 & 0 \\ \sqrt{|k|}\sinh(K) & \cosh(K) & 0 & 0 & 0 & 0 \\ 0 & 0 & \cos(K) & \frac{1}{\sqrt{|k|}}\sin(K) & 0 & 0 \\ 0 & 0 & -\sqrt{|k|}\sin(K) & \cos(K) & 0 & 0 \\ 0 & 0 & 0 & 0 & 1 & 0 \\ 0 & 0 & 0 & 0 & 0 & 1 \end{pmatrix}. \quad (2.25)$$

At this time, it is convenient to write down the transfer matrix of a drift of length L.

This can be obtained by taking the limit of Eqn. (2.24) as $k \to 0$,

$$\mathbf{M}_D = \begin{pmatrix} 1 & L & 0 & 0 & 0 & 0 \\ 0 & 1 & 0 & 0 & 0 & 0 \\ 0 & 0 & 1 & L & 0 & 0 \\ 0 & 0 & 0 & 1 & 0 & 0 \\ 0 & 0 & 0 & 0 & 1 & 0 \\ 0 & 0 & 0 & 0 & 0 & 1 \end{pmatrix}. \qquad (2.26)$$

2.3.3 Transfer Matrix of a Dipole

Our goal is to derive transfer matrices for the three basic types of accelerator element necessary to make a simple storage ring. This simple storage ring will be used to launch into our discussion of eigen modes and coupling. We have the quadrupole and drift in hand, next we derive the transfer matrix for a bend.

ρ^{-1} is finite in a bend and the magnetic vector potential in curvilinear coordinates is given by [47],

$$A_s = -\left(x + \frac{x^2}{2\rho}\right) B_y. \qquad (2.27)$$

Taking the curl of Eqn. (2.27) we obtain,

$$\begin{aligned} \vec{B} &= \nabla \times \vec{A} \\ &= -\frac{\partial A_s}{\partial x}\hat{y} \\ &= -\Psi_1 \hat{y} \\ &= B_y \hat{y}, \end{aligned} \qquad (2.28)$$

21

which is indeed the magnetic field inside a dipole. Clearly, $-\Psi_1$ is B_y, and we have written it as such.

The Hamiltonian for a particle propagating through a dipole is,

$$H_{s,\text{dipole}} = -\left(1 + \frac{x}{\rho}\right)\sqrt{(1 + p_z)^2 - p_x^2 - p_y^2}$$

$$+ \frac{1}{\beta_0}\sqrt{(1 + p_z)^2 + \frac{m^2 c^2}{P_0^2}} + \frac{qB_y}{P_0}\left(x + \frac{x^2}{2\rho}\right). \quad (2.29)$$

The bending radius ρ is for the ideal particle and can obtained from the usual expression,

$$\rho = \frac{P_0}{eB_y}, \quad (2.30)$$

where e is the electric charge. We will assume this is a sector bend and ignore edge focusing.

Applying Hamilton's equations to Eqn. (2.29) gives the equations of motion,

$$\frac{dx}{ds} = \left(1 + \frac{x}{\rho}\right)\frac{p_x}{p_s}$$

$$\frac{dp_x}{ds} = \frac{1}{\rho}p_s - \frac{1}{\rho}\left(\frac{1}{\rho} + \frac{x}{\rho}\right)$$

$$\frac{dy}{ds} = \left(1 + \frac{x}{\rho}\right)\frac{p_y}{p_s}$$

$$\frac{dp_y}{ds} = 0$$

$$\frac{dz}{ds} = -\left(1 + \frac{x}{\rho}\right)\frac{1 + p_z}{ps} + \frac{1}{\beta_0}\frac{1 + p_z}{\sqrt{(1 + p_z)^2 + \frac{m^2 c^2}{P_0^2}}}$$

$$\frac{dp_z}{ds} = 0. \quad (2.31)$$

In the paraxial approximation where $p_x, p_y \ll 1$, and assuming $\frac{m^2 c^2}{P_0^2} \ll 1$, and keeping terms up to 2nd order in coordinate and momentum,

$$H_{s,\text{dipole}} \approx -\frac{xp_z}{\rho}p_z + \frac{x^2}{2\rho^2} + \frac{p_x^2 + p_y^2}{2(1 + p_z)}, \quad (2.32)$$

22

and the equations of motion become,

$$\frac{dx}{ds} = \frac{p_x}{1 + p_z}$$

$$\frac{dp_x}{ds} = \frac{1}{\rho}p_z - \frac{x}{\rho^2}$$

$$\frac{dy}{ds} = \frac{p_y}{1 + p_z}$$

$$\frac{dp_y}{ds} = 0$$

$$\frac{dz}{ds} = -\frac{x}{\rho} + O^2(x, x', y, y')$$

$$\frac{dp_z}{ds} = 0. \tag{2.33}$$

The general solutions of Eqs. (2.33) give us the particle trajectory through a dipole,

$$x(s) = x_0 \cos(\kappa s) + \frac{p_{x0}}{\kappa} \sin(\kappa s) + \rho p_{z0}(1 - \cos(\kappa s))$$

$$p_x(s) = -\kappa x_0 \sin(\kappa s) + p_{x0} \cos(\kappa s) + p_{z0}\rho\kappa \sin(\kappa s)$$

$$y(s) = y_0 + \frac{p_{y0}}{1 + p_z}s$$

$$p_y(s) = p_{y0}$$

$$z(s) = z_0 - \frac{x_0}{\rho\kappa} \sin(\kappa s) + \frac{p_{x0}}{\rho\kappa^2}(\cos(\kappa s) - 1) - p_{x0}\left(s - \frac{1}{\kappa}\sin(\kappa s)\right)$$

$$p_z(s) = p_{z0}, \tag{2.34}$$

where $\kappa^2 = \dfrac{1}{\rho^2(1 + p_z)}$.

If we assume that $1 + p_{z0} \approx 0$, we can write the transfer matrix of a dipole of length

23

L,

$$\mathbf{M}_B = \begin{pmatrix} \cos\left(\frac{L}{\rho}\right) & \rho\sin\left(\frac{L}{\rho}\right) & 0 & 0 & 0 & \rho\left(1 - \cos\left(\frac{L}{\rho}\right)\right) \\ -\frac{1}{\rho}\sin\left(\frac{L}{\rho}\right) & \cos\left(\frac{L}{\rho}\right) & 0 & 0 & 0 & \sin\left(\frac{L}{\rho}\right) \\ 0 & 0 & 1 & L & 0 & 0 \\ 0 & 0 & 0 & 1 & 0 & 0 \\ -\sin\left(\frac{L}{\rho}\right) & \rho\left(\cos\left(\frac{L}{\rho}\right) - 1\right) & 0 & 0 & 1 & -L + \rho\sin\left(\frac{L}{\rho}\right) \\ 0 & 0 & 0 & 0 & 0 & 1 \end{pmatrix}. \qquad (2.35)$$

Notice that the transfer matrices for the quadrupole and drift, Eqs. (2.24) and (2.26) are block diagonal. These elements do not couple particle motion. The motion in any one dimension is independent of the motion in the other two dimensions. For example, the motion in the horizontal coordinates, xp_x does not depend on the motion in yp_y and zp_z. A bend, however, introduces coupling between the horizontal and longitudinal coordinates.

A transfer matrix can be divided into nine 2×2 blocks,

$$\mathbf{M}_{\text{generic}} = \begin{pmatrix} xx & xy & xz \\ yx & yy & yz \\ zx & zy & zz \end{pmatrix}. \qquad (2.36)$$

Non-zero values in the off-diagonal blocks indicate coupling. For example, non-zero values in the xy block indicate that motion in (x, p_x) is coupled to motion in (y, p_y).

The xz and zx blocks of the transfer matrix for a bend are non-zero, indicating that the horizontal and longitudinal motion is coupled. The x coordinate of a particle at the exit end of the element depends on the p_z coordinate at the entrance end. This agrees

24

with intuition. A particle with slightly more momentum, $p_{z0} > 0$, will be bent slightly less than the reference particle. This contributes a positive x displacement to the particle coordinates at the end of the element. Similarly, a particle that enters the dipole with a positive x coordinate will follow a longer path and exit with a smaller z offset. The xz coupling introduced by a bend is commonly referred to as dispersion.

2.3.4 A Simple FODO Storage Ring

Accelerators are composed of sequences of elements. A particle at the exit end of one element will be at the entrance end of the next. In so far as the forces are linear, the coordinates of a particle at the end of a string of elements can be found by successively multiplying the transfer matrices for each element. For example, a particle with initial coordinates $\vec{x}_i$ that travels through a focusing quadrupole→drift→bend→drift→defocusing quadrupole→ drift→bend→drift→ focusing quadrupole sequence of elements would exit the bend with coordinates

$$\vec{x}_f = \mathbf{M}_{QF}\mathbf{M}_D\mathbf{M}_B\mathbf{M}_D\mathbf{M}_{QD}\mathbf{M}_D\mathbf{M}_B\mathbf{M}_D\mathbf{M}_{QF}\vec{x}_i$$

$$= \mathbf{M}_{FODO}\vec{x}_i. \tag{2.37}$$

The sequence of elements just shown is called a FODO cell. Accelerators are often constructed out of cells, which are a sequence of elements that is repeated throughout the machine. FODO cells are typically defined to be symmetric. The first quad is half-length, the middle quad is full-length, and the last quad is half-length.

At this point we have enough tools in hand to construct a simple storage ring out of FODO cells. The sequence of elements defining an entire accelerator is called a lattice. Our lattice will be 200 m in circumference and composed of 16 FODO cells. Since a FODO cell has two bend magnets, each magnet will need to bring the particles through

Table 2.2: Physical parameters of demonstration FODO lattice. The dipole bending radius ρ is $\frac{160}{2\pi} \approx 25.465$ m.

Element	Length Each (m)	Quantity	Total Length (m)
Bend Dipoles	5	32	160
Focusing Quadrupoles	0.5	16	8
Defocusing Quadrupoles	0.5	16	8
Drifts	0.375	64	24
Total Circumference			200

$\frac{2\pi}{32} \approx 0.3927$ radians of arc. Each bend magnet will be 5 m long. Each quadrupole will be 0.5 m long. The physical parameters of this demonstration lattice are summarized in Tab. 2.2.

To introduce longitudinal focusing, we will replace two of the drifts, at opposite ends of the lattice, with,

$$\mathbf{M}_{fL} = \begin{pmatrix} 1 & L & 0 & 0 & 0 & 0 \\ 0 & 1 & 0 & 0 & 0 & 0 \\ 0 & 0 & 1 & L & 0 & 0 \\ 0 & 0 & 0 & 1 & 0 & 0 \\ 0 & 0 & 0 & 0 & 1 & 0 \\ 0 & 0 & 0 & 0 & f_L & 1 \end{pmatrix}. \tag{2.38}$$

This transfer matrix is simply a drift with the m_{65} element set to f_L. This will result in a z-dependent kick to p_z. Equation (2.38) resembles the transfer matrix for a simple RF cavity model [6].

Up to this point we have specified the sequence of elements, their lengths, and the bending radius of the dipoles. Two additional quantities are necessary: the quadrupole strength k and longitudinal focusing strength f_L.

It is a well-known result of linear dynamics that, for 1-dimensional systems,

$$|\text{Tr}\left(\mathbf{M}\right)| < 2.0, \tag{2.39}$$

is necessary and sufficient condition for motion to be stable over repeated application of the transfer matrix $\mathbf{M}$.

In the case of higher-dimensional coupled systems, it is necessary to first transform the system to an eigenbasis and then calculate the trace for each mode of oscillation. If the transfer matrix in the eigenbasis coordinates is stable, then the diagonal blocks will be 2×2 rotation matrices with phase advance between 0 and 2π. If the transfer matrix is unstable, then the diagonal blocks will have phase advance 0 or 2π or contain exponentially growing terms. Exponentially growing terms correspond to imaginary phase advance. This topic will be continued in Sec. 2.4.

For now, we note that the motion in our storage ring is only weakly coupled. As is often the case in accelerator physics, assuming that the machine is uncoupled and linear is a good place to start. In the presence of mode coupling, Eqn. (2.39) is a valuable, though inexact, guide for finding magnet strengths that yield stable motion.

The vertical motion in our model storage ring is completely independent of the horizontal and longitudinal, and the horizontal and longitudinal are coupled by the non-zero off-diagonal blocks in Eqn. (2.35). The coupling is weak because the off-diagonal blocks contain terms proportional to $\sin\left(\frac{L}{\rho}\right)$ and $1 - \cos\left(\frac{L}{\rho}\right)$, whereas the diagonal blocks contain terms proportional to $\cos\left(\frac{L}{\rho}\right)$ and unity. $\frac{L}{\rho}$ is typically ~ 0.05.

Transfer matrices Eqn. (2.24), (2.25), (2.26), (2.35), and (2.38) have been coded into a `Mathematica` notebook along with the demonstration lattice described in Tab. 2.2. This notebook computes the 1-turn transfer matrix for the lattice, from which we can calculate the traces of the diagonal blocks and observe how the phase space coordinates

evolve turn-by-turn.

We find that a quadrupole strength of $k = 0.1$ and longitudinal focusing of $f_L = -0.0005$ yields a stable lattice. The numerical expression of the transfer matrices for each element are located in Appendix A. The 1-turn transfer matrix is,

$$\mathbf{M}_{1\text{-turn}} =$$

$$
\begin{pmatrix}
-0.653306 & 20.1491 & 0. & 0. & 0.027270 & 29.5258 \\
-0.027775 & -0.658743 & 0. & 0. & 0.000145 & 0.523929 \\
0. & 0. & 0.170534 & -34.825 & 0. & 0. \\
0. & 0. & 0.027880 & 0.170534 & 0. & 0. \\
-0.513052 & -30.2019 & 0. & 0. & 0.929245 & -96.51 \\
0.000170 & -0.009484 & 0. & 0. & 0.000984 & 0.963229
\end{pmatrix}. \quad (2.40)
$$

The traces are,

$$
\text{Tr}\begin{pmatrix}
-0.825785 & 16.8939 \\
-0.021221 & -0.825115
\end{pmatrix} = -1.6509
$$

$$
\text{Tr}\begin{pmatrix}
-0.47686 & 175.338 \\
-0.004406 & -0.47686
\end{pmatrix} = -0.95372
$$

$$
\text{Tr}\begin{pmatrix}
0.575359 & -298.571 \\
0.001854 & 0.845118
\end{pmatrix} = 1.42048. \quad (2.41)
$$

Each of these traces has magnitude less than 2, and we find that particle motion in this lattice is stable.

Inspecting the 1-turn transfer matrix, we notice that the xz and zx blocks are non-zero, while the xy, yx, yz, and zy blocks are zero. This same pattern would be followed

28

by the 1-turn map were it computed at any location in ring. This pattern reflects the horizontal-longitudinal coupling introduced by the bend magnets, and the fact that there is no source of transverse coupling in the ring.

Shown in Figs. 2.1(a), 2.1(c), and 2.1(e) are phase space plots for the three lab-frame coordinates for a particle tracked repeatedly through one FODO cell for 500 iterations. No longitudinal focusing is included. From these plots we confirm that the motion is indeed stable. Shown in Figs. 2.1(b), 2.1(d), and 2.1(f) are the x, y, and z coordinates of the particle tracked repeatedly through a FODO cell. For the x and y plots, the FODO cell without longitudinal focusing was used. For the z plot, the FODO cell with longitudinal focusing was used.

From these plots we see that the x coordinate makes one complete oscillation approximately every 11.71 cells. This tells us that the phase advance is approximately 0.5366 radians/cell. The y coordinate completes an oscillation after approximately 20.6 cells, for a phase advance of 0.3050 radians/cell. In the z coordinate there is evident coupling. z versus turn appears to be a fast signal superimposed on a slow signal. The frequency of the fast signal is 0.5366 radians/cell, which matches the frequency of the horizontal oscillations. The frequency of the slow signal is 0.0582 radians/cell and is due to the longitudinal focusing element $\mathbf{M}_{fL}$.

There are 16 FODO cells in the demonstration lattice, 2 of which contain the longitudinal focusing element. The expected phase advances per turn are

$$Q_x = 1.3664 \tag{2.42}$$

$$Q_y = 0.7767 \tag{2.43}$$

$$Q_z = 0.1482. \tag{2.44}$$

The phase advance per cell in the x coordinate is about twice the phase advance per

29

(a) xp_x

(b) x cell-by-cell

(c) yp_y

(d) y cell-by-cell

(e) zyp_z

(f) z cell-by-cell
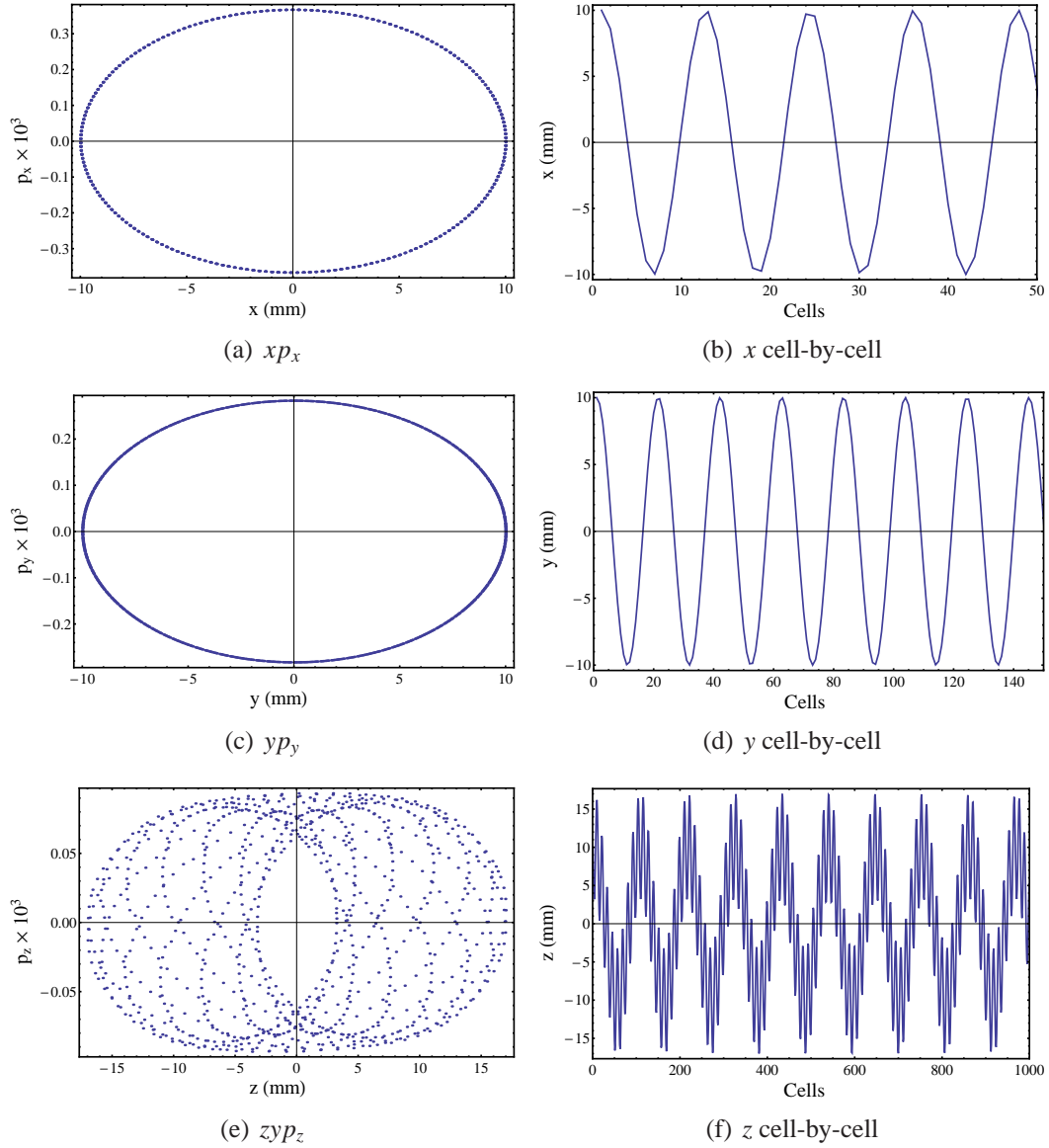
Figure 2.1: Trajectory of particle with initial coordinates $(0.01, 0, 0.01, 0, 0.01, 0)$ tracked repeatedly through a single FODO cell.

cell in the y coordinate, even though the quadrupole focusing is the same for both dimensions. The extra focusing in x comes from the dipoles and is called weak focusing. Particles which enter a sector bend with a positive x offset will follow a longer path and be subject to more bending. The upper right 2×2 block of the transfer matrix for a focusing quadrupole, Eqn. (2.24), looks similar to the upper right 2×2 block of the transfer matrix for a bend, Eqn. (2.35), with $\frac{1}{\rho^2} \sim k$. For our cell, $\frac{1}{\rho^2} \approx 0.0015$ and

$k = 0.01$. The quadrupole focusing is much stronger than the dipole focusing, but there are 10 m of dipole per cell and only 0.5 meters of focusing quadrupole. For our simple FODO ring, weak focusing makes a significant contribution to the total horizontal focusing.

Shown in Figs. 2.2(a), 2.2(c), and 2.2(e) are the phase space diagrams of a particle tracked repeatedly through the entire demonstration lattice. The initial coordinates are $x_0 = 0.01$ m, $y_0 = 0.01$ m, and $z_0 = 0.01$ m with $p_x = p_y = p_z = 0$.

Shown in Figs. 2.3(a), 2.3(b), and 2.3(c) are the absolute values of the Fourier transforms of the x, y, and z particle motion over 300 turns. The tune of an accelerator is the number of orbits in phase space that a particle makes during one turn around the machine. This is typically a whole number plus a fractional part. There are three tunes to a machine representing horizontal, vertical, and longitudinal motion. A Fourier transform of turn-by-turn data is only sensitive to the fractional part of the tune.

The Fourier transform data is mirrored about the abscissa midpoint. This is we measure only the position, rather than the position and angle. We know what the tunes are because we calculated them earlier from the phase advance per cell. This knowledge of the actual machine allows us to pick the correct peak out of the Fourier spectrum calculated from position measurements at one point in the machine.

We see that the horizontal motion has components at 0.3617 and 0.0519 oscillations per revolution. These are the horizontal and longitudinal tunes. The longitudinal motion has components at the same frequencies, but the signal at 0.0519 is stronger than the signal at 0.3617. The vertical motion is uncoupled and has one peak at 0.7767.

In Sec. 2.4.1 we will see how the 1-turn transfer matrix can be used to decompose the particle motion into eigen modes. Particle motion is uncoupled in the eigenbasis, and

(a) xp_x

(b) x turn-by-turn

(c) yp_y

(d) y turn-by-turn

(e) zp_z

(f) z turn-by-turn
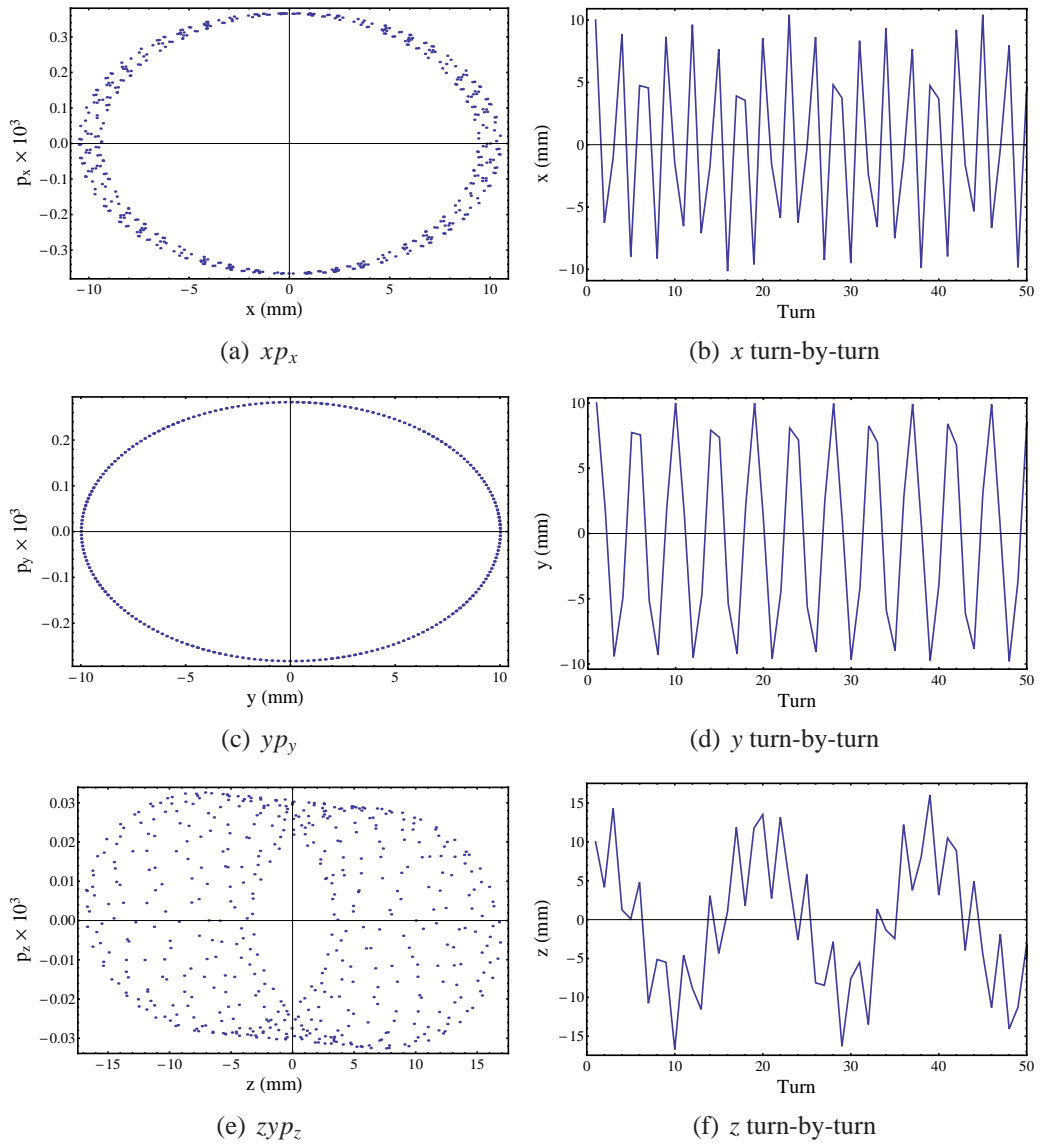
Figure 2.2: Trajectories in phase space of particle with initial coordinates $(0.01 \text{ m}, 0, 0.01 \text{ m}, 0, 0.01 \text{ m}, 0)$ tracked 500 turns through the demonstration lattice.

can be described using action-angle variables. We will see that the action of a particle is an invariant.

(a) horizontal

(b) vertical
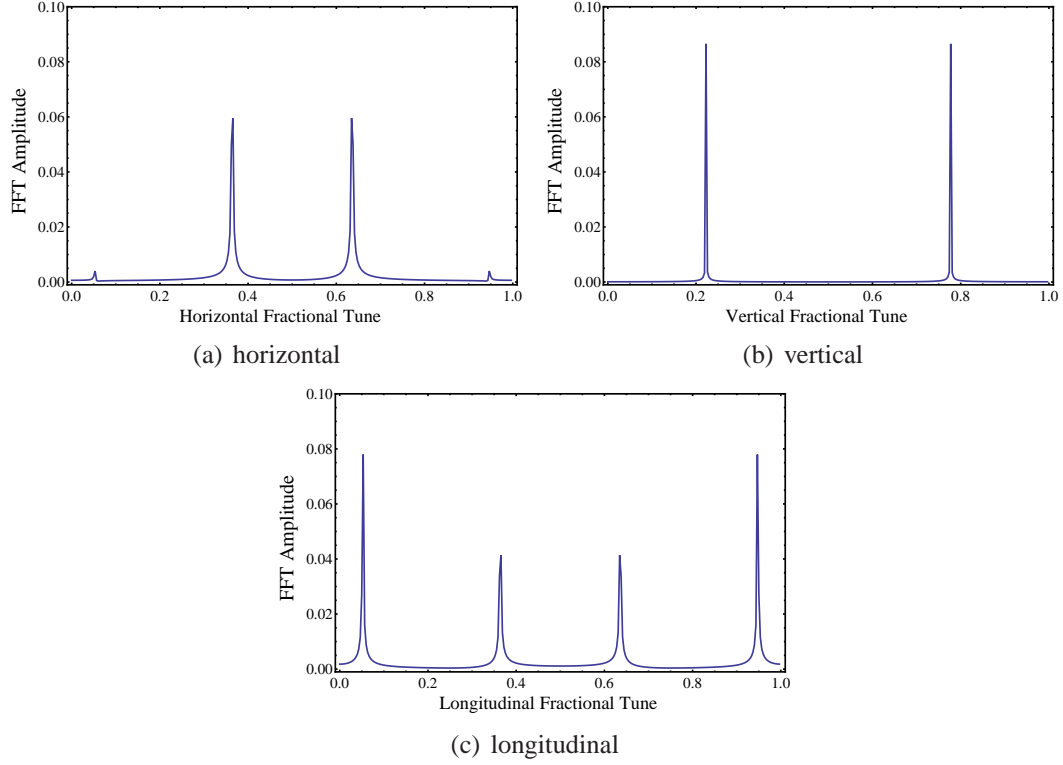
(c) longitudinal

Figure 2.3: Fourier transform of particle motion in *x*, *y*, and *z* over 300 turns. Coupling is evident between the horizontal (a) and longitudinal (c) motion, while the vertical (b) motion is uncoupled.

2.3.4.1 Horizontal-Vertical Coupling: Tilted Quadrupole

Before moving on to eigen mode decompositions, we will first make the particle motion more interesting by introducing horizontal-vertical coupling using a tilted quadrupole. A tilted quadrupole is an ordinary quadrupole that has been tilted by some angle ϕ about the *s*-axis. Tilted quadrupoles can result from magnet misalignments, or they can be deliberate. For example, a skew quadrupole is a quadrupole that has been tilted by $45°$ and is used to manipulate transverse coupling.

A transfer matrix $\mathbf{M}_{\text{ideal}}$ for some un-tilted element can be transformed into the transfer matrix $\mathbf{M}_{\text{tilted}}$ of an element tilted by an angle ϕ using [36]

$$\mathbf{M}_{\text{tilted}} = \mathbf{R}\left(-\phi\right)\mathbf{M}_{\text{ideal}}\mathbf{R}\left(\phi\right), \tag{2.45}$$

33

where

$$\mathbf{R}\left(\phi\right) = \begin{pmatrix} \cos\phi & 0 & \sin\phi & 0 & 0 & 0 \\ 0 & \cos\phi & 0 & \sin\phi & 0 & 0 \\ -\sin\phi & 0 & \cos\phi & 0 & 0 & 0 \\ 0 & -\sin\phi & 0 & \cos\phi & 0 & 0 \\ 0 & 0 & 0 & 0 & 1 & 0 \\ 0 & 0 & 0 & 0 & 0 & 1 \end{pmatrix}. \tag{2.46}$$

This transformation works because transporting a coordinate vector through a tilted quadrupole is the same as transporting a tilted coordinate vector through a non-tilted quadrupole.

The transfer matrix for a 0.5 m long defocusing quadrupole with $k = -0.1$ that has been rotated $10°$ is

$$\mathbf{M}_{\text{qf,tilted}} =$$

$$\begin{pmatrix} 1.01177 & 0.50196 & 0.004275 & 0.000713 & 0. & 0. \\ 0.047193 & 1.01177 & 0.017101 & 0.004275 & 0. & 0. \\ 0.004275 & 0.000713 & 0.98828 & 0.498045 & 0. & 0. \\ 0.017101 & 0.004275 & -0.046777 & 0.98828 & 0. & 0. \\ 0. & 0. & 0. & 0. & 1. & 0. \\ 0. & 0. & 0. & 0. & 0. & 1. \end{pmatrix}, \tag{2.47}$$

and the 1-turn transfer matrix becomes,

$\mathbf{M}_{\text{1-turn,tilted}} =$

$$
\begin{pmatrix}
-0.65956 & 20.300 & -0.012636 & -2.2365 & 0.02737 & 29.796 \\
-0.02612 & -0.69869 & 0.00334 & 0.59081 & 0.00012 & 0.45262 \\
0.16286 & -3.9408 & 0.16029 & -36.637 & -0.00262 & -7.0338 \\
0.01193 & -0.28864 & 0.02713 & 0.03781 & -0.00019 & -0.51525 \\
-0.51190 & -30.230 & 0.00233 & 0.4120 & 0.92923 & -96.560 \\
0.00014 & -0.00884 & -0.00005 & -0.00957 & 0.00098 & 0.96439
\end{pmatrix}.
$$

$$(2.48)$$

Notice in Eqn. (2.48) that the y coordinates are now coupled to the z coordinates. This is indirect coupling. By design, there are no elements in the ring which couple longitudinal motion into vertical motion, but there are elements which couple longitudinal motion into horizontal and also elements which couple horizontal into vertical. This results in a 1-turn map with longitudinal-vertical coupling.

Shown in Fig. 2.4 are the phase space and turn-by-turn trajectories of a particle tracked through the FODO ring with the tilted quadrupole. The addition of horizontal-vertical coupling makes motion more complicated than in 2.2.

Shown in Fig. 2.5 are the Fourier spectra of a particle tracked for 500 turns in the demonstration lattice with one tilted quadrupole.

(a) xp_x

(b) x turn-by-turn

(c) yp_y

(d) y turn-by-turn

(e) zyp_z

(f) z turn-by-turn
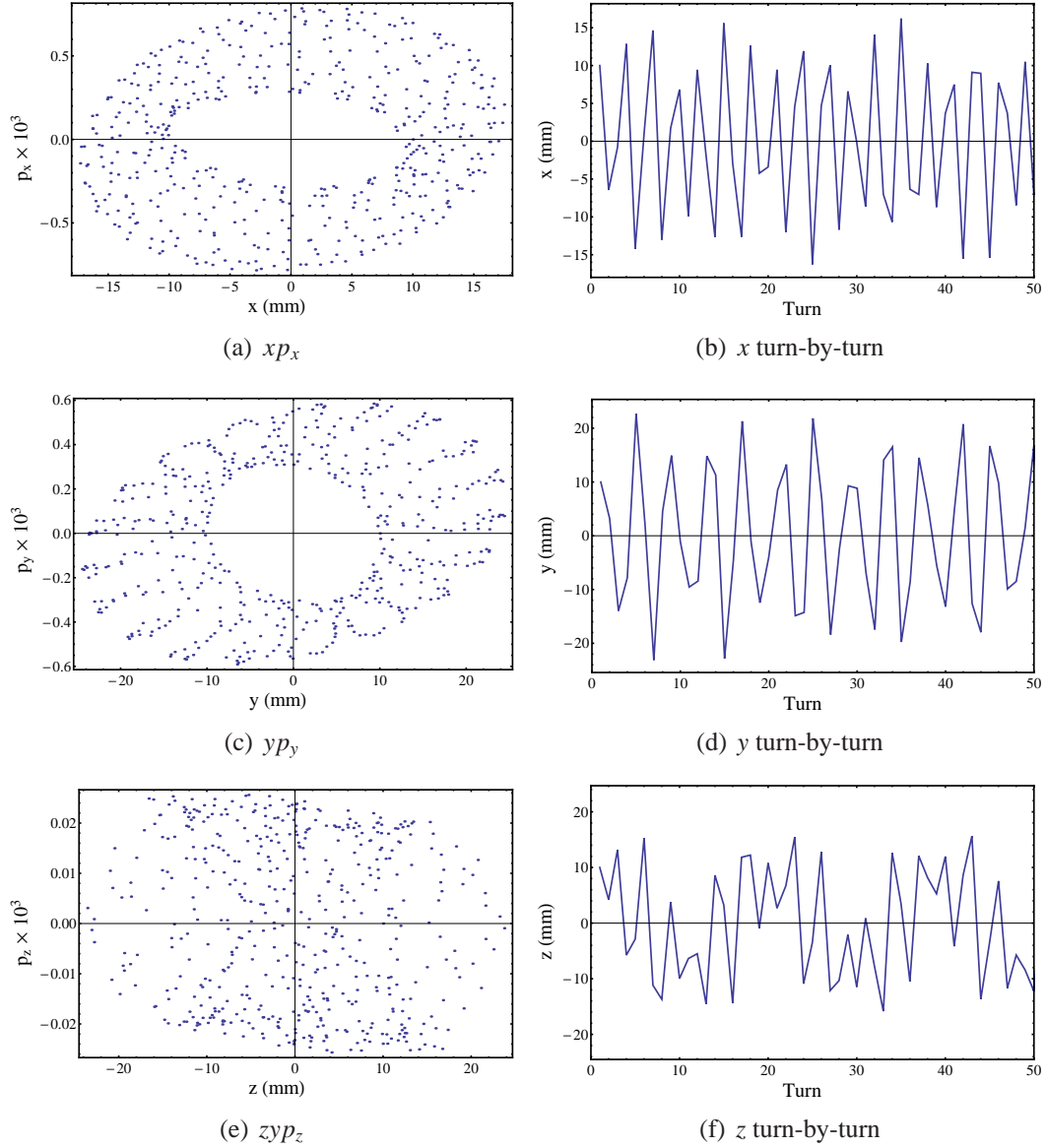
Figure 2.4: Phase space and trajectory of particle tracked through lattice with xy coupling.

2.4 Invariants of Particle Motion

In a machine without mode coupling, particle motion can be described as independent modes in the horizontal, vertical and longitudinal dimensions. Viewed from a fixed location in the ring, particles trace out perfect ellipses in (x, p_x), (y, p_y), and (z, p_z)

(a) horizontal

(b) vertical

(c) longitudinal
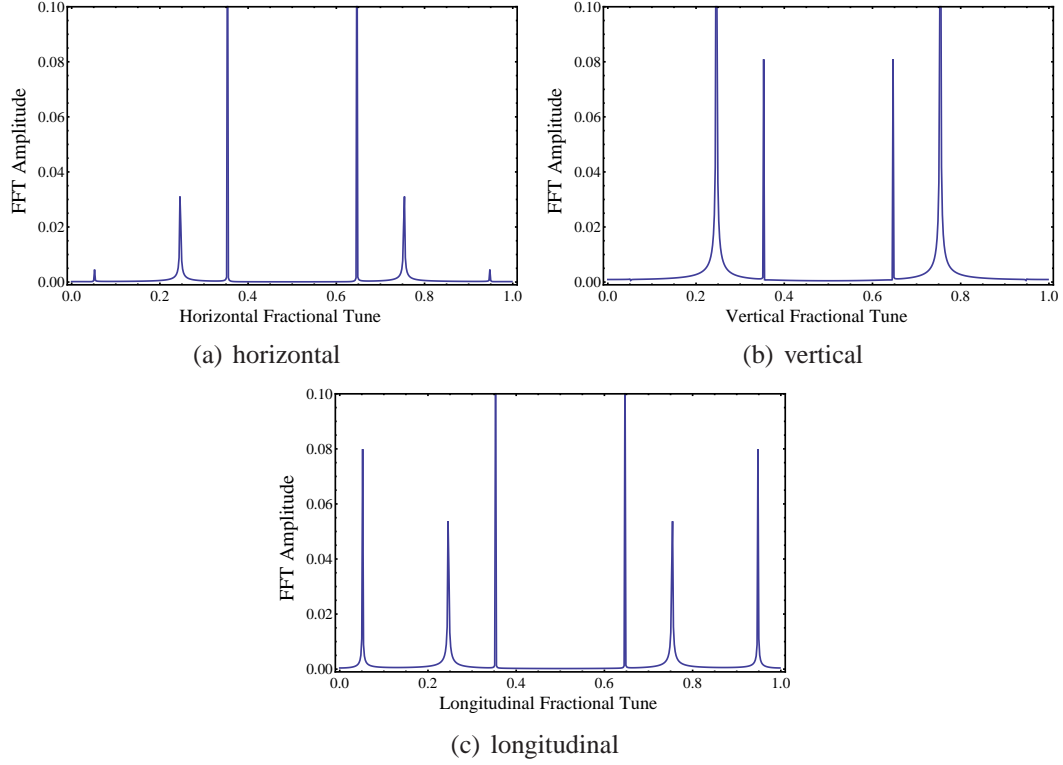
Figure 2.5: Fourier transform of x, y, and z particle motion over 500 turns in demonstration lattice with horizontal-vertical coupling.

phase space as they make successive revolutions in the accelerator.

The area of the phase space ellipse traced out by a particle over many turns is related to an invariant of particle's motion called the action J. Calling the area of the ellipse traced out in (x, p_x) space A_{xpx}, the action is defined as,

$$
\begin{aligned}
J_x &= \frac{A_{xpx}}{2\pi} \\
J_y &= \frac{A_{ypy}}{2\pi} \\
J_z &= \frac{A_{zpz}}{2\pi},
\end{aligned}
\tag{2.49}
$$

where we have made corresponding definitions for A_{ypy} and A_{zpz}. The area of an ellipse is given by $A = \pi \times a \times b$, where a and b are the major and minor axes of the ellipse. In the convenient case where the phase space ellipse is not tilted, we can calculate the

37

action of the particle as,

$$J_{x,y,z} = \frac{a_{x,y,z}b_{x,y,z}}{2}, \tag{2.50}$$

where $a_{x,y,z}$ and $b_{x,y,z}$ are the axes of the ellipse traced out in horizontal, vertical, and longitudinal phase space. The units of action are meters·radians or m·rad.

Inspecting Fig. 2.2(c), we find the axes of the ellipse traced out in vertical phase space are 0.010 and 0.000283. The action of the particle is,

$$J_y = 1.42\mu\text{m} \cdot \text{rad.} \tag{2.51}$$

Louiville's theorem states that the volume of an element of phase space remains constant if the motion of the particle is Hamiltonian. As a consequence, the shape of the ellipse may change depending on where in the ring it is evaluated, but the area of the ellipse, and hence the action, will remain the same.

An uncoupled machine is unrealistic. Bend magnets couples horizontal and longitudinal motion. Magnets cannot be perfectly aligned and have some finite alignment precision. Quadrupoles with a vertical misalignment offset create a vertical bend which couples vertical and longitudinal motion. Tilted (skewed) quadrupoles introduce transverse coupling.

The vertical action is well-defined if the motion is uncoupled and the trajectory in phase space traces out a neat ellipse. However, if coupling is present, then particle action in lab-frame coordinates (J_x, J_y, and J_z) is not a well-defined concept. This is because the phase space coordinate in one dimension on any particular turn will depend on the coordinates in the other two dimensions. The phase space trajectory will not form a closed ellipse. For the fully coupled demonstration lattice, depicted in Fig. 2.4, particle action is not well-defined in any of the lab frame coordinates. The quantities horizontal, vertical, and longitudinal action lose their meaning in a coupled machine.

38

In an uncoupled machine with a stable orbit, particle motion can be described in action-angle coordinates that correspond to the horizontal, vertical, and longitudinal dimensions. The three invariant actions we call J_x, J_y, and J_z. The angle variables are ϕ_x, ϕ_y, and ϕ_z. For example, the horizontal coordinate at any location can be described entirely by J_x and ϕ_x. Similarly for motion in the vertical and longitudinal. The coordinates of a particle at any location in the ring can be found simply by knowing its action and angle at that location of the ring.

In a coupled machine, particle motion can still be described by three invariant actions and three angles. However, the actions and angles need to be defined in the eigenbasis of the machine, typically called a, b, and c (as opposed to x, y, and z). The actions and angles are referred to as J_a, J_b, J_c and ϕ_a, ϕ_b, ϕ_c. These quantities correspond to the three eigen modes of the accelerator.

The orientation of the eigenbasis coordinates relative to the lab frame coordinates change with location in the accelerator. Motion in the a-mode can be described entirely by J_a and ϕ_a, but the orientation of a and p_a relative to $\hat{x}$, $\hat{p}_x$, $\hat{y}$, $\hat{p}_y$, $\hat{z}$, $\hat{p}_y$, changes from one location to the next.

The eigenbasis is related to the eigenvectors of the 1-turn transfer matrix. In the Sec. 2.4.1, we will decompose the 1-turn map of our fully-coupled demonstration lattice and obtain, among other interesting properties, the invariants of the particle motion. In Sec. 2.4.3.1, the tunes of the machines are obtained from the eigenvalues of the 1-turn matrix. In Sec. 2.6, these single-particle ideas will be extended to describe distributions of particles.

2.4.1   Eigen Mode Decomposition of the 6x6 Transfer Matrix

The derivation shown here follows the eigen mode analysis introduced in [58] and bridges that derivation to the normal mode analysis introduced in [41]. The ultimate result, presented in Sec. 2.7, will be a 6-dimensional normal mode decomposition.

In what follows, the eigenvectors of the 1-turn matrix are arranged into a matrix $\mathbf{E}$ and normalized to yield a unique symplectic transformation between lab-frame coordinates and eigen mode coordinates.

2.4.1.1   Eigenvectors and eigenvalues of the a transfer matrix

In linear beam optics, a particle with coordinate $\vec{x}$ can be propagated once around the storage ring from i to turn $i + 1$ using,

$$\vec{x}_{i+1} = \mathbf{M}_{1\text{turn}}\vec{x}_i, \tag{2.52}$$

where $\mathbf{M}_{1\text{turn}}$ is the 1-turn transfer matrix.

As described in Sec. 2.3.4, $\mathbf{M}_{1\text{turn}}$ is the product of the transfer matrices for the individual elements that make up the accelerator. These element-by-element transfer matrices are derived from a Hamiltonian and are therefore symplectic. The product of two symplectic matrices is itself symplectic, and so $\mathbf{M}_{1\text{turn}}$ is symplectic. Note that we are ignoring non-symplectic processes such as radiation damping and excitation and intrabeam scattering. Those processes transfer energy between particles and are not symplectic.

It is a necessary and sufficient condition for the symplecticity of the transformation

$\mathbf{M}_{1\text{turn}}$ that it satisfy the symplectic condition [15],

$$\mathbf{M}^T \mathbf{S} \mathbf{M} = \mathbf{S}, \tag{2.53}$$

where $\mathbf{S}$ is defined in Eqn. (2.12). Note that the symplectic condition is met for each of the transfer matrices derived in Sec. 2.2.

A vector $\vec{e}_i$ is an eigenvector of the square matrix $\mathbf{M}$ with corresponding eigenvalue λ_i if it satisfies,

$$\mathbf{M}\vec{e}_i = \lambda_i \vec{e}_i. \tag{2.54}$$

If $\mathbf{M}$ is stable, then the λ_i will lie on the unit circle in the complex plane. A symplectic matrix of dimension $2n$ will have $2n$ eigenvectors and eigenvalues. The eigenvectors and eigenvalues are in general complex. If $|\text{Tr } \mathbf{M}| < 2$, then they occur in reciprocal pairs such that the full set of eigenvalues is,

$$\{\lambda_1, \lambda_1^*, \lambda_2, \lambda_2^*, \lambda_3, \lambda_3^*\} \tag{2.55}$$

and the full set of eigenvectors is,

$$\{\vec{e}_1, \vec{e}_1^*, \vec{e}_2, \vec{e}_2^*, \vec{e}_3, \vec{e}_3^*\}. \tag{2.56}$$

where * indicates the complex conjugate.

2.4.1.2 Sorting the eigenvectors and forming E

Provided the beam is not strongly coupled, the eigenvectors can be sorted according to the magnitude of their elements. The assumption is that the horizontal, vertical, and longitudinal modes can each be clearly associated with one of the three eigen modes. This is true for our demonstration lattice and for nominal conditions in CesrTA. In the case of a strongly coupled lattice, more detailed bookkeeping is necessary [41]. That can happen if the tunes are near a coupling resonance or a stop band resonance.

This sorting puts the matrix of eigenvectors into a convenient form. It results in the normal mode Twiss information laying along the 2×2 diagonal blocks of the matrix of eigenvectors, see Eqn. 2.67.

Among the 3 complex-conjugate pairs of eigenvectors, for one pair the magnitude of the first element will be clearly larger than the magnitude of the other elements. This pair should be placed in the first two columns of $\mathbf{E}$. Similarly, there will be a pair whose third element is clearly dominant and should be placed into the third and forth columns of $\mathbf{E}$. The fifth element of the remaining pair of eigenvectors will be clearly dominant and should be placed into the last two columns of $\mathbf{E}$.

Thus sorted, the eigenvectors are arranged in columns to form the complex matrix of eigenvectors,

$$\mathbf{E} = (\vec{e}_1 \; \vec{e}_1^* \; \vec{e}_2 \; \vec{e}_2^* \; \vec{e}_3 \; \vec{e}_3^*) . \tag{2.57}$$

Next, it may be necessary to swap $\vec{e}_1$ with $\vec{e}_1^*$, $\vec{e}_2$ with $\vec{e}_2^*$, or $\vec{e}_3$ with $\vec{e}_3^*$. This is done to remove ambiguity when calculating the phase advance per turn from the eigenvalues. Compute the determinant of $\left(\begin{smallmatrix} E_{11} & E_{12} \\ E_{21} & E_{22} \end{smallmatrix} \right)$. Because $\vec{e}_1$ and $\vec{e}_1^*$ are complex conjugates, the determinant will be purely imaginary,

$$\begin{vmatrix} x_1 + \iota y_1 & x_1 - \iota y_1 \\ x_2 + \iota y_2 & x_2 - \iota y_2 \end{vmatrix} = 2\iota \left(y_1 x_2 - x_2 y_1 \right) . \tag{2.58}$$

If the imaginary part of the determinant is negative, swap the first and second columns. Then, compute the determinant of $\left(\begin{smallmatrix} E_{33} & E_{34} \\ E_{43} & E_{44} \end{smallmatrix} \right)$. If the imaginary part is negative, swap the third and fourth columns. Lastly, compute the determinant of $\left(\begin{smallmatrix} E_{55} & E_{56} \\ E_{65} & E_{66} \end{smallmatrix} \right)$. If the imaginary part is negative, swap the fifth and sixth columns. Swapping columns in this manner removes ambiguity in the tunes and ensures that the Twiss functions we calculate later on will have the correct sign. Without this step, the fractional tunes calculated from the eigenvalues might be reflected about the half-integer.

42

Arranging the eigenvalues along a diagonal matrix $\mathbf{D}$ in the same ordering as $\mathbf{E}$ allows us to write the eigendecomposition as,

$$\mathbf{M} = \mathbf{E}\mathbf{\Lambda}\mathbf{E}^{-1}. \tag{2.59}$$

2.4.1.3 Make E symplectic and adjust complex phase

The columns of $\mathbf{E}$ (eigenvectors of $\mathbf{M}$) are unique only up to a non-zero complex multiplier. Here we compute a column-by-column complex normalization that renders $\mathbf{E}$ symplectic and unique.

First, the columns of $\mathbf{E}$ are scaled by a real multiplier such that [58],

$$\mathbf{E}^T \mathbf{S} \mathbf{E} = i\mathbf{S}. \tag{2.60}$$

This is done by computing three normalization factors,

$$
\begin{aligned}
n_1 &= \sqrt{\mathrm{Im}\left(\vec{E}_{.1}^T S \vec{E}_{.2}\right)} \\
n_2 &= \sqrt{\mathrm{Im}\left(\vec{E}_{.3}^T S \vec{E}_{.4}\right)} \\
n_3 &= \sqrt{\mathrm{Im}\left(\vec{E}_{.5}^T S \vec{E}_{.6}\right)},
\end{aligned}
\tag{2.61}
$$

where $\vec{E}_{.i}$ refers to the ith column of $\mathbf{E}$.

Second, we multiply each column of $\mathbf{E}$ by $e^{i\theta_i}$, where θ_i is chosen to make $E_{11}e^{-i\theta_1}$, $E_{33}e^{-i\theta_2}$, and $E_{55}e^{-i\theta_3}$ real valued. θ_1, θ_2, and θ_3 are the principal values of the arguments of E_{11}, E_{33}, and E_{55},

$$
\begin{aligned}
\theta_1 &= \mathrm{Arg}\left(E_{11}\right) \\
\theta_2 &= \mathrm{Arg}\left(E_{33}\right) \\
\theta_3 &= \mathrm{Arg}\left(E_{55}\right)
\end{aligned}
\tag{2.62}
$$

where,

$$\mathrm{Arg}\,(x + \iota y) = \begin{cases} 2\arctan\left(\dfrac{y}{\sqrt{x^2 + y^2} + x}\right) & x > 0 \text{ or } y \neq 0 \\[2ex] \pi & x < 0 \text{ and } y = 0 \\[2ex] \text{undefined} & x = 0 \text{ and } y = 0 \end{cases} \tag{2.63}$$

Finally, define

$$\tilde{\mathbf{R}} = \begin{pmatrix} \dfrac{e^{-\iota\theta_1}}{n_1} & 0 & 0 & 0 & 0 & 0 \\[1.5ex] 0 & \dfrac{e^{\iota\theta_1}}{n_1} & 0 & 0 & 0 & 0 \\[1.5ex] 0 & 0 & \dfrac{e^{-\iota\theta_2}}{n_2} & 0 & 0 & 0 \\[1.5ex] 0 & 0 & 0 & \dfrac{e^{\iota\theta_2}}{n_2} & 0 & 0 \\[1.5ex] 0 & 0 & 0 & 0 & \dfrac{e^{-\iota\theta_3}}{n_3} & 0 \\[1.5ex] 0 & 0 & 0 & 0 & 0 & \dfrac{e^{\iota\theta_3}}{n_3} \end{pmatrix}, \tag{2.64}$$

and apply the normalization,

$$\mathbf{E} \leftarrow -\mathbf{E}\tilde{\mathbf{R}}. \tag{2.65}$$

The matrix of eigenvectors $\mathbf{E}$ is now unique and symplectic up to a factor of ι. It also still satisfies Eqn. (2.59). This form for $\mathbf{E}$ is the same as that in Eqn. (18) of Wolski's paper [58], except that here we have specified the complex phase of each eigenvector. The reason for doing this will become apparent when we introduce normal mode Twiss parameters and the coupling matrix in Sec. 2.7.

2.4.2 Transformation to a real basis

The eigendecomposition Eqn. (2.59) can be transformed into a real basis,

$$\mathbf{M} = \mathbf{E}\mathbf{\Lambda}\mathbf{E}^{-1}$$

$$= (\mathbf{E}\mathbf{Q})\left(\mathbf{Q}^{-1}\mathbf{\Lambda}\mathbf{Q}\right)\left(\mathbf{Q}^{-1}\mathbf{E}^{-1}\right)$$

$$= \mathbf{N}\mathbf{D}\mathbf{N}^{-1}, \tag{2.66}$$

where we have introduced the real matrices

$$\mathbf{N} = \mathbf{E}\mathbf{Q} \tag{2.67}$$

$$\mathbf{D} = \mathbf{Q}^{-1}\mathbf{\Lambda}\mathbf{Q}, \tag{2.68}$$

and,

$$\mathbf{Q} = \frac{1}{\sqrt{2}}\begin{pmatrix} 1 & \iota & 0 & 0 & 0 & 0 \\ 1 & -\iota & 0 & 0 & 0 & 0 \\ 0 & 0 & 1 & \iota & 0 & 0 \\ 0 & 0 & 1 & -\iota & 0 & 0 \\ 0 & 0 & 0 & 0 & 1 & \iota \\ 0 & 0 & 0 & 0 & 1 & -\iota \end{pmatrix}. \tag{2.69}$$

Note that $\mathbf{Q}$ is symplectic, and because the product of symplectic matrices is also symplectic, $\mathbf{N}$ and $\mathbf{D}$ are symplectic.

2.4.3 Invariants of Motion

By rearranging Eqn. (2.66), we can transform $\mathbf{M}$ into a block diagonal matrix,

$$\mathbf{D} = \mathbf{N}^{-1}\mathbf{M}\mathbf{N}, \tag{2.70}$$

45

The definition of $\mathbf{D}$ in Eqn. (2.68) can be written as

$$\mathbf{D} = \begin{pmatrix} \mathbf{Q}_2^{-1} & & \\ & \mathbf{Q}_2^{-1} & \\ & & \mathbf{Q}_2^{-1} \end{pmatrix} \begin{pmatrix} \mathbf{\Lambda}_a & & \\ & \mathbf{\Lambda}_b & \\ & & \mathbf{\Lambda}_c \end{pmatrix} \begin{pmatrix} \mathbf{Q}_2 & & \\ & \mathbf{Q}_2 & \\ & & \mathbf{Q}_2 \end{pmatrix} \tag{2.71}$$

where,

$$\mathbf{\Lambda}_i = \begin{pmatrix} \lambda_i & 0 \\ 0 & \lambda_i^* \end{pmatrix} \tag{2.72}$$

and,

$$\mathbf{Q}_2 = \frac{1}{\sqrt{2}} \begin{pmatrix} 1 & \iota \\ 1 & -\iota \end{pmatrix}. \tag{2.73}$$

If we put λ_i in modulus-argument notation,

$$\lambda_i = r_i e^{\iota\theta_i}, \tag{2.74}$$

where $r_i = \|\lambda_i\| = 1$ (we noted earlier the eigenvalues of a stable 1-turn matrix lie on the unit circle) and $\theta_i = \mathrm{Arg}\,(\lambda_i)$, we can write,

$$\mathbf{Q}_2^{-1}\mathbf{\Lambda}_i\mathbf{Q}_2 = \frac{1}{2} \begin{pmatrix} 1 & 1 \\ -\iota & \iota \end{pmatrix} \begin{pmatrix} e^{\iota\theta_i} & 0 \\ 0 & e^{-\iota\theta_i} \end{pmatrix} \begin{pmatrix} 1 & \iota \\ 1 & -\iota \end{pmatrix} \tag{2.75}$$

$$= \frac{1}{2} \begin{pmatrix} e^{\iota\theta_i} + e^{-\iota\theta_i} & \iota\left(e^{\iota\theta_i} - e^{-\iota\theta_i}\right) \\ -e^{\iota\theta_i} + e^{-\iota\theta_i} & e^{\iota\theta_i} + e^{-\iota\theta_i} \end{pmatrix} \tag{2.76}$$

$$= \begin{pmatrix} \cos\theta_i & \sin\theta_i \\ -\sin\theta_i & \cos\theta_i \end{pmatrix}, \tag{2.77}$$

where we made use of Euler's Formula in the last step. We see that $\mathbf{D}$ is a block-diagonal

matrix of the form,

$$\mathbf{D} = \begin{pmatrix} \mathbf{R}\,(\theta_a) & & \\ & \mathbf{R}\,(\theta_b) & \\ & & \mathbf{R}\,(\theta_c) \end{pmatrix}, \tag{2.78}$$

where

$$\mathbf{R}\,(\theta_i) = \begin{pmatrix} \cos\theta_i & \sin\theta_i \\ -\sin\theta_i & \cos\theta_i \end{pmatrix}. \tag{2.79}$$

Let $\vec{x}_1$ be the canonical coordinates of a particle at some location. Let $\mathbf{M}_{1\to2}$ be a transfer matrix that takes $\vec{x}_1$ to $\vec{x}_2$, $\vec{x}_2 = \mathbf{M}_{1\to2}\vec{x}_1$. Define a new vector $\vec{a}_i = \mathbf{N}^{-1}\vec{x}_i$, where $\mathbf{N}$ is from the eigen mode decomposition of $\mathbf{M}_{1\to2}$, so that,

$$\vec{a}_1 = \mathbf{N}^{-1}\vec{x}_1. \tag{2.80}$$

Then for $\vec{a}_2$ we have,

$$\begin{aligned} \vec{a}_2 &= \mathbf{N}^{-1}\vec{x}_2 \\ &= \mathbf{N}^{-1}\mathbf{M}\vec{x}_1 \\ &= \mathbf{N}^{-1}\mathbf{N}\mathbf{D}\mathbf{N}^{-1}\vec{x}_1 \\ &= \mathbf{D}\mathbf{N}^{-1}\vec{x}_1 \\ &= \mathbf{D}\vec{a}_1, \end{aligned} \tag{2.81}$$

and we see that $\vec{a}_2$ is a rotation of $\vec{a}_1$. If $\vec{a}$ is written in the following form [58],

$$
\vec{a} = \begin{pmatrix} \sqrt{2J_a}\cos\phi_a \\ -\sqrt{2J_a}\sin\phi_a \\ \sqrt{2J_b}\cos\phi_b \\ -\sqrt{2J_b}\sin\phi_b \\ \sqrt{2J_c}\cos\phi_c \\ -\sqrt{2J_c}\sin\phi_c \end{pmatrix},
\tag{2.82}
$$

then the quantities J_a, J_b, J_c are invariant under $\mathbf{D}$,

$$
\mathbf{D}\vec{a} = \begin{pmatrix} \cos\theta_a & \sin\theta_a & 0 & 0 & 0 & 0 \\ -\sin\theta_a & \cos\theta_a & 0 & 0 & 0 & 0 \\ 0 & 0 & \cos\theta_b & \sin\theta_b & 0 & 0 \\ 0 & 0 & -\sin\theta_b & \cos\theta_b & 0 & 0 \\ 0 & 0 & 0 & 0 & \cos\theta_c & \sin\theta_c \\ 0 & 0 & 0 & 0 & -\sin\theta_c & \cos\theta_c \end{pmatrix} \begin{pmatrix} \sqrt{2J_a}\cos\phi_a \\ -\sqrt{2J_a}\sin\phi_a \\ \sqrt{2J_b}\cos\phi_b \\ -\sqrt{2J_b}\sin\phi_b \\ \sqrt{2J_c}\cos\phi_c \\ -\sqrt{2J_c}\sin\phi_c \end{pmatrix}
$$

$$
= \begin{pmatrix} \sqrt{2J_a}(\cos\theta_a\cos\phi_a - \sin\theta_a\sin\phi_a) \\ -\sqrt{2J_a}(\sin\theta_a\cos\phi_a + \cos\theta_a\sin\phi_a) \\ \sqrt{2J_b}(\cos\theta_b\cos\phi_b - \sin\theta_b\sin\phi_b) \\ -\sqrt{2J_b}(\sin\theta_b\cos\phi_b + \cos\theta_b\sin\phi_b) \\ \sqrt{2J_c}(\cos\theta_c\cos\phi_c - \sin\theta_c\sin\phi_c) \\ -\sqrt{2J_c}(\sin\theta_c\cos\phi_c + \cos\theta_c\sin\phi_c) \end{pmatrix}
$$

$$
= \begin{pmatrix} \sqrt{2J_a}\cos(\theta_a+\phi_a) \\ -\sqrt{2J_a}\sin(\theta_a+\phi_a) \\ \sqrt{2J_b}\cos(\theta_b+\phi_b) \\ -\sqrt{2J_b}\sin(\theta_b+\phi_b) \\ \sqrt{2J_c}\cos(\theta_c+\phi_c) \\ -\sqrt{2J_c}\sin(\theta_c+\phi_c) \end{pmatrix}
\tag{2.83}
$$

and we see that $\mathbf{R}(\theta_i)\,\phi_i \rightarrow \phi_i + \theta_i$.

For a particle with coordinates $\vec{x}$, $\vec{a}$ is obtained as,

$$
\vec{a} = \mathbf{N}^{-1}\vec{x}.
\tag{2.84}
$$

Call the components of the vector $\vec{a} = (a, p_a, b, p_b, c, p_c)$, then the invariants can be obtained as,

$$
\begin{aligned}
J_a &= \frac{1}{2}\left(a^2 + p_a^2\right) \\
J_b &= \frac{1}{2}\left(b^2 + p_b^2\right) \\
J_c &= \frac{1}{2}\left(c^2 + p_c^2\right).
\end{aligned}
\tag{2.85}
$$

48

These invariants will become useful in later sections when we examine processes, such as photon emission and scattering, that can change the total momentum of the particle.

2.4.3.1 Calculating Phase Advance from Transfer Matrices

The three phase advances of the 6×6 transfer matrix $\mathbf{M}$ are simply the arguments of its eigenvalues. This appears to be a simple concept, but there is ambiguity over which complex conjugate to use and whether to calculate the angle clockwise or counter-clockwise. In this section, these ambiguities are resolved by specifying exactly how to perform the calculation.

The eigenvalues of a stable transfer matrix have unit length and are written as,

$$\{\lambda_a, \lambda_a^*, \lambda_b, \lambda_b^*, \lambda_c, \lambda_c^*\}. \tag{2.86}$$

If the ordering of the eigenvalues is consistent with the ordering that has been applied to the matrix of eigenvectors, then the horizontal, vertical, and longitudinal tunes of the machine can each be obtained from the second, fourth, and sixth eigenvalues by the following algorithm. Note that the first, third, and fifth eigenvalues could also be used, but the calculation would be somewhat different.

The eigenvalues are in general complex and their argument is the one turn phase advance $\Delta \phi_k$,

$$\lambda_k^* = e^{\imath \Delta \phi_k}. \tag{2.87}$$

Plotted in Fig. 2.6 is an eigenvector λ plotted in $x + \imath y$ format.

Functions which return the argument of a complex number often have a branch cut in the complex plane from 0 to $-\infty$. Examples of such functions are "atan2", `Arg` in
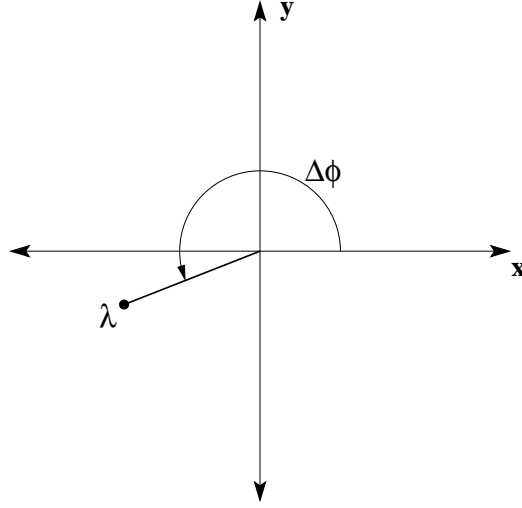
Figure 2.6: Eigenvector $\lambda = x + \iota y$ plotted on complex plane. The phase advance of the transfer matrix is $\Delta\phi$.

`Mathematica`, or the Arg function defined in Eqn. (2.63) of this thesis.

(a, p_a) and (b, p_b) advance clockwise in the a-mode and b-mode phase planes. For the a and b mode phase advance, if the eigenvector has positive imaginary part, then the phase advance is given by,

$$\Delta\phi_k = \text{Arg}\left(\lambda_k\right). \tag{2.88}$$

If the eigenvector has negative imaginary part, then the result given by $\text{Arg}\left(\lambda_k\right)$ will be negative. In that case the phase advance is given by,

$$\Delta\phi_k = 2\pi + \text{Arg}\left(\lambda_k\right). \tag{2.89}$$

At highly relativistic energies, the velocity of a particle does not change significantly with momentum, but its mass does. A particle with more momentum, a positive p_c, will be bent less by the dipoles and follow a longer path and fall behind the other particles in the bunch. Similarly, a particle with a negative p_c will follow a shorter path and move ahead of the other particles in the bunch. This is called the "negative mass" effect and

50

it causes the particle to advance counter-clockwise in the phase space. Hence, $\Delta\phi_c$ is expected to be negative.

If λ_c has negative real part, then the phase advance is given by,

$$\Delta\phi_c = \text{Arg}\,(\lambda_c)\,. \tag{2.90}$$

If λ_c has positive real part, then the phase advance is given by,

$$\Delta\phi_c = -2\pi + \text{Arg}\,(\lambda_c)\,. \tag{2.91}$$

If the transfer matrix in question happens to be the 1-turn transfer matrix, then $\Delta\phi_a$, $\Delta\phi_b$, and $\Delta\phi_c$ are the tunes of the machine.

2.4.3.2 Summary

We have shown that a symplectic transformation $\mathbf{M}_{1\to2}$ that takes the lab frame coordinates x_1 at one location in the accelerator to another can be decomposed as,

$$\vec{x}_2 = \mathbf{M}_{1\to2}\vec{x}_1$$
$$= \mathbf{N}\mathbf{D}\mathbf{N}^{-1}\vec{x}_1, \tag{2.92}$$

where $\mathbf{D}$ is a pure rotation. We have also shown that lab frame coordinates can be transformed into eigen mode coordinates,

$$\vec{a} = \mathbf{N}^{-1}\vec{x}, \tag{2.93}$$

and shown that $\vec{a}$ reduces to three invariants and three angles.

The relationship between lab coordinates $\vec{x}$ and eigen mode coordinates of the accelerator $\vec{a}$ are depicted in Fig. 2.7. $\mathbf{N}^{-1}$ can be viewed as a transformation that takes

51
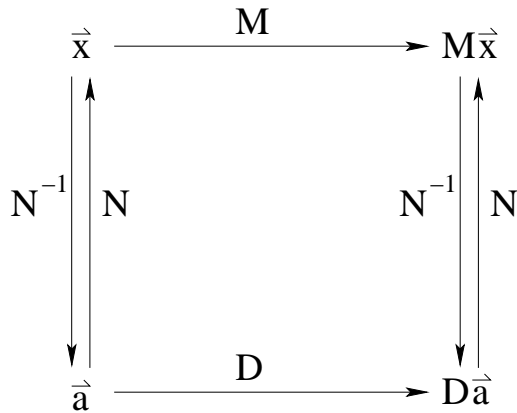
Figure 2.7: Relationship between lab coordinates $\vec{x}$ and the eigen mode coordinates of the accelerator $\vec{a}$.

canonical lab-frame coordinates into an uncoupled eigen space. In the eigen space, moving from one location in the accelerator to another is a simple rotation in (a, p_a), (b, p_b), (c, p_c) phase space. The matrix $\mathbf{N}$ takes eigen mode coordinates and transforms them back to canonical lab-frame coordinates.

In the next section, we apply these ideas to the coupled demonstration storage ring that was developed in 2.3.4.

2.5   Eigen Mode Analysis of a Simple FODO Storage Ring

When we left off in Sec. 2.3.4 we had introduced transverse coupling to our FODO storage ring by tilting one of the quadrupoles. Combined with the horizontal-longitudinal coupling from the bend magnets, this resulted in a machine with the motion coupled in all three dimensions. We had pointed out how an invariant of the particle motion, called action J, could be calculated from the area of the phase space ellipse that the particle traces out over successive turns, and that this quantity was not well defined in the presence of coupling. We also had questions about how the stability of a coupled machine

could be determined from its 1-turn matrix.

In Sec. 2.4.1 we developed an eigendecomposition of symplectic transfer matrices and used it to develop a transformation $\mathbf{N}$ between lab frame coordinates and eigen mode coordinates. We also defined three invariants of the particle motion, J_a, J_b, and J_c.

In this section we apply the eigendecomposition of the 1-turn transfer matrix to the fully-coupled demonstration FODO lattice and calculate the invariants of the particle motion and the phase advance per turn.

The 1-turn transfer matrix of the fully coupled lattice, reproduced here for convenience, is

$$\mathbf{M}_{\text{1-turn,tilted}} =$$

$$\begin{pmatrix} -0.65956 & 20.300 & -0.012636 & -2.2365 & 0.02737 & 29.796 \\ -0.02612 & -0.69869 & 0.00334 & 0.59081 & 0.00012 & 0.45262 \\ 0.16286 & -3.9408 & 0.16029 & -36.637 & -0.00262 & -7.0338 \\ 0.01193 & -0.28864 & 0.02713 & 0.03781 & -0.00019 & -0.51525 \\ -0.51190 & -30.2300 & 0.00233 & 0.4120 & 0.92923 & -96.560 \\ 0.00014 & -0.00884 & -0.00005 & -0.00957 & 0.00098 & 0.96439 \end{pmatrix}.$$

$$(2.94)$$

The sorted and normalized matrix of eigenvectors, Eqn. (2.65), for this transfer ma-

trix is,

$$\mathbf{E} =$$

$$\begin{pmatrix}
3.76319 & 3.76319 & -0.971744 - 0.173611i \\
0.006819 - 0.148647i & 0.006819 + 0.148647i & -0.020251 - 0.064565i \\
-2.009010 - 0.200563i & -2.009010 + 0.200563i & 4.64371 \\
-0.021551 - 0.031833i & -0.021551 + 0.031833i & 0.015199 - 0.120399i \\
-0.076588 - 2.832979i & -0.076588 + 2.832979i & 0.538940 - 1.618365i \\
-0.000065 + 0.000772i & -0.000065 - 0.000772i & -0.000031 - 0.000145i
\end{pmatrix}$$

$$\begin{pmatrix}
-0.971744 + 0.173611i & 0.029919 + 0.705920i & 0.029919 - 0.705920i \\
-0.020251 + 0.064565i & 0.000106 - 0.002893i & 0.000106 + 0.002893i \\
4.64371 & -0.066759 + 0.144334i & -0.066759 - 0.144334i \\
0.015199 + 0.120399i & -0.000104 - 0.007762i & -0.000104 + 0.007762i \\
0.538940 + 1.618365i & 12.74198 & 12.74198 \\
-0.000031 + 0.000145i & -0.002645 + 0.039211i & -0.002645 - 0.039211i
\end{pmatrix}. \quad (2.95)$$

Which when converted to a real basis, Eqn. (2.67), yields,

$$\mathbf{N} =$$

$$\begin{pmatrix}
5.32195 & 0 & -1.37425 & 0.24552 & 0.04231 & 0.99832 \\
0.00964 & 0.21022 & -0.02864 & 0.09131 & 0.00015 & -0.00409 \\
-2.84117 & 0.28364 & 6.56720 & 0 & -0.09441 & 0.20412 \\
-0.03048 & 0.04502 & 0.02149 & 0.17027 & -0.00015 & -0.01098 \\
-0.10831 & 4.00644 & 0.76218 & 2.28871 & 18.01989 & 0 \\
-0.00009 & -0.00109 & -0.00004 & 0.00020 & -0.00374 & 0.05545
\end{pmatrix}. \quad (2.96)$$

Recall that the initial coordinate of the particle is

$\vec{x} = (0.01 \text{ m}, 0, 0.01 \text{ m}, 0, 0.01 \text{ m}, 0)$. Calculating $\vec{a} = \mathbf{N}^{-1}\vec{x}$ gives,

$$\vec{a} = \begin{pmatrix} 0.00254 \\ 0.00021 \\ 0.00262 \\ 0.00007 \\ -0.00040 \\ -0.00004 \end{pmatrix}. \tag{2.97}$$

Applying Eqs. (2.85) yields the three invariant actions of the particle in the fully-coupled FODO lattice,

$$J_a = 3.25 \ \mu\text{m·rad}$$

$$J_b = 3.44 \ \mu\text{m·rad}$$

$$J_c = 0.08 \ \mu\text{m·rad}.$$

Comparing these numbers to the phase space ellipses in Fig.2.4 these numbers seem reasonable, but the ellipses in the phase space portraits are not well defined, so it is difficult to judge.

Repeating the same calculation for the lattice without a tilted quadrupole, depicted in Fig. 2.2, yields,

$$J_a = 1.82 \times 10^{-6}$$

$$J_b = 1.41 \times 10^{-6}$$

$$J_c = 0.15 \times 10^{-6}.$$

This value for J_b compares favorably with the value of 1.41 for J_y that was calculated in Eqn. (2.51).
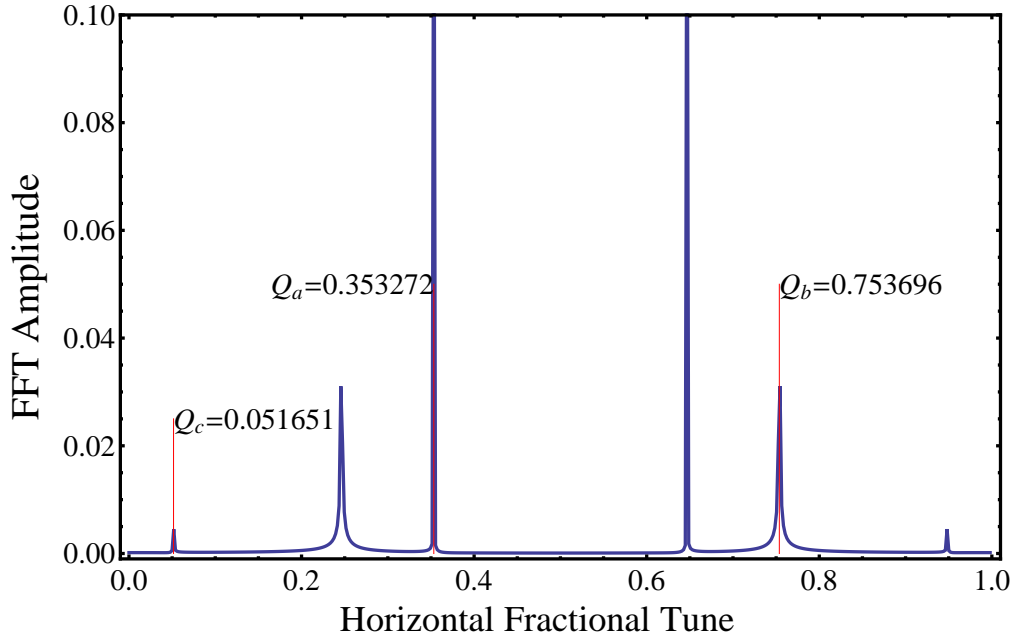
Figure 2.8: Comparing horizontal Fourier transform of particle motion in fully coupled machine to the eigen mode tunes calculated from eigenvalues of the 1-turn map.

The tunes of the fully coupled lattice are obtained by following the instructions in Sec 2.4.3.1,

$$Q_a = \frac{\Delta\phi_a}{2\pi} = 0.353272$$
$$Q_b = \frac{\Delta\phi_b}{2\pi} = 0.753696$$
$$Q_c = \frac{\Delta\phi_c}{2\pi} = -0.051651. \tag{2.98}$$

In Fig. 2.8 these calculated tunes are superimposed on the horizontal Fourier transform from the fully coupled demonstration lattice. The red lines indicate the calculated tunes. Q_a and Q_b compare favorably with the expected phase advances calculated in Eqn. (2.44). Q_c does not agree with the calculated Q_z because the full lattice includes two focusing elements, while the expected phase advance was calculated assuming repeated FODO cells.

Shown in Fig. 2.9 is the phase space and trajectory in eigen mode coordinates of a particle tracked through the fully coupled FODO lattice. The trajectories here represent

the same particle motion as plotted in Fig. 2.4, the difference is that here the coordinates are represented in the eigenbasis of the machine. As expected, the trajectories trace out circles in phase space (note that the axes of the plot are not square). The apparent amplitude modulation in the a and b turn-by-turn data is due to aliasing. The c turn-by-turn plot does not show this modulation because Q_c is a small fraction of 2π.

(a) ap_a
(b) a turn-by-turn
(c) bp_b
(d) b turn-by-turn
(e) cp_c
(f) c turn-by-turn
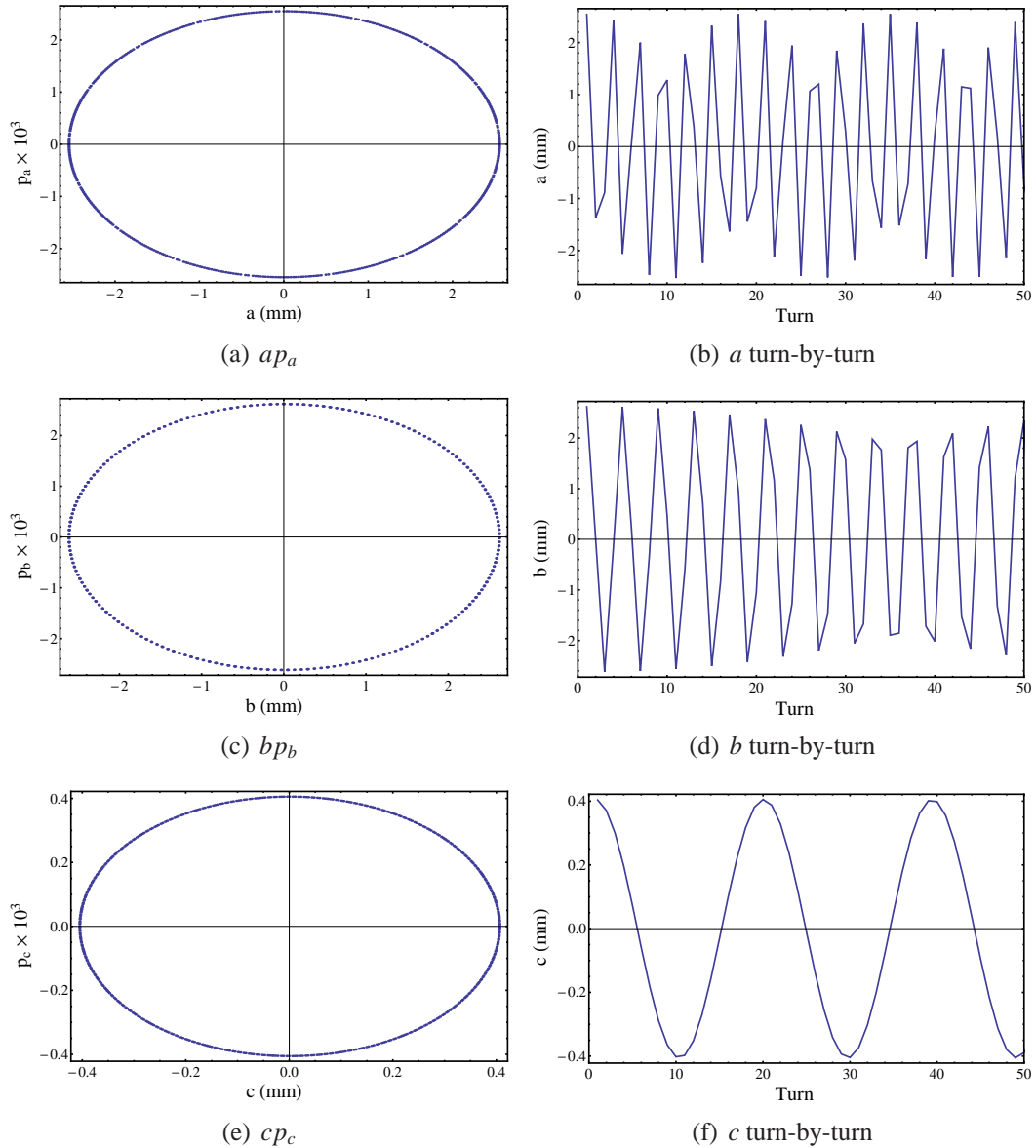
Figure 2.9: Phase space and trajectory in the eigenbasis of the machine.

Shown in Fig. 2.10 are Fourier transform of the a, b, and c coordinates of the particle

over 3000 turns. Each spectrum contains only one signal.

(a) a-mode

(b) b-mode

(c) c-mode
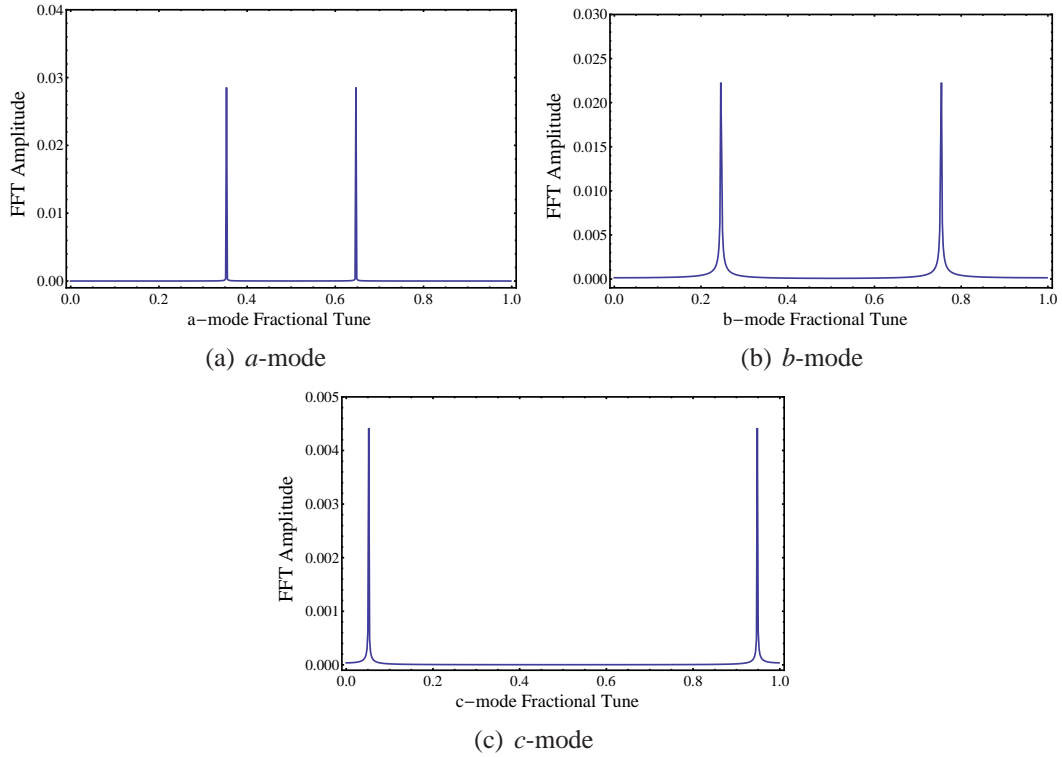
Figure 2.10: Fourier transform of particle motion in a, b, and c over 300 turns.

The stability of the lattice is determined by taking the traces of the 2×2 diagonal blocks of D, as defined in Eqn. (2.68),

$$\text{Tr}\left(D_a\right) = -1.208 \tag{2.99}$$

$$\text{Tr}\left(D_b\right) = 0.0464 \tag{2.100}$$

$$\text{Tr}\left(D_c\right) = 1.896, \tag{2.101}$$

where D_a, D_b, and D_c are the 2×2 blocks down the diagonal of D. For a stable machine, $\text{Tr}\left(D_{a,b,c}\right) = 2 \cos \Delta \phi a, b, c$.

2.5.0.3 Summary

Without eigen mode decomposition, the invariants of the particle motion in the fully coupled demonstration lattice are not well defined. Using eigen mode analysis we have obtained those invariants. We have also demonstrated how an exact tune calculation can be done using the eigenvalues of the 1-turn transfer matrix.

Using a transformation $\mathbf{N}^{-1}$ that takes lab frame coordinates $\vec{x}$ to eigen mode coordinates $\vec{a}$ we showed that over successive turns on the machine the particle traces out perfect ellipses in phase space. Additionally, a Fourier transform of the eigen mode particle motion shows one distinct signal in each of the three dimensions.

2.6 Gaussian Distributions of Particles

Thus far we have limited our discussion to a single particle. Beginning with the Hamiltonian for a particle traveling through an electromagnetic potential we developed a simple FODO storage ring. We explored the horizontal-longitudinal coupling due to bend magnets and introduced transverse coupling by tilting a quadrupole $10°$. We then developed a formalism for transporting particle coordinates into the eigenbasis of the accelerator. This allowed us to identify 3 invariants of the particle motion.

In this section we will extend these concepts to a Gaussian distribution of particles.

In storage rings with significant radiation loss in bend magnets, RF cavities are used to restore the energy that is lost as synchrotron radiation. RF cavities have a time-varying longitudinal field that is able to add energy only to those particles that are in the correct phase relationship with the field. The amount of energy added depends on when

exactly the particle arrives at the cavity. Particles which arrive early receive a stronger kick than those which arrive later. Because of the negative mass effect (see Sec. 2.4.3.1), this results in longitudinal focusing towards the ideal energy.

RF "buckets" exist at 2π intervals of the frequency of the RF system. Inside these buckets are bunches of particles which are focused longitudinally by the RF system, and transversely by the magnetic guide field (i.e. quadrupoles, bends, etc,).

Photon emission in bend magnets is a stochastic process. As a particle travels through a bend, photon emission delivers small kicks at random locations along its trajectory. Depending upon the local optics at the time of the emission, the canonical momentum may increase or decrease. The photon carries momentum away, but the RF system will add longitudinal momentum back. Over time, the distribution of momenta in a bunch of particles becomes dominated by this stochastic process. The central limit theorem predicts that, provided the random momentum changes are drawn from a distribution with a finite mean and variance, the resulting distribution of particle momenta will be Gaussian.

A three-dimensional Gaussian distribution of particles subject to linear transformations can be described by the matrix of second order moments,

$$
\Sigma =
\begin{pmatrix}
\langle xx \rangle & \langle xp_x \rangle & \langle xy \rangle & \langle xp_y \rangle & \langle xz \rangle & \langle xp_z \rangle \\
\langle p_x x \rangle & \langle p_x p_x \rangle & \langle p_x y \rangle & \langle p_x p_y \rangle & \langle p_x z \rangle & \langle p_x p_z \rangle \\
\langle yx \rangle & \langle yp_x \rangle & \langle yy \rangle & \langle yp_y \rangle & \langle yz \rangle & \langle yp_z \rangle \\
\langle p_y x \rangle & \langle p_y p_x \rangle & \langle p_y y \rangle & \langle p_y p_y \rangle & \langle p_y z \rangle & \langle p_y p_z \rangle \\
\langle zx \rangle & \langle zp_x \rangle & \langle zy \rangle & \langle zp_y \rangle & \langle zz \rangle & \langle zp_z \rangle \\
\langle p_z x \rangle & \langle p_z p_x \rangle & \langle p_z y \rangle & \langle p_z p_y \rangle & \langle p_z z \rangle & \langle p_z p_z \rangle
\end{pmatrix},
\tag{2.102}
$$

where we have assumed that the first-order moments vanish. This matrix is called the

Σ-matrix of the beam.

A Σ-matrix is properly matched to a machine if it is invariant under the 1-turn map,

$$\Sigma = \mathbf{M}\Sigma\mathbf{M}^T. \tag{2.103}$$

Because $\mathbf{M}$ is symplectic, $\mathbf{M}^T\mathbf{SM} = \mathbf{S}$, we have[58],

$$\mathbf{M}\Sigma\mathbf{M}^T\mathbf{SM} = \Sigma\mathbf{SM}$$

$$\mathbf{M}\Sigma\mathbf{S} = \Sigma\mathbf{SM}$$

$$(\Sigma\mathbf{S})^{-1}\mathbf{M}(\Sigma\mathbf{S}) = \mathbf{M}. \tag{2.104}$$

Say that $\Sigma\mathbf{S}$ has the eigendecomposition,

$$\Sigma\mathbf{S} = \tilde{\mathbf{E}}\mathbf{F}\tilde{\mathbf{E}}^{-1}. \tag{2.105}$$

Then Eqn. (2.104) is satisfied by any matrix $\mathbf{M}$ that can be written as $\mathbf{M} = \tilde{\mathbf{E}}\tilde{\mathbf{\Lambda}}\tilde{\mathbf{E}}^{-1}$,

$$(\Sigma\mathbf{S})^{-1}\mathbf{M}(\Sigma\mathbf{S}) = \mathbf{M}$$

$$\tilde{\mathbf{E}}\mathbf{F}^{-1}\tilde{\mathbf{E}}^{-1}\tilde{\mathbf{E}}\tilde{\mathbf{\Lambda}}\tilde{\mathbf{E}}^{-1}\tilde{\mathbf{E}}\mathbf{F}\tilde{\mathbf{E}}^{-1} = \tilde{\mathbf{E}}\tilde{\mathbf{\Lambda}}\tilde{\mathbf{E}}^{-1}$$

$$\mathbf{F}^{-1}\tilde{\mathbf{\Lambda}}\mathbf{F} = \tilde{\mathbf{\Lambda}}$$

$$\tilde{\mathbf{\Lambda}} = \tilde{\mathbf{\Lambda}}, \tag{2.106}$$

because $\mathbf{F}$ and $\tilde{\mathbf{\Lambda}}$ are diagonal and therefore commute.

However, the matrix $\tilde{\mathbf{E}}$ that diagonalizes $\mathbf{M}$ is given uniquely by its eigendecomposition. $\tilde{\mathbf{E}}$ must be the matrix of eigenvectors which are unique up to a non-zero complex normalization. We have,

$$\tilde{\mathbf{E}} = \mathbf{E},$$

$$\tilde{\mathbf{\Lambda}} = \mathbf{\Lambda}, \tag{2.107}$$

Therefore, the eigenvectors of the 1-turn transfer matrix $\mathbf{M}$ are the same as the eigenvectors of a Σ-matrix matched to the machine.

In [58], Wolski shows that the eigenvalues of $\mathbf{\Sigma S}$ are invariant under any symplectic transformation, not just the 1-turn map. The eigenvalues of $\mathbf{\Sigma S}$ are the same no matter where in the machine it is evaluated. They are therefore invariants of the bunch distribution. The eigenvalues are typically written as ϵ_a, ϵ_b, and ϵ_c,

$$\{-\iota\epsilon_a, \ \iota\epsilon_a, \ -\iota\epsilon_b, \ \iota\epsilon_b, \ -\iota\epsilon_c, \ \iota\epsilon_c, \ \} \tag{2.108}$$

The three invariants ϵ_a, ϵ_b, and ϵ_c of the beam distribution are commonly referred to as emittances. These are particle distributions analogous to the invariant actions of a single particle's trajectory J_a, J_b, and J_c.

In the case of an uncoupled machine, the invariants are referred to as ϵ_x, ϵ_y, and ϵ_z and can be calculated from,

$$\begin{aligned}
\epsilon_x &= \sqrt{\langle x^2 \rangle \langle p_x^2 \rangle} \\
\epsilon_y &= \sqrt{\langle y^2 \rangle \langle p_y^2 \rangle} \\
\epsilon_z &= \sqrt{\langle z^2 \rangle \langle p_z^2 \rangle},
\end{aligned} \tag{2.109}$$

where $\langle \cdot \rangle$ indicates averaging over all particles in the bunch.

In the case of a coupled machine, ϵ_x, ϵ_y, and ϵ_z calculated in this manner are not invariant, but ϵ_a, ϵ_b, ϵ_c are.

Note that ϵ_a, ϵ_b, ϵ_c are simply the eigen mode emittances and can be calculated using,

$$\begin{aligned}
\epsilon_a &= \sqrt{\langle a^2 \rangle \langle p_a^2 \rangle} \\
\epsilon_b &= \sqrt{\langle b^2 \rangle \langle p_b^2 \rangle} \\
\epsilon_c &= \sqrt{\langle c^2 \rangle \langle p_c^2 \rangle}.
\end{aligned} \tag{2.110}$$

2.6.1 Building the Σ-matrix of a Matched Beam Distribution

From Eqn. (2.107) we have that a matched beam distribution has the same eigenvectors as the 1-turn matrix. From [58] we have that the eigenvalues of the beam distribution are the eigen mode emittances.

The Σ-matrix of a matched beam can be obtained from the eigenvectors of the 1-turn transfer matrix and the eigen mode emittances of the beam. With the eigenvectors arranged as in Eqn. (2.107), and the three emittances ϵ_a, ϵ_b, and ϵ_c, the Σ-matrix is given by,

$$\Sigma S = E \begin{pmatrix} -\iota\epsilon_a & 0 & 0 & 0 & 0 & 0 \\ 0 & \iota\epsilon_a & 0 & 0 & 0 & 0 \\ 0 & 0 & -\iota\epsilon_b & 0 & 0 & 0 \\ 0 & 0 & 0 & \iota\epsilon_b & 0 & 0 \\ 0 & 0 & 0 & 0 & -\iota\epsilon_c & 0 \\ 0 & 0 & 0 & 0 & 0 & \iota\epsilon_c \end{pmatrix} E^{-1}, \tag{2.111}$$

or in terms of real-valued matrices by,

$$\Sigma S = N \begin{pmatrix} 0 & \epsilon_a & 0 & 0 & 0 & 0 \\ -\epsilon_a & 0 & 0 & 0 & 0 & 0 \\ 0 & 0 & 0 & \epsilon_b & 0 & 0 \\ 0 & 0 & -\epsilon_b & 0 & 0 & 0 \\ 0 & 0 & 0 & 0 & 0 & \epsilon_c \\ 0 & 0 & 0 & 0 & -\epsilon_c & 0 \end{pmatrix} N^{-1}$$

$$= N\Lambda_{\text{real}}N^{-1}, \tag{2.112}$$

where the real matrix of eigenvalues has been defined as Λ_{real}. The horizontal and vertical beam sizes and bunch length are simply $\sqrt{\Sigma_{11}}$, $\sqrt{\Sigma_{33}}$, and $\sqrt{\Sigma_{55}}$.

2.7   Normal Mode Twiss Parameters and the Coupling Matrix

Parameterizing accelerator optics in terms of Twiss parameters is a well-established technique [8]. Each lab frame coordinate is parameterized with three variables: β, α, and ϕ. β and α are related by,

$$\alpha = -\frac{1}{2}\frac{d\beta}{ds},$$

(2.113)

where s is the longitudinal coordinate. ϕ is an angle.

The beam envelope in a particular dimension is defined as exactly 1σ of the Gaussian distribution of particles. σ_x, σ_y, and σ_z are usually used to refer to the horizontal, vertical, and longitudinal beam envelope. The transverse beam envelopes are often referred to as the beam sizes. The longitudinal beam envelope is usually called the bunch length.

Using emittance ϵ_x to characterize the horizontal phase space volume of the beam, the envelope is given by

$$\begin{pmatrix} \sigma_x \\ \sigma'_x \end{pmatrix} = \sqrt{\epsilon_x}\begin{pmatrix} \sqrt{\beta_x} & 0 \\ -\frac{\alpha_x}{\sqrt{\beta_x}} & \frac{1}{\sqrt{\beta_x}} \end{pmatrix}\begin{pmatrix} \sin\phi_x \\ \cos\phi_x \end{pmatrix}.$$

(2.114)

Similar equations exist for the vertical y and longitudinal z coordinates.

For the transverse dimensions, Sagan and Rubin extend the the Twiss formalism to normal mode coordinates in [41]. Normal mode space is similar to eigen space, except that phase space ellipses in normal mode space are sheared and stretched by

normal mode Twiss parameters. This shearing and stretching in normal mode space is analogous to that in the lab coordinates.

In normal mode space, the coordinates are simply uncoupled. They preserve optical properties similar to those of the lab frame coordinates. In an eigen space, the coordinates are uncoupled and the phase space ellipse is reduced to a circle.

Sagan and Rubin derive a matrix $\mathbf{V}$ that takes lab frame transverse phase space coordinates $\vec{x}_2$ into two dimensional normal mode phase space coordinates,

$$\vec{q}_2 = \mathbf{V}^{-1}\vec{x}_2, \tag{2.115}$$

where $\vec{q}$ refers to coordinates in the normal mode basis.

They also derive a block-diagonal matrix $\mathbf{G}$ that contains normal mode Twiss parameters,

$$\mathbf{G}_2 = \left(\begin{array}{c:c} \mathbf{G}_a & 0 \\ \hdashline 0 & \mathbf{G}_b \end{array} \right). \tag{2.116}$$

where,

$$\mathbf{G}_{a,b} = \left(\begin{array}{cc} \frac{1}{\sqrt{\beta_{a,b}}} & 0 \\ \frac{\alpha_{a,b}}{\sqrt{\beta_{a,b}}} & \sqrt{\beta_{a,b}} \end{array} \right) \tag{2.117}$$

$\mathbf{G}$ tells us about the shape of the beam envelope in normal mode space.

If $\vec{q}$ is normalized by the normal mode Twiss parameters, then the motion is reduced to a circle and the coordinates in the transverse eigen space are obtained,

$$\vec{a}_2 = \mathbf{G}\vec{q}. \tag{2.118}$$

It is then easy to derive the relationship between lab frame coordinates and eigen

65

mode coordinates within the normal mode formalism,

$$\vec{a}_2 = \mathbf{G}\mathbf{V}^{-1}\vec{x}_2. \tag{2.119}$$

Notice that the conversion between lab frame coordinates and eigen mode coordinates put forth by Wolski and reproduced in Sec. 2.4.1 is

$$\vec{a} = \mathbf{N}^{-1}\vec{x}. \tag{2.120}$$

If we say that $\mathbf{G}$ and $\mathbf{V}$ are now 6×6, then we see an important connection between the eigen mode formalism and normal mode formalism,

$$\mathbf{N} = \mathbf{V}\mathbf{G}^{-1}. \tag{2.121}$$

In Eqn. (2.64) the matrix of eigenvectors is normalized with a specially calculated phase factor. The effect of this normalization is to put the resulting $\mathbf{N}$ into a form such that its 2×2 diagonal blocks are simply the symplectic conjugates of the normal mode Twiss factors times γ_a, γ_b, or γ_c. Comparisons between the $\mathbf{G}$ matrix and $\gamma_{a,b,c}$ obtained by the normal mode formalism and the $\mathbf{G}$ obtained from the eigen modes formalism agree completely.

The three parameters γ_a, γ_b, and γ_c that are used in the normal mode formalism can

be obtained from the eigen modes formalism as,

$$\gamma_a^2 = \text{Det} \begin{pmatrix} N_{11} & N_{12} \\ N_{21} & N_{22} \end{pmatrix} \tag{2.122}$$

$$\gamma_b^2 = \text{Det} \begin{pmatrix} N_{33} & N_{34} \\ N_{43} & N_{44} \end{pmatrix} \tag{2.123}$$

$$\gamma_c^2 = \text{Det} \begin{pmatrix} N_{55} & N_{56} \\ N_{65} & N_{66} \end{pmatrix}. \tag{2.124}$$

The block-diagonal matrix $\mathbf{G}_2$ defined in Eqn. (2.116) is a 4×4 matrix. The full 6×6 matrix is

$$\mathbf{G} = \begin{pmatrix} \mathbf{G}_a & 0 & 0 \\ 0 & \mathbf{G}_b & 0 \\ 0 & 0 & \mathbf{G}_c \end{pmatrix}, \tag{2.125}$$

where the diagonal blocks can be obtained from $\mathbf{N}$,

$$\mathbf{G}_{a,b,c} = \frac{1}{\gamma_a} \begin{pmatrix} N_{11} & N_{12} \\ N_{21} & N_{22} \end{pmatrix}^\dagger. \tag{2.126}$$

Dagger † represents the symplectic conjugate,

$$\begin{pmatrix} A_{11} & A_{12} \\ A_{21} & A_{22} \end{pmatrix}^\dagger = \begin{pmatrix} A_{22} & -A_{12} \\ -A_{21} & A_{11} \end{pmatrix}. \tag{2.127}$$

Shown in Fig. 2.11 are the turn-by-turn trajectories and phase space plots in normal mode coordinates of a particle tracked for 500 turns through the fully coupled demonstration lattice. Notice that the motion does not appear to be coupled. The effect of the

67

normal mode Twiss parameters is evident in the shearing and stretching of the phase space ellipses.

(a) $q_1 p_{q1}$

(b) q_1 cell-by-cell

(c) $q_2 p_{q2}$

(d) q_2 cell-by-cell

(e) $q_3 p_{q3}$

(f) q_3 cell-by-cell
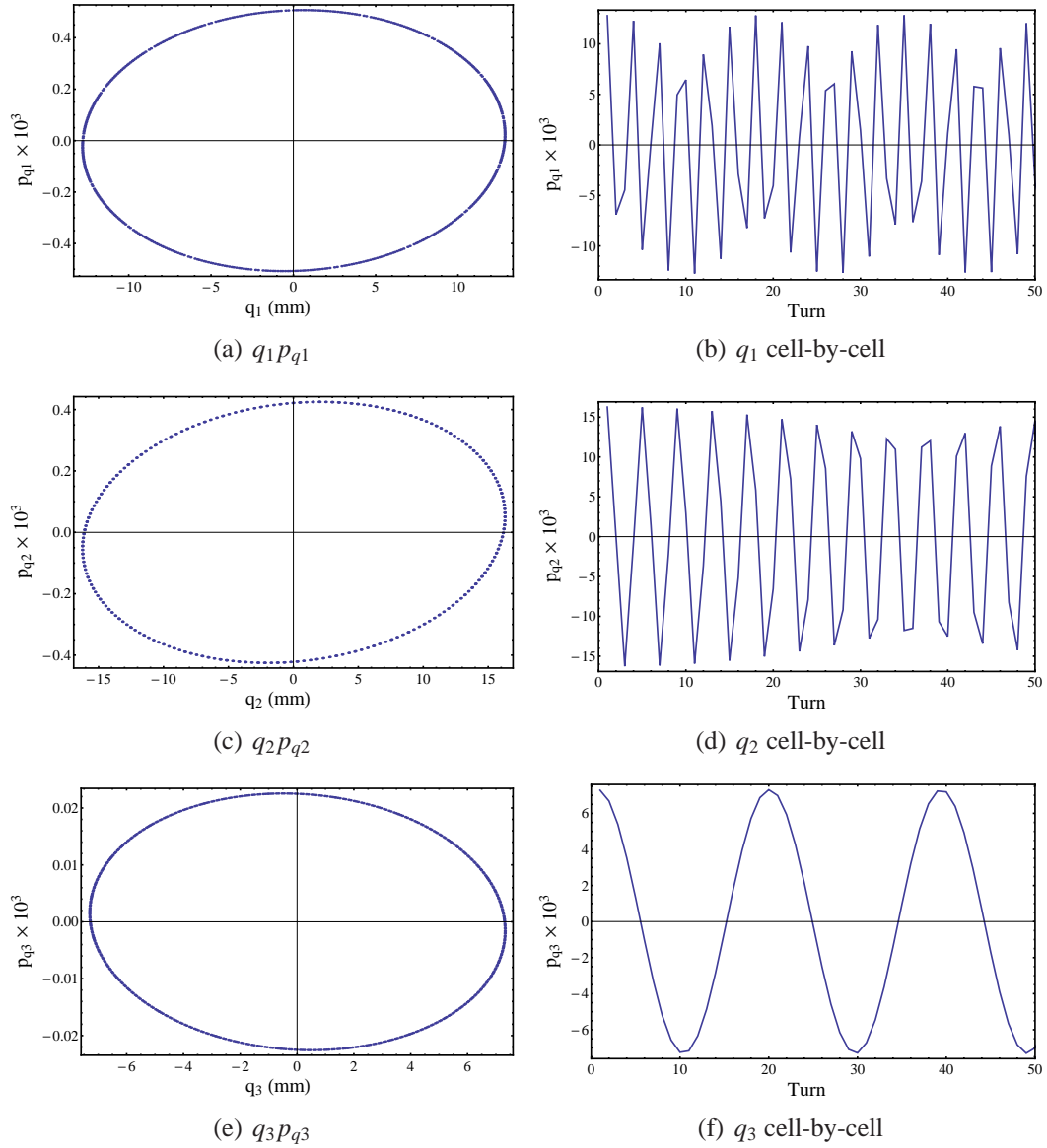
Figure 2.11: Trajectory in normal coordinates of particle with initial lab frame coordinates $(0.01 \text{ m}, 0, 0.01 \text{ m}, 0, 0.01 \text{ m}, 0)$. Particle is tracked for 500 turns.

Shown in Fig. 2.12 are the three normal mode β-functions plotted versus location in meters. Smaller values of β indicated stronger focusing and larger phase advance. The steep segments indicate the location of focusing and defocusing quadrupoles. The long

segments indicate the location of bend magnets.

(a) β_a

(b) β_b

(c) β_c
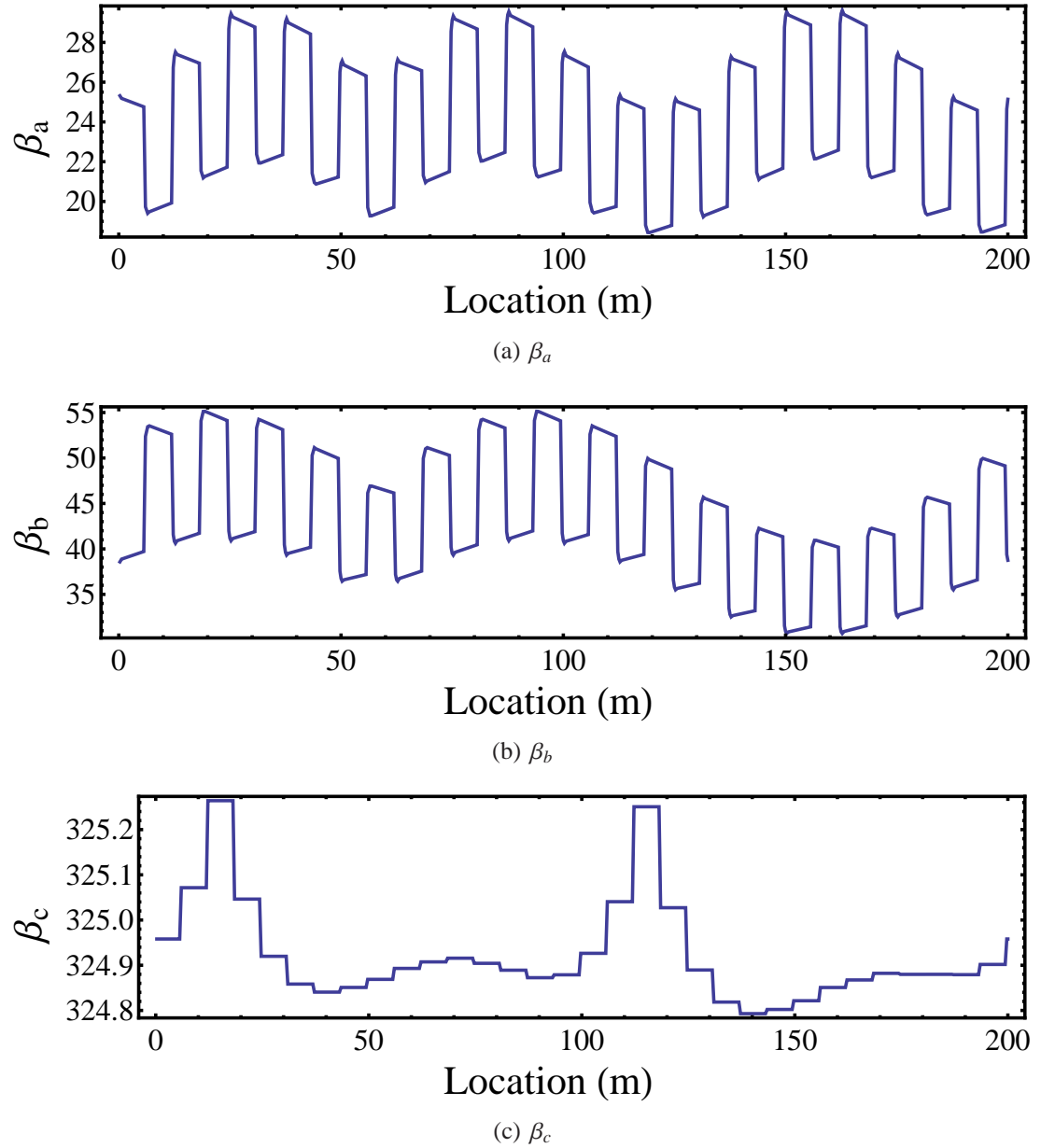
Figure 2.12: Normal mode β-functions calculated from eigen-decomposition of the 1-turn transfer matrix. The lattice elements are not symmetric about $s = 0$ m.

With **G** thus easily obtained from **N**, the transformation from lab coordinates to normal mode coordinates via the eigen decomposition is obtained,

$$\mathbf{V} = \mathbf{NG}. \tag{2.128}$$

$\mathbf{N}$ transforms from lab frame coordinates to the eigen mode coordinates. It "removes" both the coupling and Twiss parameters from the coordinate system. One way to think of $\mathbf{N}$ is that it has information about both the coupling in the accelerator and the local optics. By decomposing $\mathbf{N}$ into $\mathbf{V}$ and $\mathbf{G}$ we have separated the coupling information from the optics.

It is convenient to normalize the optics dependence out of $\mathbf{V}$,

$$\bar{\mathbf{V}} = \mathbf{GVG}^{-1}. \tag{2.129}$$

Plugging $\mathbf{V} = \mathbf{NG}$ into Eqn. (2.129), we obtain

$$\bar{\mathbf{V}} = \mathbf{GN}. \tag{2.130}$$

$\mathbf{N}$, $\mathbf{G}$, $\mathbf{V}$, are $\bar{\mathbf{V}}$ all symplectic. $\mathbf{V}$ can be written in the form,

$$\mathbf{V} = \begin{pmatrix} \gamma_a \mathbf{I} & \mathbf{C}_{ab} & \mathbf{C}_{ac} \\ -\mathbf{D}_{ba}^\dagger & \gamma_b \mathbf{I} & \mathbf{C}_{bc} \\ -\mathbf{D}_{ca}^\dagger & -\mathbf{D}_{cb}^\dagger & \gamma_c \mathbf{I} \end{pmatrix}, \tag{2.131}$$

where $\mathbf{I}$ is the 2×2 identity matrix and The $\mathbf{C}$ and $\mathbf{D}$ matrices describe coupling between the modes. $\bar{\mathbf{V}}$ can be written in the form,

$$\bar{\mathbf{V}} = \begin{pmatrix} \gamma_a \mathbf{I} & \bar{\mathbf{C}}_{ab} & \bar{\mathbf{C}}_{ac} \\ -\bar{\mathbf{D}}_{ba}^\dagger & \gamma_b \mathbf{I} & \bar{\mathbf{C}}_{bc} \\ -\bar{\mathbf{D}}_{ca}^\dagger & -\bar{\mathbf{D}}_{cb}^\dagger & \gamma_c \mathbf{I} \end{pmatrix}. \tag{2.132}$$

In machines with coupling between only two of the modes, $\mathbf{C}_{ij} = \mathbf{D}_{ji}$. If the motion is uncoupled, then the $\mathbf{C}$'s and $\mathbf{D}$'s are $\mathbf{0}$ (matrix of zeros), and $\mathbf{V} = \bar{\mathbf{V}} = \mathbf{I}$.

If all three modes are coupled, and the coupling is not too strong, then the off-diagonal blocks resemble the symplectic conjugate of their opposite diagonal counterpart. Intuitively, it feels like it should be possible to derive a relationship between the

three $\mathbf{C}$ matrices and three $\mathbf{D}$ matrices. I have not been able to find such a relationship, but if such a relationship were found, it could allow for the optics correction procedures described in [1] to be extended from the two transverse to all three modes. This would concise optics correction procedures that account for coupling between all three modes.

2.7.0.1   Beam Size Calculations

A method is given in [41] for obtaining the horizontal and vertical beam sizes from the 4D normal mode Twiss parameters and emittances. Here we use Eqn. (2.112) and Eqn. (2.121) to obtain formulas for the horizontal, vertical, and longitudinal beam sizes. The result is a 6D counterpart to the 4D formulas in [41].

Starting from $\mathbf{\Sigma}$-matrix in terms of real-valued matrices, Eqn. (2.112),

$$\mathbf{\Sigma S} = \mathbf{N}\mathbf{\Lambda}_{\mathrm{real}}\mathbf{N}^{-1}, \tag{2.133}$$

we use the definition of $\mathbf{N}$ in terms of the normal mode matrices $\bar{\mathbf{V}}$ and $\mathbf{G}$ to obtain,

$$\mathbf{\Sigma S} = \mathbf{G}^{-1}\bar{\mathbf{V}}\mathbf{\Lambda}_{\mathrm{real}}\bar{\mathbf{V}}^{-1}\mathbf{G}. \tag{2.134}$$

Taking $\sigma_x^2 = \mathbf{\Sigma}_{11}$, $\sigma_y^2 = \mathbf{\Sigma}_{33}$, and $\sigma_z^2 = \mathbf{\Sigma}_{55}$ and simplifying gives the projections of the beam envelope into the lab frame,

$$\sigma_x^2 = \beta_a \left(\gamma_a^2 \epsilon_a + \left(\bar{C}_{ab11}^2 + \bar{C}_{ab12}^2 \right) \epsilon_b + \left(\bar{C}_{ac11}^2 + \bar{C}_{ac12}^2 \right) \epsilon_c \right) \tag{2.135}$$

$$\sigma_y^2 = \beta_b \left(\gamma_b^2 \epsilon_b + \left(\bar{D}_{ba12}^2 + \bar{D}_{ba22}^2 \right) \epsilon_a + \left(\bar{C}_{bc11}^2 + \bar{C}_{bc12}^2 \right) \epsilon_c \right) \tag{2.136}$$

$$\sigma_z^2 = \beta_c \left(\gamma_c^2 \epsilon_c + \left(\bar{D}_{ca12}^2 + \bar{D}_{ca22}^2 \right) \epsilon_a + \left(\bar{D}_{cb12}^2 + \bar{D}_{cb22}^2 \right) \epsilon_b \right) \tag{2.137}$$

Note that γ_a, γ_b, and γ_c are not the Twiss γ functions, but are coupling parameters as defined in Eqn. (2.132). The following property of symplectic matrices was useful in deriving these formulas: $\mathbf{M}^{-1} = \mathbf{S}^{-1}\mathbf{M}^T\mathbf{S}$.

These projections are stated in terms of $\mathbf{V}$ in Appendix B.

Equations (2.135), (2.136), and (2.137) are the lab frame projections of the beam envelope and are what is typically measured by the instrumentation. Written in this format, it is clear how the various coupling terms in $\bar{\mathbf{V}}$ contribute to the projected beam sizes.

2.7.0.2 Summary

We have obtained the 6×6 $\bar{\mathbf{V}}$ coupling matrix simply by extracting $\mathbf{G}$ from a properly normalized eigen mode decomposition. This is a novel and direct method for obtaining $\bar{\mathbf{V}}$. We have also established clear and simple relations between normal mode coordinates and eigen mode coordinates.

Normal mode analysis has been applied to the fully-coupled demonstration storage ring and the phase space and trajectory plots have been obtained. Additionally, the normal mode Twiss parameters have been obtained from the eigen decomposition.

The beam size calculations given in [41], which project the normal mode quantities into the lab frame, have been extended from two-dimensions to three-dimensions. Writing the projected beam sizes in terms of $\bar{\mathbf{V}}$ reveals how the coupling terms effect the measured beam sizes.

2.8 Analytic Intrabeam Scattering Calculations

2.8.1 Kubo

The IBS formalism outlined here is described succinctly by Kubo in [20] and in detail by Kubo and Oide in [21]. It is based on changes to the second-order moments of the Σ-matrix of the beam distribution in the frame of the bunch, as

$$\Delta \left\langle \bar{p}_i \bar{p}_j \right\rangle = c_I \mathbf{R} \left\langle \delta \mathbf{w}^2 \right\rangle \mathbf{R}^T, \tag{2.138}$$

where,

$$\left\langle \delta \mathbf{w}^2 \right\rangle = \begin{pmatrix} \left\langle \delta w_1^2 \right\rangle & 0 & 0 \\ 0 & \left\langle \delta w_2^2 \right\rangle & 0 \\ 0 & 0 & \left\langle \delta w_3^2 \right\rangle \end{pmatrix} \tag{2.139}$$

and $\mathbf{R}$ is a matrix of eigenvectors defined below, $\left\langle \delta w_1^2 \right\rangle$, $\left\langle \delta w_2^2 \right\rangle$, and $\left\langle \delta w_3^2 \right\rangle$ are the rates of change of the normal mode 2nd order moments, and c_I is proportional to the bunch charge.

IBS refers to scattering among nearby particles. The 2nd order moments of the Σ-matrix describe the momentum spread of the entire bunch. What is needed is the "local" momentum spread, or the spread in the momentum of particles inside a small spatial element of the bunch. The difference between the Σ-matrix 2nd order moments and the "local" moments is depicted in Fig. 2.13. The local momentum spread is obtained as

$$\Sigma_{lpp} \equiv \left\langle \bar{p}_{li} \bar{p}_{lj} \right\rangle = \Sigma_{pp} - \Sigma_{xp}^T \Sigma_{xx}^{-1} \Sigma_{xp}, \tag{2.140}$$

where $\Sigma_{pp} \equiv \left\langle \bar{p}_i \bar{p}_j \right\rangle$, $\Sigma_{xx} \equiv \left\langle \bar{x}_i \bar{x}_j \right\rangle$, and $\Sigma_{xp} \equiv \left\langle \bar{x}_i \bar{p}_j \right\rangle$.

73
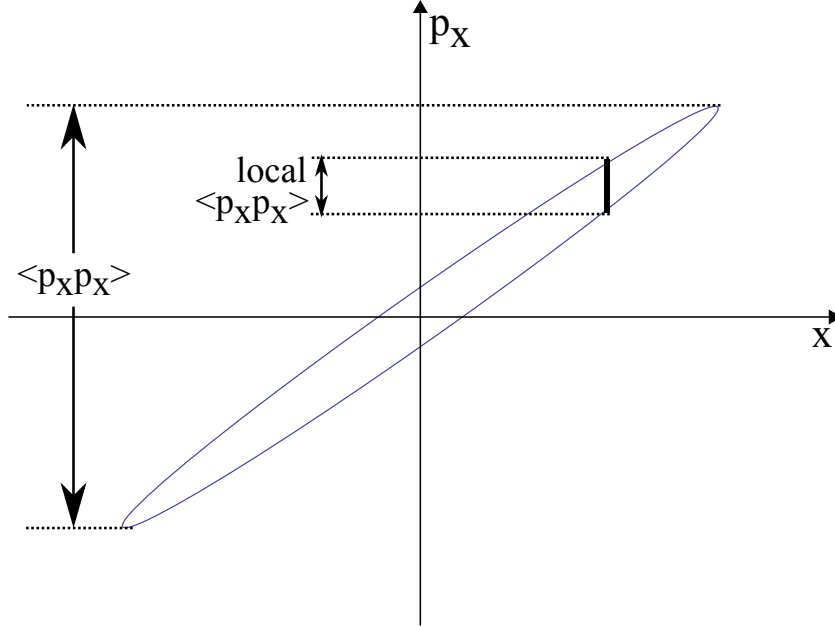
Figure 2.13: The local momentum $\boldsymbol{\Sigma}$-matrix describes the distribution of momentum in a small spatial element of the bunch.

$\boldsymbol{\Sigma}_{lpp}$ is symmetric and positive-definite and can be decomposed as

$$\boldsymbol{\Sigma}_{lpp} = \mathbf{R}\mathbf{G}\mathbf{R}^T, \qquad (2.141)$$

where $\mathbf{G}$ is a diagonal matrix of the eigenvalues of $\boldsymbol{\Sigma}_{lpp}$ and the columns of $\mathbf{R}$ are the eigenvectors. The eigenvalues are denoted u_1, u_2, u_3. Note that $\mathbf{R}^T = \mathbf{R}^{-1}$.

$\left\langle \delta \mathbf{w}^2 \right\rangle$ is obtained from

$$\left\langle \delta w_1^2 \right\rangle = g_2 + g_3 - 2g_1, \qquad (2.142)$$

$$\left\langle \delta w_2^2 \right\rangle = g_1 + g_3 - 2g_2, \qquad (2.143)$$

$$\left\langle \delta w_3^2 \right\rangle = g_1 + g_2 - 2g_3, \qquad (2.144)$$

where

$$g_1 = g\left(u_1, u_2, u_3\right), \qquad (2.145)$$

$$g_2 = g\left(u_2, u_1, u_3\right), \qquad (2.146)$$

$$g_3 = g\left(u_3, u_1, u_2\right), \qquad (2.147)$$

74

and

$$g(a, b, c) = \int_0^{\pi/2} \frac{2a \sin^2 s \cos s}{\sqrt{\left(\sin^2 s + \frac{a}{b}\cos^2 s\right)\left(\sin^2 s + \frac{a}{c}\cos^2 s\right)}} ds. \qquad (2.148)$$

g_1, g_2, and g_3 are analogous to the temperatures of the 3 normal modes of the bunch.

c_I is defined as

$$c_I = \frac{r_e^2 N_e \Delta s}{4\pi \gamma^4 \epsilon_a \epsilon_b \epsilon_c} C_\Lambda, \qquad (2.149)$$

where ϵ_a, ϵ_b, and ϵ_c are the normal mode emittances of the beam, and the Coulomb Logarithm C_Λ will be defined in the next section. N_e is the number of particles in the bunch, r_e is the classical electron radius, γ is the relativistic factor, and Δs is the length of the element.

2.8.2 Coulomb Logarithm

The Coulomb Log, C_Λ, appears in the integration of the Rutherford scattering cross-section over all scattering angles. The integral diverges for small scattering angles, which correspond to large impact parameters. This requires the introduction of a largest impact parameter cutoff. We follow the prescription by Kubo and Oide [21] and use the smaller of the mean inter-particle distance and smallest beam dimension as the maximum impact parameter,

$$b_{max} = \min\left(n^{-1/3}, \sigma_x, \sigma_y, \gamma\sigma_z\right), \qquad (2.150)$$

where n is the particle density in the bunch frame,

$$n = \frac{N_e}{(4\pi)^{3/2}\,\sigma_x\sigma_y\gamma\sigma_z}. \qquad (2.151)$$

As for the largest scattering angle (smallest impact parameter), both Piwinski and Bjorken-Mtingwa assume that $\theta_{max} = \pi/2$. It was suggested in [33] that scattering events

which occur less frequently than once per radiation damping time should be excluded from the calculation of the IBS rise time. This is because such events do not occur frequently enough for the central limit theorem to apply and therefore do not contribute to the Gaussian core of the beam. Such infrequent events will generate non-Gaussian tails. It is the size of the Gaussian core that we can measure, so for comparison with the data, we exclude contributions to the tails.

In an electron/positron storage ring, photons are emitted when the beam travels through bend magnets and wigglers. The emitted photon carries away some transverse momenta, which reduces action, but the sudden change of the total particle momenta causes an increase in its betatron oscillation amplitude. The overall change to the particle's action depends on the local optics and betatron phase of the particle at the time of photon emission. Photon emission is a stochastic process that occurs at unpredictable locations along the particle's trajectory. Each time a photon is emitted, the amount of transverse momentum carried away and amount by which the closed orbit jumps are drawn from stochastic distributions.

Very many photon emission events occur per damping period. The number of photons emitted per second by a beam particle is [53],

$$\dot{N}_{\mathrm{ph}} = \frac{15\sqrt{3}}{8} \frac{P_\gamma}{\epsilon_c},$$

(2.152)

where P_γ is the rate at which the particle radiates energy and ϵ_c is the critical photon energy of the synchrotron radiation. For CesrTA at 2.1 GeV, P_γ is 0.2 MeV/turn, and the damping time is 20000 turns. For a 2.1 GeV beam and a bending radius of 122 m, the critical photon energy ϵ_c is 156 eV. Each electron emits about 20×10^6 photons per damping period.

The central limit theorem predicts that the average of a large number of stochastic events drawn from a distribution with a finite mean and variance is a Gaussian distribu-

Table 2.3: Nominal conditions for a bunch with 6.4×10^{10} particles.	
Beam Energy γ	4080
Average Density ρ	4.2×10^{21} part/m^3
Twiss γ_x	0.51 m^{-1}
Emittance ϵ_a	3.0 nm-rad

tion. Because the momenta of each particle in the bunch is the average of very many stochastic momentum kicks, the distribution of particle momenta in a bunch is Gaussian.

Similarly, there are a large number of small-angle intrabeam scattering events that likewise excite oscillations. The IBS momentum kicks are stochastic and have a well-defined mean and variance. These IBS events increase the width of the momentum distribution. However, very few large-angle scattering events occur per damping time.

A particle with velocity v, traveling through a gas with density ρ, and an interaction cross-section σ, will undergo scattering events at a rate $1/\tau = \rho v \sigma$. Writing $\sigma = \pi b^2$, where b is the effective impact parameter yields

$$\frac{1}{\tau} = \pi \rho v b^2. \tag{2.153}$$

For non-relativistic Coulomb scattering, the impact parameter is related to the scattering angle ψ by

$$b = \frac{r_e}{2\bar{\beta}^2} \cot \frac{\psi}{2} \tag{2.154}$$

where $\bar{\beta}c$ is the velocity of the particles in their center-of-momentum frame. Substituting Equation (2.154) into (2.153) gives the rate at which particles are scattered into angles less than or equal to ψ:

$$\frac{1}{\tau} = \frac{1}{\gamma} \frac{\pi \rho c r_e^2}{4\gamma^3 \left(\epsilon \gamma_a\right)^{\frac{3}{2}}} \cot^2 \frac{\psi}{2} \tag{2.155}$$

where $\sqrt{\epsilon \gamma_a}$ has been used for $\bar{\beta}$, ϵ is emittance, and γ_a is the a-mode Twiss γ. The relevant beam parameters for CesrTA are shown in Table 2.3. The rate of scattering
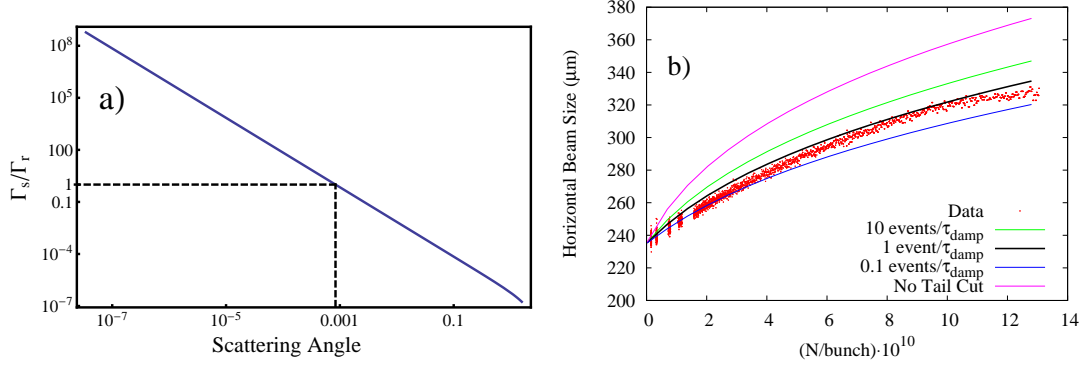
Figure 2.14: (a) Events which occur less than once per damping time are excluded from the calculated growth rate. (b) Equilibrium beam size calculations assuming different cut-offs.

events, Γ_s, in units of radiation damping time, Γ_r, as a function of maximum scattering angle is shown in Fig. 2.14(a). The tail-cut consists of excluding those events which occur less than once per radiation damping period. A measure of the sensitivity to the cutoff is illustrated in Fig. 2.14(b). The calculated equilibrium beam size is shown for a range of two orders of magnitude of the cutoff. The data shown are the same as plotted in Fig. 2.28(a).

The tail-cut consists of restricting the calculation of the IBS growth rate to include only those events which occur at least once per damping period. Events which occur less frequently than once per damping period generate lightly populated non-Gaussian tails that do not contribute to the Gaussian core. The Gaussian core is what determines luminosity in a collision experiment and brightness of a light source. It is the Gaussian core that we measure in our beam size measurements.

The tail-cut is applied by setting the minimum impact parameter as

$$b_{min} = \sqrt{\frac{1}{n\pi\tau_b v}}, \tag{2.156}$$

where τ_b is the longest damping time in the bunch frame and v is the average particle velocity in the bunch frame. If ϵ_a is greater than ϵ_b and $\frac{\sigma_p \sigma_z}{\gamma^2}$, then $v \approx c\gamma \sqrt{\frac{\epsilon_a}{\beta_a}}$.

78

The computed IBS growth rate is directly proportional to the Coulomb Log and is expressed as the logarithm of the maximum impact parameter over the minimum,

$$C_\Lambda = \log \frac{b_{max}}{b_{min}}. \tag{2.157}$$

In hadron and ion machines, such as the Tevatron and RHIC, the damping time is very long and there are enough of even the very large-angle scatters to populate a Gaussian distribution. A tail-cut does not significantly affect the calculated IBS distributions for those machines. However, for machines with strong damping, such as lepton storage rings, very few large-angle scattering events occur per damping time, and applying the tail-cut is essential to reliably computing the equilibrium distribution of the Gaussian core of the bunch. In CesrTA, applying the tail-cut significantly changes the calculated growth rate. With the tail-cut, the average Coulomb log in CesrTA at 1.6×10^{10} particles/bunch is 9.4. Without the tail-cut, that is, if we assume that the maximum scattering angle is $90°$, the average Coulomb log is 17.6.

2.8.3 Eigen decomposition as a patch between beam-envelope matrix and Twiss-based schemes

The IBS formalism described in Sec. 2.8.1 is an example of a Σ-matrix based formalism, also known as a beam-envelope formalism. In such formalisms the beam-envelope is propagated using,

$$\Sigma_2 = \mathbf{M}_{1\to2}\Sigma_1\mathbf{M}_{2\to1}^T, \tag{2.158}$$

where $\mathbf{M}_{1\to2}$ is the transfer matrix that takes coordinates from location 1 to location 2, and could easily be the 1-turn matrix. In the beam-envelope formalism, radiation damping is incorporated into the transfer matrix and quantum excitation is added as a

diffusion term [27],

$$\Sigma_2 = \mathbf{M}\Sigma_1\mathbf{M}^T + \mathbf{B}, \tag{2.159}$$

where $\mathbf{B}$ contains changes to the 2nd-order moments of the Σ matrix due to photon emission.

Twiss based formalisms, on the other hand, parameterize the beam in terms of 3 emittances and 9 optics functions ($\beta_{a,b,c}$, $\alpha_{a,b,c}$, and $\phi_{a,b,c}$). Radiation damping and excitation are applied as kicks which depend on the optics functions and bend angles [16].

Using the relationships between the eigen decomposition and the Σ-matrix developed in Sec. 2.6.1 and the normal mode decomposition and eigen decomposition established in Sec. 2.7, it is possible to switch between Twiss & emittance-based descriptions of the beam and Σ-matrix descriptions of the beam.

`Bmad` is a Twiss-based environment, while Kubo's IBS formalism is based on the Σ-matrix. Beam tracking and synchrotron radiation are are handled in `Bmad`'s Twiss-based infrastructure. To calculate IBS growth, we first build the Σ-matrix using the normal mode emittances and eigen decomposition of the 1-turn map. Then we adjust the 2nd order moments of the Σ-matrix according to Kubo's formalism. Finally, we calculate the new emittances by calculating the eigenvalues of $\Sigma\mathbf{S}$.

2.8.4 Modified Piwinski with Tail Cut

2.8.4.1 Introduction

The first widely used formalism for the calculation of IBS scattering rates was by Anton Piwinski in 1974 [30]. The original derivation contained a cumbersome 3-dimensional

integral. In 1980, Evans and Zotter made an exact replacement of the triple integral with a single integral [25]. This formalism was extended by Martini in 1984 [25] to include derivatives of the lattice optics.

Piwinski's original formalism contains a Coulomb Logarithm that assumes a maximum scattering angle of $\pi/2$ and contains the momentum dependence of the scattering particles. The formalism was originally intended for hadron and ion accelerators. As discussed in Sec. 2.8.2, large angle scattering events are rare in lepton accelerators on the time scale of a damping time.

In this section, Piwinski's original formalism for the calculation of IBS scattering rates is re-derived assuming a constant Coulomb Logarithm of the same form used by Kubo [21] and Bjorken & Mtingwa [5]. This makes it possible to apply Piwinski's original formalism to lepton rings and compare the results to those obtained by the Kubo and Bjorken & Mtingwa formalisms.

As a bonus, this derivation puts Piwinski's formalism in a very simple form. Even with Zotter's integral, Piwinski's formalism is considered cumbersome to evaluate and opaque approximations of varying reliability are often used [58].

When a constant Coulomb Logarithm is assumed, two of the three integrals in Piwinski's original derivation can be solved exactly. The result is an IBS scattering formula that is quick to evaluate, and which can be derived from Piwinski's original formula with the application of only one easy to understand approximation.

2.8.4.2 Derivation

Piwinski's original formalism differs from the Bjorken-Mtingwa formalism in that it preserves the relative momentum dependence in the Coulomb Logarithm. It may be

argued that preserving this dependence is more accurate. However, when applied to machines with significant damping it is found that the Coulomb Log must be adjusted according to the tail-cut procedure. The tail-cut procedure assumes a Coulomb Log that is not dependent on momentum.

In the classic theory, the smallest scattering is calculated from the smallest beam dimension and the largest scattering angle is $\frac{\pi}{2}$,

$$\log \frac{\sin \frac{\pi}{2}}{\sin \frac{\psi_{min}}{2}} \approx \log \frac{1}{\psi_{min}} \approx \log \frac{2\beta^2 b_{max}}{r_e}, \tag{2.160}$$

where b_{max} is the largest impact parameter (typically the beam height), r_e is the electron radius, β is the relative velocity of the two colliding particles, and we have used,

$$\tan \psi = \frac{r_e}{2\beta^2 b}. \tag{2.161}$$

In the tail-cut theory, the largest scattering angle is also small, typically less than 0.01 radians, and the relative velocity of the two particles drops out,

$$\log \frac{\sin \frac{\psi_{max}}{2}}{\sin \frac{\psi_{min}}{2}} \approx \log \frac{\psi_{max}}{\psi_{min}} \approx \log \frac{b_{max}}{b_{min}}. \tag{2.162}$$

Note, however, that b_{min}, Eqn. (2.156), is proportional to the square root of the particle velocity. Kubo's formula for the tail-cut replaces the relative velocity of individual particles with the average particle velocity.

The integral for Piwinski's original derivation is [30],

$$f(a, b, c) = 2 \int_0^\infty \int_0^\pi \int_0^{2\pi} \log\left(q^2 r\right) \left(1 - 3\cos^2 \theta\right)$$
$$\exp\left(-r\left(\cos^2 \theta + \left(a^2 \cos^2 \phi + b^2 \sin^2 \phi\right) \sin^2 \theta\right)\right) \sin \theta \, d\phi \, d\theta \, dr, \quad (2.163)$$

where the Coulomb Logarithm is the log factor inside the integral.

Before assuming the constant Coulomb Logarithm, we apply the first few steps from Evans and Zotter's derivation [12], where they convert the triple integral to a single integral.

First, notice that $\cos^2 \theta$ and $\sin^2 \theta$ are symmetric about $\pi/2$. Replace the integration of θ over 0 to π with an integration over 0 to $\pi/2$ and multiply the integral by 2,

$$f(a,b,c) = 4 \int_0^\infty \int_0^{\frac{\pi}{2}} \int_0^{2\pi} \log\left(q^2 r\right) \left(1 - 3\cos^2 \theta\right)$$
$$\exp\left(-r\left(\cos^2 \theta + \left(a^2 \cos^2 \phi + b^2 \sin^2 \phi\right) \sin^2 \theta\right)\right) \sin\theta \, d\phi \, d\theta \, dr. \quad (2.164)$$

The same can be applied to the variable ϕ, replacing the integration over 0 to 2π with and integration over 0 to $\pi/2$ and multiplying the integral by 4,

$$f(a,b,c) = 16 \int_0^\infty \int_0^{\frac{\pi}{2}} \int_0^{\frac{\pi}{2}} \log\left(q^2 r\right) \left(1 - 3\cos^2 \theta\right)$$
$$\exp\left(-r\left(\cos^2 \theta + \left(a^2 \cos^2 \phi + b^2 \sin^2 \phi\right) \sin^2 \theta\right)\right) \sin\theta \, d\phi \, d\theta \, dr. \quad (2.165)$$

Next make use of the identities $\sin^2 \phi = \frac{1-\cos 2\phi}{2}$ and $\sin^2 \phi = \frac{1+\cos 2\phi}{2}$,

$$f(a,b,c) = 16 \int_0^\infty \int_0^{\frac{\pi}{2}} \int_0^{\frac{\pi}{2}} \log\left(q^2 r\right) \left(1 - 3\cos^2 \theta\right)$$
$$\exp\left(-r\left(\cos^2 \theta + \left(a^2 + b^2 + \left(a^2 - b^2\right) \cos 2\phi\right) \sin^2 \theta\right)\right) \sin\theta \, d\phi \, d\theta \, dr. \quad (2.166)$$

Replace 2ϕ with y,

$$f(a,b,c) = 8 \int_0^\infty \int_0^{\frac{\pi}{2}} \int_0^{\pi} \log\left(q^2 r\right) \left(1 - 3\cos^2 \theta\right)$$
$$\exp\left(-r\left(\cos^2 \theta + \left(a^2 + b^2 + \left(a^2 - b^2\right) \cos y\right) \sin^2 \theta\right)\right) \sin\theta \, dy \, d\theta \, dr. \quad (2.167)$$

Replace $\cos\theta$ with x,

$$f(a,b,c) = 8 \int_0^\infty \int_0^1 \int_0^\pi \log\left(q^2 r\right)\left(1 - 3x^2\right)$$
$$\exp\left(-r\left(x^2 + \frac{1}{2}\left(a^2 + b^2 + \left(a^2 - b^2\right)\cos y\right)\left(1 - x^2\right)\right)\right) dy\,dx\,dr. \quad (2.168)$$

At this point, Evans and Zotter use an identity to integrate over r exactly. We diverge from their derivation by replacing the logarithm with a constant and moving it outside the integral,

$$f(a,b,c) = 8\,(\text{clog}) \int_0^\infty \int_0^1 \int_0^\pi \left(1 - 3x^2\right)$$
$$\exp\left(-r\left(x^2 + \frac{1}{2}\left(a^2 + b^2 + \left(a^2 - b^2\right)\cos y\right)\left(1 - x^2\right)\right)\right) dy\,dx\,dr. \quad (2.169)$$

The integration over r is now straightforward,

$$f(a,b,c) =$$
$$16\,(\text{clog}) \int_0^1 \int_0^\pi \frac{1 - 3x^2}{a^2 + b^2 + \left(2 - a^2 - b^2\right)x^2 + \left(a^2 - b^2\right)\left(1 - x^2\right)\cos y}\,dy\,dx. \quad (2.170)$$

The integration over y is also straightforward and yields the final result,

$$f(a,b,c) = 8\pi\,(\text{clog}) \int_0^1 \frac{1 - 3x^2}{\sqrt{a^2 + \left(1 - a^2\right)x^2}\,\sqrt{b^2 + \left(1 - b^2\right)x^2}}\,dx. \quad (2.171)$$

2.8.4.3 Discussion

Equation (2.171) is a numerically easy to integrate form of the integral in Piwinski's original derivation. The only approximation made is that the Coulomb Log was assumed to not depend on the relative momentum of the colliding particles.

Note that this equation is very similar to Evans and Zotter's derivation. Their result has a logarithmic term inside the integral that is the momentum-dependent version of

84

the Coulomb Logarithm,

$$f(a, b, c) = 8\pi \int_0^1 \frac{1 - 3x^2}{\sqrt{PQ}} \left(2\log\left(\frac{C}{2} \left(\frac{1}{\sqrt{P}} + \frac{1}{\sqrt{Q}} \right) \right) - \tilde{\gamma} \right) dx, \qquad (2.172)$$

where $\tilde{\gamma}$ is Euler's constant and,

$$P(x) = a^2 + \left(1 - a^2 \right) x^2 \qquad (2.173)$$

$$Q(x) = b^2 + \left(1 - b^2 \right) x^2. \qquad (2.174)$$

Equation (2.171) is also very similar to Bane's approximation [58] to the Bjorken-Mtingwa formalism, except that our equation treats x and y equally, where Bane's derivation does not give sensible results when the vertical dispersion is zero.

2.8.5 Method Comparison

In addition to Kubo and Oide's method, two other commonly used methods for calculating IBS growth rates are one by Bjorken and Mtingwa [5] and a version of Piwinski's original derivation that includes derivatives of the lattice optics [30]. The constant Coulomb Log integral derived in Sec. 2.8.4 is used here. Shown in Fig. 2.15 are horizontal beam size versus current calculated using the three methods.

We treat the Coulomb Log the same way in each method and apply the tail-cut. Applying the tail-cut to Piwinski's original method requires modifying the derivation so that the minimum and maximum scattering angles can be set as parameters.

Bjorken & Mtingwa's and Piwinski's methods are based on Twiss parameters. We use normal mode Twiss parameters in place of lab frame Twiss parameters when evaluating either formalism. The growth rates given by the formulas are applied to the normal mode emittances.
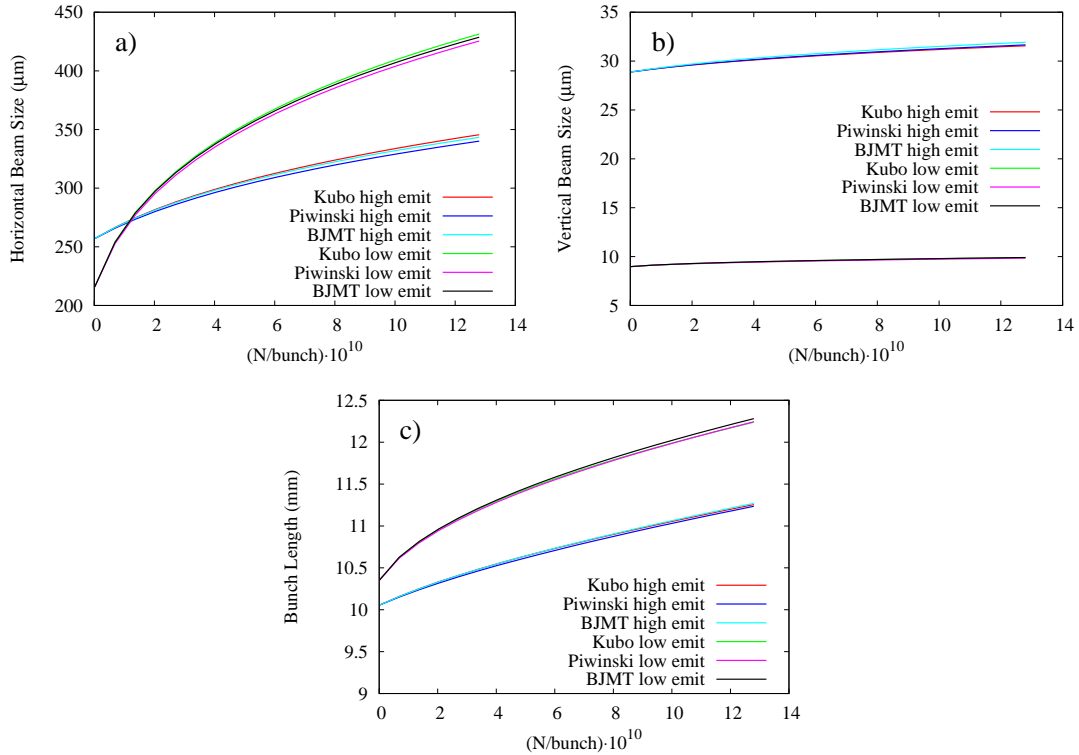
Figure 2.15: Comparing (a) horizontal, (b) vertical, and (b) longitudinal beam size versus current for three different IBS formalisms. The high emittance lattice has $\epsilon_{x0} = 4.6$ nm·rad, $\epsilon_{y0} = 14.3$ pm·rad, and $\sigma_{z0} = 10.0$ mm. The low emittance lattice has $\epsilon_{x0} = 2.8$ nm·rad, $\epsilon_{y0} = 1.5$ pm·rad, and $\sigma_{z0} = 10.3$ mm.

These calculations suggest that, provided the Coulomb Log is treated the same, the three most general IBS formalisms predict similar equilibrium beam sizes.

2.9 Intrabeam Scattering Monte Carlo Simulations

In addition to the analytic IBS calculations discussed above, we have developed a Monte Carlo simulation based on Takizuka and Abe's plasma collision model [48]. An ensemble of 2000 particles representing the bunch distribution is tracked element-by-element using the `Bmad` standard tracking methods [37]. Tracking through the strong, nonlinear field of the superconducting damping wigglers is done with a symplectic Lie method

based on a map of the wiggler field [39].

At each element, the ensemble is converted from canonical to spatial coordinates and boosted into its center of momentum frame where the particles are non-relativistic. Then Takizuka and Abe's collision model is applied:

1. The bunch is divided into cells. This enforces locality.

2. Particles in each cell are paired off. Each particle undergoes only one collision.

3. The change in the momentum of the pair is calculated, taking into account their relative velocities and the density of particles in the cell.

The ensemble is then boosted back to the lab frame and transformed back into canonical coordinates.

Note that this is not a Monte Carlo simulation of individual scattering events. Such a simulation would require the calculation of $\frac{N!}{2}$ scattering events per element and is not computationally feasible. Takizuka & Abe's formalism calculates the expectation value of the change in the momentum of a test particle traveling through a "wind" of nearby particles. The relative velocity of the paired particles determines the velocity vector of the wind. The rate of change of the particle momentum due to scattering events is assumed to be constant through the length of the element.

A log term corresponding to the Coulomb Log appears in Takizuka & Abe's formalism. The calculation of the expectation value of the change in the momentum of the particles assumes many small-angle scattering events. This method of Monte Carlo simulation is subject to the central limit theorem and tail-cut in the same way as the analytic calculations.

2.9.1 Generating a Distribution of Particles Matched to the Machine

The equilibrium beam distribution in a lepton storage ring is the result of stochastic radiation damping and excitation. Any arbitrary distribution injected into a storage ring will in time assume a Gaussian distribution that is invariant under the 1-turn map. For CESR, this occurs on the a scale of approximately 20000 turns, or about 50 ms.

In principle, the Monte Carlo simulation could be seeded with any arbitrary distribution and end up with the same result. However, the Monte Carlo simulation is time consuming. If the simulation is seeded with a distribution that corresponds to the equilibrium distribution, then it will equilibrate faster. Tracking 2000 particles for 20000 turns on a 32 CPU Xeon E5-4650 cluster takes about 12 hours.

A distribution of particles matched to the machine is generated by first generating the distribution in the eigen basis. In the eigen basis the particle coordinates are simply given by,

$$
\vec{a} = \begin{pmatrix}
\sqrt{2J_a}\cos\phi_a \\
-\sqrt{2J_a}\sin\phi_a \\
\sqrt{2J_b}\cos\phi_b \\
-\sqrt{2J_b}\sin\phi_b \\
\sqrt{2J_c}\cos\phi_c \\
-\sqrt{2J_c}\sin\phi_c
\end{pmatrix}.
\tag{2.175}
$$

This is identical to Eqn. (2.82) and is reproduced here for convenience. In one dimension, a distribution of particles in equilibrium has a flat distribution in ϕ, and a Gaussian

distribution in action J,

$$\rho(J, \phi) = \frac{1}{2\pi\epsilon} e^{-\frac{J}{\epsilon}},\qquad(2.176)$$

where ϵ is the emittance.

A flat distribution in ϕ for N particles is easily obtained by generating a set of N random real numbers between 0 and 1 and multiplying the set by 2π.

A Gaussian distribution in J is obtained using inverse transform sampling. A set of N random real numbers with a flat distribution between 0 and 1 is transformed into a Gaussian distribution with vanishing first order moment and width ϵ using

$$J_i = -\epsilon \log(X_i),\qquad(2.177)$$

where $X_1 \cdots X_N$ is the flat distribution of random real numbers.

Generating three distributions of N particles in (J_a, ϕ_a), (J_b, ϕ_b), and (J_c, ϕ_c) we now have a distribution of particles in the eigenbasis of the machine. This is converted into a distribution of particles matched to the machine using Eqn. (2.67),

$$\vec{x} = \mathbf{N}\vec{a}.\qquad(2.178)$$

2.9.2 Coordinate Transformations

2.9.2.1 Bmad **coordinates to spatial coordinates**

After tracking a distribution of particles to some location s in the lattice, for each particle we know $(x(s), p_x(s), y(s), p_y(s), z(s), p_z(s))$. These are the canonical coordinates of the particles at the location s, and do not represent the spatial distribution of the bunch.

To find the spatial distribution, we need to find the location of the particles at the time t_0, this is the time that the reference particle arrived at s. The z coordinate of each particle is $z(s) = -\beta(s) c (t(s) - t_0(s))$, from which we obtain,

$$\Delta t \equiv t(s) - t_0(s) = \frac{z(s)}{-\beta(s) c}. \tag{2.179}$$

At this point each particle with $\Delta t < 0$ should be propagated backwards through the previous element for a time Δt, and each particle with $\Delta t > 0$ should be propagated forward through the next element for a time Δt. For simplicity, we simply propagate the particles through a drift. This approximation is reasonable as long as the betatron phase advance over the length of the bunch is much much less than $\pi/2$ and the guide field strength not too strong.

The time-dependent Hamiltonian for a particle of charge e and mass m moving through a field-free region is [46],

$$H_t(x, p_x, y, p_y, s, p_s; t) = c \left(\left(\frac{mc}{P_0} \right)^2 + p_x^2 + p_y^2 + p_s^2 \right)^{1/2} = \frac{\gamma mc^2}{P_0}, \tag{2.180}$$

where $p_{x,y,s} = P_{x,y,s}/P_0$, $P_{x,y,s}$ is the momentum of the particle and P_0 is the momentum of the reference particle. The equations of motion are obtained as,

$$\frac{dx}{dt} = \frac{\partial H_t}{\partial p_x} = \frac{p_x c}{\sqrt{\left(\frac{mc}{P_0} \right)^2 + p_x^2 + p_y^2 + p_s^2}} \qquad \frac{dp_x}{dt} = -\frac{\partial H_t}{\partial x} = 0$$

$$\frac{dy}{dt} = \frac{\partial H_t}{\partial p_y} = \frac{p_y c}{\sqrt{\left(\frac{mc}{P_0} \right)^2 + p_x^2 + p_y^2 + p_s^2}} \qquad \frac{dp_y}{dt} = -\frac{\partial H_t}{\partial y} = 0$$

$$\frac{ds}{dt} = \frac{\partial H_t}{\partial p_s} = \frac{p_s c}{\sqrt{\left(\frac{mc}{P_0} \right)^2 + p_x^2 + p_y^2 + p_s^2}} \qquad \frac{dp_s}{dt} = -\frac{\partial H_t}{\partial s} = 0.$$

Note that making the paraxial approximation $p_x, p_y \ll 1$ and assuming $mc/P_0 \ll 1$ yields,

$$\frac{dx}{dt} = \frac{p_x}{p_s}c \qquad\qquad \frac{dy}{dt} = \frac{p_y}{p_s}c \qquad\qquad \frac{ds}{dt} = c.$$

The longitudinal momentum $p_s = P_s/P_0$ of the particle can obtained from its canonical coordinates,

$$P_s^2 = P_0^2 \left((1 + p_z)^2 - p_x^2 - p_y^2 \right). \qquad (2.181)$$

We can now write the map from canonical coordinates $\mathbf{x}_c$ to spatial coordinates $\mathbf{x}_s = (x_s, p_{xs}, y_s, p_{ys}, s, p_s)$,

$$x_s = x_c + \Delta t \frac{dx}{dt} \qquad (2.182)$$

$$p_{xs} = p_{xc} \qquad (2.183)$$

$$y_s = y_c + \Delta t \frac{dy}{dt} \qquad (2.184)$$

$$p_{ys} = p_{yc} \qquad (2.185)$$

$$s = \Delta t \frac{ds}{dt} \qquad (2.186)$$

$$p_s = \frac{P_s}{P_0}, \qquad (2.187)$$

where Δt is given by Eqn. (2.179).

Shown in Fig. 2.16 are the xy, xz, and yz projections of a bunch at $s = 0$ (Bmad coordinates) and $t = 0$ (spatial coordinates). The bunch lies on a non-zero closed orbit.

2.9.2.2 Spatial coordinates to Bmad coordinates

The map from spatial coordinates back to Bmad coordinates is obtained from the s-dependent Hamiltonian of a particle in a field-free region [46],

$$H_s(x, p_x, y, p_y, t, -E; s) = -\sqrt{\left(\frac{E}{c}\right)^2 - p_x^2 - p_y^2 - m^2 c^2} = \beta_s \gamma mc, \qquad (2.188)$$

which is the kinetic momentum in the s direction. The equations of motion are,

(a) *xy*

(b) *xz*

(c) *yz*
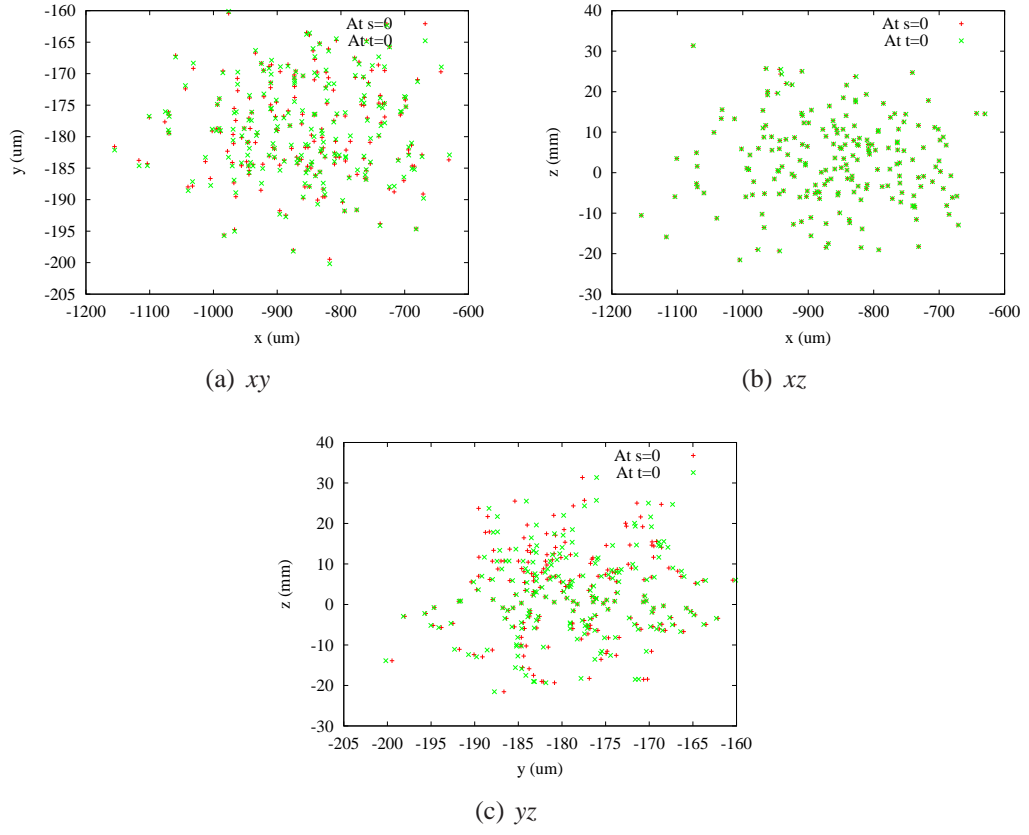
Figure 2.16: *x*, *y*, and *z* coordinates of a bunch at *s* = 0 and *t* = 0. The bunch lies on a non-zero closed orbit.

$$\frac{dx}{ds} = \frac{\partial H_s}{\partial p_x} = \frac{p_x c}{\sqrt{\left(\frac{mc}{P_0}\right)^2 + p_x^2 + p_y^2 + p_s^2}} \qquad \frac{dp_x}{ds} = -\frac{\partial H_s}{\partial x} = 0$$

$$\frac{dy}{ds} = \frac{\partial H_s}{\partial p_y} = \frac{p_y c}{\sqrt{\left(\frac{mc}{P_0}\right)^2 + p_x^2 + p_y^2 + p_s^2}} \qquad \frac{dp_y}{ds} = -\frac{\partial H_s}{\partial y} = 0$$

$$\frac{dz}{ds} = \frac{\partial H_s}{\partial E} = \frac{p_s c}{\sqrt{\left(\frac{mc}{P_0}\right)^2 + p_x^2 + p_y^2 + p_s^2}} \qquad \frac{dp_z}{ds} = -\frac{\partial H_s}{\partial s} = 0.$$

2.9.2.3 Spatial coordinates to COM frame

The Monte Carlo IBS formalism applied at CesrTA is based on Takizuka & Abe's binary collision model [49]. It is a non-relativistic plasma collision model. Particles in an

electron/positron accelerator are typically ultra-relativistic. However, in bunched beams with a small energy spread and divergence, one can boost into the center of momentum (COM) frame of the bunch where the particles will be non-relativistic. We calculate the particle interactions in the COM frame, then boost the particles back into the lab frame.

All coordinates in this section are spatial coordinates where x, y, and s represent the spatial coordinates of the particle relative to the reference particle, and p_x, p_y, and p_s are the horizontal, vertical, and longitudinal momentum of the particle normalized by P_0.

At first glance, one might simply boost along s using the reference momentum. However, this is not ideal if the closed orbit is non-zero. In that case, the boost will be not be parallel with the bunch COM and particles in the boosted frame will have an unnecessarily large relativistic β. Misalignments and strong wiggler fields are two possible contributions to a non-zero closed orbit.

The Lorentz transformation for a boost in any direction $\vec{\beta} = (\beta_x, \beta_y, \beta_s)$ is,

$$
\Lambda = \begin{pmatrix}
\gamma & -\gamma\beta_x & -\gamma\beta_y & -\gamma\beta_s \\
-\gamma\beta_x & 1 + (\gamma-1)\dfrac{\beta_x^2}{\beta^2} & (\gamma-1)\dfrac{\beta_x\beta_y}{\beta^2} & (\gamma-1)\dfrac{\beta_x\beta_s}{\beta^2} \\
-\gamma\beta_y & (\gamma-1)\dfrac{\beta_y\beta_x}{\beta^2} & 1 + (\gamma-1)\dfrac{\beta_y^2}{\beta^2} & (\gamma-1)\dfrac{\beta_y\beta_s}{\beta^2} \\
-\gamma\beta_s & (\gamma-1)\dfrac{\beta_s\beta_x}{\beta^2} & (\gamma-1)\dfrac{\beta_s\beta_y}{\beta^2} & 1 + (\gamma-1)\dfrac{\beta_s^2}{\beta^2}
\end{pmatrix},
\tag{2.189}
$$

where $\gamma = \sqrt{1 - \dfrac{1}{|\vec{\beta}|^2}}$. A particle with four-momentum (E, p_x, p_y, p_s) in the lab frame

will have momentum $\left(E', p'_x, p'_y, p'_s\right)$ in the boosted frame,

$$
\begin{pmatrix} E' \\ p'_x \\ p'_y \\ p'_s \end{pmatrix} = \begin{pmatrix} \gamma & -\gamma\beta_x & -\gamma\beta_y & -\gamma\beta_s \\ -\gamma\beta_x & 1 + (\gamma - 1)\dfrac{\beta_x^2}{\beta^2} & (\gamma - 1)\dfrac{\beta_x\beta_y}{\beta^2} & (\gamma - 1)\dfrac{\beta_x\beta_s}{\beta^2} \\ -\gamma\beta_y & (\gamma - 1)\dfrac{\beta_y\beta_x}{\beta^2} & 1 + (\gamma - 1)\dfrac{\beta_y^2}{\beta^2} & (\gamma - 1)\dfrac{\beta_y\beta_s}{\beta^2} \\ -\gamma\beta_s & (\gamma - 1)\dfrac{\beta_s\beta_x}{\beta^2} & (\gamma - 1)\dfrac{\beta_s\beta_y}{\beta^2} & 1 + (\gamma - 1)\dfrac{\beta_s^2}{\beta^2} \end{pmatrix} \begin{pmatrix} E \\ p_x \\ p_y \\ p_s \end{pmatrix},
$$

$$(2.190)$$

where $E = \sqrt{P_x^2 + P_y^2 + P_s^2 + m_0^2 c^2}$.

We want to boost into a frame where the sum of the individual particle momentum is zero,

$$\sum_{i=1}^{n} \vec{p}'_{xi} = 0 \tag{2.191}$$

$$\sum_{i=1}^{n} \vec{p}'_{yi} = 0 \tag{2.192}$$

$$\sum_{i=1}^{n} \vec{p}'_{si} = 0 \tag{2.193}$$

where $\vec{p}_1, \vec{p}_2, ... \vec{p}_n$ are the lab-frame momenta in spatial coordinates. Solving this system of equations via `Mathematica` yields,

$$
\beta_x = \frac{\sum\limits_{i=1}^{n} \vec{p}_{xi}}{\sum\limits_{i=1}^{n} E_i} \qquad\qquad \beta_y = \frac{\sum\limits_{i=1}^{n} \vec{p}_{yi}}{\sum\limits_{i=1}^{n} E_i} \qquad\qquad \beta_s = \frac{\sum\limits_{i=1}^{n} \vec{p}_{si}}{\sum\limits_{i=1}^{n} E_i}
$$

$$(2.194)$$

After boosting the distribution of particles according to Eqn. (2.189) and (2.194), the momentum of the particles will average to zero.

The spatial coordinates (x, y, z) must also be transformed. The four-vector is $\tilde{x} = (0, x, y, z)$. By setting the first element of the four-vector $c\tau$ to zero, we are stating that an observer measures the location of each particle simultaneously. The transformed distribution is obtained by applying $\tilde{\mathbf{x}}_i = \Lambda \mathbf{x}_i$ for each particle i in the ensemble.

Time dilation reduces the amount of time passed in the boosted frame by a factor of γ,

$$\Delta t' = \frac{\Delta t}{\gamma} = \Delta t \sqrt{1 - \beta^2},\tag{2.195}$$

where $\beta = \sqrt{\beta_x^2 + \beta_y^2 + \beta_z^2}$. In the lab frame, $\frac{l}{\beta c}$ seconds pass as the particle travels through an element of length l. In the boosted frame, the amount of time passed is much shorter, $\frac{l}{\gamma \beta c}$.

The total energy of a particle i in the boosted frame is,

$$E_i = c \sqrt{P_{i,x}'^2 + P_{i,y}'^2 + P_{i,s}'^2 + m_e^2 c^2},\tag{2.196}$$

where the prime indicates quantities in the boosted frame. The velocity of particle a in the boosted frame in units of meters per second is

$$v_{i,x} = \frac{P_{i,x} c^2}{E_i},\tag{2.197}$$

$$v_{i,y} = \frac{P_{i,y} c^2}{E_i},\tag{2.198}$$

$$v_{i,s} = \frac{P_{i,s} c^2}{E_i},\tag{2.199}$$

$$v_i = \sqrt{v_{i,x}^2 + v_{i,y}^2 + v_{i,s}^2}.\tag{2.200}$$

Takizuka and Abe's plasma collision algorithm is non-relativistic. Figure 2.17 is a histogram of the relative velocity between particle pairs in the boosted frame. There are 100000 particles in the ensemble.
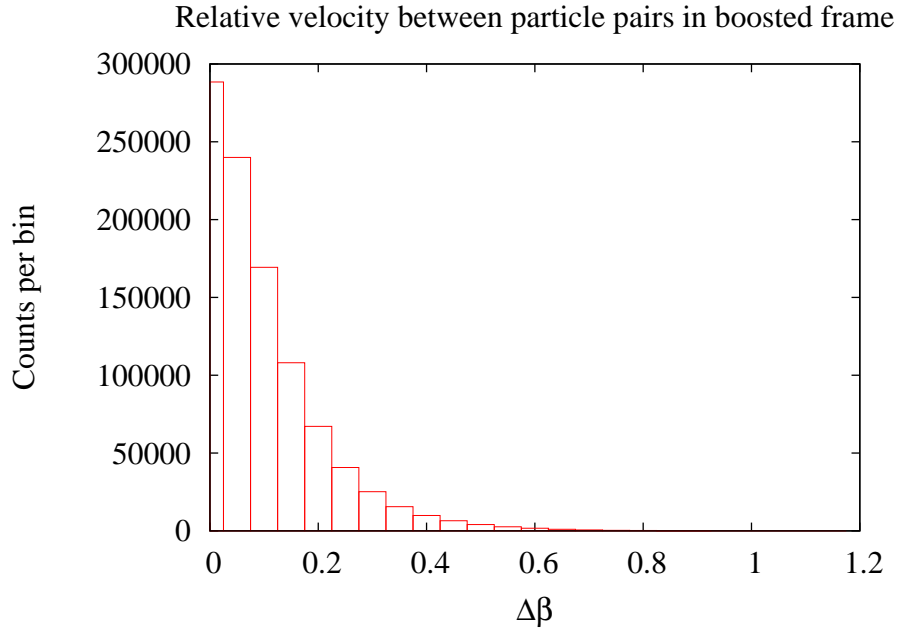
Figure 2.17: Relative velocity of particle pairs in the center of momentum frame of the ensemble.

2.9.3 Collisions

Intrabeam scattering considers only those collision events with an impact parameter small enough to significantly perturb the momentum of the colliding particles in a single event. Only the collisions that a particle has with nearby particles contribute to the IBS growth rate. In Monte Carlo simulation, this requirement is enforced by binning the distribution of particles.

In the boosted frame, the particles are divided into cells defined by a $10 \times 10 \times 15$ grid. In each cell, the particles are paired off for collision. If there are an odd number of particles in the cell, then one triplet is selected and the collision is calculated such that particle 1 imparts a momentum change to particle 2, which imparts a momentum change to particle 3, which imparts a momentum change to particle 1. The pre-collision momentum of particle 3 is used when calculating the momentum change imparted to

particle 1.

If a cell happens to have only one particle, then no collisions are calculated for that particle. This will usually happen only for particles at the extremities of the bunch where particle density, and thus the collision rate, is very low.

The pairing must be done such that each particle is matched to exactly one other particle. This is done efficiently using Durstenfeld's algorithm for generating a random permutation of a finite set [10]. The algorithm is $O(n)$. Naive methods for determining the pairs tend to be $O(n^2)$ and can significantly slow down the simulation.

Each particle in the ensemble represents the same number n_e of actual particles. If a bunch of $N = 10^{11}$ electrons is represented by an ensemble of 2000 particles, then each particle in the ensemble represents $n_e = 0.5 \times 10^8$ electrons. The density of particles in the cell is calculated from the total number of ensemble particles n in the cell and the dimensions of the cell w, h, and l,

$$\rho = \frac{n * n_e}{w \times h \times l}. \tag{2.201}$$

At this point we have selected two particles for collision and will refer to them as particle a and particle b.

Particle a is treated as a test particle taking a random walk through a "wind" of particles all with the same velocity vector as particle b. The density of particles in the wind is determined by the density of particles in the cell.

As a result of travelling through the wind, the relative velocity of the two particles is changed. The change is computed in the center of momentum frame of the two particles, where the collision is head on. This change is parameterized as zenith θ and azimuth ϕ. To calculate the change in ϕ, a random number is selected between 0 and 2π. To

97

calculate the change in θ, a random number is selected from a Gaussian distribution with variance,

$$\delta^2 = \frac{e^4 \rho \Delta t}{4\pi m_e^2 \epsilon_0^2 \Delta u^3} \log \frac{b_{\max}}{b_{\min}}, \qquad (2.202)$$

where e is the electric charge, ρ is the density of particles in the cell, Δt is the length of time over which the particles interact, m_e is the electron mass, ϵ_0 is the permittivity of free space, Δu is the relative speed of the two particles in their center of momentum frame, $b_{\max}$ is the maximum impact parameter (typically taken as the height of the bunch), and

$$b_{\min} = \frac{1}{\pi \tau \rho \Delta u}, \qquad (2.203)$$

where τ is the damping time. This calculation for $b_{\min}$ represents the tail-cut. It says that as the particle makes its random walk through the wind, only those collisions which occur more than once per damping time are included in the calculation.

With change in azimuth ϕ and zenith θ thus obtained, the change in the relative momentum of two particles is,

$$\Delta u_x = \frac{u_x}{u_\perp} u_z \sin\theta \cos\phi - \frac{u_y}{u_\perp} u \sin\theta \sin\phi - u_x \left(1 - \cos\theta\right) \qquad (2.204)$$

$$\Delta u_y = \frac{u_y}{u_\perp} u_z \sin\theta \cos\phi + \frac{u_x}{u_\perp} u \sin\theta \sin\phi - u_y \left(1 - \cos\theta\right) \qquad (2.205)$$

$$\Delta u_z = -u_\perp \sin\theta \cos\phi - u_z \left(1 - \cos\theta\right), \qquad (2.206)$$

where,

$$u = \sqrt{u_x^2 + u_y^2 + u_z^2} \qquad (2.207)$$

$$u_\perp = \sqrt{u_x^2 + u_y^2}, \qquad (2.208)$$

and u_x, u_y, and u_z are the x, y, and z components of the relative velocity of the particles.

Particle a receives a $+u_x$, $+u_y$, and $+u_z$ kick. Particle b receives a $-u_x$, $-u_y$, and $-u_z$ kick. After all particle pairs have been collided, the ensemble is boosted back to
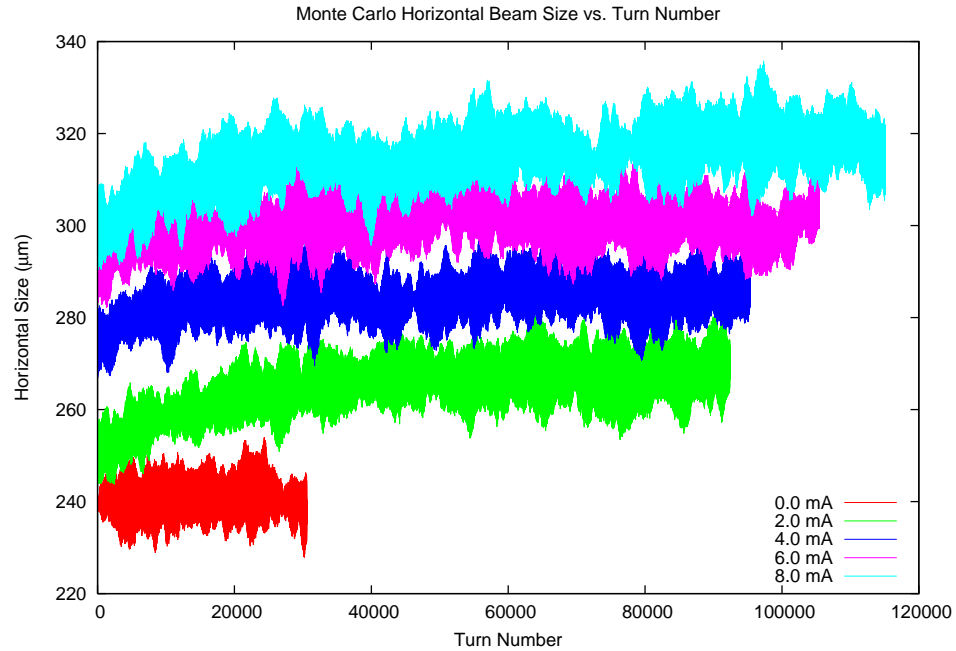
Figure 2.18: Horizontal beam size versus turn from Monte Carlo simulation that incorporates intrabeam scattering. The equilibrium distribution from the lower current runs are used to seed the higher current runs.

the lab frame and tracked to the next element. This process is repeated until the beam distribution reaches equilibrium. Figure 2.18 shows the horizontal beam size versus turn for current ranging from 0.0 mA to 8.0 mA. The initial beam size is different for each run because the equilibrium distribution from the low current runs are used as the initial distribution of the higher current runs. The beam sizes are determined by calculating the Σ-matrix, Eqn. (2.102). The horizontal, vertical, and longitudinal beam sizes $\sqrt{\Sigma_{11}}$, $\sqrt{\Sigma_{33}}$, and $\sqrt{\Sigma_{55}}$. Shown in Fig. 2.28 are the equilibrium beam sizes versus current compared with analytic results and data.

In Sec. 2.12.2, Monte Carlo simulation of direct space charge is discussed in the context of incoherent tune shift.

2.10 Potential Well Distortion (PWD)

Another current-dependent effect that impacts the bunch dimensions in a storage ring is potential well distortion. Potential well distortion is due to interactions between the bunch and its surrounding environment.

The field of the bunch interacts with structures in the vacuum system, resulting in wake fields that act back on the bunch. One consequence of this is a voltage gradient along the length of the bunch. Particles at the head of the bunch lose energy to the vacuum system. Part of this energy is reflected back to the tail of the bunch, effectively transferring energy from the head of the bunch to the tail. In machines that operate above transition, particles with less energy move ahead relative to the reference particle, and those with more energy move back. The result is bunch lengthening. The amount of lengthening is sensitive to the total bunch charge, but not to the transverse dimensions of the bunch.

Energy that is reflected back into the bunch does not change the total energy of the bunch and is referred to as the inductive (L) or capacitive (C) part of the impedance. Energy absorbed by the vacuum system does change the total energy of the bunch and is referred to as the resistive part of the impedance (R). The effect of potential well distortion can be modeled as an effective current-dependent RF voltage. The effective RF voltage is [4]

$$V(\tau) = V_{rf} \cos(\omega\tau + \phi) + RI_b(\tau) + L\frac{dI_b(\tau)}{d\tau}, \qquad (2.209)$$

where τ is relative to the bunch center. The resistive impedance R tends to shift the synchronous phase but does not contribute to lengthening. The inductive part L changes the Gaussian profile of the bunch, leading to real bunch lengthening.
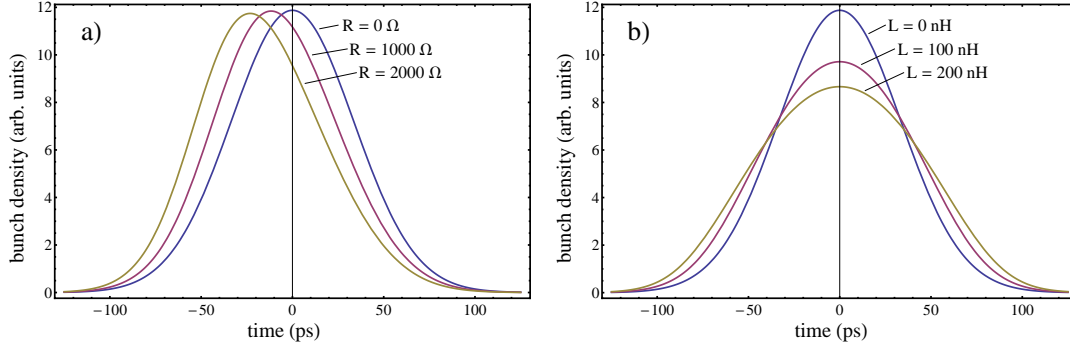
Figure 2.19: Effect of (a) resistive and (b) inductive parts of the longitudinal impedance on the longitudinal profile of the bunch.

In principle, there is also a capacitive part to the impedance. Its effect is to shorten the bunch. In CesrTA, only bunch lengthening is observed. This is because the inductive term in the overall impedance is much larger than the capacitive. Hence, the reactive part of the impedance is modeled as entirely inductive. In theory, the inductive, capacitive, and resistive parts of the impedance could each be determined from the shape of the longitudinal profile of the bunch. However, our measurements are not detailed enough to determine if there is a significant capacitive component.

A derivation of PWD based on Vlassov theory results in a differential equation for the longitudinal profile of the bunch [4],

$$\frac{\partial \psi}{\partial \tau} = -\frac{eE_0\psi}{\sigma_E^2 \alpha T_0} \left(\frac{V_{rf} \cos\left(\omega\tau + \phi\right) + QR\psi - U_0}{1 + \frac{eE_0 QL\psi}{\sigma_E^2 \alpha T_0}} \right), \tag{2.210}$$

where E_0 is the beam energy, σ_E is energy spread, α is momentum compaction, T_0 is the period of the ring, V_{rf} is the total RF cavity voltage, ω is the RF frequency, ϕ is the phase of the reference particle with respect to the RF, Q is the bunch charge, U_0 is the energy lost per particle per turn, R is the resistive part of the longitudinal impedance, and L is the inductive part of the longitudinal impedance. $\psi\left(\tau\right)$ is the longitudinal profile of the bunch. Equation (2.210) is used to compute the effect of various resistive and inductive impedances on the longitudinal profile of the bunch. The results are shown in Fig. 2.19.

101
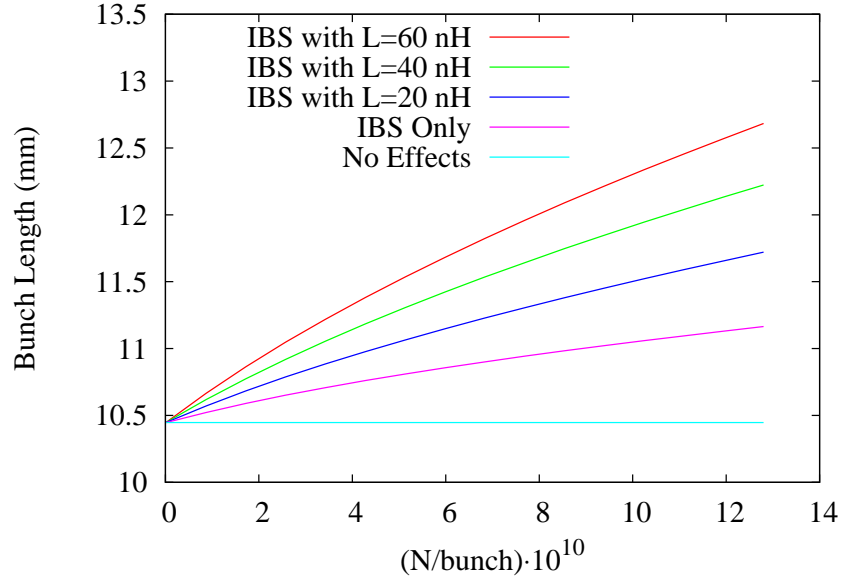
Figure 2.20: Simulated effect on bunch length of PWD in combination with IBS.

We have incorporated the effect of PWD in our analytic model of IBS. Equation (2.210) is used to compute bunch length, including the energy spread resulting from intrabeam scattering. Comparing the measured bunch length versus current data to the simulation result, L is determined to be between 15 and 19 nH. Our bunch length predictions are largely insensitive to R, and we use the published value of 1523 Ω given by Holtzapple et al. [17]. At the time of this writing, PWD has not been implemented in the Monte Carlo simulation.

As shown in Fig. 2.19, resistive impedance has a negligible effect on the shape of the longitudinal profile, whereas the inductive impedance L distorts the Gaussian profile and generates bunch lengthening. Figure 2.20 shows the contribution of the potential well distortion to the bunch length assuming various values for the inductive impedance.

The current-dependent energy spread in CesrTA is determined by measuring the dependence of the horizontal beam size on the horizontal dispersion at the instrument source point. The dispersion is varied with the help of a closed dispersion bump around the source-point. The horizontal beam size is measured under two sets of conditions as

the number of particles in a single bunch decays from 1.3×10^{11} down to 2.4×10^{10}. Horizontal dispersion is 2.28 cm in the first set of conditions, and 22.1 cm in the second. The measured energy spread is $\sigma_E/E = (8.505 \pm 0.314) \times 10^{-4}$ and is independent of current within the measurement uncertainty. The design value of the fractional energy spread as determined using the standard radiation integrals theory is 8.129×10^{-4}. There is no evidence of a microwave instability, which would appear as an energy spread that increases with current above some threshold current.

2.11   Simulation Lattices

An element-by-element description of CesrTA is used for the analytic and tracking calculations shown here. This description includes quadrupoles, sextupoles, bends, steerings, skew quadrupole correctors, wigglers, and RF cavities. Systematic multipoles are included for those sextupoles which have skew quadrupole or vertical steering windings. We use an analytic model of the damping wiggler field, which is based on a fit to a finite element calculation [40]. Tracking through wigglers is by symplectic integration.

The vertical IBS rise time depends on the dispersion. However, vertical dispersion is zero for an ideal flat ring. Vertical dispersion is included in our analytic IBS calculations by introducing *yz* coupling into the 1-turn transfer matrix. This is done at each element by augmenting the 1-turn transfer matrix before utilizing it in the analytic IBS

calculation. The transfer matrix $\mathbf{T}$ is replaced with with $\tilde{\mathbf{T}}$, where $\tilde{\mathbf{T}} = \mathbf{TW}$, and

$$
\mathbf{W} = \begin{pmatrix}
1 & 0 & 0 & 0 & 0 & 0 \\
0 & 1 & 0 & 0 & 0 & 0 \\
0 & 0 & 1 & 0 & 0 & -\tilde{\eta}_y \\
0 & 0 & 0 & 1 & 0 & -\tilde{\eta}_y' \\
0 & 0 & \tilde{\eta}_y' & -\tilde{\eta}_y & 1 & 0 \\
0 & 0 & 0 & 0 & 0 & 1
\end{pmatrix}.
\tag{2.211}
$$

This transformation preserves the symplecticity of the transfer matrix. $\tilde{\eta}_y$ and $\tilde{\eta}_y'$ are dispersion-like quantities. An ideal lattice modified according to the above prescription with $\tilde{\eta}_y = 0.01$ m and $\tilde{\eta}_y' = 0.002$ has an rms vertical dispersion of 10.9 mm and a vertical IBS rise time similar to that of a lattice with an rms vertical dispersion of 10 mm.

The vertical dispersion in CesrTA is measured to be less than 15 mm. The upper bound is limited by the resolution of our measurement technique. The coupling is determined by direct measurement to be $\bar{C}_{12} < 0.003$, using an extended Edwards-Teng formalism [41].

The analytic simulation takes the measured low current horizontal and vertical beam sizes and bunch length as input parameters and computes the current dependence. The horizontal emittance used in the calculation is chosen to match the measured near zero current emittance. The vertical emittance is also set to agree with the measurement extrapolated to zero current. (The vertical emittance of the design simulation lattice is zero.) The energy spread and bunch length used in the simulation are obtained by evaluating the standard radiation integrals.

The Monte Carlo simulation includes photon emission and so requires a realistic ver-

tical dispersion function. This is generated by applying a distribution of misalignments to the ideal lattice, then correcting the phase advance, coupling, orbit, and vertical dispersion according to the same procedure that is applied to CesrTA [44]. The magnitude of the misalignments is set such that the zero current vertical emittance is roughly 15 pm-rad.

2.12   IBS Experiments at CesrTA

2.12.1   Horizontal-Longitudinal Coupling in CesrTA

The horizontal beam sizes measured at the start of our IBS investigations at CesrTA were about 240 um. This is significantly larger than the 175 um that was expected. Using $\epsilon = \frac{\sigma^2}{\beta}$, 240 um corresponds to about 6 nm-rad horizontal emittance. 3 nm-rad is what is expected from radiation integrals calculations.

Initial investigations focused on identifying discrepancies between the design optics and actual machine optics. Discrepancies large enough to double the horizontal emittance were not found. We also investigated the horizontal beam size monitor for systematics. The horizontal beam size monitor is calibrated using a source of known size. Additionally, the instrument is validated by measuring the beam size while varying horizontal β-function at the source point. These investigations ruled out instrumentation systematics as a cause of the larger-than-expected horizontal measurements.

The cause of the large horizontal beam sizes was found while developing the Monte Carlo IBS simulation. Beam sizes are obtained from the Monte Carlo simulation by computing the beam envelope matrix of the particle distribution. The horizontal and
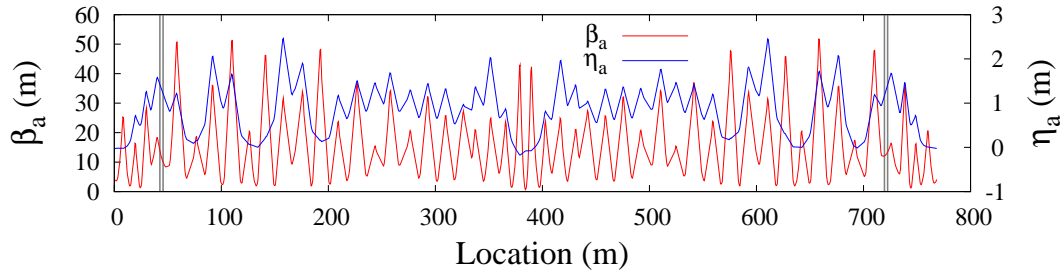
Figure 2.21: CesrTA design *a*-mode (horizontal-like) β and dispersion η. The gray vertical bars indicate the locations of CesrTA's four RF cavities. Horizontal dispersion in the RF cavities is about 1 m.

vertical beam size and bunch length are obtained from the 11, 33, and 55 components of the beam envelope matrix. The horizontal beam sizes obtained from the Monte Carlo simulation agreed with the larger-than-expected measurements we were obtaining from the machine.

It was then quickly discovered that the particle distribution was tilted in the *xz* plane. Tilt in the *xz* plane increases the *x*-projection of the particle distribution, yielding a larger measured horizontal beam size.

The source of the *xz* tilt is *xz* coupling introduced by horizontal dispersion in the RF cavities. For low-emittance operation, it is necessary to eliminate dispersion in the damping wigglers. This requirement constrains on the optics such that the horizontal dispersion in the RF cavities cannot be zero. The horizontal β-function and dispersion, along withe locations of the four RF cavities, are shown in Fig. 2.21.

The *xz* tilt of the beam is given by the C_{ac11} term of the coupling matrix. C_{ac11} is the 15 term of the **V** matrix and is also known as V_{15} Shown in Fig. 2.22 is V_{15} along CesrTA. Also shown is the location of the horizontal beam size monitor instrumentation source points. The horizontal source point for positrons is 374.247 m, and for electrons is 493.1812.

106
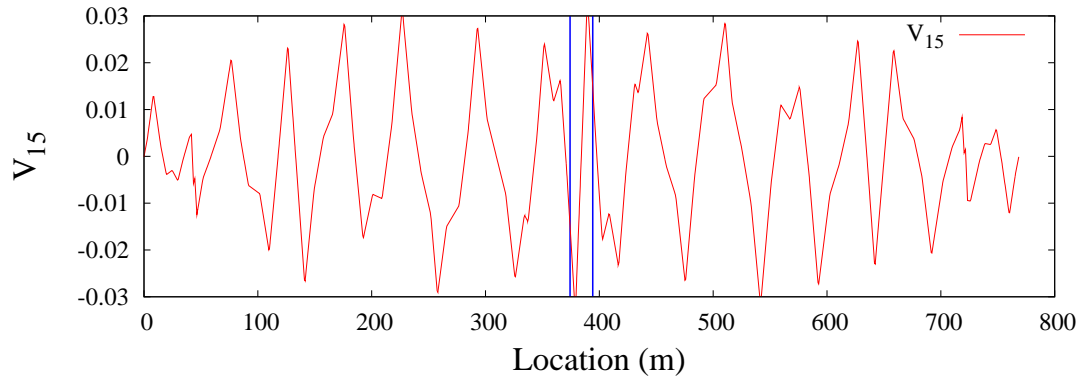
Figure 2.22: *xz* coupling term V_{15} along CesrTA. The blue bands show the locations of the horizontal beam size monitor source points for positrons (374.247 m) and electrons (394.1812 m).

Horizontal (*a*-mode) emittance in CesrTA is about 3 nm-rad. Longitudinal (*c*-mode) emittance is about 9 μm-rad. The coupling parameter γ_a is very close to one. At locations where V_{15} is large, the *c*-mode emittance can make as much of a contribution to the projected horizontal beam size as the *a*-mode emittance.

xz tilt can be managed by adjusting the phase advance between the RF cavities. There are two pairs of RF cavities in CesrTA. Through the South region, they are separated by approximately 1.5 betatron wavelengths. To mitigate the *xz* tilt, the horizontal betatron phase advance between the two pairs is adjusted such that the *xz* coupling generated in one pair of RF cavities cancels that generated in the other pair. This results in more tilt in the South region, but reduces tilt near the instrumentation source points.

Data taken during the April 2012 CesrTA run, shown in Sec. 2.12.3.1, is affected by the *xz* tilt. This is evident in the large zero-current horizontal beam size. Data taken in December 2012, shown in Sec. 2.12.3.2, was taken on a lattice with V_{15} compensation. The horizontal beam sizes in the December data are noticeably smaller.

In and of themselves, tilted beams are not problematic. The difficulty is in calculating the beam size. In the presence of *xz* coupling, the commonly used expression for

107
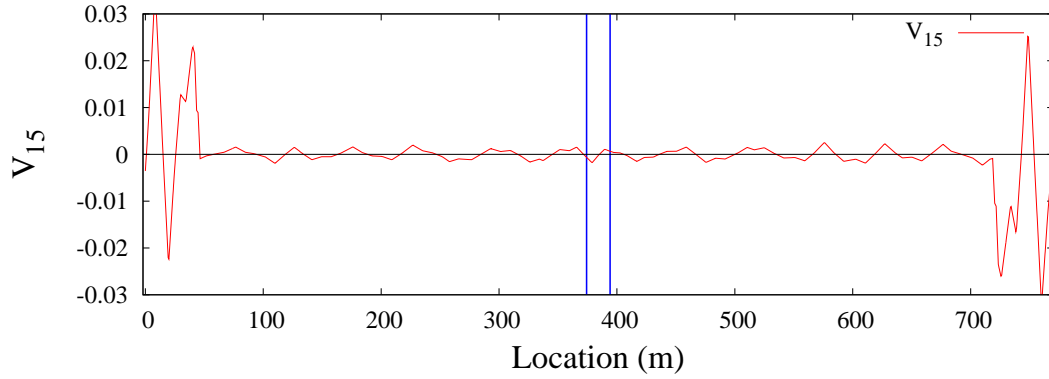
Figure 2.23: *xz* coupling term V_{15} along CesrTA with V_{15} compensation. The blue bands show the locations of the horizontal beam size monitor source points for positrons (374.247 m) and electrons (394.1812 m).

calculating the beam size,

$$\sigma = \sqrt{\epsilon\beta + \eta^2\sigma_p^2}, \tag{2.212}$$

is no longer valid and should not be used. However, calculating the beam size from the beam envelope matrix, as discussed in Secs. 2.6.1 and 2.7.0.1, is valid.

2.12.2   Coherent and Incoherent Tune Shift

A current-dependent shift of the coherent tune is observed in CesrTA. At 2.1 GeV, the vertical shift was measured to be -0.505 ± 0.006 kHz/mA. The horizontal shift was measured to be -0.072 ± 0.006 kHz/mA. (1 kHz corresponds to a change in fractional tune of 0.0026.) The synchrotron tune has been measured versus current, and no shift was observed. These tune shifts are relevant to IBS studies because the beam size will in general depend on proximity of the coherent tune to resonance lines in the tune plane. Preparation for IBS studies includes identifying a region of the tune plane where the effect of resonance lines is minimized for the range of currents to be explored. The tune plane is scanned with direct measurement as well as tracking simulation. The experimental tune scans are performed by recording the beam sizes as the tune is varied

by adjusting quadrupole strengths.

Figure 2.24 shows the measured dependence of vertical and horizontal coherent tune on bunch current. The betatron frequencies are measured via a pair of spectrum analyzers connected to beam position monitor (BPM) buttons.

Incoherent tune shifts may also contribute to the current-dependence of the measured beam size. The difference between coherent and incoherent tunes is well-described by Schindl [42]. In short, coherent tune refers to the motion of the bunch centroid. Incoherent tune refers to the distribution of tunes in the bunch. One source of incoherent tune shift is direct space charge, which is discussed in the context of linear collider damping rings in [9, 51, 60]. Under the influence of direct space charge, each particle in the bunch will in general have a different betatron tune that depends on the particle's invariants J_x and J_y. The betatron tune will also depend on J_z and the longitudinal phase of the particle, as the defocusing force due to space charge depends on where the particle is relative to the bunch center. The width of this distribution can become very large at a few mA, making it difficult to position the bunch in the tune plane so that no particles encounter resonance lines. If a particle encounters a difference resonance, its motion becomes coupled and action can be transferred from the longitudinal or horizontal to the vertical. If a particle encounters a sum resonance, its actions can become arbitrarily large [46]. These effects will cause the vertical emittance to increase, and may also lead to particle loss. A bunch with a large tune footprint may be influenced by the effect of several resonance lines at once, making it difficult to predict beam behavior.

The incoherent tune shift due to direct space charge forces for a particle with spatial coordinates x, y, and z, is given by [9]

$$\Delta Q_{sc;x|y} \approx \frac{L r_e N_e e^{\frac{-z^2}{2\sigma_z^2}}}{(2\pi)^{3/2} \gamma^3 \sqrt{\epsilon_x \epsilon_y} \sigma_z}, \tag{2.213}$$

109
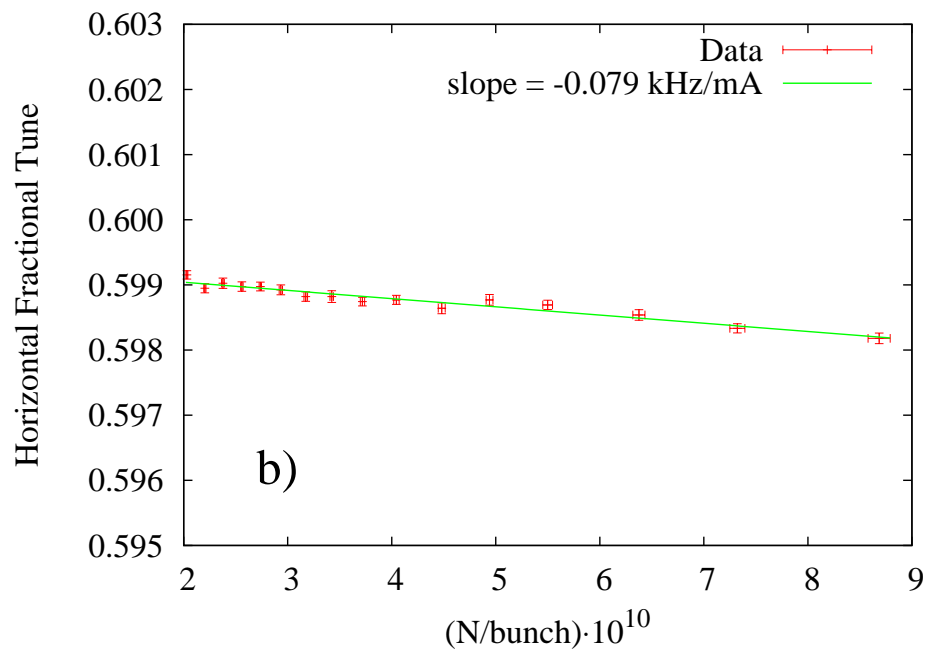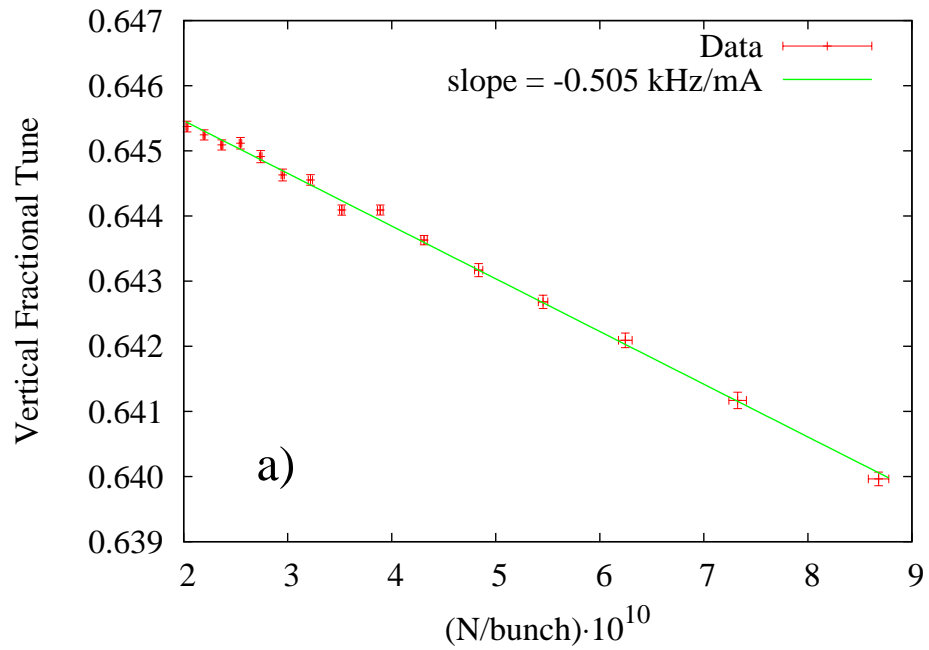
Figure 2.24: Fractional coherent tune versus current for (a) the vertical and (b) the horizontal plane. The resolution of the measurement is 10^{-4}. The revolution frequency is 390.1 kHz.
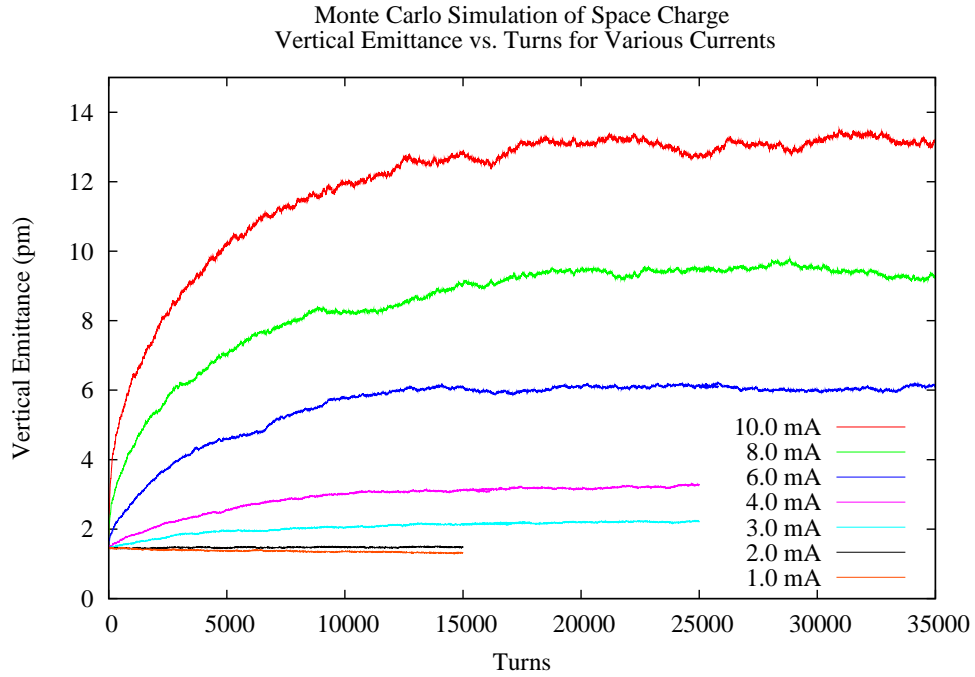
Figure 2.25: Monte Carlo simulation of direct space charge. The vertical beam size equilibrates to a larger value as current is increased.

where L is the ring circumference, r_e is the electron radius, N_e is the number of particles in the bunch, σ_z is the bunch length, γ is the relativistic factor, and $\epsilon_{x,y}$ are the geometric emittances. A particle will sample a space charge focusing that varies as it executes synchrotron oscillations.

Evaluating Eqn. (2.213) under typical CesrTA conditions for a particle at $z = 0$ in a bunch with 1.6×10^{10} particles yields a fractional tune shift of -0.01. At $z = \sigma_z$, the shift is -0.004. The predicted shift scales linearly with current. Figure 2.26 shows Monte Carlo simulations of the tune spread produced by direct space charge. At each element in the lattice, for each particle, the electric field due to space charge is calculated using the Bassetti-Erskine formula [3]. This electric field is used to apply a kick to the particle.

Figure 2.25 shows the effect of direct space charge on the equilibrium vertical beam

size. As current is added to the bunch, direct space charge generates a large tune spread among the particles in the bunch. This drives the tune of individual particles over resonance lines, which increases the vertical beam size and diminishes the effect of direct space charge.

The simulation tracks 2000 particles for 5000 turns each. For each particle, the tune over the last 2048 turns is extracted with a fast Fourier transform (FFT). The FFT spectra of the individual particles are averaged to give the plotted result. This plot shows that the spread in horizontal tune is small, but spread in vertical tunes becomes very large above a few mA.

Figure 2.27 shows a simulated tune scan. The color scale shows the rms value of the vertical-like normal mode action J_b of a particle tracked for 2000 turns, normalized by its initial value J_{b0}. The thin lines are analytic calculations of the form $rQ_x + sQ_y + tQ_z = n$. The labels are of the form (r, s, t, n). Amplitude-dependent tune-shift causes the resonance lines in the simulation to be offset from the analytic calculations. The initial action of the tracked particle is set to be about ten times the equilibrium emittance. The yellow line shows the range of coherent tune spanned as a bunch decays from 1.3×10^{11} particles to 1.6×10^9 particles. The upper right hand point is the zero current tune. Comparing Figs. 2.26 and 2.27, we see that above a few mA, the tune footprint spans a significant region of the tune plane.

The simulated and experimental tune scans are generally only in approximate agreement. The lower order resonances, such as $(1, -1, -1, 0)$, tend to be much broader in the experimental tune scan. The higher order resonances seen in the simulated scan do not appear in the experimental scan. The choice of working point for the IBS measurements is based on consideration of both of the tune scans and may be adjusted further depending on machine behavior.
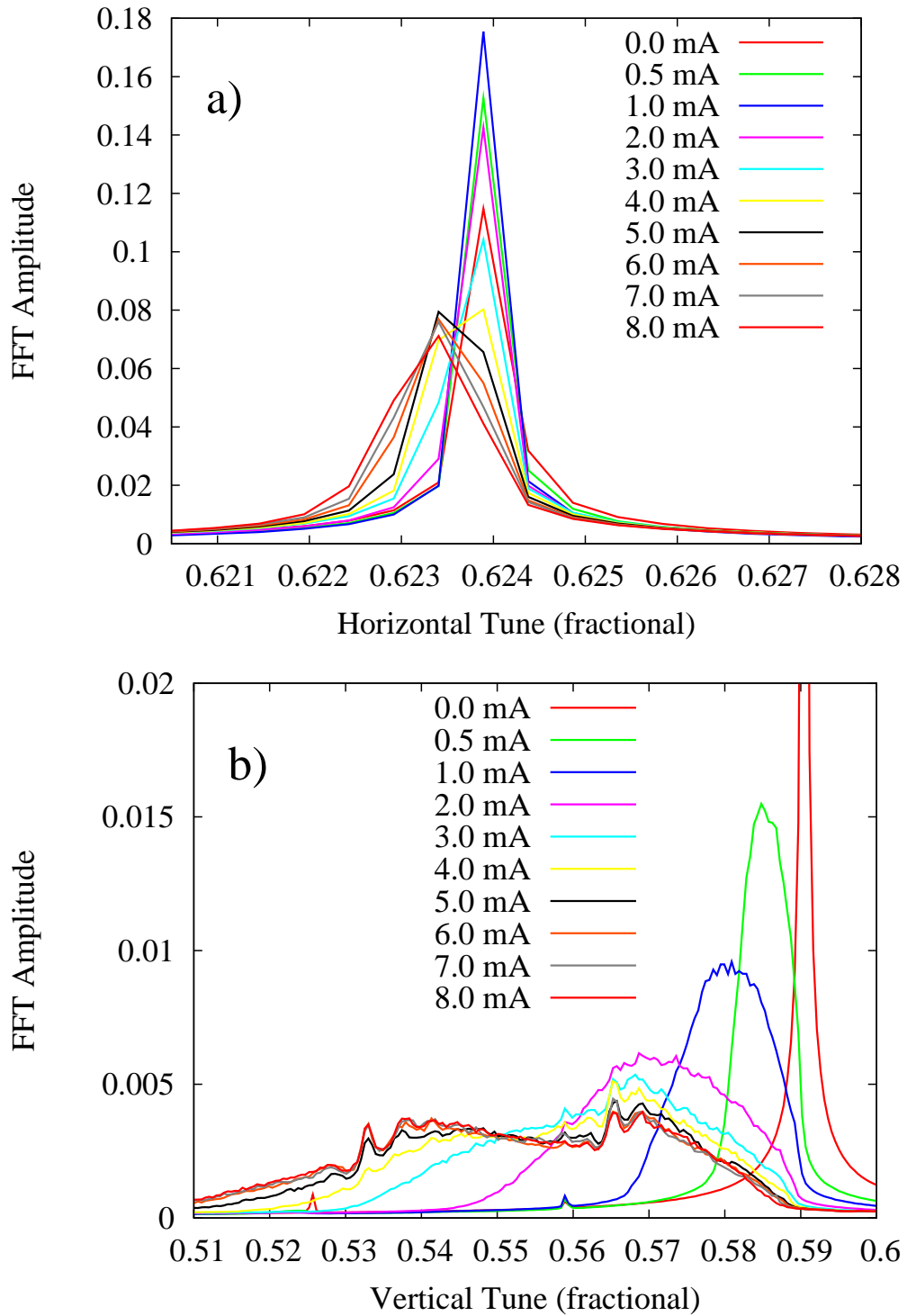
Figure 2.26: Monte Carlo simulation of direct space charge showing the (a) horizontal and (b) vertical tune spread predicted for various currents. The conversion factor between mA and particles/bunch in CesrTA is 1.6×10^{13} seconds/Coulomb.
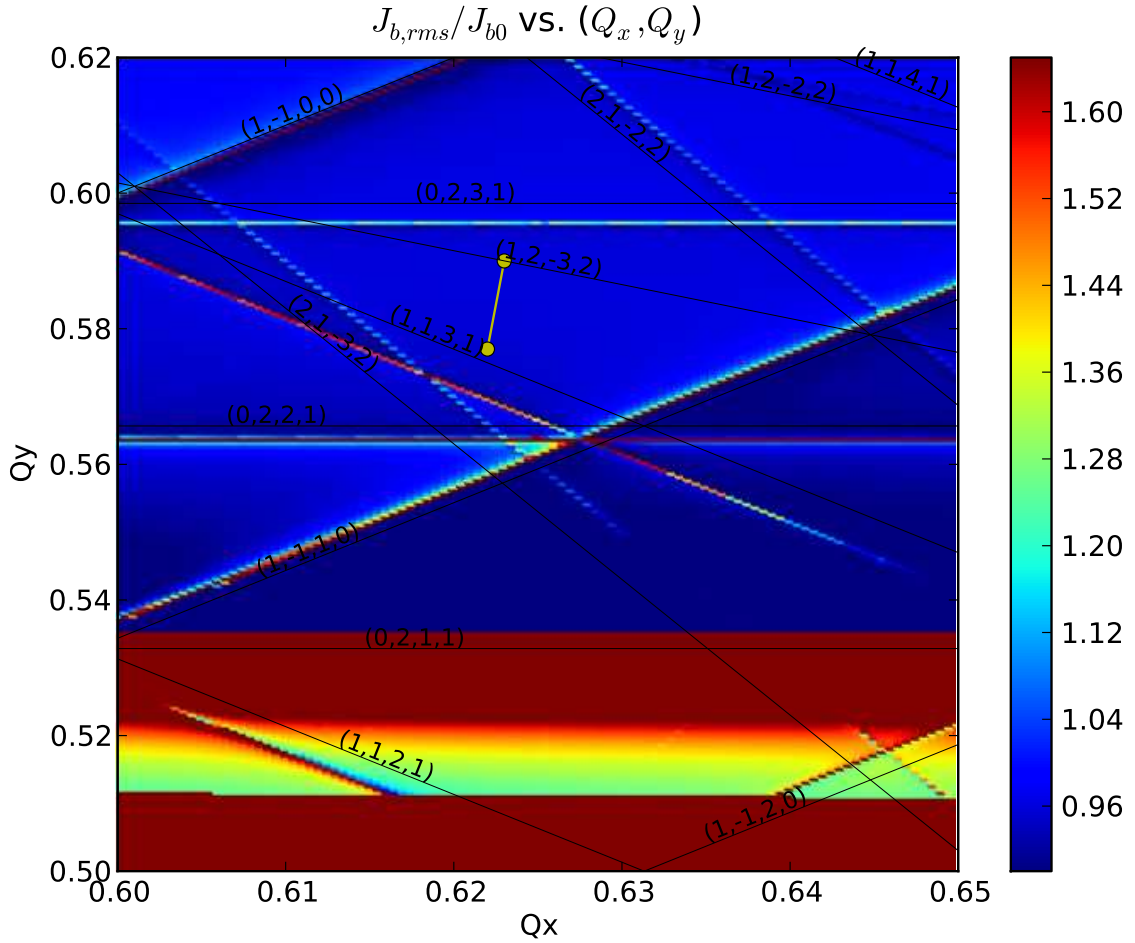
Figure 2.27: Simulated tune scan based on a lattice model that includes magnet mis-alignments and corrector magnet settings determined according to our emittance tuning procedure. The yellow line shows how the coherent tunes increase as a bunch decays from 1.3×10^{11} down to to 1.6×10^9 particles.

2.12.3 Intrabeam Scattering Experiments

For measurements of intrabeam scattering, we load a specific lattice configuration, and set beam energy, working point, and RF voltage. The machine is tuned for minimum vertical emittance according to the algorithm given in [44]. For experiments requiring a larger ϵ_y, the vertical emittance is increased by adjusting a closed coupling and vertical dispersion bump that propagates vertical dispersion through the wigglers.

A single bunch of about 1.6×10^{11} particles (10 mA) is allowed to decay. The measurements include horizontal and vertical beam sizes, streak camera measurements of the longitudinal profile, and tunes in all three dimensions. The short beam lifetime is due to Touschek scattering. In about 20 minutes, the beam current decays from 10 mA to 1 mA. Below 1 mA the beam lifetime improves significantly. In the interest of time, a large-amplitude pulsed orbit bump is used to scrape particles out of the beam in 0.25 mA increments. The discontinuities in the data at bunch charge $< 2 \times 10^{10}$ particles correspond to the regime where beam is scraped out.

IBS measurements were done during dedicated periods of CesrTA operation in April 2011, June 2011, December 2011, April 2012, and December 2012. The IBS measurements in 2011 led us through iterative improvements in our understanding of how to operate the accelerator and how to measure IBS effects. Improvements on the accelerator side included a better understanding of the tunes and the selection of the working point (tunes as determined by lattice optics), a better understanding of the coupling and its impact on the measurements, and the development of more exact procedures for establishing the desired machine configuration. Improvements to the instrumentation included the implementation of beam size measurements for both electrons and positrons and the development of more accurate and robust analysis software.

This thesis includes data from the April and December 2012 machine studies. The configuration procedures, analysis methods, and simulation methods implemented in April yielded data where it seems clear that the horizontal beam size versus current is dominated by IBS and agrees well with simulations.

The December results confirm and build upon the April measurements. The exact same IBS calculation method that yielded good agreement with the April 2012 data, also yielded fair agreement when applied to the December 2012 data. The December

Figure 2.28: (a) horizontal, (b) vertical, and (c) longitudinal beam size versus current for e^+ bunch in conditions tuned for minimum vertical emittance.

2012 includes measurements at 2.3 GeV and data taken versus RF voltage. The April measurements are all at 2.1 GeV and the IBS calculation methods we use were developed on 2.1 GeV data. The fact that the model worked, without modification, on the 2.3 GeV data was reassuring. IBS growth rates have a strong $\frac{1}{\gamma^4}$ dependence.

2.12.3.1 April 2012 Data

Shown in Fig. 2.28 is data from a positron bunch in conditions tuned for minimum vertical emittance.

The approximate statistical uncertainties at high current are shown in Tab. 2.4. For the bunch length and horizontal beam size measurements, the statistical uncertainty in the current and size is plotted for each data point. The error bars may be below the

Table 2.4: Approximate statistical uncertainties at high current.

Measurement	Uncertainty
Current (horiz. binning)	0.3%
Current (bunch length binning)	0.9%
Horizontal Size	0.2%
Bunch Length	1.0%
Vertical Size	0.2%

resolution of the plot.

The vertical measurement represents the average of the fits over 1024 consecutive turns. Error bars representing the statistical uncertainty are plotted, though they may be below the resolution of the plot. Much of the point-to-point fluctuation can be attributed to noisy transverse feedback amplifiers that were diagnosed after this data was taken. The sharp decrease in the vertical beam size and subsequent real fluctuations in beam size at low current is puzzling. Our first reaction is that the data looks like a low-current instrumentation systematic. However, our analysis of the raw instrument data has not pointed to any particular systematic which could cause the drop-off. We have been unable to explain the drop-off with any of the current-dependent effects that have been addressed in our studies.

The vertical measurements are subject to a $\sim \pm 2$ micron systematic that will be addressed in detail in my colleagues thesis [45]. For now we note that IBS is sensitive to the vertical beam size, but not so sensitive that ± 2 micron is significant. The theory results shown below are evaluated over a range of vertical beam sizes that covers the the potential systematic uncertainty. As will be explained below, we observe IBS blow-up in the horizontal dimension, but not so much in the vertical dimension. The vertical dimension is important to our IBS predictions because it sets the particle density, which in turn affects the horizontal IBS blow-up.

Analytic results from the Σ-matrix formalism described in Sec. 2.8.1 and the Monte Carlo simulation described in Sec. 2.9 are shown along with the data. The accuracy of the simulation is limited by the ambiguity of the Coulomb Log and limited knowledge of the zero current vertical beam size of the machine. The simulation result shown here follows the usual convention for the tail-cut of 1 event/damping time as the cutoff.

A major contribution to the vertical measurement systematic uncertainty is the "pinhole subtractor". The pinhole subtractor is the size that would be reported by the instrument if the beam has zero vertical size. It is calculated using a simulation of the vertical beam size monitor. The vertical beam size measurement σ_m is

$$\sigma_m = \sqrt{\sigma_D^2 - \sigma_P^2},\qquad(2.214)$$

where σ_D is the size reported by the instrument and σ_P is the pinhole subtractor. The value of the pinhole subtractor at 2.1 GeV is $(15. \pm 2.)$ micron, and at 2.3 GeV is $(13.5 \pm 2.)$ micron. The systematic uncertainty in the beam size $\sigma_{\sigma m}$ due to uncertainty in the pinhole subtractor $\sigma_{\sigma P}$ is calculated from,

$$\sigma_{\sigma m} = \frac{\sigma_P}{\sigma_m}\sigma_{\sigma p}.\qquad(2.215)$$

This gives a systematic uncertainty of about ±1.2 um at 2.1 GeV for a 25 um beam, and ±1.4 um at 2.3 GeV for a 20 um beam. Other sources of systematic uncertainty include magnification of the pinhole optic and uncertainty of the lattice optics at the image source point.

The Σ-matrix IBS simulation is run twice, once with a zero current vertical emittance that extends to the bottom range of the measurement uncertainty, and once that extends to the upper range of the measurement uncertainty. The shaded region is the area between those two results. This serves two purposes. First, it reflects our uncertainty about the vertical beam size. Second, it gives the reader an idea of how the horizontal simulation result depends upon particle density as determined by the vertical beam size.
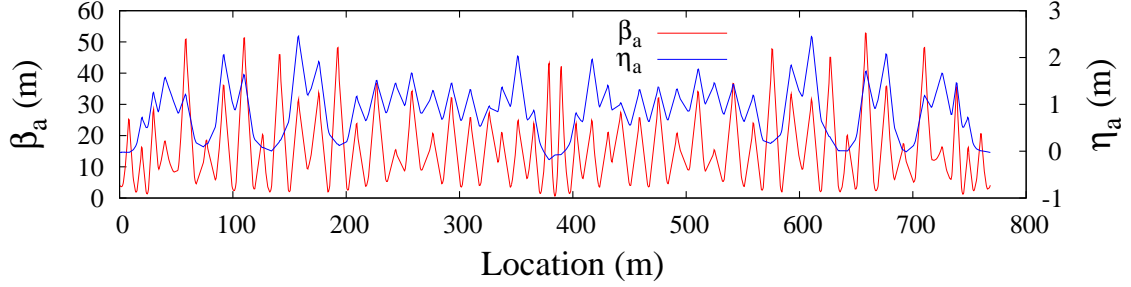
Figure 2.29: CesrTA design a-mode (horizontal-like) β and dispersion η.

The zero current vertical emittances that bound the data in Fig. 2.28(b) are 17.4 pm and 24.6 pm. The shaded regions of 2.28(a) and 2.28(c) show how the horizontal and vertical simulation results change as the zero current vertical emittance is varied from the lower bound to the upper bound.

The measured zero current horizontal emittance, which is an input parameter to the simulation, is 3.8 nm-rad. The calculated value is 2.7 nm-rad for the perfectly aligned lattice. This discrepancy between the measured and calculated horizontal emittance is not well understood. For the bunch length and energy spread, we use the values calculated from the radiation integrals.

The simulation uses a perfectly aligned CesrTA lattice. Vertical dispersion is included by modifying the 1-turn transfer matrix with **W** before passing it to the IBS rise-time calculation. $\tilde{\eta}$ is set to 10 mm. The horizontal emittance increases from 3.8 nm-rad at low current ($< 1.5 \times 10^9$ particles/bunch) to 10.4 nm-rad at 1.3×10^{11} particles/bunch. The reason for the relatively large horizontal blow-up is the large horizontal dispersion in CesrTA. The lattice functions β_a and η_a are shown in Fig. 2.29. The rms horizontal dispersion, η_a, is 1.0 m and peaks at 2.46 m. For comparison, the rms vertical dispersion is less than 15 mm.

In Fig. 2.30 the zero current vertical emittance of the bunch was increased by propagating vertical dispersion through the damping wigglers with the help of a closed cou-
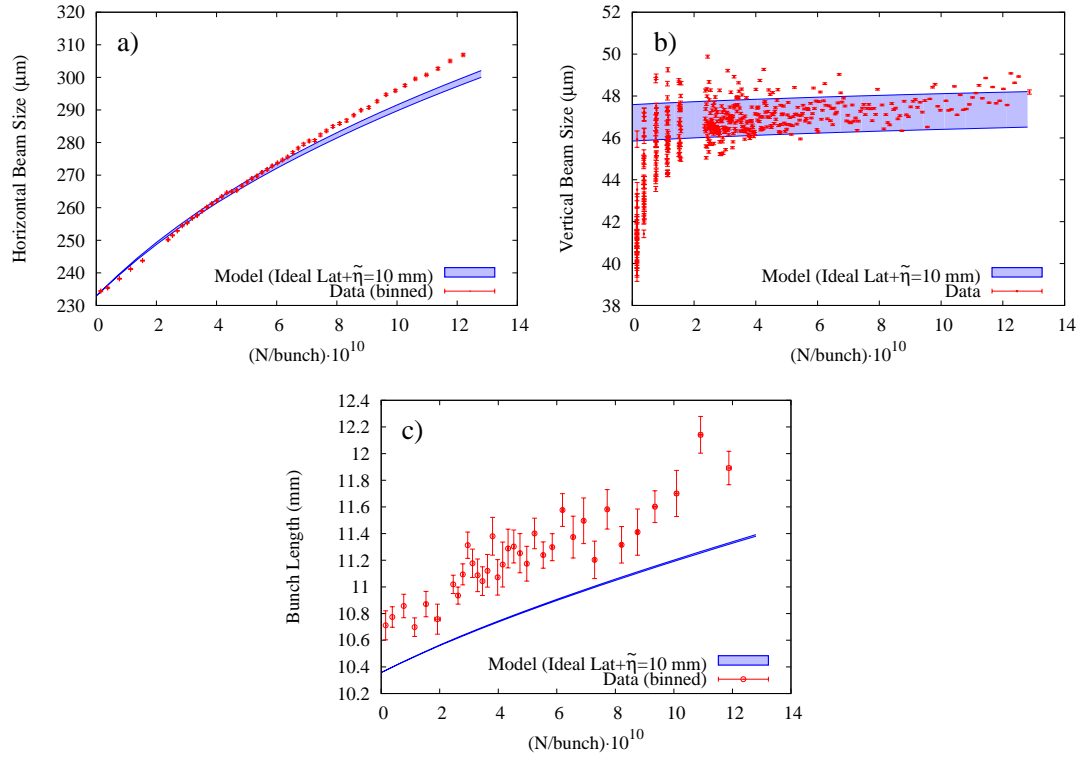
Figure 2.30: (a) horizontal, (b) vertical, and (c) longitudinal beam size versus current for e^+ bunch with increased zero current vertical emittance.

pling and dispersion bump. The larger vertical beam size decreases the particle density, which in turn reduces the amount by which IBS blows up the horizontal beam size. The zero current horizontal emittance is 3.7 nm-rad. The zero current vertical emittances that bound the data are 48.0 pm and 56.3 pm.

IBS theory is species-independent. Measurements of both e^- and e^+ can help identify machine and instrumentation systematics and distinguish IBS from species-dependent beam physics such as electron cloud and ion effects.

Figure 2.31 shows data from an electron bunch in conditions tuned for minimum vertical emittance. During the electron experiments, an improperly setup transverse feedback system was mistakenly left on. It drove the coherent tunes onto the $(1, -1, 1, 0)$ resonance line at currents above 5.6×10^{10} part/bunch. The measured horizontal emit-
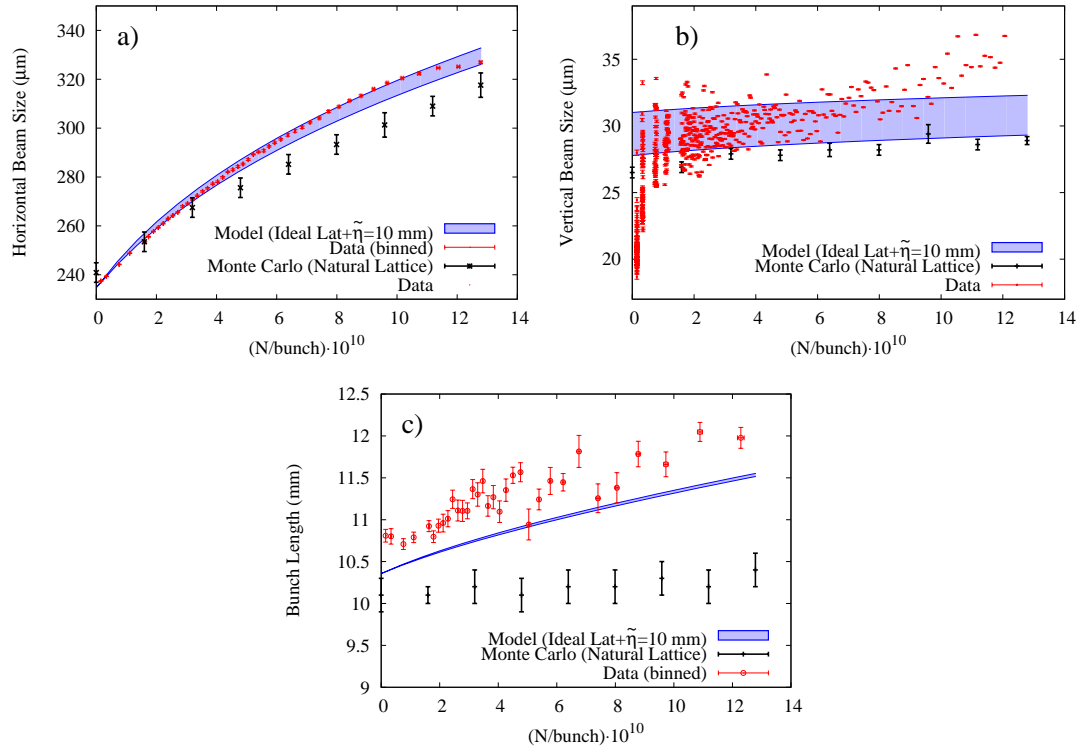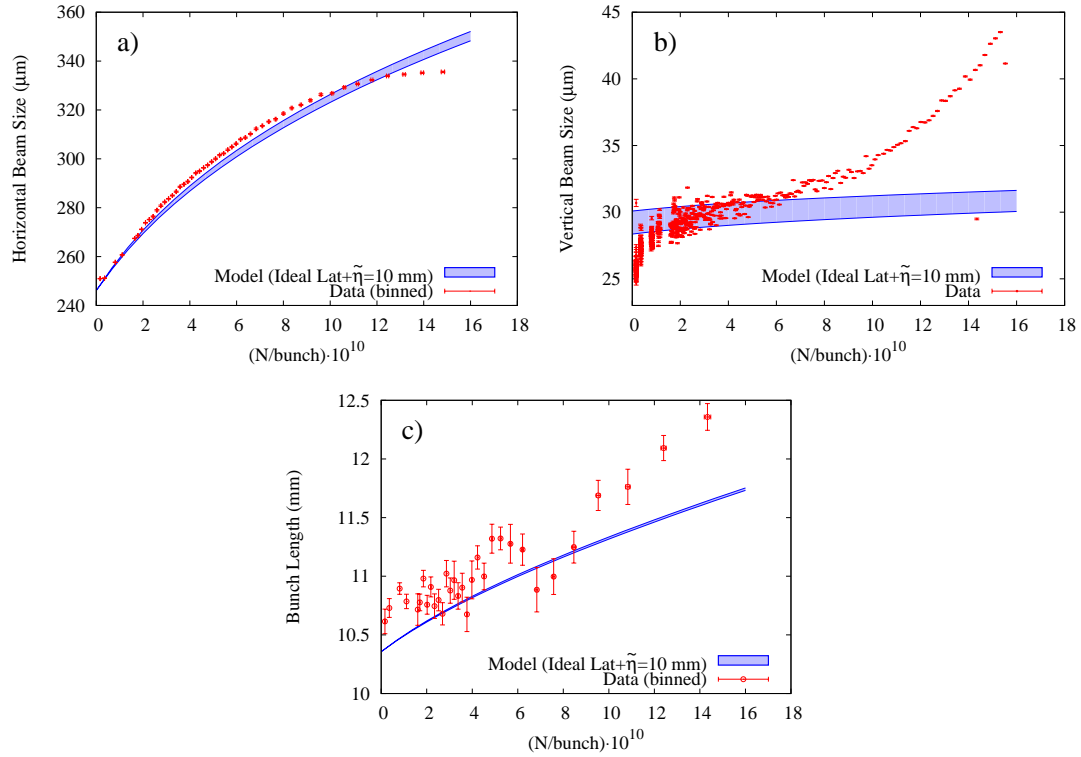
Figure 2.31: (a) horizontal, (b) vertical, and (c) longitudinal beam size versus current for e^- bunch in conditions tuned for minimum vertical emittance. An uninitialized transverse feedback system was mistakenly turned on during this run. It drove the coherent tunes onto the $(1, -1, 1, 0)$ resonance line at currents 5.6×10^{10} above part/bunch.

tance is 4.3 nm-rad at zero current and 8.2 nm-rad at 4.8×10^{10} particles/bunch. The zero current vertical emittances that bound the data are 17.0 pm and 22.5 pm.

Shown in Fig. 2.32 is data from an e^- run where the vertical emittance was increased. The horizontal emittance is 4.2 nm-rad at zero current and 5.5 nm-rad at 4.8×10^{10} particles/bunch. The vertical emittances that bound the data are 172 pm and 188 pm.

Figure 2.33 shows the combined data from the two e^- and two e^+ April 2012 data sets. Simulation parameters for the April 2012 data are summarized in Tab. 2.5.
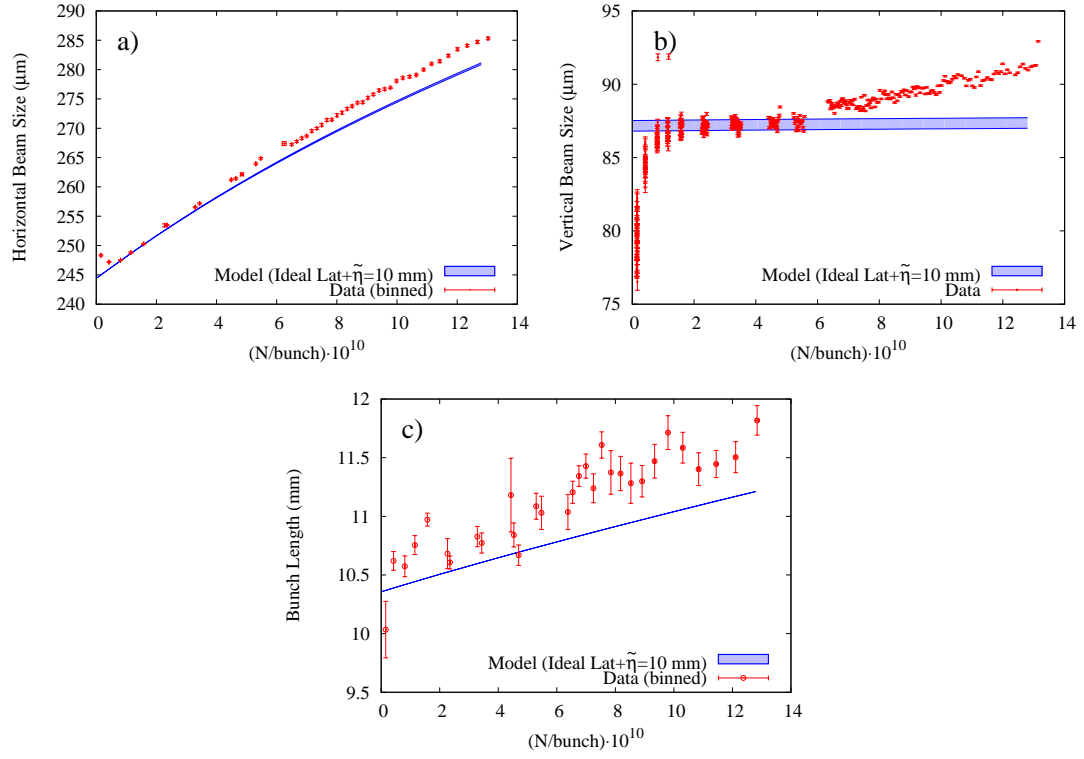
Figure 2.32: (a) horizontal, (b) vertical, and (c) longitudinal beam size versus current for e^- bunch with increased zero current vertical emittance. An uninitialized transverse feedback system was mistakenly turned on during this run. It drove the coherent tunes onto the $(1, -1, 1, 0)$ resonance line at currents above 5.6×10^{10} part/bunch.

Table 2.5: Simulation parameters used to model April 2012 data.

	Min. ϵ_{y0} (pm rad)	Max. ϵ_{y0} (pm rad)	ϵ_{x0} (nm rad)	ϵ_x at high current (nm rad)
e^+ Low ϵ_{y0}	17.4	24.6	3.8	10.6
e^+ High ϵ_{y0}	48.0	56.3	3.7	8.1
e^- Low ϵ_{y0}	17.0	22.5	4.3	-
e^- High ϵ_{y0}	172.	188.	4.2	-

Figure 2.33: Aggregated (a) horizontal, (b) vertical, and (c) longitudinal data comparing e^+ and e^- in minimum emittance conditions and conditions where the zero current vertical emittance was blown up using closed coupling and dispersion bumps.

2.12.3.2 December 2012 Data

Prior to the December 2012 machine studies, the same lattice had been used for all IBS experiments. This lattice is referred to as "CD40" and has 12 wigglers at full power, and the optics are configured for low emittance. This lattice also has about 1 m of horizontal dispersion in the RF cavities.

In the April 2012 measurements, and during all earlier machine studies, the horizontal beam size was observed to be about 80 μm larger than calculated. Around 160 μm was expected, but around 240 μm was measured.

The large horizontal beam size was puzzling. There were many investigations into possible optics problems and instrumentation systematics. Then, during the development of the Monte Carlo simulations discussed in Sec. 2.9, it was noticed that the same large horizontal beam sizes were being reproduced. Simulation investigations led us to the conclusion that the cause was dispersion in the RF cavities.

Dispersion in the RF cavities creates horizontal-longitudinal coupling that is reflected in non-zero V_{15} coupling terms. These coupling terms tilt the beam in the horizontal-longitudinal plane. This was the cause of the large horizontal beam size measurements. The beam was tilted in the $x - z$ plane at the instrumentation source points.

In preparation for the December 2012 machine studies, two remedies were prepared. The first remedy was to create a new lattice that controlled the horizontal phase advance between the RF cavities. The phase advance was adjusted in order to cancel the V_{15} terms in the regions where the instrumentation is located. This lattice is referred to as "V15 Managed".

Table 2.6: Simulation parameters used to model December 2012 2.1 GeV data. All data is from positron beams. Optics adjusted to minimize V_{15} at the beam size instrumentation source points.

| | Min. ϵ_{y0} | Max. ϵ_{y0} | ϵ_{x0} | ϵ_x at high current |
	(pm rad)	(pm rad)	(nm rad)	(nm rad)
Low ϵ_{y0}	12.9	17.7	3.6	10.8
Med. ϵ_{y0}	59.6	69.6	4.1	8.1
High ϵ_{y0}	180.	197.	3.4	5.8

The second remedy was to prepare a lattice with 6 of the 12 damping wigglers powered off. Powering off the extra wigglers frees up the constraints on the lattice optics and allows for the dispersion at the RF cavities to be set to zero. This naturally eliminates the V_{15} coupling, at the expense of half the damping. This lattice is referred to as "eta-free".

To validate these remedies, beam size versus RF voltage measurements were taken on all 3 lattices: CD40, V15 Managed, and eta-free. The results are shown in Figs. 2.41, 2.42, and 2.43. The V_{15} coupling term varies with the RF voltage and so changing the RF voltage adjusts the tilt at the instrumentation source points. A reduction in the RF voltage is expected to reduce the tilt at the instrumentation source point and therefore reduce the measured horizontal beam size. However, reducing the RF voltage also lengthens the bunch, which reduces IBS effects. The beam size versus RF voltage measurements were done at low current, 0.5 mA and 1.0 mA to minimize the effect of IBS. Nonetheless, IBS effects are still present in the horizontal at these low currents and the predicted results for these experiments include IBS calculations.

The V15 Managed lattice proved to be a success not only for the beam size versus current measurements, but also for the beam size versus current measurements. Beam size versus current data for the V15 Managed lattice is shown in Figs 2.34, 2.35, 2.36, and 2.37. Simulation parameters are shown in Tab. 2.6.

The beam size versus current data for the eta-free lattice was dominated by non-IBS current-dependent effects. Beam size versus current measurements for the eta-free lattice are not shown. Loading the eta-free lattice into CesrTA, obtaining decent injection, and tuning for low emittance were very challenging. This lattice will be revisited in future CesrTA machine studies and more attention will be spent on working out its systematics.

Prior to the December 2012 machine studies, it was found that the transverse feedback amplifiers were adding a substantial amount of noise to the beam. The amplifiers were exciting beam motion at the betatron tunes and increasing the emittance of the beam. This effect was seen even if feedback was not being applied to the beam. To remedy this solution, the feedback amplifiers were physically turned off during the IBS measurements. This resulted in a 5 pm reduction in vertical emittance and substantially less measurement-to-measurement scatter in the horizontal beam size measurement.

Difficulties were encountered when trying to obtain data with electrons during the December 2012 machine studies. We were not able to obtain reliable IBS data with electron beams. It is not known whether species-dependent beam physics, such as ions or electron cloud, played a role, or if there were problems with the instrumentation. Positron beams and electron beams are measured with different instrumentation. All reported data from the December 2012 machine studies is from positron beams.
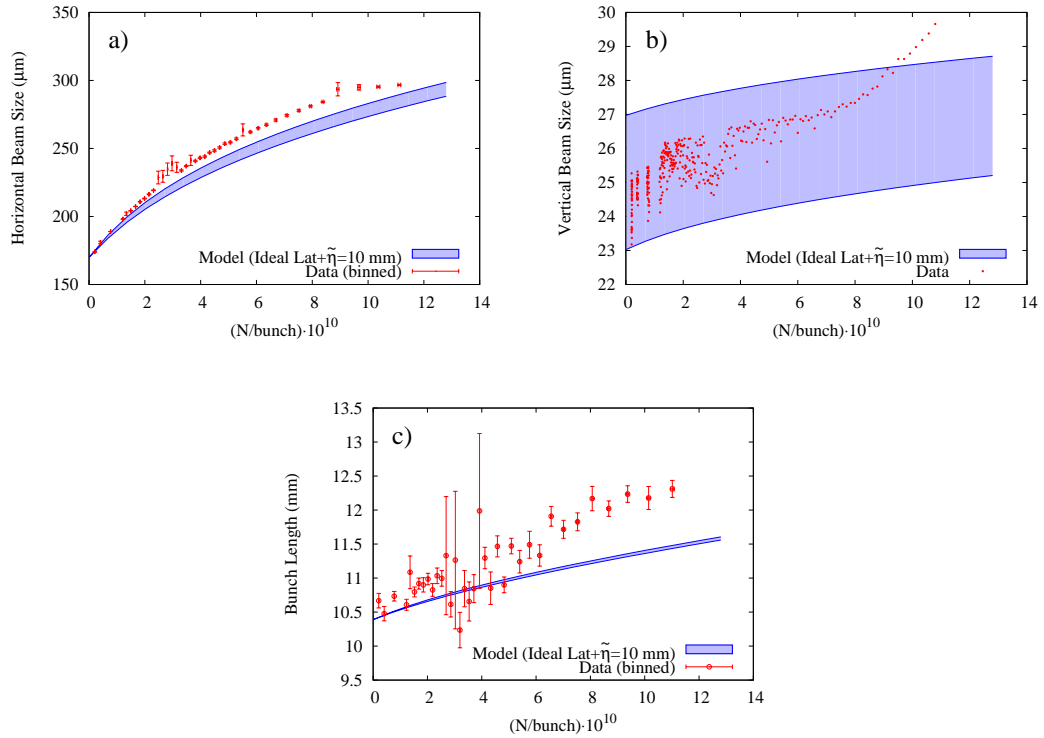
Figure 2.34: Measurements on V15 Managed lattice. (a) horizontal, (b) vertical, and (c) longitudinal beam size versus current for e^+ bunch in CesrTA configured for low emittance. The simulation is run twice. Once with a zero-current vertical beam size that extends to the bottom range of vertical size measurements, and once that extends to the upper range. The area between these two simulation results is shaded in blue. The lower range vertical emittance is 12.9 pm-rad, and the upper range is 17.7 pm-rad. Zero current horizontal emittance is 3.6 nm-rad.
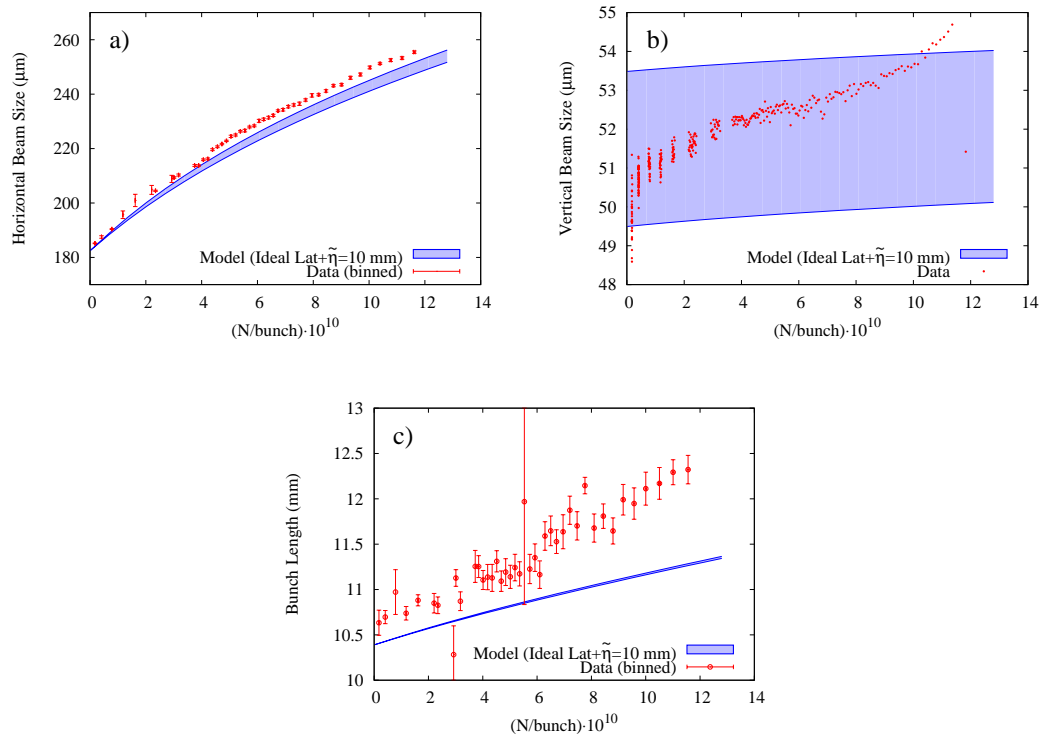
Figure 2.35: Measurements on V15 Managed lattice. (a) horizontal, (b) vertical, and (c) longitudinal beam size versus current for e^+ bunch in CesrTA configured for approximately 55 pm vertical emittance.
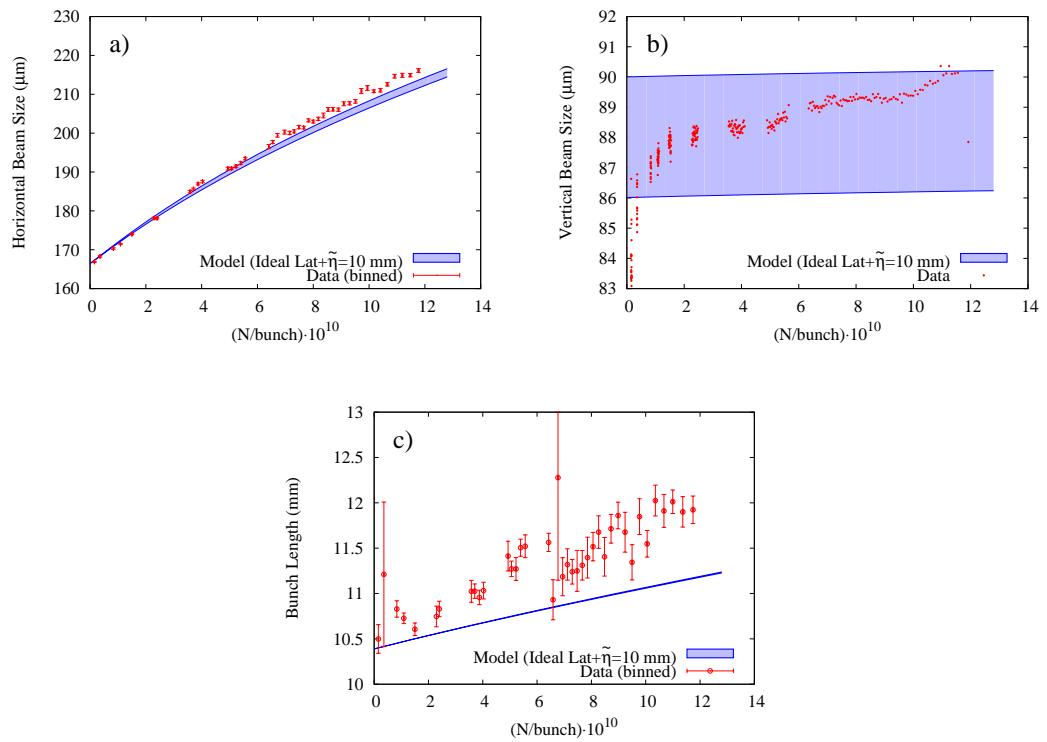
Figure 2.36: Measurements on V15 Managed lattice. (a) horizontal, (b) vertical, and (c) longitudinal beam size versus current for e^+ bunch in CesrTA configured for approximately 160 pm vertical emittance
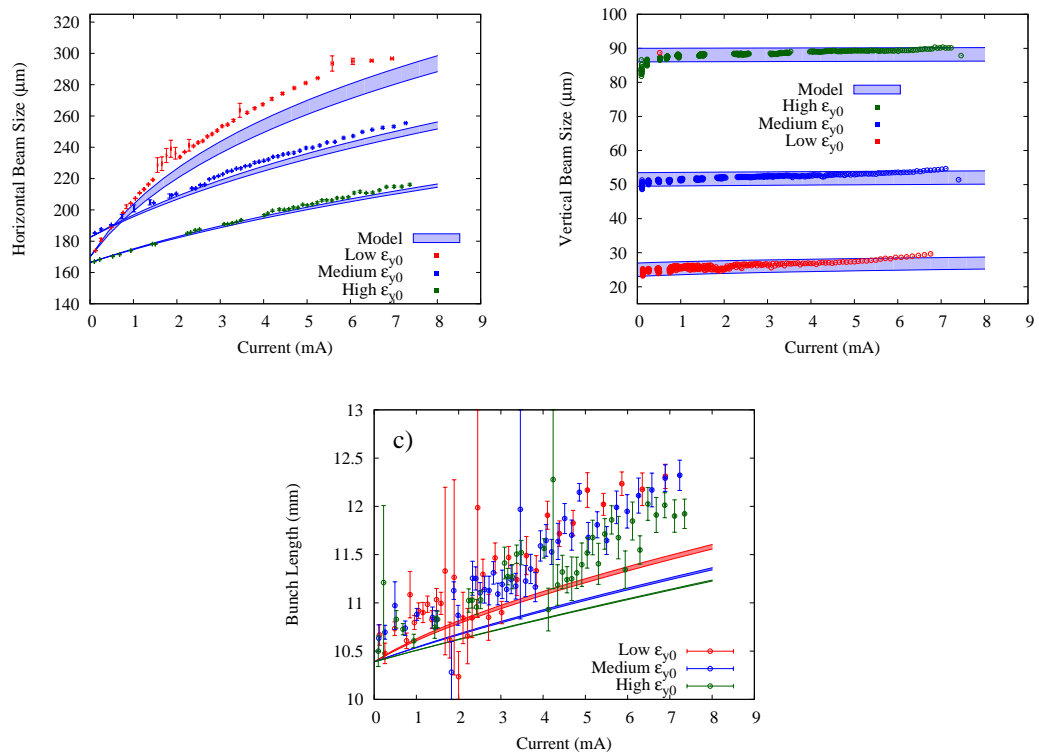
Figure 2.37: Measurements on V15 Managed lattice. Aggregated (a) horizontal, (b) vertical, and (c) longitudinal data comparing e^+ in minimum emittance conditions and conditions where the zero current vertical emittance was blown up using closed coupling and dispersion bumps.

Comparison of data and simulation result over a range of beam energies is an important check of the accuracy of IBS theory and our method for predicting current-dependent beam sizes.

Intrabeam scattering growth rates have a $\dfrac{1}{\gamma^4}$ dependence on beam energy. Two of these factors of $\dfrac{1}{\gamma}$ come from adiabatic damping of the geometric emittance. One factor of $\dfrac{1}{\gamma}$ comes from length contraction. In the center of momentum frame of the bunch, the particle density is reduced by a factor of $\dfrac{1}{\gamma}$. The last factor of γ comes from time dilation in the center of momentum frame.

Shown in Figs. 2.38 and 2.39 is data from CesrTA positron beams at 2.3 GeV. In Fig. 2.38, the machine is tuned for minimum vertical emittance. In Fig. 2.39, the zero current vertical emittance is increased using a closed optics bump that increased the coupling and vertical dispersion in the wiggler regions.

Shown in Tab. 2.7 are the simulation parameters used to model the December 2012 2.3 GeV IBS data.

Shown in Fig. 2.40 is the aggregated data from the December 2012 2.3 GeV IBS studies.

Note that the vertical beam sizes observed in CesrTA at 2.3 GeV are smaller than those observed at 2.1 GeV. This suggests that the current-independent vertical emittance of the machine is generated in large part by noise in the machine. Emittance generated due to photon emission goes as γ^2, while emittance generated due to noise is reduced as beam energy is increased.
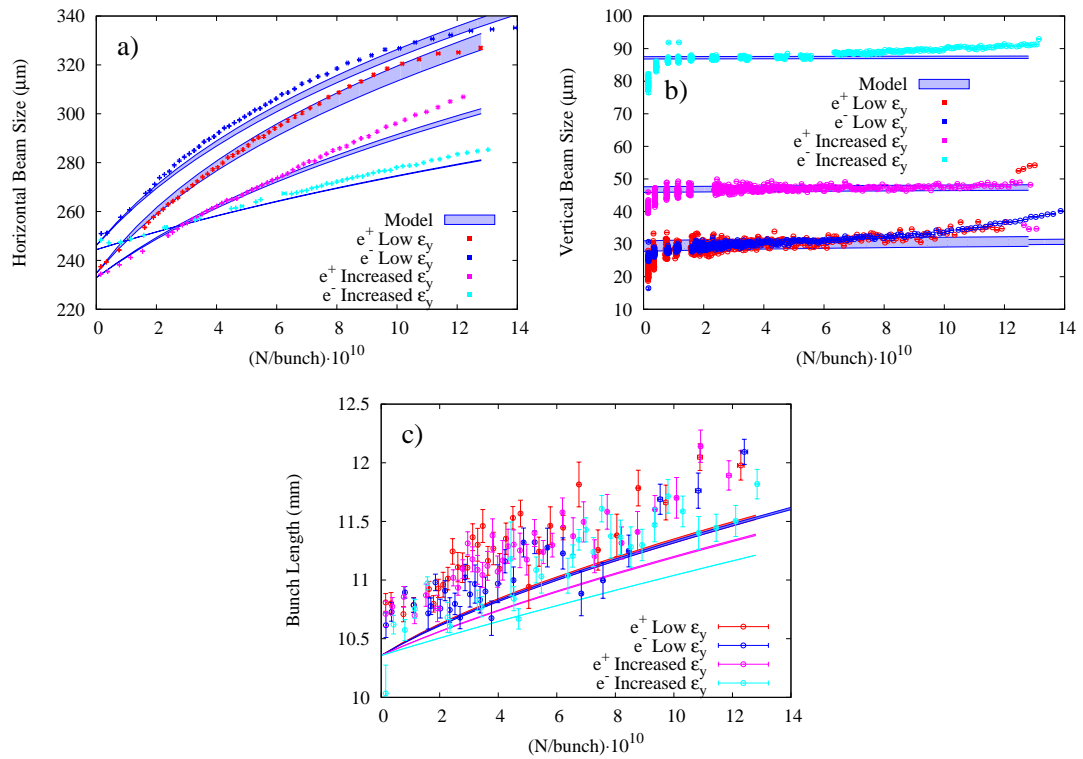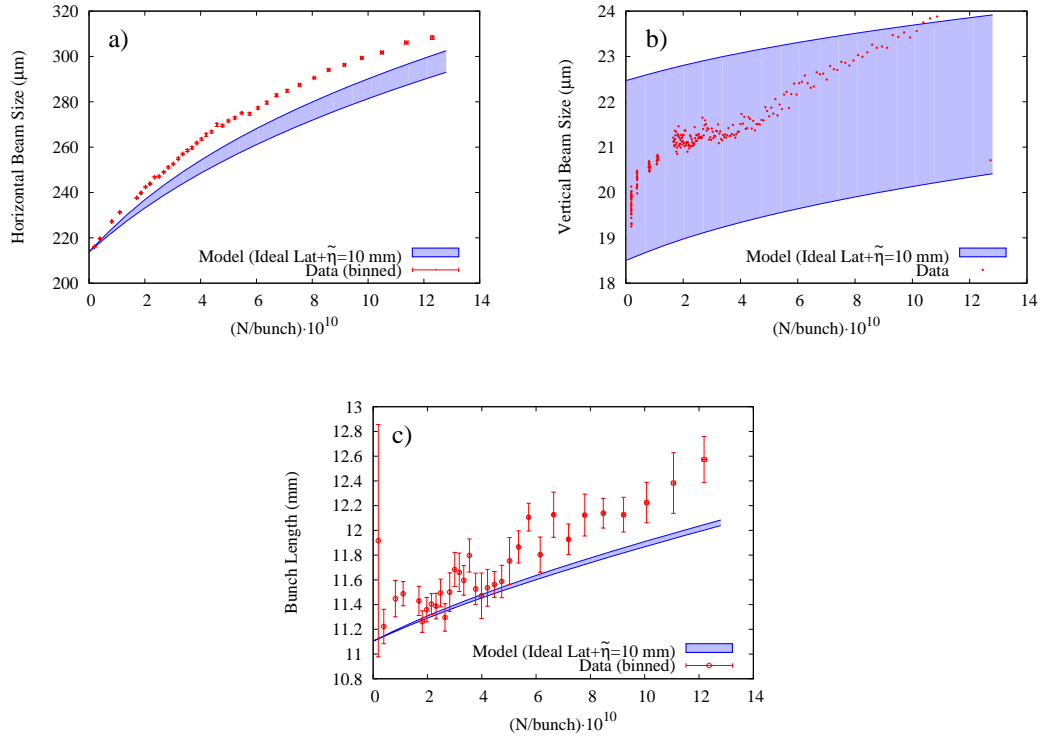
Figure 2.38: (a) horizontal, (b) vertical, and (c) longitudinal beam size versus current for 2.3 GeV e^+ bunch in CesrTA configured for approximately 6 pm vertical emittance.

Table 2.7: Simulation parameters used to model December 2012 2.3 GeV data. All data is from positron beams. Optics are adjusted to minimize V_{15} coupling at the beam size instrumentation source points.

| | Min. ϵ_{y0} | Max. ϵ_{y0} | ϵ_{x0} | ϵ_x at high current |
	(pm rad)	(pm rad)	(nm rad)	(nm rad)
Low ϵ_{y0}	8.68	12.8	5.63	11.3
High ϵ_{y0}	63.4	73.9	5.63	8.05

Figure 2.39: (a) horizontal, (b) vertical, and (c) longitudinal beam size versus current for 2.3 GeV e^+ bunch in CesrTA configured for approximately 54 pm vertical emittance.
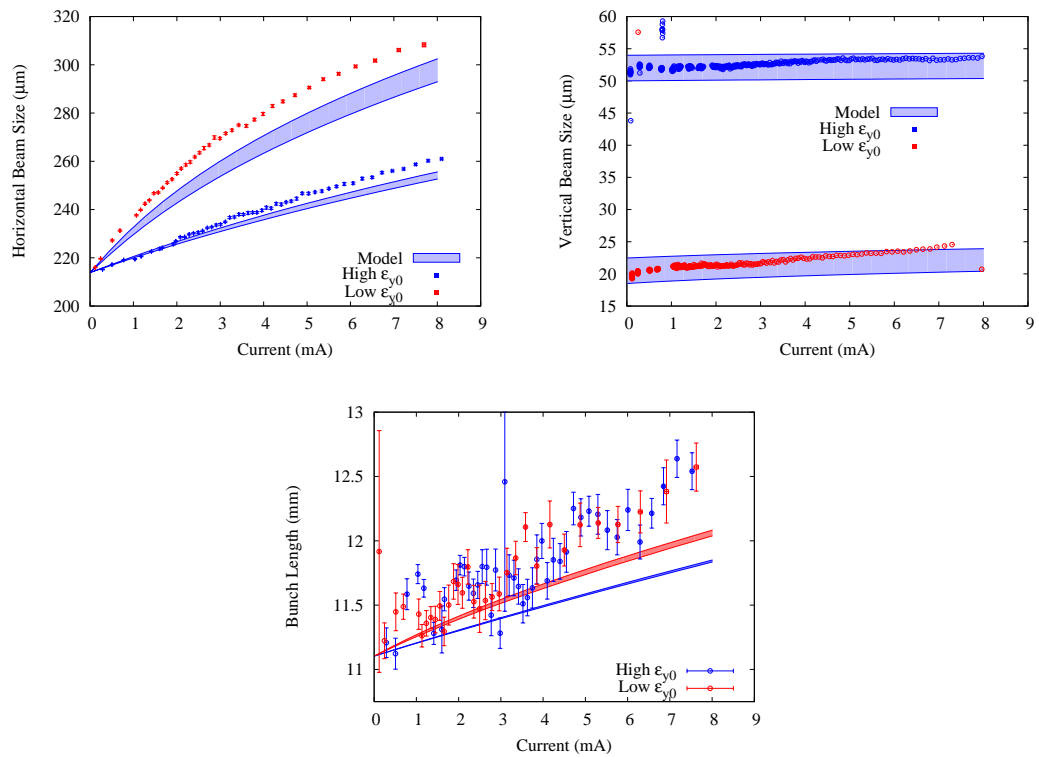
Figure 2.40: Aggregated 2.3 GeV data. (a) horizontal, (b) vertical, and (c) longitudinal beam size versus current. Optics are configured to minimize V_{15} coupling at the horizontal beam size monitor source point.
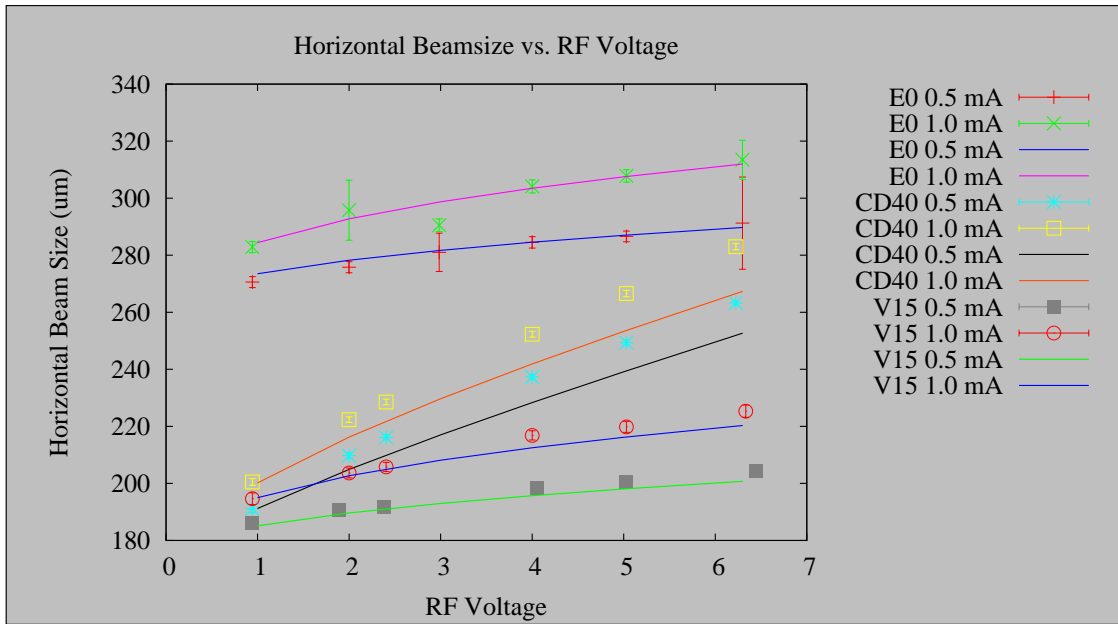
Figure 2.41: Horizontal beam size versus RF voltage. Both V15 tilt and IBS effects are observed in this data.
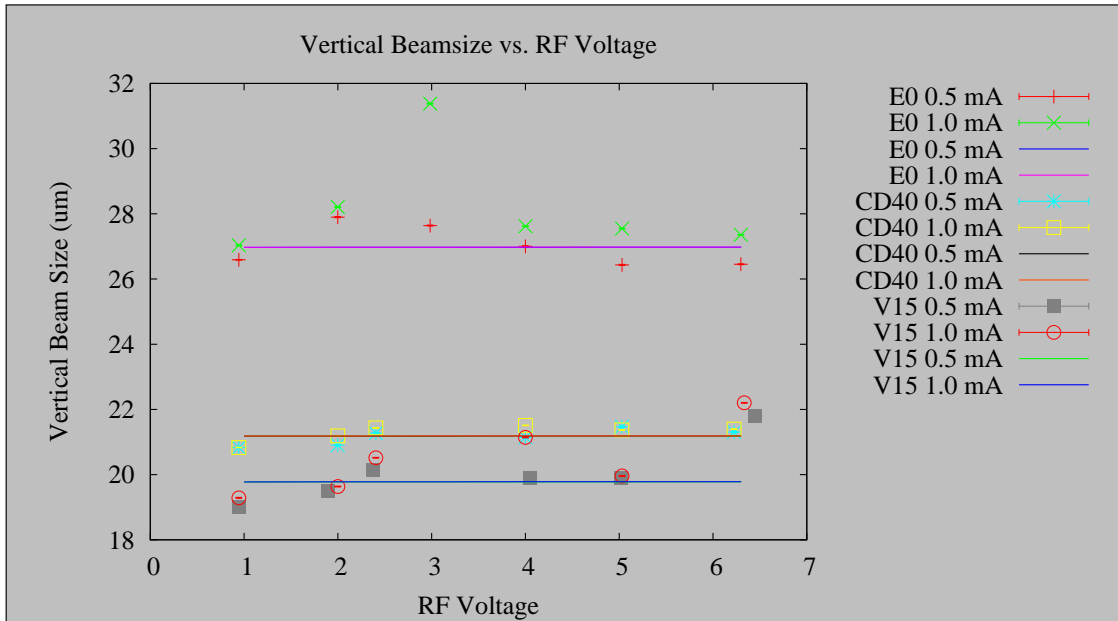
Figure 2.42: Vertical beam size versus RF voltage. The simulation lattices here are ideal with no vertical dispersion. Expected response is flat versus RF voltage.
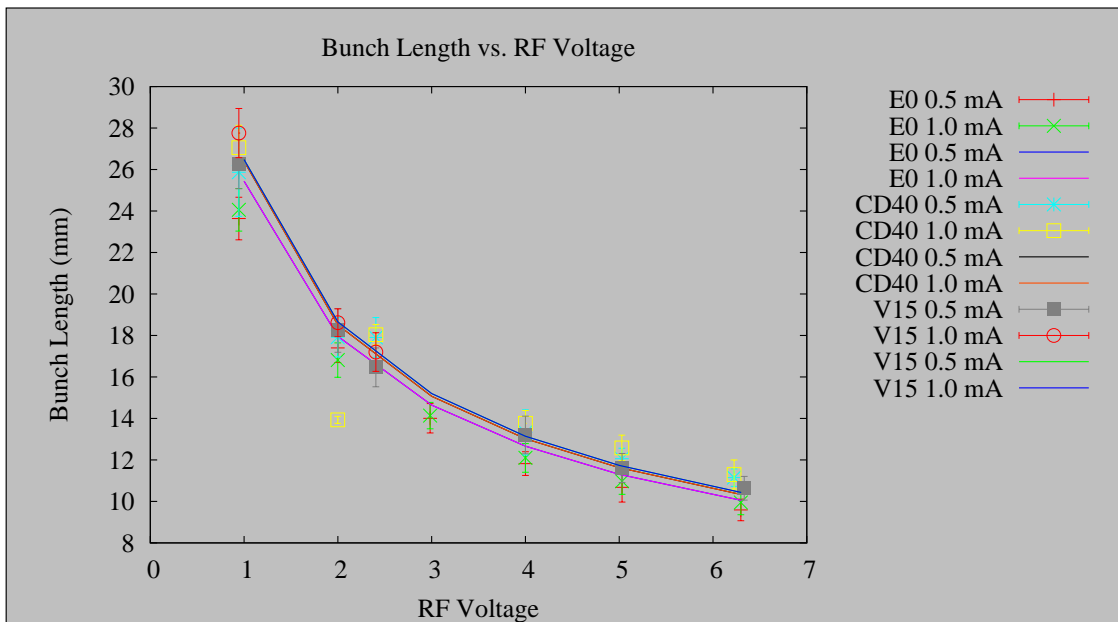
Figure 2.43: Bunch length versus RF voltage. The primary effect see here is the change in bunch length due to change in RF cavity voltage.

2.13 Discussion

2.13.1 Data

IBS effects are most evident in the horizontal dimension, where large horizontal dispersion leads to significant blow-up. In comparison, IBS is not a strong effect in the vertical. This is because the vertical dispersion and transverse coupling are so small. The direct transfer of momentum from the horizontal to the vertical by IBS is small at 2.1 GeV.

The amount of the blow-up can be controlled by varying the zero-current vertical emittance, and thus the particle density. The simulations show bunch lengthening due to IBS, but we are unable to distinguish IBS lengthening from potential well distortion in our measurements.

An interesting anomaly we have encountered is the behavior of the vertical beam size at high currents. The effect is seen in Fig. 2.28(b) above 9×10^{10} particles/bunch, Fig. 2.38(b) above about 5×10^{10} particles/bunch, and also in Fig. 2.34(b), Fig. 2.35(b), and Fig. 2.36(b). We observe that vertical beam size plotted versus current increases with positive curvature. Much more severe cases of this blow-up have been observed during the machine studies. We find that adjusting betatron and synchrotron tunes during experiments affects the blow-up, but in a somewhat unpredictable way.

The horizontal beam size is observed to decrease when the vertical size increases. This is expected behavior in an IBS-dominated beam. The increase in the vertical size decreases the particle density, which therefore reduces the strength of the IBS effect.

The blow-up is believed to be due in part to coherent tune shift and incoherent tune

footprint. When the coherent tune we measure approaches a resonance line, the vertical beam size is seen to increase. While the incoherent tune cannot be measured, analytic calculations and Monte Carlo space charge simulation suggests that, at high current, the footprint of the bunch in the tune plane is very large and spans many resonance lines.

At high current, the vertical beam centroid position over 32768 turns was recorded using the turn-by-turn vertical beam size-monitor. An FFT of these data does not show a clear signal above background, so we cannot attribute the anomalous growth in vertical size to an instability. Adjustments to the corrected chromaticity did not impact the blow up.

Coupling measurements at high current have been taken in conditions where the anomalous blow-up was observed, and no evidence was found of current-dependent transverse coupling.

The low current bunch length we measure is consistently about 0.5 mm longer than the predicted value, or about 5%. Given that bunch length is a fairly simple, and presumably robust, calculation, it is puzzling why our measurements are systematically off. The size of the discrepancy seems to have been smaller during the December run. The streak camera has been checked thoroughly for systematics and a cause has not been found.

Good agreement between our IBS calculation methods and experiment were found in April and December for 2.1 GeV beams. In December, we also obtained data at 2.3 GeV. We find that the predictions of our IBS calculation methods are in good agreement with the 2.3 GeV data. No modifications to the simulation method were necessary, and no parameters were adjusted aside from loading in the 2.3 GeV lattice. We believe this is a strong argument in support of our IBS calculation methods.

2.13.2 Theory

The presence of the Coulomb Log is a well-known ambiguity in IBS theory as it requires the introduction of loosely defined cutoffs in the minimum and maximum scattering angle. The choice of one event per damping time as the boundary between multiple-event and single-event scattering is somewhat arbitrary. That said, the data shown here are in reasonable agreement with theory, suggesting that with implementation of the tail-cut, the IBS theory is a reasonable model of performance for electron machines. Furthermore, as shown in Fig. 2.14(b), the theory gives a good description of the data even when the large angle cutoff used in the calculation is varied by more than an order of magnitude.

The theory used here is Kubo & Oide's Σ-matrix based IBS formalism. This model is a generalization of Bjorken & Mtingwa's formalism that can handle arbitrary coupling of the horizontal, vertical, and longitudinal motion. It includes the tail-cut. Coupling in CesrTA for the experiments shown here was not large enough to noticeably impact the IBS growth rates. If coupling were significantly larger, then the predictions from Kubo & Oide's method may diverge from those of Bjorken & Mtingwa's method. Such will be the subject of future investigations.

2.13.3 Conclusions

In this first half of the thesis, we have derived methods for calculating IBS growth rates and incorporated them into a normal modes simulation environment. These methods have been used to predict beam size versus current behavior in CesrTA.

Measurements in all three dimensions of beam size versus current in single-bunch

beams dominated by IBS effects at 2.1 and 2.3 GeV have been taken. The measurements compare well with predictions over the range of currents where IBS effects are dominant.

At high current, another effect takes over causing the vertical beam size versus current to increase with positive curvature. Early investigations suggest that this blow-up could be due to incoherent tune due to direct space charge. Analytic calculations suggest that the tune shift due to direct space charge will be large above a few mA, and Monte Carlo simulations have produced a tune foot print that encounters the half-integer resonance. Future CesrTA experiments will examine this effect by exploring regions of the tune plane far away from low-order resonance lines.

We have discussed other current-independent effects, such as working point, and current-dependent effects such as potential well distortion, coherent tune shift, and direct space charge. We have shown that these additional effects need to be considered when studying low-emittance electron/positron beams.

Measurements of beam size versus RF voltage at low current have been taken and confirm our hypothesis that the larger-than-expected horizontal beam sizes that were observed in CesrTA were due to horizontal-longitudinal coupling introduced by horizontal dispersion in the RF cavities.

CHAPTER 3

PARTICLE LOSS DUE TO TOUSCHEK EFFECT IN ENERGY RECOVERY LINEAR ACCELERATOR

3.1 Introduction

Intra-beam scattering (IBS) refers to collisions among the particles that make up a beam. All particle beams occupy a finite region of phase space, and therefore the particles are constantly moving relative to the center of momentum (c.o.m.) of the bunch and can collide with each other. These collisions change the energy of the particles. Changes in energy in the c.o.m. frame translate to changes in energy relative to the magnetic lattice that guides the beam, and collisions between particles therefore change the trajectories of the colliding particles through the accelerator.

The energy difference between two scattering particles is typically on the order of the beam's energy spread and thus several orders of magnitude smaller than their average energy. A scattering event can transfer energy from transverse motion to the longitudinal which, as it turns out, is larger by the relativistic factor γ in the lab frame than in the center of momentum frame. Collisions that change a particle's momentum parallel to the average momentum can therefore result in energy changes large enough to significantly perturb the trajectory of particles when γ is large, causing the particle to collide with the beam chamber downstream of the scattering event.

Particles lost along the chamber walls due to single-event IBS are called Touschek losses and have been explored theoretically [32, 23] and experimentally [28, 18]. Touschek losses can reduce the beam lifetime [22], and cause radiation hazards as discussed in this chapter.

141

Intra-beam scattering that does not result in particle losses can change the emittance and energy spread of a beam [30, 5]. The effect can impose a current limit on low-emittance storage rings such at ATF at KEK [2] and CesrTA at Cornell [11].

This chapter discusses IBS and Touschek losses in linear accelerators. Because the beam in a linear accelerator does not circulate, there is no beam lifetime to be concerned about, but the radiation hazard from particles lost along the chamber walls and the change in energy spread and emittance of the beam can be significant.

Touschek scattering is of particular interest for Energy Recovery Linear accelerators (ERLs), where the beam undergoes deceleration. This increases the relative energy deviation $\Delta E/E$ of the particles which increases the dispersive contribution to the oscillation amplitude of the particles' trajectories. When a particle scatters in a dispersive region and its energy changes, so does its action invariant J. This effect is of increased importance in an ERL because J increases with $1/\gamma$ by adiabatic anti-damping during deceleration.

In an ERL, a particle that has lost energy in a scattering event that occurred at high energy can be stopped in an RF cavity and accelerated backwards during the energy recovery (deceleration) phase. These stopped particles may pose a problem for super-conducting RF cavities.

The theory for our study of IBS in ERLs is based on a derivation by Piwinski [32]. Here we offer an alternative derivation of Piwinski's formula that is more rigorous and gives the orders in divergence, momentum spread, and relativistic γ to which the result is accurate. Whereas the earlier derivation in [32] is used to define a beam lifetime for storage rings, our derivation is used to determine the distribution of scattered particles generated at each element in an accelerator. This distribution of scattered particles is

tracked along the accelerator to determine where each particle is lost, yielding a distribution of particle loss along the accelerator. This method of simulating Touschek losses was first developed at APS for their ERL design[59].

To facilitate the tracking, an additional simulation is used to determine the element-by-element energy aperture of the accelerator. This aperture is the largest positive or negative energy change that a particle can be given at a particular element such that the particle is not lost further down the accelerator. This information allows us to avoid tracking particles that are not lost, and therefore not of interest. The energy aperture is allowed to be non-symmetric.

Additionally, we determine the background of scattered particles exiting the linac. Capturing this background is an important requirement for a beam dump design.

A methodology for placing collimators to control where IBS losses occur is described. The trajectories of scattered particles are analyzed to determine the best locations for collimators. We demonstrate how this methodology has been applied to the Cornell ERL.

Large energy-change scattering events are infrequent enough that multiple scattering events do not lead to significant losses, but multiple small energy change events can change the emittance or energy spread of the beam. IBS formulas from [5] are applied to determine emittance growth due to multiple scattering events along the ERL.

3.2 Theory

The rate R at which particles are scattered out of a bunch is found by integrating over the scattering cross-section σ for particle loss. This cross-section is obtained by integrating

the Moller differential scattering cross-section over all scattering events that result in particle loss. In general, σ depends on the momenta $\vec{p}_1$ and $\vec{p}_2$ of the scattering particles, and it can depend on the location $\vec{r}$ within the beam at which a scattering event occurs.

A test particle with momentum $\vec{p}_1$ at position $\vec{r}_1$ moving with velocity Δv relative to other particles in the bunch at position $\vec{r}$ will make

$$r\left(\vec{r}\vec{p}_1\right) = \int \Delta v\left(\vec{p}_1, \vec{p}_2\right) \rho\left(\vec{r}, \vec{p}_2\right) \sigma d^3 p_2 \tag{3.1}$$

collisions per time, where $\rho\left(\vec{r}, \vec{p}\right)$ is the phase space density of the bunch and σ is the cross-section for collisions that lead to particle loss. Integrating over each particle in the bunch colliding with all of the other particles yields

$$R = \frac{1}{2} \int \int \Delta v\left(\vec{p}_1, \vec{p}_2\right) \int \sigma \rho\left(\vec{r}, \vec{p}_1\right) \rho\left(\vec{r}, \vec{p}_2\right) d^3 r d^3 p_1 d^3 p_2. \tag{3.2}$$

The factor $1/2$ comes from the fact that particle 1 colliding with particle 2 is the same event as particle 2 colliding with particle 1.

For bunches with Gaussian distribution and without x-y coupling in the accelerator,

$$\rho\left(\vec{r}, \vec{p}\right) = N \exp\left(-Q\left(x, x'\right) - Q\left(y, y'\right) - Q\left(\Delta s, \delta\right)\right), \tag{3.3}$$

where N is a normalization and the Qs are quadratic forms that depend on the Twiss parameters.

We now restrict to the common case where the beam's cross section is much smaller than the beam pipe. In this case, the initial position coordinate of the particle is small compared to the trajectories that result in particle loss. It is then a good approximation that the cross-section for particle loss σ does not depend on initial coordinate $\vec{r}$.

Subsequently, Δv and σ are approximated in orders of the following small quantities:

1. the angle χ between $\vec{p}_1$ and $\vec{p}_2$.

2. energy spread δ_E of the bunch.

3. relativistic $1/\gamma_0^2$ of the reference particle.

Collectively, approximations in these three parameters are referred to as of order O. It is one of the main contributions of this chapter to rigorously carry the order of these small quantities to estimate the theory's degree of accuracy.

To leading order, it will be shown that Δv and σ depend only on χ^2, allowing the integration over all terms in the exponential except $\chi_{x,y}$, yielding

$$R = N \int \Delta v \sigma \exp\left(-Q\left(\chi_x, \chi_y\right)\right) d\chi_x d\chi_y. \tag{3.4}$$

With $\chi_x = \chi \cos\phi$ and $\chi_y = \chi \sin\phi$, one can further integrate over ϕ where the exponential of a trigonometric function generates a Bessel function,

$$R = N \int \Delta v\left(\rho\right) \sigma\left(\rho\right) \exp\left(-a\chi\right) I_0\left(b\chi\right) d\chi. \tag{3.5}$$

The derivation that leads to the scattering rate is organized as follows: (a) integrate Gaussians over $\vec{r}$, (b) approximate Δv, (c) approximate σ, (d) integrate over the initial angle ϕ between the two particles.

3.2.1 Integrate Gaussians over $\vec{r}$

The integration over $\vec{r}$ can be performed immediately. It is assumed that the bunch with N_p particles has a Gaussian distribution which can be written in Twiss parameters as,

$$\begin{aligned}
\rho\left(\vec{r}, \vec{p}\right) \quad &= \frac{N_p}{8\pi^3 \epsilon_x \epsilon_y \sigma_s \sigma_p} \exp\left[-\frac{x_\beta^2 + \left(\alpha_x x_\beta + \beta_x x_\beta'\right)^2}{2\sigma_{x\beta}^2} \right. \\
&\left. -\frac{y_\beta^2 + \left(\alpha_y y_\beta + \beta_y y_\beta'\right)^2}{2\sigma_{y\beta}^2} - \frac{\Delta s^2}{2\sigma_s^2} - \frac{\delta_p^2}{2\sigma_p^2} \right],
\end{aligned} \tag{3.6}$$

145

where, with the dispersion (D_x, D_y) and the reference momentum p_r,

$$
\begin{aligned}
x_\beta &= x - D_x \delta_p, \\
y_\beta &= y - D_y \delta_p, \\
x'_\beta &= x' - D'_x \delta_p, \\
y'_\beta &= y' - D'_y \delta_p, \\
x' &= p_x / p_r, \\
y' &= p_y / p_r.
\end{aligned}
\tag{3.7}
$$

The integration over $\vec{r} = \{x, y, \Delta s\}$ can be written in the form,

$$
\int_{-\infty}^{\infty} \exp\left(-\frac{\Delta s^2}{2\sigma_s^2}\right) d\Delta s \int_{-\infty}^{\infty} \exp\left(-\left(a_x x^2 + b_x x + c_x\right)\right) dx \times
$$

$$
\int_{-\infty}^{\infty} \exp\left(-\left(a_y y^2 + b_y y + c_y\right)\right) dy, \quad (3.8)
$$

where the coefficients of x^2, x^1, and x^0 have been collected into $a_{x,y}$, $b_{x,y}$, and $c_{x,y}$, which are not functions of x, y, and Δs, but are functions of p_x, p_y, and δ_p. Evaluating the three integrals in Eqn. (3.8) yields,

$$
\sqrt{\pi} \sigma_s \times \sqrt{\frac{\pi}{a_x}} \exp\left(\frac{b_x^2}{4 a_x} - c_x\right) \times \sqrt{\frac{\pi}{a_y}} \exp\left(\frac{b_y^2}{4 a_y} - c_y\right).
\tag{3.9}
$$

The result is,

$$
R = \frac{N_p^2}{128 \pi^5 \epsilon_x^2 \epsilon_y^2 \sigma_s \sigma_p^2} \sqrt{\frac{\pi}{a_x a_y}} \iint_{\vec{p}_1 \vec{p}_2} \Delta v\left(\vec{p}_1, \vec{p}_2\right) \sigma\left(\vec{p}_1, \vec{p}_2\right) \times
$$

$$
\exp\left(-\left\{\frac{\delta_{p1}^2 + \delta_{p2}^2}{2\sigma_p^2} + \frac{b_x^2}{4 a_x} - c_x + \frac{b_y^2}{4 a_y} - c_y\right\}\right) d^3 p_1 d^3 p_2. \quad (3.10)
$$

3.2.2 Approximate Δv

Here we find formulas for the relative velocity Δv between two particles. We begin by constructing a coordinate system based on the momenta of two particles that are about to collide. The particles' coordinates are transformed into this coordinate system and their relative velocity in terms of the initial angle between their momenta is determined. Next, the particles are boosted into their center-of-momentum frame where their post-collision momenta are written in terms of scattering angles. The post-collision momenta are transformed back into the lab frame for the change in energy. Thresholds on scattering angles leading to particle loss are obtained by evaluating this formula for a maximum allowable change in energy. The Moller scattering cross-section is integrated over these angles to obtain the cross-section for particle loss used in Eqn. (3.10).

The pre-collision momenta of the two particles in the lab-frame are,

$$
\vec{p}_{1,2} = \begin{pmatrix} E_{1,2}/c \\ p_{x1,2} \\ p_{y1,2} \\ p_{z1,2} \end{pmatrix}_{(\hat{x},\hat{y},\hat{z})} . \tag{3.11}
$$

The sum of these two momenta is defined as $\vec{p} \equiv \frac{1}{2}\left(\vec{p}_1 + \vec{p}_2\right)$. A new orthonormal coordinate system, depicted in Fig. 3.1 is defined by,

$$
\hat{j} = \hat{k} \times \hat{l}, \quad \hat{k} = \frac{\vec{p}_2 \times \vec{p}_1}{|\vec{p}_1 \times \vec{p}_2|}, \quad \hat{l} = \frac{\vec{p}}{|\vec{p}|}.
$$

In this coordinate system, the momenta of the particles can be written as a longitudinal part $\vec{p}_{l1,2}$ and a transverse part $\vec{p}_\perp$. As constructed, the momenta of the incident particles

147
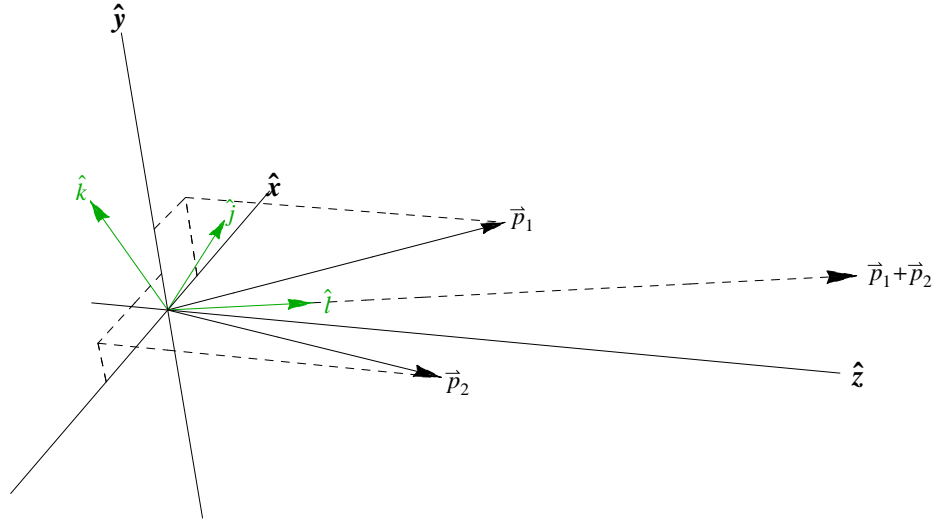
Figure 3.1: $\hat{j}, \hat{k}, \hat{l}$ coordinate system.

are in the $\hat{j}, \hat{k}, \hat{l}$ system:

$$
\vec{p}_{1,2}^{\,\mu} = \begin{pmatrix} E_{1,2}/c \\[6pt] \pm p_\perp \\[6pt] 0 \\[6pt] p_{l1,2} \end{pmatrix}_{(\hat{j},\hat{k},\hat{l})} , \tag{3.12}
$$

$$
p_\perp = \vec{p}_1 \cdot \hat{j} = \frac{|\vec{p}_2 \times \vec{p}_1|}{2\,|\vec{p}|}, \tag{3.13}
$$

$$
p_{l1,2} = \frac{\vec{p}_{1,2} \cdot \vec{p}}{|\vec{p}|}. \tag{3.14}
$$

The following quantities are introduced, which will be used throughout this chapter:

$$E_0 \;\equiv\; \frac{E_1 + E_2}{2}, \delta_E \equiv \frac{E_1 - E_2}{E_0}, \tag{3.15}$$

$$\gamma_0 \;\equiv\; \frac{E_0}{m_0 c^2}, \beta_0 \equiv \sqrt{1 - \frac{1}{\gamma_0^2}}, \tag{3.16}$$

$$p_0 \;\equiv\; c^{-1} E_0 \beta_0, \tag{3.17}$$

$$p_{1,2} \;\equiv\; c^{-1} E_0 \sqrt{\left(1 \pm \frac{\delta_E}{2}\right)^2 - \frac{1}{\gamma_0^2}}. \tag{3.18}$$

Note that $p_{1,2} = |\vec{p}_{1,2}|$ and,

$$p_0 \;=\; \frac{p_1 + p_2}{2}\left(1 + \mathcal{O}^2\right), \tag{3.19}$$

$$p_1 p_2 \;=\; p_0^2 \left(1 + \mathcal{O}^2\right), \tag{3.20}$$

$$E_1 E_2 \;=\; E_0^2 \left(1 + \mathcal{O}^2\right). \tag{3.21}$$

From Eqn. (3.14) the velocity of the particles in the $(\hat{j}, \hat{k}, \hat{l})$-frame is,

$$\begin{pmatrix} v_{j1,2} \\ v_{k1,2} \\ v_{l1,2} \end{pmatrix}_{(\hat{j},\hat{k},\hat{l})} = \frac{1}{\gamma_{1,2} m_0} \begin{pmatrix} \pm p_\perp \\ 0 \\ p_{l1,2} \end{pmatrix}_{(\hat{j},\hat{k},\hat{l})},$$

where $\gamma_{1,2} \equiv E_{1,2}/m_0 c^2$. The relative velocity of the two particles is $\Delta v = \vec{v}_1 - \vec{v}_2$. Defining χ as the angle between $\vec{p}_1$ and $\vec{p}_2$, the $\hat{j}$-component of the velocity simplifies as,

$$\begin{aligned} \Delta v_j \;&=\; \frac{p_\perp}{\gamma_1 m_0} - \frac{-p_\perp}{\gamma_2 m_0} \\ &=\; \frac{|\vec{p}_2 \times \vec{p}_1|}{2 |\vec{p}| m_0}\left(\frac{1}{\gamma_1} + \frac{1}{\gamma_2}\right) \\ &=\; \frac{1}{m_0} \frac{p_1 p_2 \sin\chi}{|\vec{p}_1 + \vec{p}_2|}\left(\frac{m_0 c^2}{E_1} + \frac{m_0 c^2}{E_2}\right) \\ &=\; c^2 \frac{p_1 p_2}{p_1 + p_2}\chi\left(1 + \mathcal{O}^2\right)\left(\frac{E_1 + E_2}{E_1 E_2}\right), \\ &=\; c^2 \frac{p_0}{E_0}\chi\left(1 + \mathcal{O}^2\right) \\ &=\; c\beta_0 \chi\left(1 + \mathcal{O}^2\right). \tag{3.22} \end{aligned}$$

149

The $\hat{l}$-component of the velocity simplifies as,

$$
\begin{aligned}
\Delta v_l &= \frac{1}{m_0} \left(\frac{p_{l1}}{\gamma_1} - \frac{p_{l2}}{\gamma_2} \right) \\
&= \frac{1}{|\vec{p}|m_0} \left(\frac{1}{2} (\vec{p}_1 + \vec{p}_2) \cdot \left(\frac{\vec{p}_1}{\gamma_1} - \frac{\vec{p}_2}{\gamma_2} \right) \right) \\
&= \frac{1}{2|\vec{p}|m_0} \left(\frac{p_1^2 + p_1 p_2 \cos\chi}{\gamma_1} - \frac{p_2^2 + p_1 p_2 \cos\chi}{\gamma_2} \right) \\
&= \frac{c^2}{2\,|\vec{p}|} \left(\frac{\frac{E_0^2}{c^2}\left(\left(1 + \frac{\delta_E}{2}\right)^2 - \frac{1}{\gamma_0^2} \right) + p_0^2 \left(1 + \mathcal{O}^2\right)}{E_1} \right. \\
&\qquad\qquad \left. - \frac{\frac{E_0^2}{c^2}\left(\left(1 - \frac{\delta_E}{2}\right)^2 - \frac{1}{\gamma_0^2} \right) + p_0^2 \left(1 + \mathcal{O}^2\right)}{E_2} \right) \\
&= \frac{E_0}{2\,|\vec{p}|} \left(\frac{\delta_E}{\gamma_0^2} + \mathcal{O}^2 \right) = \frac{E_0}{2\,|\vec{p}|} \mathcal{O}^2.
\end{aligned}
\tag{3.23}
$$

Therefore, for high-energy accelerators with small divergence and energy spread,

$$
\Delta v\,(\chi) = \beta_0 c \chi \left(1 + \mathcal{O}^2\right).
\tag{3.24}
$$

3.2.3 Change in energy due to a scattering event

Continuing from Eqn. (3.14), we derive the formula for the energy change in terms of scattering angles. Boosting along the $\hat{l}$-axis gives,

$$
\bar{p}_{1,2}^\mu = \begin{pmatrix} \gamma_c \left(E_{1,2}/c - \beta_c p_{l1,2}\right) \\[1em] \pm p_\perp \\[1em] 0 \\[1em] \gamma_c \left(-\beta_c E_{1,2}/c + p_{l1,2}\right) \end{pmatrix}_{(\hat{j},\hat{k},\hat{l})}.
\tag{3.25}
$$

The relativistic factors γ_c and β_c are chosen to boost into the c.o.m. frame, i.e. such that $\bar{p}_{l1} = -\bar{p}_{l2} \equiv p_\|$, resulting in,

$$\beta_c = \frac{c|\vec{p}|}{E_0}, \tag{3.26}$$

with $\gamma_c = 1/\sqrt{1 - \beta_c^2}$. The momenta in the boosted frame can be written as,

$$\bar{p}_{1,2}^\mu = \begin{pmatrix} \gamma_c \left(E_{1,2}/c - \beta_c p_{l1,2} \right) \\ \pm p_\perp \\ 0 \\ \pm p_\| \end{pmatrix}_{(\bar{j},\bar{k},\bar{l})}.$$

Next we rotate by an angle $\arctan\left(\frac{p_\perp}{p_\|}\right)$ so that the momenta are entirely along one axis. The rotated frame is denoted by $(\tilde{j}, \tilde{k}, \tilde{l})$,

$$\tilde{p}_{1,2}^\mu = \begin{pmatrix} \gamma_c \left(E_{1,2}/c - \beta_c p_{l1,2} \right) \\ 0 \\ 0 \\ \pm \bar{p} \end{pmatrix}_{(\tilde{j},\tilde{k},\tilde{l})}$$

where,

$$\bar{p}^2 = p_\perp^2 + p_\|^2.$$

After the particles collide, the magnitude of the momenta do not change in the $(\tilde{j}, \tilde{k}, \tilde{l})$-frame, but their direction does change. Using ψ for the zenith from $\tilde{l}$ and ϕ for the azimuth about $\tilde{l}$ measured from $\tilde{k}$, the momenta following the collision are,

$$\tilde{p}_{1,2}^{\prime\mu} = \begin{pmatrix} \gamma_c \left(E_{1,2}/c - \beta_c p_{l1,2} \right) \\ \pm \bar{p} \sin\psi \sin\phi \\ \pm \bar{p} \sin\psi \cos\phi \\ \pm \bar{p} \cos\psi \end{pmatrix}_{(\tilde{j},\tilde{k},\tilde{l})} \tag{3.27}$$

Next we rotate back from $(\tilde{\tilde{j}}, \tilde{\tilde{k}}, \tilde{\tilde{l}})$ to $(\bar{j}, \bar{k}, \bar{l})$, then boost back from $(\bar{j}, \bar{k}, \bar{l})$ to $(\hat{j}, \hat{k}, \hat{l})$. The result is,

$$
\vec{p}_{1,2}^{\prime\mu} =
\begin{pmatrix}
\gamma_c^2 \left(\frac{E_{1,2}}{c} - \frac{p_{l1,2}}{\beta_c^{-1}} \right) \mp \beta_c \gamma_c \left(p_\perp \sin\psi \sin\phi - p_\parallel \cos\psi \right) \\
\pm p_\parallel \sin\psi \sin\phi \pm p_\perp \cos\psi \\
\pm \bar{p} \sin\psi \cos\phi \\
\beta_c \gamma_c^2 \left(\frac{E_{1,2}}{c} - \frac{p_{l1,2}}{\beta_c^{-1}} \right) \mp \gamma_c \left(p_\perp \sin\psi \sin\phi - p_\parallel \cos\psi \right)
\end{pmatrix}_{(\hat{j},\hat{k},\hat{l})}.
$$
(3.28)

From Eqn. (3.28) the energy of each particle following the collision is,

$$
E_{1,2}' = \gamma_c^2 \left(E_{1,2} - \beta_c c p_{l1,2} \right) \mp \beta_c \gamma_c c \left(p_\perp \sin\psi \sin\phi - p_\parallel \cos\psi \right).
$$
(3.29)

We are interested in the change in energy. However, in order to derive a concise form for the change in energy, we must first derive another relation. From Eqn. (3.25),

$$
\begin{aligned}
p_\parallel &= \gamma_c \left(p_{l1} - \beta_c E_1/c \right) \\
+ \quad p_\parallel &= -\gamma_c \left(p_{l2} - \beta_c E_2/c \right) \\
\hline
2p_\parallel &= -\gamma_c \left(p_{l2} - p_{l1} - \beta_c \frac{E_2 - E_1}{c} \right)
\end{aligned}
$$

Then applying Eqn. (3.14) we obtain,

$$
\begin{aligned}
p_\parallel &= \frac{\gamma_c}{2} \left(-\frac{\beta_c}{c} (E_1 - E_2) - \frac{\vec{p}_2 \cdot \vec{p}}{|\vec{p}|} + \frac{\vec{p}_1 \cdot \vec{p}}{|\vec{p}|} \right) \\
&= \frac{\gamma_c}{2} \left(-\frac{\beta_c}{c} (E_1 - E_2) - \frac{(\vec{p}_1 + \vec{p}_2)}{2|\vec{p}|} \cdot (\vec{p}_2 - \vec{p}_1) \right).
\end{aligned}
$$

Now applying $E_{1,2}^2 = p_{1,2}^2 c^2 + m_0^2 c^4$ and then using Eqn. (3.26),

$$
\begin{aligned}
p_\| &= \frac{\gamma_c}{2c}(E_1 - E_2)\left(-\beta_c + \frac{E_2 + E_1}{2|\vec{p}|c}\right) \\
&= \frac{\gamma_c}{2c}(E_1 - E_2)\left(-\beta_c + \frac{1}{\beta_c}\right) \\
&= \frac{\Delta E}{2c\gamma_c\beta_c},
\end{aligned}
\tag{3.30}
$$

where $\Delta E \equiv E_1 - E_2$.

The change in energy is defined as $\Delta E'_{1,2} = E'_{1,2} - E_{1,2}$,

$$
\begin{aligned}
\Delta E'_{1,2} &= \left(\gamma_c^2 - 1\right)E_{1,2} - \gamma_c^2\beta_c c p_{l1,2} \\
&\quad \mp \beta_c\gamma_c c\left(p_\perp \sin\psi \sin\phi - p_\| \cos\psi\right) \\
&= -\beta_c\gamma_c^2 c\left(-\frac{\beta_c E_{1,2}}{c} + p_{l1,2}\right) \\
&\quad \mp \beta_c\gamma_c c\left(p_\perp \sin\psi \sin\phi - p_\| \cos\psi\right) \\
&= \mp \beta_c\gamma_c c\left(p_\perp \sin\psi \sin\phi + p_\| - p_\| \cos\psi\right),
\end{aligned}
$$

using Eqn. (3.25) for the last line.

Finally, making use of Eqn. (3.30), we obtain,

$$
\Delta E'_{1,2} = \mp\gamma_c\beta_c c p_\perp\left(\frac{\Delta E}{\gamma_c\beta_c c p_\perp}\sin^2\left(\frac{\psi}{2}\right) + \sin\psi \sin\phi\right).
\tag{3.31}
$$

If $cp_\perp$ is of the same order or larger than ΔE, then the ΔE term in the parentheses goes as $1/\gamma_c$ and can be neglected at high energy,

$$
\Delta E'_{1,2} = \mp\gamma_c\beta_c c p_\perp \sin\psi \sin\phi\left(1 + O\left(\frac{1}{\gamma_c}\right)\right).
\tag{3.32}
$$

Equation (3.32) is the change in energy in the lab frame due to a collision between two co-propagating relativistic particles. ψ and ϕ are the scattering angles in the $(\tilde{j}, \tilde{k}, \tilde{l})$-frame.

153

3.2.4 Derive scattering cross-section σ

The minimum energy change that results in particle loss is referred to as ΔE_{max}. Using this threshold, Eqn. (3.32) is rewritten to give a condition for particle loss in terms of scattering angles in the $(\tilde{j}, \tilde{k}, \tilde{l})$-frame,

$$\sin \psi \sin \phi > \frac{\Delta E_{max}}{\gamma_c \beta_c c p_\perp} \equiv B. \tag{3.33}$$

To first order, B depends only on the initial angle between the two particles. This is seen from,

$$
\begin{aligned}
B &= \frac{\Delta E_{max}}{\gamma_c \beta_c c} \frac{2|\vec{p}|}{|\vec{p}_1 \times \vec{p}_2|} \\
&= \frac{\Delta E_{max}}{\gamma_c \beta_c c} \frac{p_1 + p_2}{p_1 p_2 \chi} \left(1 + \mathcal{O}^2\right) \\
&= \frac{\Delta E_{max}}{\gamma_c \beta_c c} \frac{2}{p_0 \chi} \left(1 + \mathcal{O}^2\right).
\end{aligned}
\tag{3.34}
$$

The relativistic factors of the boosted frame, β_c and γ_c can be approximated as,

$$
\begin{aligned}
\beta_c^2 &= \frac{c^2 |\vec{p}|^2}{E_0^2} = \frac{c^2 \left|\frac{1}{2}(\vec{p}_1 + \vec{p}_2)\right|^2}{E_0^2} \\
&= \frac{c^2 \left(p_1^2 + p_2^2 + 2p_1 p_2 \cos \chi\right)}{4E_0^2} = \beta_0^2 \left(1 - \frac{\chi^2}{4} + \mathcal{O}^3\right),
\end{aligned}
$$

from which follows,

$$
\begin{aligned}
\gamma_c^2 &= \frac{1}{1 - \beta_c^2} = \frac{\gamma_0^2}{1 + \frac{\chi^2 \beta_0^2 \gamma_0^2}{4} + \mathcal{O}^2} \\
&= \gamma_0^2 \left(1 - \frac{1}{4}\gamma_0^2 \chi^2 + \mathcal{O}^2\right).
\end{aligned}
\tag{3.35}
$$

Using these expressions for β_c and γ_c in Eqn. (3.34) yields,

$$
\begin{aligned}
B &= \frac{2\Delta E_{max}}{p_0 c \gamma_0 \beta_0 \chi} \times \frac{(1+\mathcal{O}^2)}{\sqrt{\left(1 - \frac{\chi^2}{4} + \mathcal{O}^3\right)\left(1 - \frac{1}{4}\beta_0^2 \gamma_0^2 \chi^2 + \mathcal{O}^2\right)}} \\
&= \frac{2\delta_{E,max}}{\gamma_0 \beta_0^2 \chi}\left(1 + \frac{1}{8}\chi^2 \gamma_0^2 + \mathcal{O}^2\right)(1 + \mathcal{O}^2) \\
&= \frac{2\delta_{E,max}}{\gamma_0 \chi}\sqrt{1 + \frac{\gamma_0^2 \chi^2}{4}}\,(1 + \mathcal{O}^1),
\end{aligned}
\tag{3.36}
$$

where $\delta_{E,\mathrm{max}} \equiv \Delta E/E_0$. A binomial expansion of the square root in the last line could be made and the result would still be accurate to the same order. However, such an approximation is not necessary to reach our final goal, and the square root is actually simpler notation than its binomial expansion.

For elastic identical-particle Coulomb scattering, the Moller scattering cross-section is used,

$$
d\bar{\sigma} = \frac{r_e^2}{4\tilde{\gamma}^2}\left(\left(1 + \frac{1}{\tilde{\beta}^2}\right)^2\left(\frac{4}{\sin^4 \psi} - \frac{3}{\sin^2 \psi}\right) + \frac{4}{\sin^2 \psi} + 1\right)\sin\psi\,d\psi\,d\phi,
\tag{3.37}
$$

where $\tilde{\gamma}$ and $\tilde{\beta}$ are the relativistic factors in the frame of the two particles.

This equation is integrated over angles that meet the condition in Eqn. (3.33),

$$
\bar{\sigma} = \frac{r_e^2}{\gamma_c \tilde{\gamma}^2}\int_{\phi min}^{\frac{\pi}{2}}\int_{\psi th(\phi)}^{\frac{\pi}{2}}\left(\left(1 + \frac{1}{\tilde{\beta}^2}\right)^2\left(\frac{4}{\sin^4 \psi} - \frac{3}{\sin^2 \psi}\right) + \frac{4}{\sin^2 \psi} + 1\right)\sin\psi\,d\psi\,d\phi,
$$

where $\psi_{th}(\phi) \equiv \arcsin\frac{B}{\sin\phi}$, $\phi_{min} \equiv \arcsin B$. The factor if $1/\gamma_c$ comes from transforming the cross-section back to the lab frame.

The integration is performed in Appendix 1. The result is,

$$
\bar{\sigma} = \frac{\pi r_e^2}{2\gamma_c \tilde{\gamma}^2}\left(\left(3 - \frac{2}{\tilde{\beta}^2} - \frac{1}{\tilde{\beta}^4}\right)\ln\left(\frac{1}{B}\right) - B + 1 + \left(1 + \frac{1}{\tilde{\beta}^2}\right)^2\left(\frac{1}{B^2} - 1\right)\right),
\tag{3.38}
$$

We see that the cross-section depends only on χ, and so make a change of variables

in Eqn. 3.10 from x_1' and x_2' to their average angle ξ and relative angle χ,

$$\xi_x = \frac{x_1' + x_2'}{2}$$

$$\xi_y = \frac{y_1' + y_2'}{2}$$

$$\chi_x = x_1' - x_2'$$

$$\chi_y = y_1' - y_2',$$

and the divergence can written as,

$$x_{\beta 1}' = \frac{\chi_x}{2} + \xi_x - D_x' \frac{\Delta p}{p}$$

$$x_{\beta 2}' = -\frac{\chi_x}{2} + \xi_x - D_x' \frac{\Delta p}{p}$$

$$y_{\beta 1}' = \frac{\chi_y}{2} + \xi_y - D_y' \frac{\Delta p}{p}$$

$$y_{\beta 2}' = -\frac{\chi_y}{2} + \xi_y - D_y' \frac{\Delta p}{p}.$$

Note that $\chi = \sqrt{\chi_x^2 + \chi_y^2}$ in the paraxial approximation. Since the relative velocity Δv and cross-section σ depend only on the angle χ between the particles' momenta, the integral for the rate, Eqn. (3.10), can be written as,

$$\frac{N_p^2}{128\pi^5 \epsilon_x^2 \epsilon_y^2 \sigma_s \sigma_p^2} \sqrt{\frac{\pi}{a_x a_y}} \iint_{\chi_x \chi_y} \Delta v\,(\chi)\,\sigma\,(\chi) \times$$

$$\iiiint_{\delta_{p2}\delta_{p1}\xi_y\,\xi_x} \exp\left(-\frac{\delta_{p1}^2 + \delta_{p2}^2}{2\sigma_p^2} + \frac{b_x^2}{4a_x} - c_x + \frac{b_y^2}{4a_y} - c_y\right) d\xi_x d\xi_y d\delta_{p1} d\delta_{p2} d\chi_y d\chi_x. \quad (3.39)$$

δ_{p2}, δ_{p1}, ξ_y, and ξ_x can be integrated at this point. The integration is done in Appendix D. The result yields,

$$\frac{N_p^2 \sigma_h}{64\pi^2 \sqrt{\pi} \epsilon_x \epsilon_y \sigma_s \sigma_p} \iint_{\chi_x \chi_y} \Delta v\,(\chi)\,\sigma\,(\chi)\exp\left(-\left(k_x \chi_x^2 + k_y \chi_y^2 - l \chi_x \chi_y\right)\right) d\chi_y d\chi_x, \quad (3.40)$$

where,

$$
\begin{aligned}
\tilde{D}_{x,y} &= D_{x,y}\alpha_{x,y} + D'_{x,y}\beta_{x,y} \\
\frac{1}{\sigma_h^2} &= \frac{1}{\sigma_p^2} + \frac{\mathcal{H}_x}{\epsilon_x} + \frac{\mathcal{H}_y}{\epsilon_y} \\
k_{x,y} &= \frac{\beta_{x,y}}{4\epsilon_{x,y}} - \frac{\sigma_h^2 \tilde{D}_{x,y}^2}{4\epsilon_{x,y}^2} \\
l &= \frac{\sigma_h^2 \tilde{D}_x \tilde{D}_y}{2\epsilon_x \epsilon_y},
\end{aligned}
\tag{3.41}
$$

where $\mathcal{H}_{x,y} = \eta_{x,y}^2 \gamma_{x,y} + 2\alpha_{x,y}\eta_{x,y}\eta'_{x,y} + \beta_{x,y}\eta'^2_{x,y}$.

3.2.5 Integration over ϕ

To integrate over the relative angle of the two particles, the following change of variables is introduced, which is true in the paraxial approximation,

$$
\chi_x = \chi \cos \phi ,
\tag{3.42}
$$

$$
\chi_y = \chi \sin \phi ,
\tag{3.43}
$$

which simplifies Eqn. (3.40) to,

$$
\frac{N_p^2 \sigma_h}{64\pi^2 \sqrt{\pi} \epsilon_x \epsilon_y \sigma_p \sigma_s} \int_{\chi_{min}^2}^{\chi_{max}^2} \Delta v (\chi) \, \sigma (\chi) \exp \left(\frac{\chi^2}{2} (k_x + k_y) \right) \times
$$
$$
\int_0^{2\pi} \exp \left(\frac{\chi^2}{2} \sqrt{l^2 + (k_x - k_y)^2} \cos (2\phi + \psi) \right) d\phi d\chi , \tag{3.44}
$$

where,

$$
\psi = \arcsin \left(\frac{k_x - k_y}{\sqrt{l^2 + (k_x - k_y)^2}} - \frac{\pi}{2} \right).
$$

The following identity for the modified Bessel function,

$$
I_0 \left(\frac{\chi^2}{2} C_0 \right) = \frac{1}{2\pi} \int_0^{2\pi} \exp \left(\frac{\chi^2}{2} C_0 \cos (2\phi + \psi) \right) d\phi,
$$

simplifies Eqn. (3.44) to,

$$\frac{N_p^2 \sigma_h}{32\pi^{3/2} \epsilon_x \epsilon_y \sigma_p \sigma_s} \int_{\chi_{min}^2}^{\chi_{max}^2} \Delta v\left(\chi\right) \sigma\left(\chi\right) \times$$

$$\exp\left(\frac{\chi^2}{2}\left(k_x + k_y\right)\right) I_0\left(\frac{\chi^2}{2}\sqrt{l^2 + \left(k_x - k_y\right)^2}\right) d\chi. \quad (3.45)$$

χ_{min} can be obtained from Eqn. (3.33), which restricts B to be less than one,

$$B_{max} = 1 = \frac{2\delta_{E,\max}}{\gamma_0 \chi_{min}},$$

$$\chi_{min}^2 = \frac{4\delta_{E,\max}^2}{\gamma_0^2}. \quad (3.46)$$

The relativistic factors in the cross-section, Eqn. (3.38), $\tilde{\gamma}$ and $\tilde{\beta}$, are of the particles in the c.o.m. frame. They can be written in terms of γ_0 and γ_c. From Eqn. (3.27) the relativistic γ of the particles in the boosted frame is,

$$\tilde{\gamma} = \tilde{\gamma}_2 = \tilde{\gamma}_1 = \frac{\gamma_c\left(E_1 - \beta_c c p_{l1}\right)}{m_0 c^2},$$

and $\tilde{\beta} = \beta\left(\tilde{\gamma}\right)$.

An exact relation relation between γ_0, γ_c, and $\tilde{\gamma}$, is derived as,

$$\begin{aligned} \tilde{\gamma} &= \frac{\tilde{\gamma}_1 + \tilde{\gamma}_2}{2} = \frac{\gamma_c}{2m_0 c^2}\left(E_1 + E_2 - \beta_c c\left(p_{l1} + p_{l2}\right)\right) \\ &= \frac{\gamma_c}{2m_0 c^2}\left(2E_0 - \beta_c c\left(\frac{\vec{p}}{|\vec{p}|} \cdot \left(\vec{p}_1 + \vec{p}_2\right)\right)\right) \\ &= \frac{\gamma_c}{2m_0 c^2}\left(2E_0 - 2\beta_c c |\vec{p}|\right) \\ &= \frac{E_0}{m_0 c^2}\sqrt{\frac{1}{1 - \beta_c^2}}\left(1 - \frac{\beta_c c |\vec{p}|}{E_0}\right) \\ &= \frac{E_0}{m_0 c^2}\sqrt{1 - \beta_c^2} = \frac{\gamma_0}{\gamma_c}. \end{aligned} \quad (3.47)$$

With Eqn. (3.47), the cross-section can be approximated and written in terms of χ. Beginning with the first term we write,

$$3 - \frac{2}{\tilde{\beta}^2} - \frac{1}{\tilde{\beta}^4} = 4 - \left(1 + \frac{1}{\tilde{\beta}^2}\right)^2, \quad (3.48)$$

158

and proceed by approximating the term in the parentheses.

$$
\begin{aligned}
1 + \frac{1}{\tilde{\beta}^2} &= \frac{2 - \frac{\gamma_c^2}{\gamma_0^2}}{1 - \frac{\gamma_c^2}{\gamma_0^2}} = \frac{2\gamma_0^2 - \frac{1}{1-\beta_c^2}}{\gamma_0^2 - \frac{1}{1-\beta_c^2}} \\
&= \frac{2\gamma_0^2 \left(1 - \beta_0^2 + \beta_0^2 \chi^2/4 + O^3\right) - 1}{\gamma_0^2 \left(1 - \beta_0^2 + \beta_0^2 \chi^2/4 + O^3\right) - 1} \\
&= 2 + \frac{4}{\gamma_0^2 \chi^2} + O^1.
\end{aligned}
$$

(3.49)

Using Eqn. (3.49) in Eqn. (3.48),

$$
\begin{aligned}
3 - \frac{2}{\tilde{\beta}^2} - \frac{1}{\tilde{\beta}^4} &= 4 - \left(2 + \frac{4}{\gamma_0^2 \chi^2} + O^1\right)^2 \\
&= -\frac{16}{\gamma_0^4 \chi^4} - \frac{16}{\gamma_0^2 \chi^2} + O^1.
\end{aligned}
$$

(3.50)

3.2.5.1 Touschek Rate

We now introduce the following parameter,

$$
\tau \equiv \frac{\gamma_0^2 \chi^2}{4},
$$

(3.51)

and then combine Eqs. (3.45), (3.24), (3.38), and (3.49) to obtain,

$$
\begin{aligned}
R &= \frac{N_p^2 \sigma_h}{32\pi \sqrt{\pi} \epsilon_x \epsilon_y \sigma_p \sigma_s} \int_{\chi^2_{min}}^{\chi^2_{max}} c\beta_0 \chi \frac{\pi r_e^2}{2\tilde{\gamma}^2 \gamma_c} \\
&\quad \left(\left(3 - \frac{2}{\tilde{\beta}^2} - \frac{1}{\tilde{\beta}^4}\right) \ln\left(\frac{1}{B}\right) - B + 1 + \left(1 + \frac{1}{\tilde{\beta}^2}\right)^2 \left(\frac{1}{B^2} - 1\right)\right) \times \\
&\quad \exp\left(-\frac{k_x + k_y}{2}\chi^2\right) I_0 \left(\frac{\sqrt{l^2 + (k_x - k_y)^2}}{2}\chi^2\right) \times \left(1 + O^2\right) d\chi
\end{aligned}
$$

(3.52)

Simplifying with Eqs. (3.47), (3.49), (3.50), (3.35), (3.36), and (3.51) gives,

$$R = \frac{N_p^2 \sigma_h r_e^2 c \beta_0}{16 \sqrt{\pi} \epsilon_x \epsilon_y \sigma_p \sigma_s \gamma_0^4} \int_{\delta_{E,\max}^2}^{\infty} \frac{\sqrt{\tau}}{\sqrt{1+\tau}}$$

$$\left(\left(\left(\frac{1}{\tau^2} + \frac{4}{\tau} \right) \ln \left(\frac{\delta_{E,\max} \sqrt{1+\tau}}{\sqrt{\tau}} \right) - \frac{\delta_{E,\max} \sqrt{1+\tau}}{\sqrt{\tau}} + 1 \right. \right.$$

$$\left. + \left(\frac{1}{\tau} + 2 \right)^2 \left(\frac{\tau}{\delta_{E,\max}^2 (1+\tau)} - 1 \right) \right) \times$$

$$\exp \left(-2 \frac{k_x + k_y}{\gamma_0^2} \tau \right) I_0 \left(2 \frac{\sqrt{l^2 + (k_x - k_y)^2}}{\gamma_0^2} \tau \right) \times \left(1 + O^1 \right) d\tau.$$

$$(3.53)$$

Note that the arguments of the exponential and the Bessel function are $O^{-1} \times \tau$.

3.2.6 Integration Bounds

The integrand is accurate to O^1 in τ, but the integration is over τ from $\delta_{E,\max}^2$, which is O^1, to ∞. It is shown that the strong exponential decay of the integrand allows us to restrict the integration range to the vicinity of O^1.

The behavior of the integrand for large χ is found by examining the behavior of an exponential times I_0. We begin by rewriting the argument of the Bessel function,

$$I_0 \left(\frac{2}{\gamma_0^2} \sqrt{l^2 + (k_x - k_y)^2} \tau \right) = I_0 \left(\frac{2}{\gamma_0^2} (k_x + k_y) \sqrt{1 - \frac{4 k_x k_y - l^2}{(k_x + k_y)^2}} \tau \right). \qquad (3.54)$$

The argument of the Bessel function is always smaller than the argument of the expo-
nential, $(k_x + k_y)$. This is seen by looking at the sign of the numerator under the square
root,

$$4 k_x k_y - l^2 = -\frac{\sigma_h^2 \tilde{D}_y^2 \beta_x}{4 \epsilon_x \epsilon_y^2} - \frac{\sigma_h^2 \tilde{D}_x^2 \beta_y}{4 \epsilon_y \epsilon_x^2} + \frac{\beta_x \beta_y}{4 \epsilon_x \epsilon_y}$$

$$\frac{4 \epsilon_x \epsilon_y}{\beta_x \beta_y} \left(4 k_x k_y - l^2 \right) = -\frac{\sigma_h^2 \tilde{D}_y^2}{\sigma_y^2} - \frac{\sigma_h^2 \tilde{D}_x^2}{\sigma_x^2} + 1.$$

160

Now look at the Eqn. (3.41),

$$\frac{1}{\sigma_h^2} = \frac{1}{\sigma_p^2} + \frac{\mathcal{H}_x}{\epsilon_x} + \frac{\mathcal{H}_y}{\epsilon_y}$$

$$1 = \frac{\sigma_h^2}{\sigma_p^2} + \sigma_h^2 \frac{\mathcal{H}_x}{\epsilon_x} + \sigma_h^2 \frac{\mathcal{H}_y}{\epsilon_y}$$

$$1 = \frac{\sigma_h^2}{\sigma_p^2} + \sigma_h^2 \frac{\tilde{D}_x^2 + D_x^2}{\sigma_x^2} + \sigma_h^2 \frac{\tilde{D}_y^2 + D_y^2}{\sigma_y^2}$$

$$-\frac{\sigma_h^2 \tilde{D}_x^2}{\sigma_x^2} - \frac{\sigma_h^2 \tilde{D}_y^2}{\sigma_y^2} + 1 = \frac{\sigma_h^2}{\sigma_p^2} + \frac{\sigma_h^2 D_x^2}{\sigma_x^2} + \frac{\sigma_h^2 D_y^2}{\sigma_y^2} > 0. \tag{3.55}$$

Since Eqn. (3.55) is always positive, the radical in Eqn. (3.54) is always less than one. Furthermore, it is clear from the LHS of Eqn. (3.54) that the radical is always real. The Bessel function can then be written as,

$$I_0 \left(\frac{2}{\gamma_0^2} (k_x + k_y) (1 - \lambda) \tau \right),$$

where λ is $\mathcal{O}^0$ and between 0 and 1. For very small arguments, $e^x I_0(x) \approx 1$. For large arguments, $I_0(x)$ expands as,

$$I_0(x) = \frac{\exp(x)}{\sqrt{2\pi x}} \left(1 + \mathcal{O}\left(\frac{1}{x}\right) \right).$$

For large values of τ our exponential times the Bessel function becomes,

$$\exp\left(-\frac{2}{\gamma_0^2} (k_x + k_y) \tau \right) I_0 \left(\frac{2}{\gamma_0^2} (k_x + k_y) (1 - \lambda) \tau \right)$$

$$\approx \exp\left(-\frac{2}{\gamma_0^2} (k_x + k_y) \tau \right) \frac{\exp\left(\frac{2}{\gamma_0^2} (k_x + k_y) (1 - \lambda) \tau \right)}{\sqrt{\frac{4\pi}{\gamma_0^2} (k_x + k_y) (1 - \lambda) \tau}}$$

$$= \frac{\exp\left(-\lambda \frac{2}{\gamma_0^2} (k_x + k_y) \tau \right)}{\sqrt{\frac{4\pi}{\gamma_0^2} (k_x + k_y) (1 - \lambda) \tau}} = \frac{\exp\left(-\mathcal{O}^{-1} \tau \right)}{\sqrt{\mathcal{O}^{-1} \tau}}. \tag{3.56}$$

The denominator makes the integrand large for small τ, and the exponential decay suppresses the integrand with a decay constant that is $\mathcal{O}^1$. Evaluating Eqn. 3.56 at $\tau = \mathcal{O}^1$ yields ~ 1. At $\tau = 10 \times \mathcal{O}^1$ the integrand is suppressed to $\mathcal{O}^1$, and at $\tau = 100 \times \mathcal{O}^1$ the

integrand is suppressed to O^7. The accuracy of our equation for the Touschek scattering rate is maintained as long as the upper integration bound is at least $100 \times O^1$, but for convenience we use 1,

$$
\begin{aligned}
R = {} & \frac{N_p^2 \sigma_h r_e^2 c \beta_0}{16 \sqrt{\pi} \epsilon_x \epsilon_y \sigma_p \sigma_s \gamma_0^4} \int_{\delta_{E,\max}^2}^1 \frac{\sqrt{\tau}}{\sqrt{1+\tau}} \\
& \left(\left(\frac{1}{\tau^2} + \frac{4}{\tau} \right) \ln \left(\frac{\delta_{E,\max} \sqrt{1+\tau}}{\sqrt{\tau}} \right) - \frac{\delta_{E,\max} \sqrt{1+\tau}}{\sqrt{\tau}} + 1 \right. \\
& \left. + \left(\frac{1}{\tau} + 2 \right)^2 \left(\frac{\tau}{\delta_{E,\max}^2 (1+\tau)} - 1 \right) \right) \times \\
& \exp \left(-2 \frac{k_x + k_y}{\gamma_0^2} \tau \right) I_0 \left(2 \frac{\sqrt{l^2 + (k_x - k_y)^2}}{\gamma_0^2} \tau \right) \times \left(1 + O^1 \right) d\tau.
\end{aligned}
$$

$$(3.57)$$

where,

$$
\begin{aligned}
B &= \frac{\delta_{E,\max}}{\sqrt{\tau}}, \\
C_1 &= 2 \frac{k_x + k_y}{\gamma_0^2}, \\
C_2 &= 2 \frac{\sqrt{l^2 + (k_x - k_y)^2}}{\gamma_0^2}.
\end{aligned}
$$

Equation (3.57) gives the Touschek scattering rate accurate to $O\left(\chi, \delta_p, \frac{1}{\gamma_0^2}\right)^1$. δ_p and $1/\gamma_0^2$ are determined by beam properties. $\delta_{E,\max}$ is the dynamic energy aperture of the accelerator. We find for the Cornell ERL that the dynamic energy aperture can range as low as 0.01%. Therefore, the χ of interest is on the order of $\delta_{E,\max}^2$.

A form of Eqn. (3.57) more accommodating to numerical integration is obtained by making a change of variables to $\omega = \log \tau$.

3.2.7 Recreation of Classical Form

With a few slight modifications to our derivation, Piwinski's classical formula for the Touschek scattering rate can be obtained. It is found that the classical formula is consistent to within factors of the relativistic β_0 of the beam.

In [32], B is written as,

$$B_p \equiv \delta_{E,\max} \frac{\sqrt{4 + \beta_0^2 \gamma_0^2 \chi^2}}{\gamma_0 \beta_0^2 \chi}, \tag{3.58}$$

where the subscript p indicates the form found in Piwinski's paper. We find that if this equation is approximated to O^1 in $1/\gamma_0^2$ and χ, Eqn. (3.36) is obtained. Additionally,

$$\tau_p \equiv \frac{\beta_0^2 \gamma_0^2 \chi^2}{4},$$

$$\tau_{pmin} \equiv \frac{\beta_0^2 \gamma_0^2 \chi_{min}^2}{4},$$

which allows Eqn. (3.59) to be written as

$$B_p = \frac{\sqrt{1 + \tau_p}}{\sqrt{\tau_p}} \frac{\delta_{E,\max}}{\beta_0}.$$

Using these quantities yields,

$$
\begin{aligned}
R &= \frac{1}{2} \frac{N_p^2 \sigma_h r_e^2 c}{8 \sqrt{\pi} \epsilon_x \epsilon_y \sigma_p \sigma_s \beta_0^3 \gamma_0^4} \int_{\tau_{pmin}}^{1} \frac{\sqrt{\tau_p}}{\sqrt{1 + \tau_p}} \\
&\quad \left(\frac{1}{\tau_p} \left(4 + \frac{1}{\tau_p} \right) \ln(B_p) - B_p + 1 + \left(\frac{1}{\tau_p} + 2 \right)^2 \left(\frac{1}{B_p^2} - 1 \right) \right) \times \\
&\quad \exp\left(-2 \frac{k_x + k_y}{\beta_0^2 \gamma_0^2} \tau_p \right) I_0 \left(2 \frac{\sqrt{l^2 + (k_x - k_y)^2}}{\beta_0^2 \gamma_0^2} \tau_p \right) d\tau_p.
\end{aligned}
\tag{3.59}
$$

The factor of one-half is because the classical formula assumes a symmetric energy aperture, so that two particles are lost for every scattering event. Our formula assumes

an non-symmetric energy aperture, where the threshold for particle loss due to energy gain may be different from the threshold for particle loss due to energy loss.

We produce Eqn. (3.59) only to demonstrate that our derivation agrees with Piwinski's classic derivation. The arguments of the exponential and Bessel function, as well as the factor, are algebraically equivalent to the classic derivation.

3.2.8 Trajectory of scattered particles

The amplitude of the trajectory of a particle that receives an energy kick is sensitive to the value of the dispersion invariant $\mathcal{H}$ at the location of the kick.

The linearized phase-space coordinate of a particle is given by,

$$
\begin{pmatrix} x_0 \\ x_0' \end{pmatrix} = \sqrt{2J_0} \begin{pmatrix} \sqrt{\beta_0} & 0 \\ -\frac{\alpha_0}{\sqrt{\beta_0}} & \frac{1}{\sqrt{\beta_0}} \end{pmatrix} \times
$$
$$
\begin{pmatrix} \cos\psi_0 & \sin\psi_0 \\ -\sin\psi_0 & \cos\psi_0 \end{pmatrix} \begin{pmatrix} \sin\phi_0 \\ \cos\phi_0 \end{pmatrix} + \begin{pmatrix} \eta_0 \\ \eta_0' \end{pmatrix} \delta_{p0} .
$$

$$(3.60)$$

A scattering event that imparts a momentum change to the particle changes its Courant-Snyder invariant J and betatron phase ϕ,

$$
\begin{pmatrix} x_0 \\ x_0' \end{pmatrix} = \sqrt{2J} \begin{pmatrix} \sqrt{\beta_0} & 0 \\ -\frac{\alpha_0}{\sqrt{\beta_0}} & \frac{1}{\sqrt{\beta_0}} \end{pmatrix} \times
$$
$$
\begin{pmatrix} \cos\psi_0 & \sin\psi_0 \\ -\sin\psi_0 & \cos\psi_0 \end{pmatrix} \begin{pmatrix} \sin\phi \\ \cos\phi \end{pmatrix} + \begin{pmatrix} \eta_0 \\ \eta_0' \end{pmatrix} \delta_p .
$$

$$(3.61)$$

Since the scattering event does not instantaneously change the position x_0 and divergence x_0', Eqn. (3.60) and 3.61 can be equated to yield, after a bit of algebra,

$$\sqrt{J}\begin{pmatrix} \sin\phi \\ \\ \cos\phi \end{pmatrix} =$$

$$\sqrt{J_0}\begin{pmatrix} \sin\phi_0 \\ \\ \cos\phi_0 \end{pmatrix} - \begin{pmatrix} \cos\psi_0 & \sin\psi_0 \\ -\sin\psi_0 & \cos\psi_0 \end{pmatrix}^{-1} \begin{pmatrix} \sqrt{\beta_0} & 0 \\ -\frac{\alpha_0}{\sqrt{\beta_0}} & \frac{1}{\sqrt{\beta_0}} \end{pmatrix}^{-1} \begin{pmatrix} \eta_0 \\ \eta_0' \end{pmatrix} \frac{\Delta\delta_p}{\sqrt{2}}$$

$$\equiv \vec{V},$$

where $\Delta\delta_p \equiv \delta_0 - \delta_{p0}$, and the RHS of the equation is defined as $\vec{V}$. Squaring $\vec{V}$ yields,

$$(\sqrt{J})^2\begin{pmatrix} \sin\phi \\ \\ \cos\phi \end{pmatrix}^2 = (\vec{V})^2$$

$$J\left(\sin^2\phi + \cos^2\phi\right) = V^2$$

$$J = V_x^2 + V_y^2. \tag{3.62}$$

And ϕ is obtained by,

$$\frac{\sin\phi}{\cos\phi} = \frac{V_x}{V_y}$$

$$\phi = \arctan\frac{V_x}{V_y} \tag{3.63}$$

Writing out Eqn. (3.62) and simplifying yields,

$$\begin{aligned} J &= \left[\sqrt{J_0}\sin\phi_0 - \frac{\Delta\delta_p}{\sqrt{2}}\left(\frac{\eta_0}{\sqrt{\beta_0}}(\cos\phi_0 - \alpha_0\sin\phi_0) - \eta_0'\sqrt{\beta_0}\sin\phi_0\right)\right]^2 \\ &+ \left[\sqrt{J_0}\cos\phi_0 - \frac{\Delta\delta_p}{\sqrt{2}}\left(\frac{\eta_0}{\sqrt{\beta_0}}(\sin\phi_0 + \alpha_0\cos\phi_0) + \eta_0'\sqrt{\beta_0}\cos\phi_0\right)\right]^2 \\ &= \mathcal{H}_0\frac{\Delta\delta_p^2}{2} + \sqrt{2}\frac{(\alpha_0\eta_0 + \beta_0\eta_0')\cos(\phi_0 + \psi_0) + \eta_0\sin(\phi_0 + \psi_0)}{\sqrt{\beta_0}}\sqrt{J_0}\Delta\delta_p + (3.64) \end{aligned}$$

where $\mathcal{H}_0$ is the familiar dispersion invariant. In the Cornell ERL, J_0 is on the order of 10^{-10}. The IBS scattering rate typically becomes appreciable at $\Delta\delta_p = 0.005$. This

makes the first term in Eqn. (3.64) of order $\Delta\delta_p^2 = 2.5 \times 10^{-5}$, the second term of order

$\Delta\delta_p \sqrt{J_0} = 5 \times 10^{-8}$, and the third term of order $J_0 = 10^{-10}$. Keeping only the lowest

order term yields,

$$J_n \cong \gamma_0 \mathcal{H}_0 \frac{\Delta\delta_p^2}{2} , \qquad (3.65)$$

where J_n has been normalized by γ_0, the boost at the time of the scattering. Equation

(3.65) is the new J of a particle that has undergone a scattering event which imparted to

it a momentum change $\Delta\delta_p$.

To linear approximation, the horizontal coordinate of a particle as it travels through

the accelerator is given by,

$$x[s] = \sqrt{2J\beta[s]\frac{\gamma_0}{\gamma[s]}} \sin[\psi[s] + \phi] + \eta[s]\delta_p\frac{\gamma_0}{\gamma[s]} . \qquad (3.66)$$

Using Eqn. (3.65) in Eqn. (3.66) yields,

$$
\begin{aligned}
x[s] &= \sqrt{\frac{\gamma_0}{\gamma[s]}\mathcal{H}_0\Delta\delta_E^2\beta[s]} \sin[\psi[s] + \phi] + \eta[s]\delta_E\frac{\gamma_0}{\gamma[s]} = \\
&\quad \delta_{E0}\left[\sqrt{\frac{\gamma_0}{\gamma[s]}}\sqrt{\mathcal{H}_0\beta[s]} \sin[\psi[s] + \phi] + \frac{\gamma_0}{\gamma[s]}\eta[s]\right] . \qquad (3.67)
\end{aligned}
$$

Equation (3.67) for the transverse displacement of a scattered particle has two terms.

The first term is a betatron contribution and the second is a dispersive contribution.

Particles scattered to a momentum change Δp_m at a location with a particular $\mathcal{H}_0$, have

the potential to be lost at locations where $\beta[s]$ and $\eta[s]$ cause $x[s]$ to exceed the radius

of the beam pipe.

3.2.8.1 Effects of nonlinearities on particle trajectories

The Bmad standard tracking routines we use in our simulations take into account nonlin-

earities, but are not fully nonlinear. The routines are designed to balance accuracy and

166

speed [38]. More accurate tracking routines are available in `Bmad`, but they are slower. To check whether the standard routines are sufficiently accurate to reliably determine if a scattered particle collides with the beam pipe, the contribution to the particle trajectory from higher orders of dispersion is examined.

Higher orders of dispersion are calculated by combining the Taylor maps of the individual elements that represent the beam line. The map picks up dispersion terms from the bend and wiggler elements. Dispersion is obtained from the matrix elements of the map with,

$$
\begin{aligned}
\eta_1 &= \frac{T_{1,6}}{T_{6,6}} \\
\eta_2 &= \frac{T_{1,6,6}}{T_{6,6}^2} \\
\eta_3 &= \frac{T_{1,6,6,6}}{T_{6,6}^3} \\
&\quad \text{...and so on...,}
\end{aligned}
\tag{3.68}
$$

where η_1, η_2, η_3, are the 1st, 2nd, and 3rd orders of dispersion. The contribution to the particle trajectory from dispersion of order n is,

$$
\Delta x_n = \eta_n \times \left(\frac{\Delta p}{p} \right)^n .
\tag{3.69}
$$

Shown in Fig. 3.2 is the contribution to the transverse coordinate from nonlinear dispersion up to order 4 for a particle with a $+10$ MeV energy defect. Figure 3.2 suggests that prior to the final decelerating stage, higher orders of dispersion displace the particle trajectory by a negligible amount. The displacement is less than 0.02 mm, and we are interested in displacements larger than 13 mm. However, during the final decelerating stage, the relative momentum spread blows up and higher orders of dispersion can become significant. This can cause a large number of particles to collide with the final decelerating cavities, which may lead to multipacting. It can also create a background
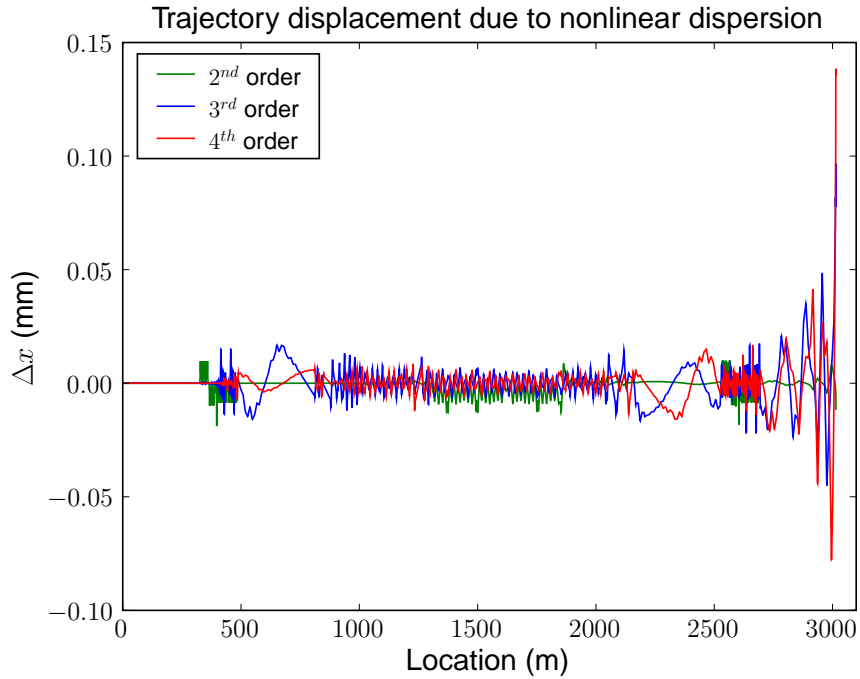
Figure 3.2: Displacement of trajectory of particle with $+10$ MeV/c momentum defect due to 2nd, 3rd, and 4th order dispersion. The beam pipe diameter is 13 mm.

of particles around the beam and impact the design of the beam dump. The effect of nonlinearities at the end of the linac is seen in Fig. 3.12.

3.3 Implementation

3.3.1 Element-by-element energy aperture

Representing IBS particles with precision requires tracking several 10's of particles through each of the several thousand optical elements that make up the Cornell ERL. This is a computationally intensive task and it is best to avoid tracking particles that are not lost and therefore not of interest. To avoid tracking particles that are not lost, an element-by-element energy aperture is determined. The element-by-element energy

aperture is the minimum energy change that needs to be given to a particle in an element such that it collides with the chamber walls somewhere down the accelerator.

Due to nonlinearities and asymmetries, along with the fact that only particles with a negative energy change have the potential to be stopped during deceleration, the positive energy aperture δ_E^+ is not symmetric with the negative energy aperture δ_E^-, i.e. $\delta_E^- \neq -\delta_E^+$. It is necessary to determine the positive and negative aperture independently.

To determine the positive aperture, at the first optical element in the accelerator a test particle is given an initial energy change δ_E. Since the beam size is on the order of 10^{-6}m and the beam pipe size is on the order of 10^{-2}m, the initial coordinate has a negligible impact on the trajectory of a particle lost to the beam pipe, and it is accurate to O^4 to assume that each particle starts in the center of the beam pipe.

The test particle is tracked to determine if it is lost. If it is lost, the energy change is decreased and the tracking done again. If it is not lost, the energy change is increased. Once an upper and lower bound for the aperture have been established, a binary search is performed to determine the aperture to arbitrary precision. The process is then repeated for the second optical element, and so on to the end of the accelerator. Similarly the negative energy aperture is determined.

An example energy aperture is shown in Fig. 3.3. This example is from a Cornell ERL lattice version 3.0. This version is characterized by a tight 40 m east turn around. The stages of the accelerator are shown in table 3.1. In this example the negative energy aperture is dominated by IBS particles stopping during deceleration. The positive aperture is determined entirely by beam pipe collisions. Notice that the energy aperture in the accelerating structures is about an order of magnitude larger than the energy aperture in high-dispersion regions.
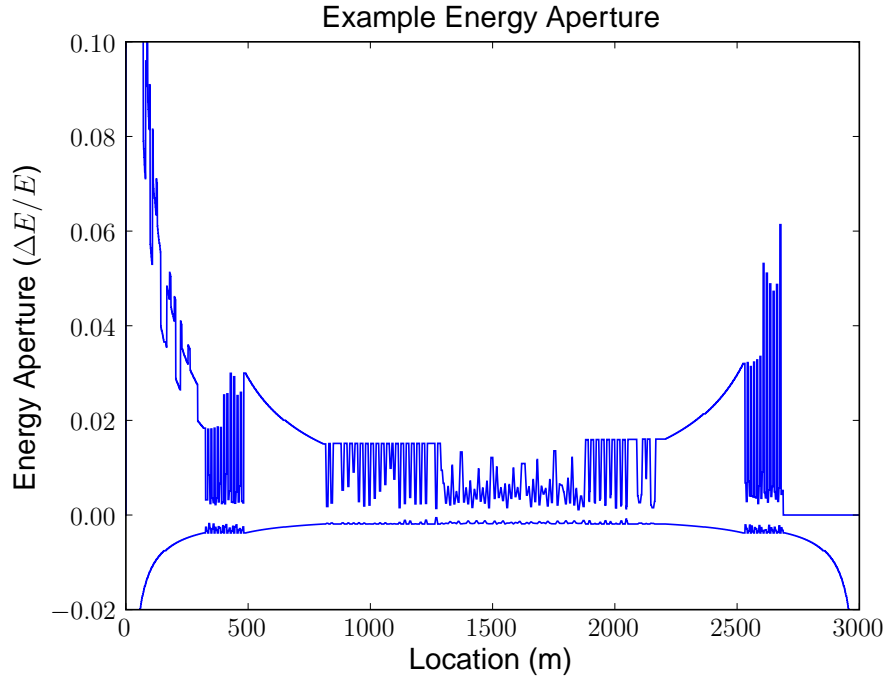
Figure 3.3: Example energy aperture from CERL lattice version 3.0. The positive aperture is determined entirely by beam pipe collisions. The negative aperture is dominated by stopping during deceleration.

Table 3.1: Stages of CERL lattice version 3.0 used for example plots in this chapter. Sections that are crossed by the beam twice are labeled by "\1" and "\2". Particles are injected at 0 m with 10 MeV.

Start (m)	End (m)	Label	Description
0	318	LA\1, LB\1	acceleration to 2.5 GeV
318	490	TA\1	East turn around
490	808	LC\1, LD\1	acceleration to 5.0 GeV
808	1284	SA	user region, x-ray prod.
1284	1889	CE	CESR turn around
1889	2207	NA	user region, x-ray prod.
2207	2525	LA\2, LB\2	deceleration to 2.5 GeV
2525	2696	TA\2	East turn around
2696	3014	LC\2, LD\2	deceleration to 10 MeV
3014	3014		beam dump
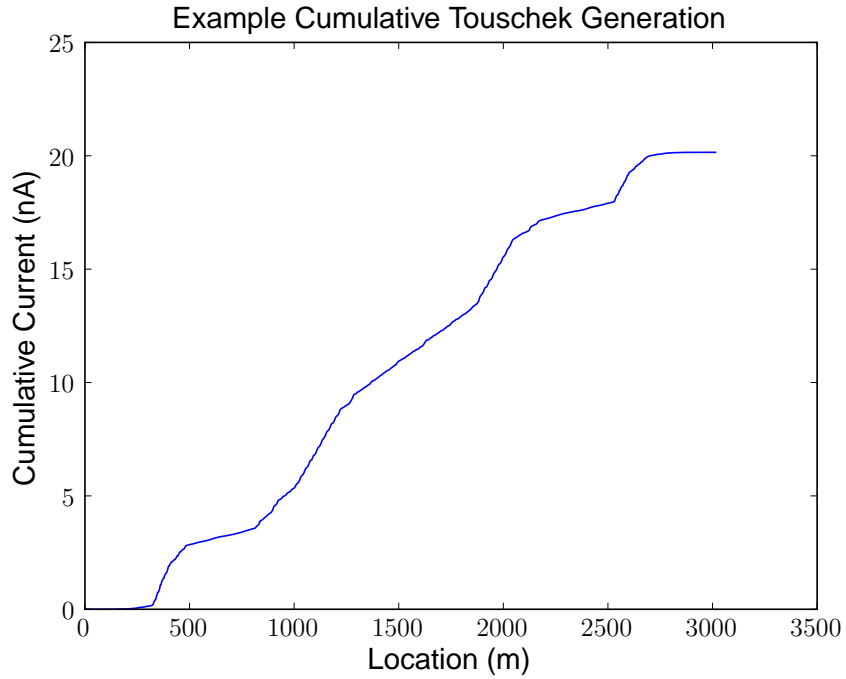
Figure 3.4: Cumulative generation of scattered particles.

3.3.2 Touschek scattering rates

The rate at which particles are scattered above $E(1 + \delta_E^+)$ or below $E(1 - \delta_E^-)$ is found by evaluating $R(\delta_E^{+,-})$, given by Eqn. 3.57, using the Twiss and beam parameters at each element. The current of scattered particles generated per bunch is found by multiplying the rate R by the fundamental charge and the time the bunch is in the element, l/c, where l is the length of the element and c is the speed of light.

The cumulative current generated for CERL 3.0 is shown in Fig. 3.4. This Fig. says that the total current of scattered particles generated is 20 nA. The slope of this curve is proportional to the scattering rate.

3.3.3 Test particle distribution

At each element in the accelerator, two distributions of test particles are tracked, one representing particles that gain energy through scattering, and one for those that lose energy. The distributions are constructed such that they contain only particles with energy greater than $E(1 + \delta_E^+)$ or less than $E(1 - \delta_E^-)$.

The distribution of particles that gain energy is constructed by calculating the rate $R(\delta_E^+)$ at which particles are scattered above the positive energy aperture δ_E^+. This rate is divided by the number of test particles to be tracked, N_t. Each test particle is taken as representing a rate of $R(\delta_E^+)/N_t$ scattered particles. The energy change represented by each test particle is determined by inverting a linear interpolation of $R(\delta_E)$. This gives $\delta_E(R)$, and the ith test particle is assigned a momentum change $\delta_E(R_i)$ where $R_i = (i+1/2)\frac{R(\delta_E)}{N_t}$. Similarly the distribution of particles that lose energy is constructed.

The number of scattered particles each test particle represents is obtained by multiplying the rate R by l/c. The current represented by each test particle is found by multiplying the number of scattered particles it represents by the bunch repitition rate and the fundamental charge. The power each test particle represents is found by multiplying its current by its energy.

In Fig. 3.5 an example $R(\delta_E^+)$ curve is shown along with the test particles used to represent it. The curve starts at the positive energy aperture of the optical element, $\delta_E^+ = 0.2\%$. It says that 5×10^7 particles are scattered above δ_E^+ per second. The distribution has 50 test particles, and each test particle represents $\frac{5 \times 10^7}{50}$ particles per second.
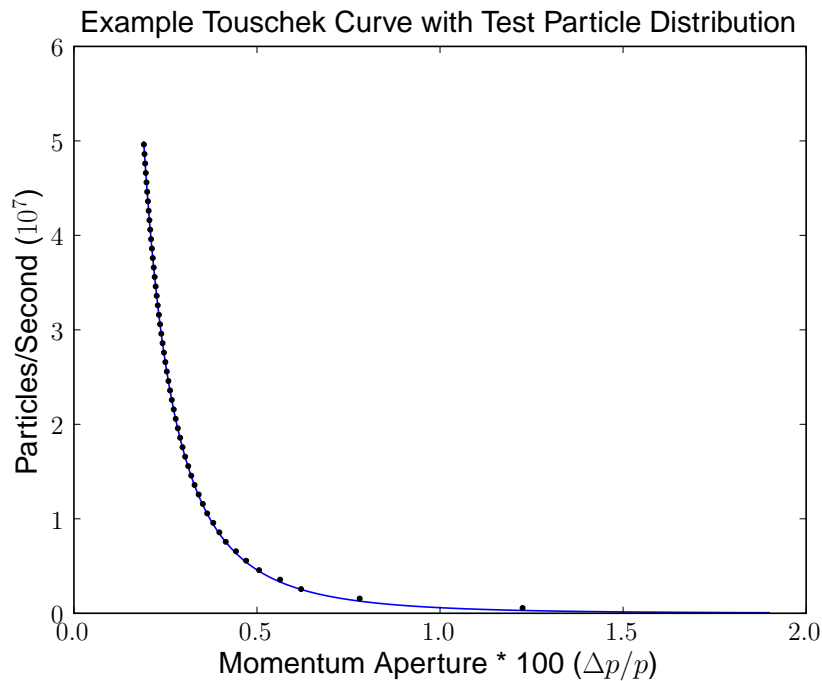
Figure 3.5: Example Touschek curve with test particle distribution used to represent it.

3.3.4 Tracking losses

Each test particle is tracked using `Bmad` standard tracking routines from the optical element where the scattering occurs to the element where it is lost.

A particle can be lost by striking the beam pipe or stopping during deceleration. If the loss is due to a beam pipe collision, the current the test particle represents is added to the current deposited into that element of the accelerator. The power is also recorded.

Shown in Fig. 3.6 is the current of scattered particles striking the beam pipe for CERL 3.0. The current stopping at the end of the linac is shown in Fig. 3.7. Where Fig. 3.4 shows where the scattering occurs, Figs. 3.6 and 3.7 show where the particles are lost. The total current deposited into the CERL 3.0 beam pipe is 7.7 nA. The current stopped during deceleration is 12.3 nA.
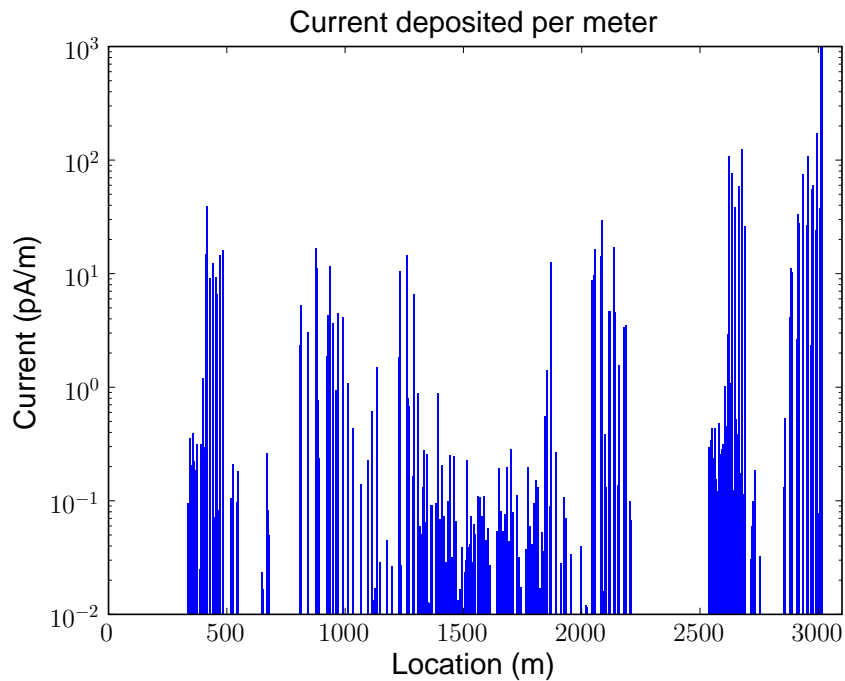
Figure 3.6: Current per meter of scattered particles striking beam pipe. The current at the end of the linac peaks at 2230 pA/m due to the $1/\gamma(s)$ dependence in Eqn. (3.67).

The tracking of test particles is parallelized with MPI. A master node is designated and its role is to send test particles to worker nodes which run the tracking routine. Each worker node tracks the test particle it received from where it is generated to where it is lost, and sends the results back to the master node. The master node will then send another test particle to the worker node if there are any left to track. The parallelization is set up to run on managed clusters, as well as ad-hoc clusters, which can be composed of idle work stations. A typical tracking run requires approximately 10 CPU-hours on 2 GHz CPUs.
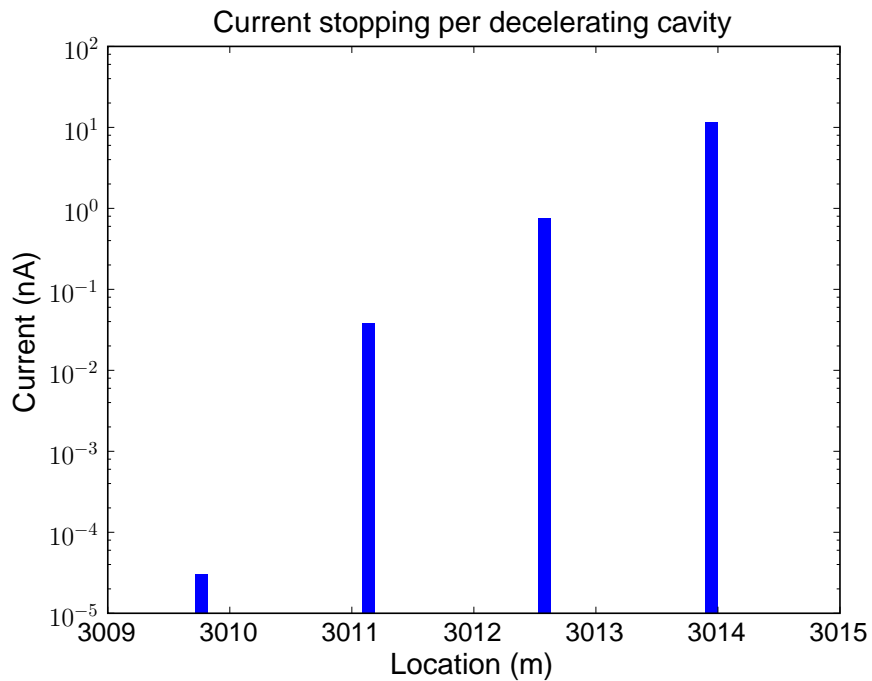
Figure 3.7: Current per decelerating cavity of scattered particles stopping at the end of the linac. The design energy at the end of the linac is 10 MeV. Each cavity decelerates the beam by 13 MeV.

3.3.5 Tracking background

In addition to tracking IBS particles that are lost in the linac, the simulations can be adjusted to track IBS particles that make it to the end of the linac but lie outside 10 sigma of the beam phase-space. These particles can be important when designing the beam dump.

An additional element-by-element energy aperture, defined as the largest momentum kick that can be introduced without the particle laying outside 10 sigma of the beam dimensions at the end of the accelerator, is required for tracking the background of scattered particles.

The background is determined by tracking test particles with energy changes larger

than the '10 sigma' aperture, but smaller than the 'loss' aperture. These particles are tracked to the end of the linac. Their phase-space coordinates and their current and energy are recorded. An example background is shown in Fig. 3.12.

3.3.6 Multiple-event IBS

3.3.6.1 Losses

Thus far only single-event IBS has been considered; we have discussed only those particles that are ejected from the beam after a single scattering event that imparts an energy change $\Delta \delta_E$. In multiple-event IBS, the cumulative effect of many small scattering events is considered.

The effect of multiple-event IBS is to increase the standard deviation of the bunch dimensions. We use the Completely Integrated Modified Piwinski (CIMP) result from reference [19] to obtain a rise time τ_x for the emittance of the bunch. This result takes into account scattering in dispersive regions.

The emittance growth due to multiple-event IBS is found to be 1.3%. This is translated into the number of particles lost by integrating over a normal distribution,

$$N_{lost} = N_{bunch} \frac{\int_{x,pipe}^{\infty} e^{-\frac{x^2}{2((1+\kappa)\sigma_x)^2}} dx - \int_{x,pipe}^{\infty} e^{-\frac{x^2}{2\sigma_x^2}} dx}{\int_{x,pipe}^{\infty} e^{-\frac{x^2}{2\sigma_x^2}} dx}, \tag{3.70}$$

where $x, pipe$ is the beam pipe radius, σ_x is the RMS beam width, N_{bunch} is the number of particles in the bunch, and κ is the emittance growth. The narrowest beam pipe in the Cornell ERL is 1.27 cm and the average RMS beam width is 35 μm. Evaluating Eqn. (3.70) with these parameters gives a result $< 10^{-20000}$. At 5×10^8 particles per bunch and 1.3 GHz, it is seen that the losses due to multiple-event IBS scattering are nil.

Looked at from another perspective, the simulations indicate that approximately 100 particles are scattered out of each bunch due to single-event IBS. Each bunch contains 5×10^8 particles. Therefore, the probability of a particle in a bunch undergoing a collision that scatters it into the beam pipe is $100/(5 \times 10^8)$. If it is estimated that the probability of a particle undergoing a collision that imparts to it half the energy change necessary for a loss is $1000/(5 \times 10^8)$, then the probability of a particle in a bunch undergoing two such collisions in the same direction is $\frac{1}{2}(1000/(5 \times 10^8))^2$. With 1.3×10^9 bunches per second, about 0.003 particles are lost per second due to two successive collisions, a negligible rate. This confirms our previous estimate that multiple-event IBS does not contribute to Touschek losses.

3.3.6.2   Energy Spread

It is worth digressing for a moment to examine the effect IBS has on energy spread in the Cornell ERL. Multiple-event IBS may not contribute to particle loss, but it does contribute to growth in energy spread. The CIMP formulation is used to calculate the growth in $\Delta E/E$ through the linac.

The growth rates $1/T_p$, $1/T_h$, and $1/T_v$ are calculated at the first element in the lattice according to equation 16 from reference [19]. These growth rates are used to calculate how the beam dimensions change due to IBS. The formula for propagating the change in σ_E due to IBS from one element to the next is,

$$\sigma_{E,i+1} = \sigma_{E,i} \times \left(1 + \frac{2\Delta t_i}{T_p}\right) \times \frac{E_i}{E_{i+1}}, \tag{3.71}$$

where Δt_i is the time the beam spends in element i, E_i is the beam energy at the start of element i, and E_{i+1} is the beam energy at the start of element $i + 1$.

A σ_E defined by the injector is started at element 1 and propagated through the linac.
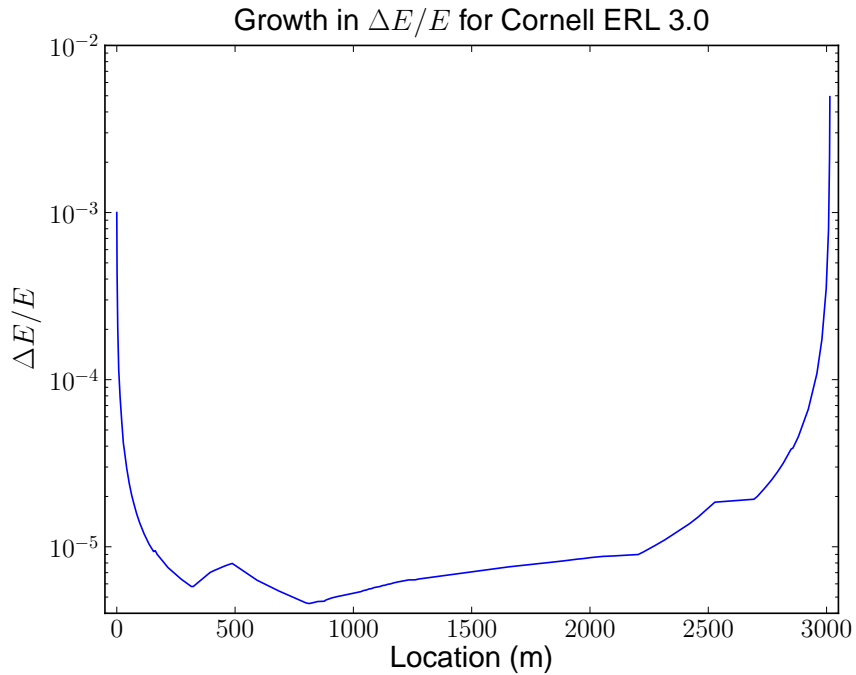
Figure 3.8: Growth $\Delta E/E$ through linac due to IBS. The injected $\Delta E/E$ is 10^{-3}. At the end of the linac, $\Delta E/E$ is 4.9×10^{-3}.

The results are shown in Fig. 3.8. Multiple event IBS increases $E\sigma_E$ by a factor of 5 from the beginning to the end of the lattice.

3.4 Results

The magnitude of $\mathcal{H}$ around CERL 3.0 is shown in the top plot in Fig. 3.9. Shown in the bottom plot is a simulation result for the number of scattered particles generated per bunch passing per meter that collide with the beam pipe somewhere down the linac. The relation between $\mathcal{H}$ and R is given by Eqn. (3.67). Notice the correlation between $\mathcal{H}$ and the number of particles generated.

Figure 3.6 shows the locations where these particles collide with the beam pipe. Notice that at the very end of the accelerator the deposited current rapidly increases to
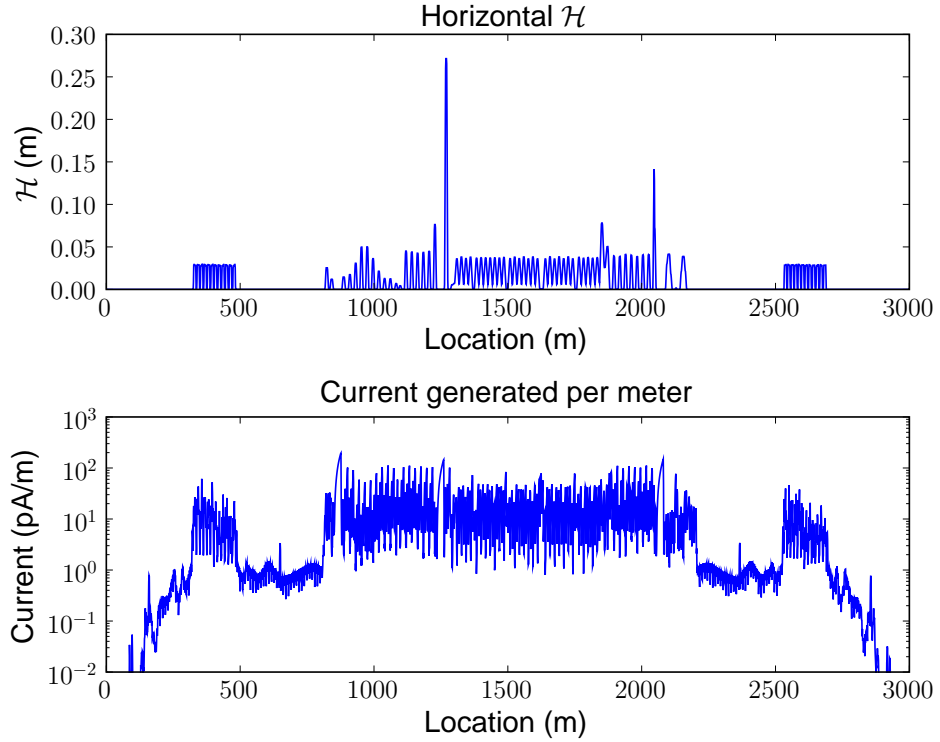
Figure 3.9: $\mathcal{H}$ and current of scattered particles produced per meter for Cornell ERL.

a peak of 2230 pA/m. This is due to the $\gamma_0/\gamma(s)$ dependence of the betatron term in Eqn. (3.67). The dispersive term is negligible since the magnitude of the dispersion at the end of the accelerator is 2×10^{-5} and $\gamma_0/\gamma(s)$ is at most 500.

The impulses shown in Fig. 3.7 are the current of particles stopped in the last four decelerating cavities. Each cavity decelerates the beam by 13 MeV, and the design energy at the end of the linac is 10 MeV. The current stopping in the final cavity is 56 nA. The trajectories of particles stopped in the cavities are unknown but expected to be exotic. Detailed tracking simulations are necessary to determine their behavior and determine if they could pose a hazard. Particles that are accelerated into the cavity wall could lead to multipacting.

3.4.1 Collimation

Shielding the user regions with a reasonable thickness of concrete requires that the current striking the beam pipe there be limited to below 3 pA/m. Additionally, radiation can decrease the MTBF of components anywhere in the accelerator tunnel. For these reasons, shielded collimators are used to control where scattered particles are lost.

Since the beam in the user regions is at full energy and has low energy spread, losses there will be mostly due to betatron oscillations. IBS particles lost due to betatron oscillations are generated in high dispersion regions of the lattice. The high dispersion regions of the Cornell ERL lattice are the east turn around, CESR turn around, and the user regions themselves.

Collimators cannot be placed in the linacs, since the linacs are constructed of cryomodules, which would make maintenance of collimators difficult. Placing collimators in the user regions is problematic due to the radiation generated. Therefore, the best location for collimators is in the turn-arounds, but collimators may be placed in the user regions if necessary.

To shield the first user region from IBS particles, note by looking at table 3.1 that it is proceeded by the east turn around. IBS particles lost in the first user region will be generated in either the East turn around or in the user region itself.

The simulation is set to look at particles scattered in the first turn around around and lost in the first user region. The trajectories of these particles through the accelerator are recorded and histogrammed. The histogram is analyzed to determine where a collimator of a given radius would be most effective.

The bars in Fig. 3.10 show the current of IBS particles that would be stopped by a
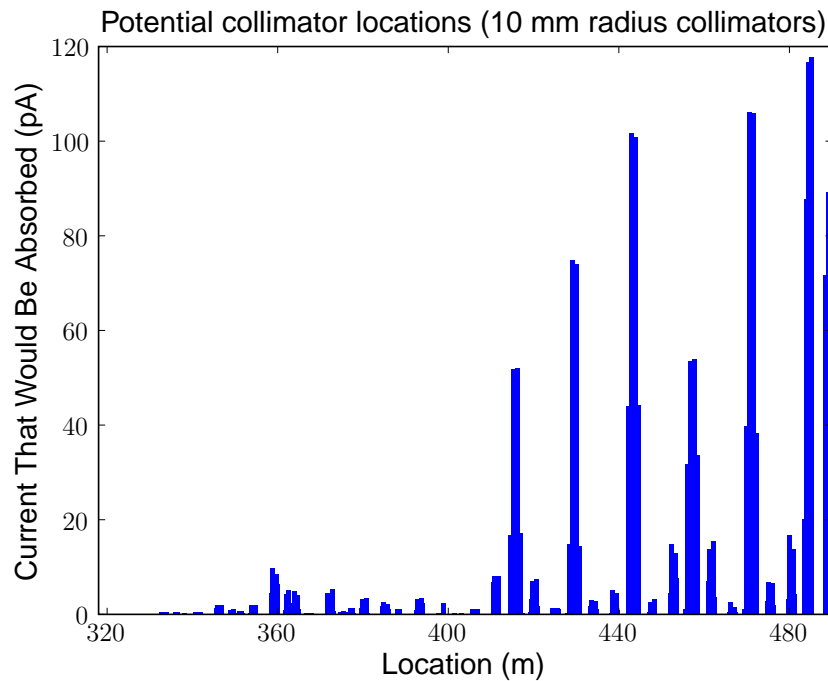
Figure 3.10: Histogram of the current of particles scattered in TA and lost in SA that would be caught by a collimator at the given location. The horizontal coordinate spans the TA region.

collimator placed at that location. The horizontal coordinate is the accelerator element index and spans the TA region. Only particles that will be lost in the first user region are counted. i.e. the plot indicates that a collimator placed at 484.6 m would stop 120 pA of electrons that would otherwise be lost in the SA user region.

The procedure for collimating the first user region consists of placing a 10 mm diameter collimator at the location of the highest peak in Fig. 3.10, then rerunning the simulation to determine both the effectiveness of the collimator and where the next collimator should be placed. This is repeated until losses in the user region from particles scattered in the East turn around are below 3 pA/m. The diameter of the collimators was chosen by balancing effective collimation that comes with a smaller diameter against the detrimental effect of wake fields.
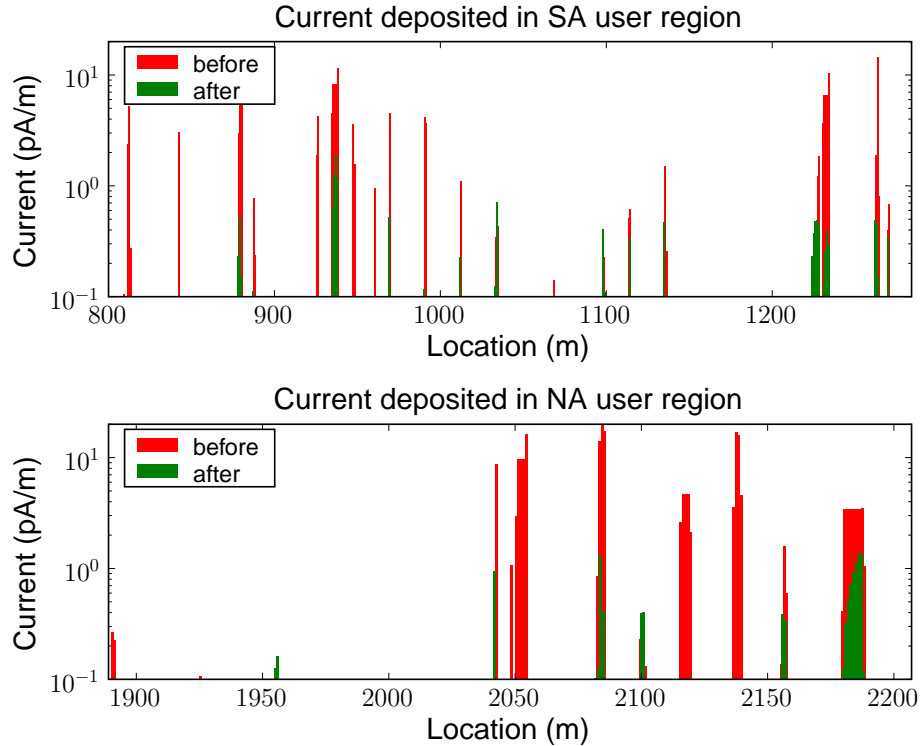
Figure 3.11: Results of collimating Cornell ERL to reduce current of scattered particles deposited into user regions. The red bars are before collimation, and the green bars after collimation. All green bars are below the 3 pA/m threshold.

If it if found that there are no locations in the turn-around where a collimator would be effective, but the losses in the user region are still above 3 pA/m, the simulation is adjusted to look at particles generated and lost in the user region. A collimator is placed where it would be effective and where there is room to surround it with shielding.

It is found that a scheme of eight 10 mm collimators are sufficient to reduce the current of scattered particles lost in the user regions to below 3 pA/m. Two collimators are located in the east turnaround, three in the CESR turnaround, one in the South user region, and two in the North user region. These results are shown in Fig. 3.11. The scheme is shown in table 3.2.

Table 3.2: Location and current absorbed for scheme of 10 mm diameter collimators that limits current deposited into user regions to below 3 pA/m. The beam passes through the TA collimators twice, once during the accelerating phase and once during the decelerating phase.

Loc. (m)	Region	Current Absorbed (pA)
470.1/2676.7	TA1/2	1949
484.6/2691.1	TA1/2	984
1147.0	SA	26
1756.9	CE	56
1852.6	CE	154
1871.9	CE	617
2041.9	NA	108
2134.7	NA	18

3.4.2 Beam dump considerations

Particles that are scattered such that the amplitude of their trajectory at the end of the linac is larger than 10-sigma of the beam dimensions, but small enough that they do not strike the beam pipe, form a background of scattered particles that needs to be dumped along with the beam. The simulation is adjusted to track these particles and their horizontal phase-space coordinates at the end of the linac are recorded.

Shown in Fig. 3.12 is the horizontal phase space of the background of scattered particles at the end of the linac. The total current of scattered particle laying outside 10-sigma of the beam dimensions is 413 nA. 413 nA is small compared to the beam current of 100 mA, but the phase space area of the scattered particles is much larger than that of the beam. The scattered particles are much more difficult to steer into the dump. The beam dump needs to be designed such that the trajectories of the scattered particles does
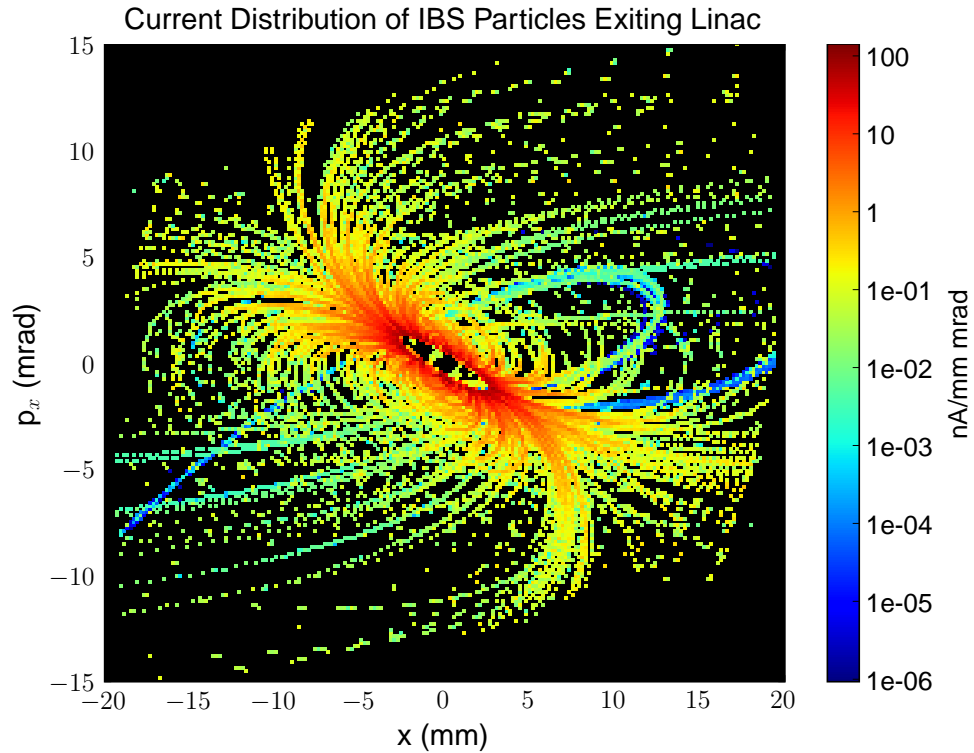
Figure 3.12: Horizontal phase-space distribution of scattered particles at the end of the linac. The total current of particles laying outside 10 sigma of the beam is 413 nA, compared to a beam current of 100 mA. The radius of the beam pipe at this part of the accelerator is 1.95 cm. This data was run on the uncollimated lattice.

not cause too much current to be deposited into sensitive structures such as magnets.

3.4.3 Touschek Scattering Between Overlapping Beams of Different Energy

Multiple turn accelerators have been proposed for ERLs. In these accelerators beams of different energy may overlap in the linacs and arcs. Here we adapt the previously derived formula for the Touschek rate to apply to scattering between overlapping bunches of different energy. The change required is to assume that the two colliding particles have an energy difference $\Delta E = E_2 - E_1$, where E_2 and E_1 are the energies of the high energy beam and low energy beam, respectively. Additionally, each bunch has different Twiss

parameters and a different energy aperture. If $\Delta E \gg \delta_{E1,2}$, then energy spread can be ignored.

The different Twiss parameters change the quadratic forms in Eqn. (3.3). This results in new expressions for k_x, k_y, and l. These new expressions are exact but complicated. Refer to Apx. E for the expressions related to Touschek scattering between overlapping beams.

The energy difference ΔE changes the relative velocity Δv of the two particles and also their cross-section σ. The components of their relative velocity can be written as,

$$
\begin{aligned}
\Delta v_j &= \frac{\beta_1 \beta_2}{2|\vec{p}|} (E_1 + E_2) \chi + \mathcal{O}^3 \\
\Delta v_l &= \frac{1}{2|\vec{p}|} (\beta_2 - \beta_1) (\beta_2 E_2 + \beta_1 E_1) \left(1 - \frac{\chi^2}{2}\right) + \mathcal{O}^4.
\end{aligned}
$$

When ΔE is large, the relative velocity between the two particles has a longitudinal component and a transverse component. The relative velocity can then be written in the form,

$$
\begin{aligned}
\Delta v &= \sqrt{\Delta v_j^2 + \Delta v_l^2} \\
&= c_1 \left(1 + c_2 \chi^2\right) + \mathcal{O}^3 .
\end{aligned}
\tag{3.72}
$$

Note that this is the velocity "seen" by the particles, not the closing velocity. From Eqn. (3.72) we see that the relative velocity has a constant part and a part that depends on χ. A plot of the relative velocity between two particles with different energy is in Fig. (3.13). The longitudinal part is significant if the relativistic γ of one of the particles is small.

Recall that the cross-section for particle loss was obtained by integrating the Moller scattering cross-section over all angles that lead to particle loss. To obtain these angles,

185
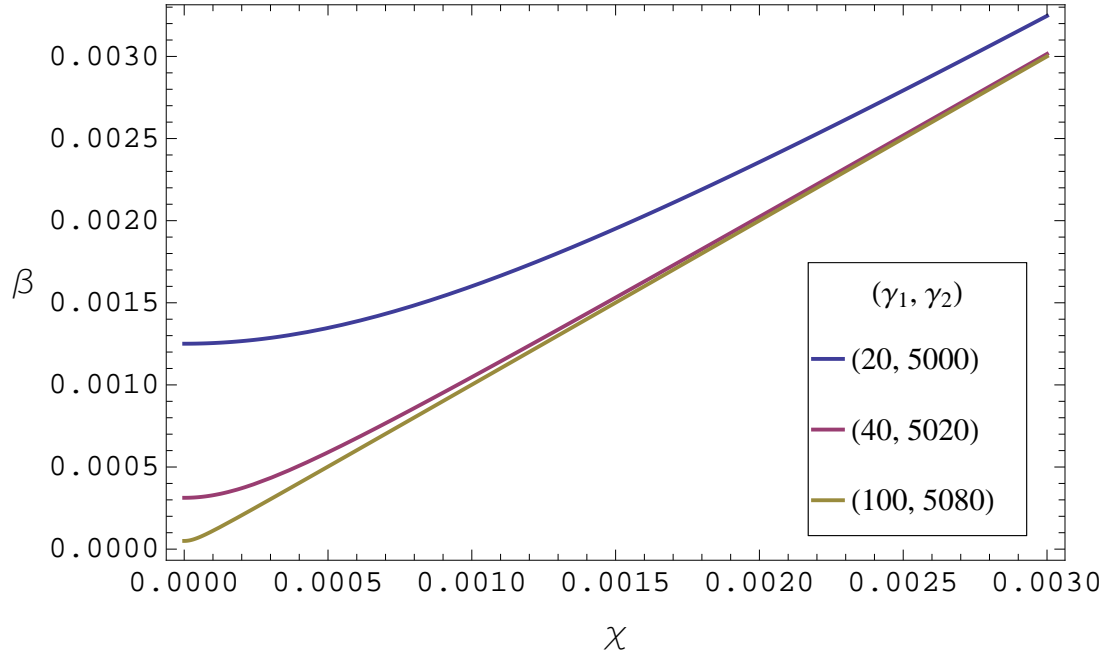
Figure 3.13: Relative velocity between two particles with different relativistic γ as a function of angle between their momenta.

Eqn. (3.31) was interpreted as a condition for particle loss,

$$\Delta E_{max} < \pm \left(\Delta E \sin^2 \left(\frac{\psi}{2} \right) + \gamma_c \beta_c c p_\perp \sin \psi \sin \phi \right). \tag{3.73}$$

There are two contributions to the energy change following the collision. The first term is due to the energy difference between the two particles. The second term is due to their relative transverse momentum. In single beam Touschek scattering, the first term is much smaller than the second and is ignored. However, if ΔE is large, then the first term needs to be taken into consideration.

A closed-form expression for the integrated cross-section is found in the one-beam case because ignoring the first term allows for an explicit expression for ψ,

$$\psi = \arcsin \frac{B}{\sin \phi}. \tag{3.74}$$

If both terms in Eqn. (3.73) are significant, then an exact expression for ψ cannot be found and our method for deriving the Touschek rate breaks down. However, if each

term is examined independently, it is found that neither term results a significant Touschek rate. This is because both cross-sections become large only when $\tilde{\beta}$ is small. If the energy difference between the two bunches is large, then there is a lower bound on $\tilde{\beta}$.

The cross-section for losses due to the ΔE contribution to the energy change is found by integrating Moller differential scattering cross-section, Eqn. (3.37) over,

$$2 \arcsin \sqrt{\frac{\Delta E_{max}}{\Delta E}} \leqslant \psi < \pi \,,$$

$$0 \leqslant \phi < 2\pi \,,$$

yields,

$$\sigma_{\Delta E} = \frac{\pi r_e^2}{\tilde{\gamma}^2} \left[\frac{1}{2} \left(3 - \frac{2}{\tilde{\beta}^2} - \frac{1}{\tilde{\beta}^4} \right) \log \left(\frac{2-D}{D} \right) \right.$$

$$\left. - D + 1 + \left(1 + \frac{1}{\tilde{\beta}^2} \right)^2 \left(\frac{2 - 2D}{D \left(2 - D \right)} \right) \right] , \quad (3.75)$$

where,

$$D = \frac{2 \Delta E_{aperture}}{E_2 - E_1} \,. \quad (3.76)$$

The higher energy beam is referred to with subscript 2, and the lower energy beam with subscript 1.

Both Eqs. (3.75) and (3.10) scale with $1/\tilde{\beta}^4$. Plotted in Fig. (3.14) is $\tilde{\beta}$ for three combinations of overlapping beams with different energies. If ΔE is large, then there are no particle pairs with small $\tilde{\beta}$. It follows that the cross-section for Touschek scattering between beams with a large ΔE is small.

Observing Fig. (3.13), a large ΔE increases the rate at which collisions occur. Observing Fig. (3.14), a large ΔE makes it less likely for those collisions to result in particle loss. To find out which contribution dominates, a numerical study is done on a prototype
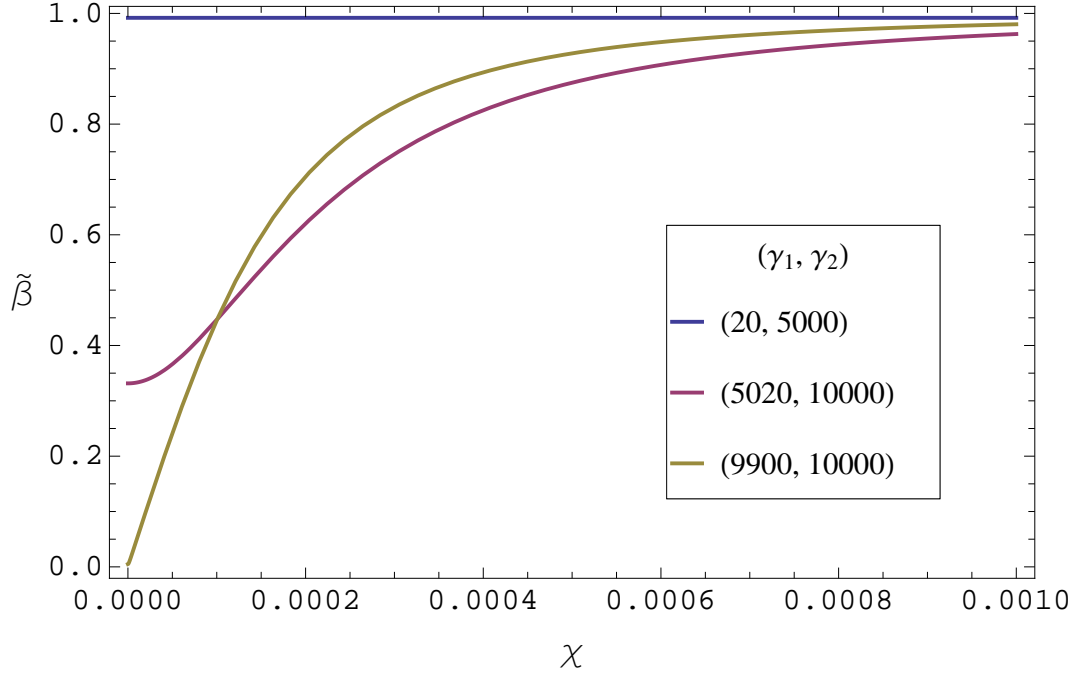
Figure 3.14: $\tilde{\beta}$, the velocity of colliding particles in the c.o.m. frame, plotted versus χ. When ΔE is large, there are no particle pairs with small $\tilde{\beta}$.

2-turn ERL lattice. In this lattice, a beam which accelerates from 10 MeV to 2510 MeV overlaps a beam which accelerates from 2510 MeV to 5000 MeV. The results are shown in Fig. (3.15). Two loss mechanisms are shown: 1) Transfer of energy between particles 2) Transfer of transverse momentum between particles. The beams overlap in the linacs. These results demonstrate that the scattering rate between overlapping bunches of different energy is small. The scattering rate among particles in the higher energy beam is shown for comparison.

3.4.4 Conclusion

Touschek scattering is relevant to ERLs because the current of lost particles can pose a radiation hazard. To facilitate proper collimator placement, the locations where scattered particles are generated and where they are lost need to be calculated. We have re-derived

Current from Scattering Between Overlapping Bunches
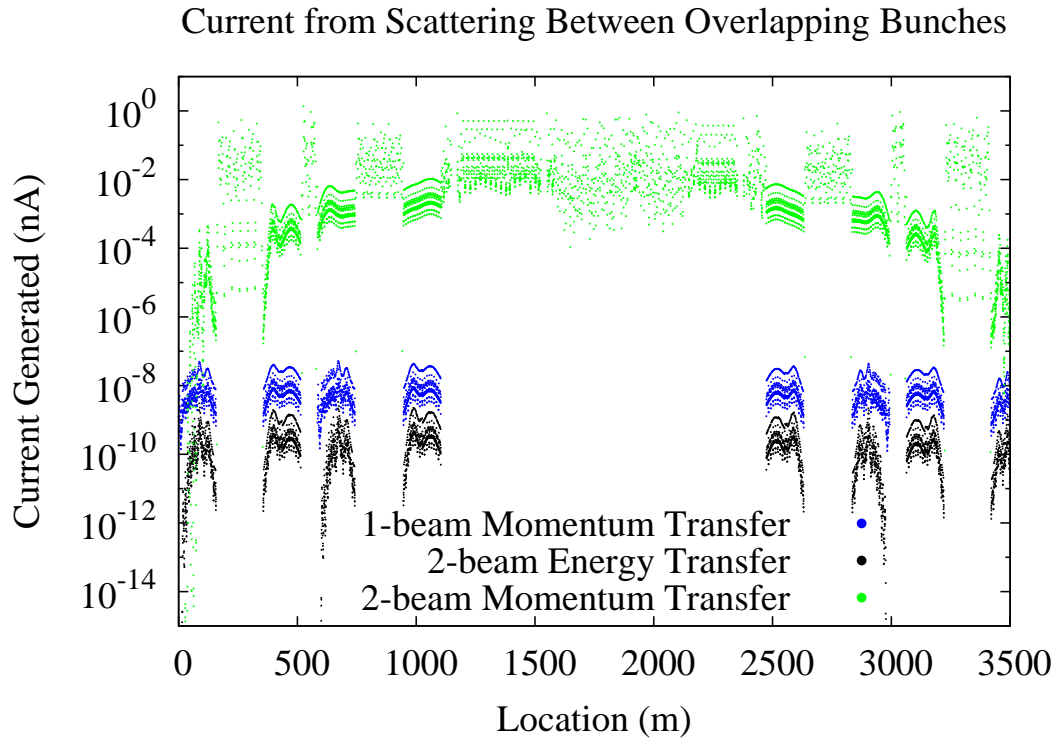
Figure 3.15: Touschek rate for scattering rate between overlapping beams of different energy. The self-scattering rate for the higher energy beam is also plotted for comparison.

Piwinski's well-known formula for Touschek scattering stored beams to determine that it is valid for ERL beams. This required reworking the calculation to keep track of approximations and determined that it is good to 1st order in combinations of Δ_E/E, $1/\gamma_0$, and χ. We then re-purposed Piwinski's formula to give the rate at which particles with a certain energy offset are generated at each location in the ERL. Using standard tracking methods we are able to determine the trajectory of these particles to where they are lost.

Scattered particles can assume large-amplitude oscillations and guide field non-linearities may become important. We have also checked whether nonlinearities need to be taken into account when tracking. Our conclusion is that non-linearities do not have a significant impact on particle trajectories until the last stages of deceleration.

These simulations have been applied to develop an effective collimation scheme for the Cornell ERL. Before collimation, loss rates in the user regions are as high as 47 pA/m. After collimation, the rate is below 3 pA/m.

The phase-space of the background of scattered particles at the beam dump has been determined. This information can be used to design a beam dump that efficiently dumps not only the beam, but also the background of scattered particles around the beam.

Acknowledgments

APPENDIX A

TRANSFER MATRICES FOR "THESIS LAT"

$$\mathbf{M}_{qf} = \begin{pmatrix} 0.996877 & 0.24974 & 0 & 0 & 0 & 0 \\ -0.024974 & 0.996877 & 0 & 0 & 0 & 0 \\ 0 & 0 & 1.00313 & 0.25026 & 0 & 0 \\ 0 & 0 & 0.025026 & 1.00313 & 0 & 0 \\ 0 & 0 & 0 & 0 & 1 & 0 \\ 0 & 0 & 0 & 0 & 0 & 1 \end{pmatrix} \quad (A.1)$$

$$\mathbf{M}_{qd} = \begin{pmatrix} 1.0025 & 0.500417 & 0 & 0 & 0 & 0 \\ 0.0100083 & 1.0025 & 0 & 0 & 0 & 0 \\ 0 & 0 & 0.997501 & 0.499583 & 0 & 0 \\ 0 & 0 & -0.00999167 & 0.997501 & 0 & 0 \\ 0 & 0 & 0 & 0 & 1 & 0 \\ 0 & 0 & 0 & 0 & 0 & 1 \end{pmatrix} \quad (A.2)$$

$$\mathbf{M}_{b} = \begin{pmatrix} 0.980785 & 4.96793 & 0. & 0. & 0. & 0.489299 \\ -0.00766118 & 0.980785 & 0. & 0. & 0. & 0.19509 \\ 0. & 0. & 1. & 5. & 0. & 0. \\ 0. & 0. & 0. & 1. & 0. & 0. \\ -0.19509 & -0.489299 & 0. & 0. & 1. & -0.0320657 \\ 0. & 0. & 0. & 0. & 0. & 1. \end{pmatrix} \quad (A.3)$$

$$\mathbf{M}_d = \begin{pmatrix} 1 & 0.375 & 0 & 0 & 0 & 0 \\ 0 & 1 & 0 & 0 & 0 & 0 \\ 0 & 0 & 1 & 0.375 & 0 & 0 \\ 0 & 0 & 0 & 1 & 0 & 0 \\ 0 & 0 & 0 & 0 & 1 & 0 \\ 0 & 0 & 0 & 0 & 0 & 1 \end{pmatrix} \tag{A.4}$$

$$\mathbf{M}_{fL} = \begin{pmatrix} 1 & 0.375 & 0 & 0 & 0 & 0 \\ 0 & 1 & 0 & 0 & 0 & 0 \\ 0 & 0 & 1 & 0.375 & 0 & 0 \\ 0 & 0 & 0 & 1 & 0 & 0 \\ 0 & 0 & 0 & 0 & 1 & 0 \\ 0 & 0 & 0 & 0 & 0.001 & 1 \end{pmatrix} \tag{A.5}$$

$$\mathbf{M}_{qdt} = \begin{pmatrix} 1.01177 & 0.50196 & 0.00427526 & 0.000712542 & 0. & 0. \\ 0.0471932 & 1.01177 & 0.0171011 & 0.00427526 & 0. & 0. \\ 0.00427526 & 0.000712542 & 0.98828 & 0.498045 & 0. & 0. \\ 0.0171011 & 0.00427526 & -0.0467765 & 0.98828 & 0. & 0. \\ 0. & 0. & 0. & 0. & 1. & 0. \\ 0. & 0. & 0. & 0. & 0. & 1. \end{pmatrix} \tag{A.6}$$

APPENDIX B

BEAM SIZE PROJECTIONS IN TERMS OF V

Equations 2.135, 2.136, and 2.137 are the projected beam sizes in terms of the $\bar{\mathbf{V}}$ coupling matrix. Writing the projections in terms of $\mathbf{V}$ reveals how the normal mode Twiss parameters affect the expression of the coupling terms.

Starting from $\boldsymbol{\Sigma}$-matrix in terms of real-valued matrices, Eqn. 2.112,

$$\boldsymbol{\Sigma}\mathbf{S} = \mathbf{N}\boldsymbol{\Lambda}_{\text{real}}\mathbf{N}^{-1}, \tag{B.1}$$

we use the definition of $\mathbf{N}$ in terms of the normal mode matrices $\mathbf{V}$ and $\mathbf{G}$ to obtain,

$$\boldsymbol{\Sigma}\mathbf{S} = \mathbf{V}\mathbf{G}^{-1}\boldsymbol{\Lambda}_{\text{real}}\mathbf{G}\mathbf{V}^{-1}. \tag{B.2}$$

Taking $\sigma_x^2 = \boldsymbol{\Sigma}_{11}$, $\sigma_y^2 = \boldsymbol{\Sigma}_{33}$, and $\sigma_z^2 = \boldsymbol{\Sigma}_{55}$ and simplifying gives the projections of the beam envelope into the lab frame,

$$\sigma_x^2 = \gamma_a^2 \beta_a \epsilon_a + \left(\left(C_{ab11} \sqrt{\beta_b} - C_{ab12} \frac{\alpha_b}{\sqrt{\beta_b}} \right)^2 + \left(C_{ab12} \frac{1}{\sqrt{\beta_b}} \right)^2 \right) \epsilon_b$$
$$+ \left(\left(C_{ac11} \sqrt{\beta_c} - C_{ac12} \frac{\alpha_c}{\sqrt{\beta_c}} \right)^2 + \left(C_{ac12} \frac{1}{\sqrt{\beta_c}} \right)^2 \right) \epsilon_c \tag{B.3}$$

$$\sigma_y^2 = \gamma_b^2 \beta_b \epsilon_b + \left(\left(-D_{ba22} \sqrt{\beta_a} - D_{ba12} \frac{\alpha_a}{\sqrt{\beta_a}} \right)^2 + \left(D_{ba12} \frac{1}{\sqrt{\beta_a}} \right)^2 \right) \epsilon_a$$
$$+ \left(\left(C_{bc11} \sqrt{\beta_c} - C_{bc12} \frac{\alpha_c}{\sqrt{\beta_c}} \right)^2 + \left(C_{bc12} \frac{1}{\sqrt{\beta_c}} \right)^2 \right) \epsilon_c \tag{B.4}$$

$$\sigma_z^2 = \gamma_c^2 \beta_c \epsilon_c + \left(\left(-D_{ca22} \sqrt{\beta_a} - D_{ca12} \frac{\alpha_a}{\sqrt{\beta_a}} \right)^2 + \left(D_{ca12} \frac{1}{\sqrt{\beta_a}} \right)^2 \right) \epsilon_a$$
$$+ \left(\left(-D_{cb22} \sqrt{\beta_b} - D_{cb12} \frac{\alpha_b}{\sqrt{\beta_b}} \right)^2 + \left(D_{cb12} \frac{1}{\sqrt{\beta_b}} \right)^2 \right) \epsilon_b \tag{B.5}$$

INTEGRATED CROSS-SECTION FOR TOUSCHEK DERIVATION

The Moller scattering cross-section is,

$$d\bar{\sigma} = \frac{r_e^2}{4\gamma^2} \left(\left(1 + \frac{1}{\beta^2}\right)^2 \left(\frac{4}{\sin^4\psi} - \frac{3}{\sin^2\psi}\right) + \frac{4}{\sin^2\psi} + 1 \right) \sin\psi\, d\psi\, d\phi. \qquad \text{(C.1)}$$

This equation is integrated such that $\sin\psi \sin\phi > B$, where B is some constant,

$$\bar{\sigma} = \frac{r_e^2}{\gamma^2} \int_{\phi_{\min}}^{\frac{\pi}{2}} \int_{\psi th(\phi)}^{\frac{\pi}{2}} \left(\left(1 + \frac{1}{\beta^2}\right)^2 \left(\frac{4}{\sin^4\psi} - \frac{3}{\sin^2\psi}\right) + \frac{4}{\sin^2\psi} + 1 \right) \sin\psi\, d\psi\, d\phi,$$

$$\text{(C.2)}$$

where $\phi_{\min} = \arcsin B$ and $\psi_{\text{th}}(\phi) = \arcsin \frac{B}{\sin\phi}$.

Integrating first over azimuth yields,

$$\bar{\sigma} = \frac{r_e^2}{\gamma^2} \int_{\phi_{\min}}^{\frac{\pi}{2}}$$

$$\left[\left(1 + \frac{1}{\beta^2}\right)^2 \left(\frac{2}{\tan\psi_{th}\sin\psi_{th}} + \log\tan\left(\frac{\psi_{th}}{2}\right)\right) - 4\log\tan\left(\frac{\psi_{th}}{2}\right) + \cos\psi_{th} \right]$$

$$d\phi. \quad \text{(C.3)}$$

The equation is written in terms of ϕ by using the following trigonometric identities,

$$\tan\arcsin\left(\frac{B}{\sin\phi}\right) = \frac{B}{\sqrt{\sin^2\phi - B^2}}, \qquad \text{(C.4)}$$

$$\sin\arcsin\left(\frac{B}{\sin\phi}\right) = \frac{B}{\sin\phi}, \qquad \text{(C.5)}$$

$$\log\tan\left(\frac{\arcsin\left(\frac{B}{\sin\phi}\right)}{2}\right) = \frac{1}{2}\log\left(\frac{\sin\phi - \sqrt{\sin^2\phi - B^2}}{\sin\phi + \sqrt{\sin^2\phi - B^2}}\right), \qquad \text{(C.6)}$$

and

$$\cos\arcsin\left(\frac{B}{\sin\phi}\right) = \frac{\sqrt{\sin^2\phi - B^2}}{\sin\phi}. \qquad \text{(C.7)}$$

Yielding,

$$\bar{\sigma} = \frac{r_e^2}{\gamma^2} \int_{\phi_{\min}}^{\frac{\pi}{2}} \left[\left(1 + \frac{1}{\beta^2}\right)^2 \left(\frac{2 \sin\phi \sqrt{\sin^2\phi - B^2}}{B^2} \right) + \frac{\sqrt{\sin^2\phi - B^2}}{\sin\phi} \right.$$
$$\left. + \left(\frac{1}{2}\left(1 + \frac{1}{\beta^2}\right)^2 - 2 \right) \log\left(\frac{\sin\phi - \sqrt{\sin^2\phi - B^2}}{\sin\phi + \sqrt{\sin^2\phi - B^2}} \right) \right] d\phi. \qquad \text{(C.8)}$$

Integrating the first two terms over ϕ is straightforward. The third term is integrated by differentiating under the integral,

$$\int_{\arcsin B}^{\frac{\pi}{2}} \log\left(\frac{\sin\phi - \sqrt{\sin^2\phi - B^2}}{\sin\phi + \sqrt{\sin^2\phi - B^2}} \right) d\phi$$
$$= \int_{\arcsin B}^{\frac{\pi}{2}} \int_{\sin\phi}^{B} \frac{\partial}{\partial \tilde{B}} \log\left(\frac{\sin\phi - \sqrt{\sin^2\phi - \tilde{B}^2}}{\sin\phi + \sqrt{\sin^2\phi - \tilde{B}^2}} \right) d\tilde{B} d\phi$$
$$= \int_{\arcsin B}^{\frac{\pi}{2}} \int_{B}^{\sin\phi} \frac{-2\sin\phi}{\tilde{B}\sqrt{\sin^2\phi - \tilde{B}^2}} d\tilde{B} d\phi$$
$$= \int_{B}^{1} \int_{\arcsin \tilde{B}}^{\frac{\pi}{2}} \frac{-2\sin\phi}{\tilde{B}\sqrt{\sin^2\phi - \tilde{B}^2}} d\phi d\tilde{B}$$
$$= \int_{B}^{1} -\frac{\pi}{\tilde{B}} d\tilde{B}$$
$$= \pi \log B. \qquad \text{(C.9)}$$

Giving for Eqn. (C.8),

$$\bar{\sigma} = \frac{\pi r_e^2}{2\gamma^2} \left[\left(3 - \frac{2}{\beta^2} - \frac{1}{\beta^4} \right) \log\frac{1}{B} - B + 1 + \left(1 + \frac{1}{\beta^2}\right)^2 \left(\frac{1}{B^2} - 1\right) \right]. \qquad \text{(C.10)}$$

APPENDIX D

INTEGRATION OVER ξ_X, ξ_Y, δ_{P1}, AND δ_{P2} FOR TOUSCHEK DERIVATION

The four inner integrations of Eqn. 3.39 can be written as,

$$\iint\limits_{\delta_{p2}\delta_{p1}} \exp\left(-\frac{\delta_{p1}^2 + \delta_{p2}^2}{2\sigma_p^2}\right) \int\limits_{\xi_x} \exp\left(\frac{b_x^2}{4a_x} - c_x\right) d\xi_x \int\limits_{\xi_y} \exp\left(\frac{b_y^2}{4a_y} - c_y\right) d\xi_y d\delta_{p1} d\delta_{p2}.$$

(D.1)

where a_x, b_x, c_x, a_y, b_y, and c_y contain ξ_x, ξ_y, δ_{p1}, and δ_{p2}. Powers of ξ_x are collected as,

$$\frac{b_x^2}{4a_x} - c_x = \xi_x^2 d_x + \xi_x e_x + f_x.$$

(D.2)

Integrating over ξ_x yields,

$$\int_{-\infty}^{\infty} \exp\left(-\left(\xi_x^2 d_x + \xi_x e_x + f_x\right)\right) d\xi_x = \sqrt{\frac{\pi}{-d_x}} \exp\left(\frac{e_x^2}{4d_x} - f_x\right).$$

(D.3)

The same is done for ξ_y. The result is,

$$\frac{\pi}{\sqrt{d_x d_y}} \exp\left(-\frac{\delta_{p1}^2 + \delta_{p2}^2}{2\sigma_p^2} + \frac{e_x^2}{4d_x} - f_x + \frac{e_y^2}{4d_y} - f_y\right).$$

(D.4)

Powers of δ_{p1} and δ_{p1} can be collected as,

$$-\frac{\delta_{p1}^2 + \delta_{p2}^2}{2\sigma_p^2} - \frac{e_x^2}{4d_x} + f_x - \frac{e_y^2}{4d_y} + f_y =$$

$$g_p\left(\delta_{p1}^2 + \delta_{p2}^2\right) + h_p\left(\delta_{p1} - \delta_{p2}\right) + i_p \delta_{p1}\delta_{p2} + j_p. \quad \text{(D.5)}$$

After integrating over δ_{p1} and δ_{p2} we find that Eqn. (D.1) evaluates to,

$$\frac{2\pi^2}{\sqrt{d_x d_y \left(4g_p^2 - i_p^2\right)}} \exp\left(\frac{h_p^2}{i_p - 2g_p} + j_p\right).$$

(D.6)

APPENDIX E

DERIVATION OF TOUSCHEK SCATTERING BETWEEN OVERLAPPING BEAMS

This appendix contains a Mathematica notebook converted into Latex. The Touschek scattering rate between overlapping beams of different energy is derived. This derivation was done in Mathematica because the algebra is very cumbersome. This formula was derived when considering the feasibility of a 2-turn energy recovery linear accelerator.

For the Cornell ERL, we found that the scattering rate between overlapping beams was negligible. This is because the relative velocity between the overlapping beams in their center of momentum is significantly larger than in the single beam case. Touschek scattering between overlapping beams made an insignificant contribution to the overall scattering rate, which includes scattering between particles in a single beam.

The Touschek scattering rate for two overlapping beams at different energies is given by:

$$R = \int \rho_1\left[\vec{r_1}, \vec{p_1}\right] \rho_2\left[\vec{r_2}, \vec{p_2}\right] \Delta v\left[\vec{p_1}, \vec{p_2}\right] \sigma\left[\vec{p_1}, \vec{p_2}\right] dV$$

$$
\begin{aligned}
dV &= d\,\vec{r_1}\, d\,\vec{r_2}\, d\,\vec{p_1}\, d\,\vec{p_2} \\
&= dx1\ dx2\ dy1\ dy2 \\
&\qquad dpx1\ dpx2\ dpy1\ dpy2\ d\Delta s1\ d\Delta s2\ d\left(\frac{\Delta p1}{p1}\right)\ d\left(\frac{\Delta p2}{p2}\right)
\end{aligned}
$$

$$\vec{r} = (x_\beta, y_\beta, \Delta s)$$
$$\vec{p_1} = (x_1', y_1', \Delta p_1)$$
$$\vec{p_2} = (x_2', y_2', \Delta p_2)$$

ρ_1 and ρ_2 are the Gaussuan phase-space densities of beam 1 and beam 2 Δv is the velocity of a particle in beam 1 with a momentum $\vec{p_1}$ relative to a particle in beam 2 with a momentum $\vec{p_2}$ σ is the scattering cross-section.

The density in phase-space of each beam is,

$$\rho_1\left[x_{\beta 1}, y_{\beta 1}, \Delta s1, x_1', y_1', \Delta p_1\right] =$$
$$\frac{1}{8\,\pi^3\,\epsilon_{x1}\,\epsilon_{y1}\,\sigma_{s1}\,p_1\,\sigma_{p1}}\ \mathrm{Exp}\left[-\frac{x_{\beta 1}^2 + (\alpha_{x1}\,x_{\beta 1} + \beta_{x1}\,x_1')^2}{2\,\sigma_{x\beta 1}^2} - \frac{y_{\beta 1}^2 + (\alpha_{y1}\,y_{\beta 1} + \beta_{y1}\,y_1')^2}{2\,\sigma_{y\beta 1}^2}\right.$$
$$\left. -\frac{\Delta s1^2}{2\,\sigma_{s1}^2} - \frac{1}{2\,\sigma_{p1}^2}\left(\frac{\Delta p1}{p1}\right)\right]$$

$$\rho_2\left[x_{\beta 2}, y_{\beta 2}, \Delta s2, x_2', y_2', \Delta p_2\right] =$$
$$\frac{1}{8\,\pi^3\,\epsilon_{x2}\,\epsilon_{y2}\,\sigma_{s2}\,p_2\,\sigma_{p2}}\ \mathrm{Exp}\left[-\frac{x_{\beta 2}^2 + (\alpha_{x2}\,x_{\beta 2} + \beta_{x2}\,x_2')^2}{2\,\sigma_{x\beta 2}^2} - \frac{y_{\beta 2}^2 + (\alpha_{y2}\,y_{\beta 2} + \beta_{y2}\,y_2')^2}{2\,\sigma_{y\beta 2}^2}\right.$$
$$\left. -\frac{\Delta s2^2}{2\,\sigma_{s2}^2} - \frac{1}{2\,\sigma_{p2}^2}\left(\frac{\Delta p2}{p2}\right)\right]$$

The position of particle 1 is given by,

$$x1 = x\beta 1 + Dx1\ \frac{\Delta p1}{p1}$$
$$y1 = y\beta 1 + Dy1\ \frac{\Delta p1}{p1}$$

which can be rearranged as,

$x\beta 1 = x1 - Dx1 \frac{\Delta p1}{p1}$

$y\beta 1 = y1 - Dy1 \frac{\Delta p1}{p1}$

The divergence of particle 1 is given by,

$xp1 = xp\beta 1 + Dpx1 \frac{\Delta p1}{p1}$

$yp1 = yp\beta 1 + Dpy1 \frac{\Delta p1}{p1}$

which can be rearranged as,

$xp\beta 1 = xp1 - Dpx1 \frac{\Delta p1}{p1}$

$yp\beta 1 = yp1 - Dpy1 \frac{\Delta p1}{p1}$

Similar equations can be written for particle 2. Since we are only interested in the difference of the divergence of the two particles we introduce the variables,

$\varsigma_x := \frac{x_1{}' + x_2{}'}{2}$

$\varsigma_y := \frac{y_1{}' + y_2{}'}{2}$

$\Theta_x := x_1{}' - x_2{}'$

$\Theta_y := y_1{}' - y_2{}'$

These variables allow the equations for $xp\beta 1$ and $yp\beta 1$ to be written as,

$xp\beta 1 = \frac{\Theta x}{2} + \varsigma x - Dpx1 \frac{\Delta p1}{p1}$

$xp\beta 2 = -\frac{\Theta x}{2} + \varsigma x - Dpx2 \frac{\Delta p2}{p2}$

$yp\beta 1 = \frac{\Theta y}{2} + \varsigma y - Dpy1 \frac{\Delta p1}{p1}$

$yp\beta 2 = -\frac{\Theta y}{2} + \varsigma y - Dpy2 \frac{\Delta p2}{p2}$

And writing out the x1, x2, y1, and y2 formulas,

$$x\beta1 = x1 - Dx1 \, \frac{\Delta p1}{p1}$$

$$x\beta2 = x2 - Dx2 \, \frac{\Delta p2}{p2}$$

$$y\beta1 = y1 - Dy1 \, \frac{\Delta p1}{p1}$$

$$y\beta2 = y2 - Dy2 \, \frac{\Delta p2}{p2}$$

$\Delta p1$, $\Delta p2$, $\Delta s1$, $\Delta s2$ remain unchanged,

$\Delta p1 = \Delta p1$
$\Delta p2 = \Delta p2$
$\Delta s1 = \Delta s1$
$\Delta s2 = \Delta s2$

The above three sets of equations give a change of variables from,
$xp\beta1$, $xp\beta2$, $yp\beta1$, $yp\beta2$, $x\beta1$, $y\beta1$, $x\beta2$, $y\beta2$, $\Delta p1/p1$, $\Delta p2/p2$, $\Delta s1$, $\Delta s2$,
to
θx, θy, ξx, ξy, $\Delta p1/p1$, $\Delta p2/p2$, $x1$, $x2$, $y1$, $y2$, $\Delta s1$, $\Delta s2$.

The Jacobian of this transformation is 1.

$$\text{Abs}\left[\text{Det}\left[\begin{pmatrix}
\frac{1}{2} & 0 & 1 & 0 & 0 & 0 & 0 & 0 & -Dpx1 & 0 & 0 & 0 \\
\frac{-1}{2} & 0 & 1 & 0 & 0 & 0 & 0 & 0 & 0 & -Dpx2 & 0 & 0 \\
0 & \frac{1}{2} & 0 & 1 & 0 & 0 & 0 & 0 & -Dpy1 & 0 & 0 & 0 \\
0 & \frac{-1}{2} & 0 & 1 & 0 & 0 & 0 & 0 & 0 & -Dpy2 & 0 & 0 \\
0 & 0 & 0 & 0 & 1 & 0 & 0 & 0 & -Dx1 & 0 & 0 & 0 \\
0 & 0 & 0 & 0 & 0 & 1 & 0 & 0 & -Dy1 & 0 & 0 & 0 \\
0 & 0 & 0 & 0 & 0 & 0 & 1 & 0 & 0 & -Dx2 & 0 & 0 \\
0 & 0 & 0 & 0 & 0 & 0 & 0 & 1 & 0 & Dy2 & 0 & 0 \\
0 & 0 & 0 & 0 & 0 & 0 & 0 & 0 & 1 & 0 & 0 & 0 \\
0 & 0 & 0 & 0 & 0 & 0 & 0 & 0 & 0 & 1 & 0 & 0 \\
0 & 0 & 0 & 0 & 0 & 0 & 0 & 0 & 0 & 0 & 1 & 0 \\
0 & 0 & 0 & 0 & 0 & 0 & 0 & 0 & 0 & 0 & 0 & 1
\end{pmatrix}\right]\right] = 1$$

The volume elemental is,

dV* = dx1 dx2 dy1 dy2 dξx dξy dθx dθy

$$d\left(\frac{\Delta p1}{p1}\right) \ d\left(\frac{\Delta p2}{p2}\right) \ d\Delta s1 \ d\Delta s2$$

The density functions are broken down into transverse and longitudinal parts,

$$\rho_1[\mathbf{x1}, \xi_x, \Delta_{p1}, \theta_x, \mathbf{y1}, \xi_y, \Delta_{p1}, \theta_y, \Delta s1, \Delta p1] =$$
$$\rho_{s1}[\Delta s1] \ \rho_{p1}[\Delta p_1] \ \rho_{x1}[\mathbf{x1}, \xi_x, \Delta_{p1}, \theta_x] \ \rho_{y1}[\mathbf{y1}, \xi_y, \Delta_{p1}, \theta_y]$$

$$\rho_{x1}[\mathbf{x1}, \xi_x, \Delta_{p1}, \theta_x] =$$
$$\frac{1}{2\pi \ \epsilon x1} \ \mathbf{Exp}\left[-\frac{\left(x1 - Dx1 \ \frac{\Delta p1}{p1}\right)^2 + \left(\alpha x1 \ \left(x1 - Dx1 \ \frac{\Delta p1}{p1}\right) + \beta x1 \ \left(\frac{\theta x}{2} + \xi x - Dpx1 \ \frac{\Delta p1}{p1}\right)\right)^2}{2 \ \sigma x\beta1^2}\right]$$

$$\rho_{y1}[\mathbf{y1}, \xi_y, \Delta_{p1}, \theta_y] =$$
$$\frac{1}{2\pi \ \epsilon y1} \ \mathbf{Exp}\left[-\frac{\left(y1 - Dy1 \ \frac{\Delta p1}{p1}\right)^2 + \left(\alpha y1 \ \left(y1 - Dy1 \ \frac{\Delta p1}{p1}\right) + \beta y1 \ \left(\frac{\theta y}{2} + \xi y - Dpy1 \ \frac{\Delta p1}{p1}\right)\right)^2}{2 \ \sigma y\beta1^2}\right]$$

$$\rho_{p1}[\Delta p1] = \frac{1}{\sqrt{2\pi} \ p1 \ \sigma p1} \ \mathbf{Exp}\left[-\frac{1}{2 \ \sigma p1^2} \ \frac{\Delta p1^2}{p1^2}\right]$$

$$\rho_{s1}[\Delta s1] = \frac{1}{\sqrt{2\pi} \ \sigma s1} \ \mathbf{Exp}\left[-\frac{\Delta s1^2}{2 \ \sigma s1^2}\right]$$

$$\rho_2[\mathbf{x2}, \xi_x, \Delta_{p2}, \theta_x, \mathbf{y2}, \xi_y, \Delta_{p2}, \theta_y, \Delta s2, \Delta p2] =$$
$$\rho_{s2}[\Delta s2] \ \rho_{p2}[\Delta p_2] \ \rho_{x2}[\mathbf{x2}, \xi_x, \Delta_{p2}, \theta_x] \ \rho_{y2}[\mathbf{y2}, \xi_y, \Delta_{p2}, \theta_y]$$

$$\rho_{x2}[\mathbf{x2}, \xi_x, \Delta_{p2}, \theta_x] =$$
$$\frac{1}{2\pi \ \epsilon x2} \ \mathbf{Exp}\left[-\frac{\left(x2 - Dx2 \ \frac{\Delta p2}{p2}\right)^2 + \left(\alpha x2 \ \left(x2 - Dx2 \ \frac{\Delta p2}{p2}\right) + \beta x2 \ \left(-\frac{\theta x}{2} + \xi x - Dpx2 \ \frac{\Delta p2}{p2}\right)\right)^2}{2 \ \sigma x\beta2^2}\right]$$

$$\rho_{y2}[\mathbf{y2}, \xi_y, \Delta_{p2}, \theta_y] =$$
$$\frac{1}{2\pi \ \epsilon y2} \ \mathbf{Exp}\left[-\frac{\left(y2 - Dy2 \ \frac{\Delta p2}{p2}\right)^2 + \left(\alpha y2 \ \left(y2 - Dy2 \ \frac{\Delta p2}{p2}\right) + \beta y2 \ \left(-\frac{\theta y}{2} + \xi y - Dpy2 \ \frac{\Delta p2}{p2}\right)\right)^2}{2 \ \sigma y\beta2^2}\right]$$

$$\rho_{p2}[\Delta p2] = \frac{1}{\sqrt{2\pi} \ p2 \ \sigma p2} \ \mathbf{Exp}\left[-\frac{1}{2 \ \sigma p2^2} \ \frac{\Delta p2^2}{p2^2}\right]$$

$$\rho_{s2}[\Delta s1] = \frac{1}{\sqrt{2\pi} \ \sigma s2} \ \mathbf{Exp}\left[-\frac{\Delta s1^2}{2 \ \sigma s2^2}\right]$$

The velocity and cross-section are dependent on only the angle between the scattering particles and so can be written as,

$$\Delta\mathbf{v}[\theta_x, \theta_y] = \Delta\mathbf{v}\left[\overrightarrow{p_1}, \overrightarrow{p_2}\right]$$
$$\sigma[\theta_x, \theta_y] = \sigma\left[\overrightarrow{p_1}, \overrightarrow{p_2}\right]$$

We require that two colliding particles have the same spatial coordinates

$x := x1 = x2$

$y := y1 = y2$

$\Delta s := \Delta s1 = \Delta s2$

These three constraints are met by inserting delta functions,

$R = \int \rho_1[x1, \xi_x, \Delta_{p1}, \theta_x, y1, \xi_y, \Delta_{p1}, \theta_y, \Delta s1, \Delta p1]$

$\rho_2[x2, \xi_x, \Delta_{p2}, \theta_x, y2, \xi_y, \Delta_{p2}, \theta_y, \Delta s2, \Delta p2]$

$\Delta v[\theta_x, \theta_y] \; \sigma[\theta_x, \theta_y] \; \delta[x1-x2] \; \delta[y1-y2]$

$\delta[\Delta s1-\Delta s1] \; dx1 \; dx2 \; dy1 \; dy2 \; d\xi_x \; d\xi_y \; d\theta x \; d\theta y$

$$d\left(\frac{\Delta p1}{p1}\right) \; d\left(\frac{\Delta p2}{p2}\right) \; d\Delta s1 \; d\Delta s2$$

$= \int \rho_1[x, \xi_x, \Delta_{p1}, \theta_x, y, \xi_y, \Delta_{p1}, \theta_y, \Delta s, \Delta p1]$

$\rho_2[x, \xi_x, \Delta_{p2}, \theta_x, y, \xi_y, \Delta_{p2}, \theta_y, \Delta s, \Delta p2]$

$\Delta v[\theta_x, \theta_y] \; \sigma[\theta_x, \theta_y] \; dx \; dy \; d\xi_x \; d\xi_y \; d\theta x \; d\theta y$

$$d\left(\frac{\Delta p1}{p1}\right) \; d\left(\frac{\Delta p2}{p2}\right) \; d\Delta s$$

Next the density functions are arranged to simplify integration,

$R = \int \rho_{s1}[\Delta s] \; \rho_{s2}[\Delta s] \; d\Delta s \; \times \; \int\int \Delta v[\theta_x, \theta_y] \; \sigma[\theta_x, \theta_y] \times$

$\qquad \int\int \rho_{p1}[\Delta p_1] \; \rho_{p2}[\Delta p_2]$

$\left[\; \int\int \rho_{x1}[x, \xi_x, \Delta p_1, \theta_x] \; \rho_{x2}[x, \xi_x, \Delta p_2, \theta_x] \; dx \; d\xi_x \; \right]$

$\left[\; \int\int \rho_{y1}[y, \xi_y, \Delta p_1, \theta_y] \; \rho_{y2}[y, \xi_y, \Delta p_2, \theta_y] \; dy \; d\xi_y \right]$

$d\left(\frac{\Delta p_1}{p1}\right) \; d\left(\frac{\Delta p_2}{p2}\right) \; d\theta_x \; d\theta_y$

The two inner transverse integrals,

$\int\int \rho_{x1}[x, \xi_x, \Delta p_1, \theta_x] \; \rho_{x2}[x, \xi_x, \Delta p_2, \theta_x] \; dx \; d\xi_x$

$\int\int \rho_{y1}[y, \xi_y, \Delta p_1, \theta_y] \; \rho_{y2}[y, \xi_y, \Delta p_2, \theta_y] \; dy \; d\xi_y$

are evaluated first.

These two integrals are symmetric. Only one needs to be evaluated, and the other can be obtained by transcribing y for x. The integral we will be evaluating is,

$$\iint \rho_{x1}[\mathbf{x}, \zeta_x, \Delta p_1, \theta_x] \, \rho_{x2}[\mathbf{x}, \zeta_x, \Delta p_2, \theta_x] \, d\mathbf{x} \, d\zeta_x$$

$$= \frac{1}{4\,\pi^2\,\epsilon x1\,\epsilon x2} \int$$

$$\int \mathbf{Exp}\left[-\frac{\left(x - Dx1\,\frac{\Delta p1}{p1}\right)^2 + \left(\alpha x1\,\left(x - Dx1\,\frac{\Delta p1}{p1}\right) + \beta x1\,\left(\frac{\theta x}{2} + \zeta x - Dpx1\,\frac{\Delta p1}{p1}\right)\right)^2}{2\,\sigma x \beta 1^2}\right.$$

$$\left. -\frac{\left(x - Dx2\,\frac{\Delta p2}{p2}\right)^2 + \left(\alpha x2\,\left(x - Dx2\,\frac{\Delta p2}{p2}\right) + \beta x2\,\left(-\frac{\theta x}{2} + \zeta x - Dpx2\,\frac{\Delta p2}{p2}\right)\right)^2}{2\,\sigma x \beta 2^2}\right]$$

$$d\mathbf{x}\,d\zeta_\mathbf{x}$$

where both variables are evaluated from $-\infty$ to $+\infty$.
The integral over x is of the form,

$$\int \mathbf{Exp}\left[a_x\,x^2 + b_x\,x + c_x\right]\,d\mathbf{x}$$

This integral has the solution,

$$\sqrt{\frac{\pi}{-ax}}\,\mathbf{Exp}\left[-\frac{bx^2}{4\,ax} + cx\right]$$

The coefficients a_x, b_x, and c_x are obtained by setting the argument of the exponential equal to $a_x\,x^2 + b_x\,x + c_x$ and comparing coefficients of like powers.

$$a_x\,x^2 + b_x\,x + c_x =$$

$$-\frac{\left(x - D_{x1}\,\frac{\Delta p1}{p1}\right)^2 + \left(\alpha_{x1}\,\left(x - D_{x1}\,\frac{\Delta p1}{p1}\right) + \beta_{x1}\,\left(\frac{\theta_x}{2} + \zeta_x - D_{x1}'\,\frac{\Delta p1}{p1}\right)\right)^2}{2\,\sigma_{x\beta 1}^2}$$

$$-\frac{\left(x - D_{x2}\,\frac{\Delta p2}{p2}\right)^2 + \left(\alpha_{x2}\,\left(x - D_{x2}\,\frac{\Delta p2}{p2}\right) + \beta_{x2}\,\left(-\frac{\theta_x}{2} + \zeta_x - D_{x2}'\,\frac{\Delta p2}{p2}\right)\right)^2}{2\,\sigma_{x\beta 2}^2}$$

This yields,

$$a_x = -\frac{1}{2\ \sigma x \beta 1^2} - \frac{\alpha x 1^2}{2\ \sigma x \beta 1^2} - \frac{1}{2\ \sigma x \beta 2^2} - \frac{\alpha x 2^2}{2\ \sigma x \beta 2^2}$$

$$b_x = \frac{Dx1\ \Delta p1}{p1\ \sigma x \beta 1^2} + \frac{Dx1\ \alpha x 1^2\ \Delta p1}{p1\ \sigma x \beta 1^2}$$

$$-\frac{\alpha x 1\ \beta x 1\ \left(-\frac{Dpx1\ \Delta p1}{p1} + \zeta x + \frac{\theta x}{2}\right)}{\sigma x \beta 1^2} - \frac{\alpha x 2\ \beta x 2\ \left(-\frac{Dpx2\ \Delta p2}{p2} + \zeta x - \frac{\theta x}{2}\right)}{\sigma x \beta 2^2}$$

$$+\frac{Dx2\ \Delta p2}{p2\ \sigma x \beta 2^2} + \frac{Dx2\ \alpha x 2^2\ \Delta p2}{p2\ \sigma x \beta 2^2}$$

$$c_x = -\frac{Dx1^2\ \Delta p1^2}{2\ p1^2\ \sigma x \beta 1^2} - \frac{Dx1^2\ \alpha x 1^2\ \Delta p1^2}{2\ p1^2\ \sigma x \beta 1^2}$$

$$+\frac{Dx1\ \alpha x 1\ \beta x 1\ \Delta p1\ \left(-\frac{Dpx1\ \Delta p1}{p1} + \zeta x + \frac{\theta x}{2}\right)}{p1\ \sigma x \beta 1^2} + \frac{Dx2\ \alpha x 2\ \beta x 2\ \Delta p2\ \left(-\frac{Dpx2\ \Delta p2}{p2} + \zeta x - \frac{\theta x}{2}\right)}{p2\ \sigma x \beta 2^2}$$

$$-\frac{Dx2^2\ \Delta p2^2}{2\ p2^2\ \sigma x \beta 2^2} - \frac{Dx2^2\ \alpha x 2^2\ \Delta p2^2}{2\ p2^2\ \sigma x \beta 2^2}$$

$$-\frac{\beta x 1^2\ \left(-\frac{Dpx1\ \Delta p1}{p1} + \zeta x + \frac{\theta x}{2}\right)^2}{2\ \sigma x \beta 1^2} - \frac{\beta x 2^2\ \left(-\frac{Dpx2\ \Delta p2}{p2} + \zeta x - \frac{\theta x}{2}\right)^2}{2\ \sigma x \beta 2^2}$$

These cumbersome coefficients can be simplified by using $\beta_{x1}\ \gamma_{x1} = 1 + \alpha_{x1}^2$ and defining the quantities below.
The y-dimension counterparts are obtained by transcribing y for x.

$\gamma\gamma px = \frac{\gamma x1}{\epsilon x1} + \frac{\gamma x2}{\epsilon x2};$

$\alpha\alpha px = \frac{\alpha x1}{\epsilon x1} + \frac{\alpha x2}{\epsilon x2};$

$\alpha\alpha mx = \frac{\alpha x1}{\epsilon x1} - \frac{\alpha x2}{\epsilon x2};$

`Dtwx1=`α`x1 Dx1+`β`x1 Dpx1;`

`Dhatx1 =Dx1 `γ`x1+`α`x1 Dpx1;`

`Djx1 = Dpx1 Dtwx1+Dhatx1 Dx1;`

`Dtwx2=`α`x2 Dx2+`β`x2 Dpx2;`

`Dhatx2 =Dx2 `γ`x2+`α`x2 Dpx2;`

`Djx2 = Dpx2 Dtwx2+Dhatx2 Dx2;`

$\gamma\gamma py = \frac{\gamma y1}{\epsilon y1} + \frac{\gamma y2}{\epsilon y2};$

$\alpha\alpha py = \frac{\alpha y1}{\epsilon y1} + \frac{\alpha y2}{\epsilon y2};$

$\alpha\alpha my = \frac{\alpha y1}{\epsilon y1} - \frac{\alpha y2}{\epsilon y2};$

`Dtwy1=`α`y1 Dy1+`β`y1 Dpy1;`

`Dhaty1 =Dy1 `γ`y1+`α`y1 Dpy1;`

`Djy1 = Dpy1 Dtwy1+Dhaty1 Dy1;`

`Dtwy2=`α`y2 Dy2+`β`y2 Dpy2;`

`Dhaty2 =Dy2 `γ`y2+`α`y2 Dpy2;`

`Djy2 = Dpy2 Dtwy2+Dhaty2 Dy2;`

`giving,`

$ax = -\frac{1}{2}\gamma\gamma px$

$bx = \frac{Dhatx1}{\epsilon x1}\left(\frac{\Delta p1}{p1}\right) + \frac{Dhatx2}{\epsilon x2}\left(\frac{\Delta p2}{p2}\right) - \alpha\alpha px\ \zeta x - \alpha\alpha mx\ \frac{\theta x}{2}$

$cx = -\frac{Djx1}{2\,\epsilon x1}\left(\frac{\Delta p1}{p1}\right)^2 - \frac{Djx2}{2\,\epsilon x2}\left(\frac{\Delta p2}{p2}\right)^2$

$\quad + \frac{Dtwx1}{\epsilon x1}\left(\zeta x + \frac{\theta x}{2}\right)\left(\frac{\Delta p1}{p1}\right) + \frac{Dtwx2}{\epsilon x2}\left(\zeta x - \frac{\theta x}{2}\right)\left(\frac{\Delta p2}{p2}\right)$

$\quad - \frac{\beta x1}{2\,\epsilon x1}\left(\zeta x + \frac{\theta x}{2}\right)^2 - \frac{\beta x2}{2\,\epsilon x2}\left(\zeta x - \frac{\theta x}{2}\right)^2$

$$ay = -\frac{1}{2} \gamma\gamma py$$

$$by = \frac{Dhaty1}{\epsilon y1}\left(\frac{\Delta p1}{p1}\right) + \frac{Dhaty2}{\epsilon y2}\left(\frac{\Delta p2}{p2}\right) - \alpha\alpha py \ \zeta y - \alpha\alpha my \ \frac{\theta y}{2}$$

$$cy = -\frac{Djy1}{2\,\epsilon y1}\left(\frac{\Delta p1}{p1}\right)^2 - \frac{Djy2}{2\,\epsilon y2}\left(\frac{\Delta p2}{p2}\right)^2$$

$$+\frac{Dtwy1}{\epsilon y1}\left(\zeta y+\frac{\theta y}{2}\right)\left(\frac{\Delta p1}{p1}\right) + \frac{Dtwy2}{\epsilon y2}\left(\zeta y-\frac{\theta y}{2}\right)\left(\frac{\Delta p2}{p2}\right)$$

$$-\frac{\beta y1}{2\,\epsilon y1}\left(\zeta y+\frac{\theta y}{2}\right)^2 - \frac{\beta y2}{2\,\epsilon y2}\left(\zeta y-\frac{\theta y}{2}\right)^2$$

The integral now looks like,

$$\frac{1}{4\,\pi^2\ \epsilon_{x1}\,\epsilon_{x2}}\ \sqrt{\frac{\pi}{-a_x}}\ \int Exp\left[-\frac{b_x{}^2}{4\ a_x}+c_x\right]\,d\zeta x$$

Similar to before, the argument of the exponential is a quadratic. Three new coefficients d_x, e_x, and f_x are obtained from,

$$d_x\ \zeta_x{}^2 + e_x\ \zeta_x + f_x = -\frac{b_x{}^2}{4\ a_x}+c_x$$

And we have,

$$\frac{1}{4\,\pi^2\ \epsilon_{x1}\,\epsilon_{x2}}\ \sqrt{\frac{\pi}{-a_x}}\ \int Exp\left[d_x\ \zeta_x{}^2 + e_x\ \zeta_x + f_x\right]\,d\zeta x$$

which yields,

$$\frac{1}{4\,\pi^2\ \epsilon x1\ \epsilon x2}\ \sqrt{\frac{\pi^2}{(-ax)\ (-dx)}}\ Exp\left[-\frac{ex^2}{4\ dx}+fx\right].$$

The new coefficients d_x, e_x, and f_x are simplified by introducing the following quantities. a_y, b_y, c_y, d_y, e_y, and f_y are obtained by replacing all x with y in the a_x, b_x, c_x, d_x, e_x, and f_x coefficients.

$$\beta\beta\text{px} = \frac{\beta\text{x1}}{\epsilon\text{x1}} + \frac{\beta\text{x2}}{\epsilon\text{x2}} ;$$

$$\beta\beta\text{mx} = \frac{\beta\text{x1}}{\epsilon\text{x1}} - \frac{\beta\text{x2}}{\epsilon\text{x2}} ;$$

$$\Gamma\text{Apx} = \beta\beta\text{px} - \frac{\alpha\alpha\text{px}^2}{\gamma\gamma\text{px}} ;$$

$$\Gamma\text{Amx} = \beta\beta\text{px} - \frac{\alpha\alpha\text{mx}^2}{\gamma\gamma\text{px}} ;$$

$$\Gamma\text{Bx} = \beta\beta\text{mx} - \frac{\alpha\alpha\text{mx} \; \alpha\alpha\text{px}}{\gamma\gamma\text{px}} ;$$

$$\Pi\text{px1} = \text{Dtwx1} - \frac{\text{Dhatx1} \; \alpha\alpha\text{px}}{\gamma\gamma\text{px}} ;$$

$$\Pi\text{px2} = \text{Dtwx2} - \frac{\text{Dhatx2} \; \alpha\alpha\text{px}}{\gamma\gamma\text{px}} ;$$

$$\Pi\text{mx1} = \text{Dtwx1} - \frac{\text{Dhatx1} \; \alpha\alpha\text{mx}}{\gamma\gamma\text{px}} ;$$

$$\Pi\text{mx2} = \text{Dtwx2} + \frac{\text{Dhatx2} \; \alpha\alpha\text{mx}}{\gamma\gamma\text{px}} ;$$

$$\text{DJx1} := \frac{\text{Dhatx1}^2}{\gamma\gamma\text{px} \; \epsilon\text{x1}} - \text{Djx1} ;$$

$$\text{DJx2} := \frac{\text{Dhatx2}^2}{\gamma\gamma\text{px} \; \epsilon\text{x2}} - \text{Djx2} ;$$

$$\beta\beta\text{py} = \frac{\beta\text{y1}}{\epsilon\text{y1}} + \frac{\beta\text{y2}}{\epsilon\text{y2}} ;$$

$$\beta\beta\text{my} = \frac{\beta\text{y1}}{\epsilon\text{y1}} - \frac{\beta\text{y2}}{\epsilon\text{y2}} ;$$

$$\Gamma\text{Apy} = \beta\beta\text{py} - \frac{\alpha\alpha\text{py}^2}{\gamma\gamma\text{py}} ;$$

$$\Gamma\text{Amy} = \beta\beta\text{py} - \frac{\alpha\alpha\text{my}^2}{\gamma\gamma\text{py}} ;$$

$$\Gamma\text{By} = \beta\beta\text{my} - \frac{\alpha\alpha\text{my} \; \alpha\alpha\text{py}}{\gamma\gamma\text{py}} ;$$

$$\Pi\text{py1} = \text{Dtwy1} - \frac{\text{Dhaty1} \; \alpha\alpha\text{py}}{\gamma\gamma\text{py}} ;$$

$$\Pi\text{py2} = \text{Dtwy2} - \frac{\text{Dhaty2} \; \alpha\alpha\text{py}}{\gamma\gamma\text{py}} ;$$

$$\Pi\text{my1} = \text{Dtwy1} - \frac{\text{Dhaty1} \; \alpha\alpha\text{my}}{\gamma\gamma\text{py}} ;$$

$$\Pi\text{my2} = \text{Dtwy2} + \frac{\text{Dhaty2} \; \alpha\alpha\text{my}}{\gamma\gamma\text{py}} ;$$

$$\text{DJy1} := \frac{\text{Dhaty1}^2}{\gamma\gamma\text{py} \; \epsilon\text{y1}} - \text{Djy1} ;$$

$$\text{DJy2} := \frac{\text{Dhaty2}^2}{\gamma\gamma\text{py} \; \epsilon\text{y2}} - \text{Djy2} ;$$

and are written as,

$$\mathbf{dx} \;=\; -\tfrac{1}{2}\,\Gamma\mathbf{Apx}$$

$$\mathbf{ex} \;=\; \frac{\Pi\mathbf{px1}}{\epsilon\mathbf{x1}}\left(\frac{\Delta\mathbf{p1}}{\mathbf{p1}}\right)+\frac{\Pi\mathbf{px2}}{\epsilon\mathbf{x2}}\left(\frac{\Delta\mathbf{p2}}{\mathbf{p2}}\right)-\Gamma\mathbf{Bx}\,\frac{\theta\mathbf{x}}{2}$$

$$\mathbf{fx} \;=\; \frac{\mathbf{DJx1}}{2\,\epsilon\mathbf{x1}}\left(\frac{\Delta\mathbf{p1}}{\mathbf{p1}}\right)^{2}+\frac{\mathbf{DJx2}}{2\,\epsilon\mathbf{x2}}\left(\frac{\Delta\mathbf{p2}}{\mathbf{p2}}\right)^{2}$$

$$+\frac{\Pi\mathbf{mx1}}{\epsilon\mathbf{x1}}\left(\frac{\Delta\mathbf{p1}}{\mathbf{p1}}\right)\frac{\theta\mathbf{x}}{2}-\frac{\Pi\mathbf{mx2}}{\epsilon\mathbf{x2}}\left(\frac{\Delta\mathbf{p2}}{\mathbf{p2}}\right)\frac{\theta\mathbf{x}}{2}$$

$$+\frac{\mathbf{Dhatx1\;Dhatx2}}{\gamma\gamma\mathbf{px}\;\epsilon\mathbf{x1}\;\epsilon\mathbf{x2}}\left(\frac{\Delta\mathbf{p1}}{\mathbf{p1}}\right)\left(\frac{\Delta\mathbf{p2}}{\mathbf{p2}}\right)-\frac{\Gamma\mathbf{Amx}}{2}\,\frac{\theta\mathbf{x}^{2}}{4}$$

$$\mathbf{dy} \;=\; -\tfrac{1}{2}\,\Gamma\mathbf{Apy}$$

$$\mathbf{ey} \;=\; \frac{\Pi\mathbf{py1}}{\epsilon\mathbf{y1}}\left(\frac{\Delta\mathbf{p1}}{\mathbf{p1}}\right)+\frac{\Pi\mathbf{py2}}{\epsilon\mathbf{y2}}\left(\frac{\Delta\mathbf{p2}}{\mathbf{p2}}\right)-\Gamma\mathbf{By}\,\frac{\theta\mathbf{y}}{2}$$

$$\mathbf{fy} \;=\; \frac{\mathbf{DJy1}}{2\,\epsilon\mathbf{y1}}\left(\frac{\Delta\mathbf{p1}}{\mathbf{p1}}\right)^{2}+\frac{\mathbf{DJy2}}{2\,\epsilon\mathbf{y2}}\left(\frac{\Delta\mathbf{p2}}{\mathbf{p2}}\right)^{2}$$

$$+\frac{\Pi\mathbf{my1}}{\epsilon\mathbf{y1}}\left(\frac{\Delta\mathbf{p1}}{\mathbf{p1}}\right)\frac{\theta\mathbf{y}}{2}-\frac{\Pi\mathbf{my2}}{\epsilon\mathbf{y2}}\left(\frac{\Delta\mathbf{p2}}{\mathbf{p2}}\right)\frac{\theta\mathbf{y}}{2}$$

$$+\frac{\mathbf{Dhaty1\;Dhaty2}}{\gamma\gamma\mathbf{py}\;\epsilon\mathbf{y1}\;\epsilon\mathbf{y2}}\left(\frac{\Delta\mathbf{p1}}{\mathbf{p1}}\right)\left(\frac{\Delta\mathbf{p2}}{\mathbf{p2}}\right)-\frac{\Gamma\mathbf{Amy}}{2}\,\frac{\theta\mathbf{y}^{2}}{4}$$

The integral for the rate now looks like,

$$R \;=\; \int\rho_{s1}[\Delta\mathbf{s}]\,\rho_{s2}[\Delta\mathbf{s}]\;\mathrm{d}\Delta\mathbf{s}\;\times$$

$$\iint\Delta\mathbf{v}[\theta_{x},\theta_{y}]\,\sigma[\theta_{x},\theta_{y}]$$

$$\iint\rho_{\mathbf{p1}}\left[\frac{\Delta\mathbf{p_{1}}}{\mathbf{p1}}\right]\rho_{\mathbf{p2}}\left[\frac{\Delta\mathbf{p_{2}}}{\mathbf{p1}}\right]\left[\;\frac{1}{4\,\pi^{2}\,\epsilon\mathbf{x1}\,\epsilon\mathbf{x2}}\sqrt{\frac{\pi^{2}}{(-\mathbf{ax})\,(-\mathbf{dx})}}\;\mathbf{Exp}\left[-\frac{\mathbf{ex}^{2}}{4\,\mathbf{dx}}+\mathbf{fx}\right]\;\right]$$

$$\left[\;\frac{1}{4\,\pi^{2}\,\epsilon\mathbf{y1}\,\epsilon\mathbf{y2}}\sqrt{\frac{\pi^{2}}{(-\mathbf{ay})\,(-\mathbf{dy})}}\;\mathbf{Exp}\left[-\frac{\mathbf{ey}^{2}}{4\,\mathbf{dy}}+\mathbf{fy}\right]\right]\;d\left(\frac{\Delta\mathbf{p_{1}}}{\mathbf{p1}}\right)d\left(\frac{\Delta\mathbf{p_{2}}}{\mathbf{p2}}\right)\mathrm{d}\theta_{x}\,\mathrm{d}\theta_{y}$$

$$=\;\frac{1}{32\,\pi^{5}\,\epsilon\mathbf{x1}\,\epsilon\mathbf{x2}\,\epsilon\mathbf{y1}\,\epsilon\mathbf{y2}\,\mathbf{p1}\,\sigma\mathbf{p1}\,\mathbf{p2}\,\sigma\mathbf{p2}}\sqrt{\frac{\pi^{2}\,\pi^{2}}{\mathbf{Abs}[(\mathbf{ax})\,(\mathbf{dx})\,(\mathbf{ay})\,(\mathbf{dy})]}}$$

$$\int\rho_{s1}[\Delta\mathbf{s}]\,\rho_{s2}[\Delta\mathbf{s}]\;\mathrm{d}\Delta\mathbf{s}$$

$$\iint\Delta\mathbf{v}[\theta_{x},\theta_{y}]\,\sigma[\theta_{x},\theta_{y}]$$

$$\iint\mathbf{Exp}\left[-\frac{1}{2\,\sigma\mathbf{p1}^{2}}\frac{\Delta\mathbf{p1}^{2}}{\mathbf{p1}^{2}}-\frac{1}{2\,\sigma\mathbf{p2}^{2}}\frac{\Delta\mathbf{p2}^{2}}{\mathbf{p2}^{2}}-\frac{\mathbf{ex}^{2}}{4\,\mathbf{dx}}+\mathbf{fx}-\frac{\mathbf{ey}^{2}}{4\,\mathbf{dy}}+\mathbf{fy}\right]$$

$$d\left(\frac{\Delta\mathbf{p_{1}}}{\mathbf{p1}}\right)d\left(\frac{\Delta\mathbf{p_{2}}}{\mathbf{p2}}\right)\mathrm{d}\theta_{x}\,\mathrm{d}\theta_{y}$$

The next integration is over Δp1 and Δp2,

$$\iint \text{Exp}\left[-\frac{1}{2\,\sigma_{p1}^2}\frac{\Delta p_1{}^2}{p_1{}^2}-\frac{1}{2\,\sigma_{p2}^2}\frac{\Delta p_2{}^2}{p_2{}^2}-\frac{e_x{}^2}{4\,d_x}+f_x-\frac{e_y{}^2}{4\,d_y}+f_y\right]p_1\,p_2\,\,d\!\left(\frac{\Delta p_1}{p_1}\right)d\!\left(\frac{\Delta p_2}{p_2}\right)$$

The argument of the exponential is of the form,

$$g_{p1}\left(\frac{\Delta p_1}{p_1}\right)^2+g_{p2}\left(\frac{\Delta p_2}{p_2}\right)^2+h_{p1}\left(\frac{\Delta p_1}{p_1}\right)+h_{p2}\left(\frac{\Delta p_2}{p_1}\right)+i\,\left(\frac{\Delta p_1}{p_1}\right)\left(\frac{\Delta p_2}{p_2}\right)+j$$

The coeffficients are found by comparing like terms,

$$g_{p1}\left(\frac{\Delta p_1}{p_1}\right)^2+g_{p2}\left(\frac{\Delta p_2}{p_2}\right)^2+h_{p1}\left(\frac{\Delta p_1}{p_1}\right)+h_{p2}\left(\frac{\Delta p_2}{p_2}\right)+i\,\left(\frac{\Delta p_1}{p_1}\right)\left(\frac{\Delta p_2}{p_1}\right)+j\,=$$
$$-\frac{1}{2\,\sigma_{p1}^2}\frac{\Delta p_1{}^2}{p_1{}^2}-\frac{1}{2\,\sigma_{p2}^2}\frac{\Delta p_2{}^2}{p_2{}^2}-\frac{e_x{}^2}{4\,d_x}+f_x-\frac{e_y{}^2}{4\,d_y}+f_y$$

The $d\Delta p_1\,d\Delta p_2$ integral now looks like,

$$\iint \text{Exp}\left[gp1\left(\frac{\Delta p1}{p1}\right)^2+gp2\left(\frac{\Delta p2}{p2}\right)^2+hp1\left(\frac{\Delta p1}{p1}\right)+hp2\left(\frac{\Delta p2}{p2}\right)+i\,\left(\frac{\Delta p1}{p1}\right)\left(\frac{\Delta p2}{p2}\right)+j\right]$$
$$p1\,p2\,\,d\!\left(\frac{\Delta p1}{p1}\right)d\!\left(\frac{\Delta p2}{p2}\right)$$

which has the solution,

$$\frac{2\,\pi\,p1\,p2}{\sqrt{4\,gp1\,gp2-i^2}}\,\text{Exp}\left[-\frac{gp2\,hp1^2+gp1\,hp2^2-hp1\,hp2\,i-4\,gp1\,gp2\,j+i^2\,j}{4\,gp1\,gp2-i^2}\right]$$

The new $g_{p1}, g_{p2}, h_{p1}, h_{p2}, i, j$ terms are simplified by introducing the following quantities,

$$\Xi1 := \frac{DJx1}{\epsilon x1} + \frac{DJy1}{\epsilon y1} + \frac{\Pi px1^2}{\Gamma Apx \ \epsilon x1^2} + \frac{\Pi py1^2}{\Gamma Apy \ \epsilon y1^2} - \frac{1}{\sigma p1^2}$$

$$\Xi2 := \frac{DJx2}{\epsilon x2} + \frac{DJy2}{\epsilon y2} + \frac{\Pi px2^2}{\Gamma Apx \ \epsilon x2^2} + \frac{\Pi py2^2}{\Gamma Apy \ \epsilon y2^2} - \frac{1}{\sigma p2^2} \ ;$$

$$\Sigma mx1 = \frac{\Pi mx1}{\epsilon x1} - \frac{\Gamma Bx \ \Pi px1}{\Gamma Apx \ \epsilon x1} \ ;$$

$$\Sigma my1 = \frac{\Pi my1}{\epsilon y1} - \frac{\Gamma By \ \Pi py1}{\Gamma Apy \ \epsilon y1} \ ;$$

$$\Sigma px2 = \frac{\Pi mx2}{\epsilon x2} + \frac{\Gamma Bx \ \Pi px2}{\Gamma Apx \ \epsilon x2} \ ;$$

$$\Sigma py2 = \frac{\Pi my2}{\epsilon y2} + \frac{\Gamma By \ \Pi py2}{\Gamma Apy \ \epsilon y2} \ ;$$

$$\Sigma\Sigma = \frac{Dhatx1 \ Dhatx2}{\gamma\gamma px \ \epsilon x1 \ \epsilon x2} + \frac{Dhaty1 \ Dhaty2}{\gamma\gamma py \ \epsilon y1 \ \epsilon y2} + \frac{\Pi px1 \ \Pi px2}{\Gamma Apx \ \epsilon x1 \ \epsilon x2} + \frac{\Pi py1 \ \Pi py2}{\Gamma Apy \ \epsilon y1 \ \epsilon y2}$$

$$\Sigma\Gamma x = \Gamma Amx - \frac{\Gamma Bx^2}{\Gamma Apx} \ ;$$

$$\Sigma\Gamma y = \Gamma Amy - \frac{\Gamma By^2}{\Gamma Apy} \ ;$$

and so the coefficients for the Δp_1 and Δp_2 integration are,

$$gp1 \ = \ \frac{1}{2} \ \Xi1$$

$$gp2 \ = \ \frac{1}{2} \ \Xi2$$

$$hp1 \ = \ \left(\Sigma mx1 \left(\frac{\theta x}{2} \right) + \Sigma my1 \left(\frac{\theta y}{2} \right) \right)$$

$$hp2 \ = \ - \left(\Sigma px2 \left(\frac{\theta x}{2} \right) + \Sigma py2 \left(\frac{\theta y}{2} \right) \right)$$

$$i \ = \ \Sigma\Sigma$$

$$j \ = \ - \frac{\Sigma\Gamma x}{2} \left(\frac{\theta x}{2} \right)^2 - \frac{\Sigma\Gamma y}{2} \left(\frac{\theta y}{2} \right)^2$$

The integral for the rate, having so far integrated with respect to x, ξ_x, y, ξ_y, Δp_1, and Δp_2, now looks like

$$R = \frac{1}{32 \ \pi^5 \ \epsilon x1 \ \epsilon x2 \ \epsilon y1 \ \epsilon y2 \ p1 \ \sigma p1 \ p2 \ \sigma p2} \sqrt{\frac{\pi^2 \ \pi^2 \ 4 \ \pi^2 \ p1^2 \ p2^2}{Abs\left[(ax) \ (dx) \ (ay) \ (dy) \left(4 \ gp1 \ gp2 - i^2 \right) \right]}}$$

$$\int \rho_{s1} (\Delta s) \ \rho_{s2} (\Delta s) \ d\Delta s \ \int\int \Delta v (\theta x, \theta y) \ \sigma(\theta x, \theta y)$$

$$Exp\left[- \frac{gp2 \ hp1^2 + gp1 \ hp2^2 - hp1 \ hp2 \ i \ - \ 4 \ gp1 \ gp2 \ j + i^2 \ j}{4 \ gp1 \ gp2 - i^2} \right] \ d\theta x \ d\theta y$$

The argument of the exponential is of the form,

$$k\theta x \ \theta x^2 + k\theta y \ \theta y^2 + l \ \theta x \ \theta y = - \frac{gp2 \ hp1^2 + gp1 \ hp2^2 - hp1 \ hp2 \ i \ - \ 4 \ gp1 \ gp2 \ j + i^2 \ j}{4 \ gp1 \ gp2 - i^2}$$

where, as before, $k\theta x$, $k\theta y$, and l are found by comparing like powers.

No additional terms are defined to simplify the $k_{\theta x}$, $k_{\theta y}$, and l coefficients. They are found to be,

$$k\theta x := -\frac{1}{8} \frac{\Xi 2\ \Sigma mx1^2 + \Xi 1\ \Sigma px2^2 + \Xi 1\ \Xi 2\ \Sigma\Gamma x + 2\ \Sigma mx1\ \Sigma px2\ \Sigma\Sigma - \Sigma\Gamma x\ \Sigma\Sigma^2}{\Xi 1\ \Xi 2 - \Sigma\Sigma^2}$$

$$k\theta x := -\frac{1}{8} \frac{\Xi 2\ \Sigma my1^2 + \Xi 1\ \Sigma py2^2 + \Xi 1\ \Xi 2\ \Sigma\Gamma y + 2\ \Sigma my1\ \Sigma py2\ \Sigma\Sigma - \Sigma\Gamma y\ \Sigma\Sigma^2}{\Xi 1\ \Xi 2 - \Sigma\Sigma^2}$$

$$l := -\frac{1}{4} \frac{\Xi 2\ \Sigma mx1\ \Sigma my1 + \Xi 1\ \Sigma px2\ \Sigma py2 + \Sigma my1\ \Sigma px2\ \Sigma\Sigma + \Sigma mx1\ \Sigma py2\ \Sigma\Sigma}{\Xi 1\ \Xi 2 - \Sigma\Sigma^2}$$

At this point we hold off from integrating over θx and θy. The relative velocity and cross-section may depend on those variables. We have,

$$R = \frac{1}{32\ \pi^5\ \epsilon x1\ \epsilon x2\ \epsilon y1\ \epsilon y2\ p1\ \sigma p1\ p2\ \sigma p2} \sqrt{\frac{\pi^2\ \pi^2\ 4\ \pi^2\ p1^2\ p2^2}{Abs\left[(ax)\ (dx)\ (ay)\ (dy)\ \left(4\ gp1\ gp2 - i^2\right)\right]}}$$

$$\int \rho_{s1}(\Delta s)\ \rho_{s2}(\Delta s)\ \mathrm{d}\Delta s \iint \Delta v(\theta_x, \theta_y)\ \sigma(\theta_x, \theta_y)$$

$$\mathrm{Exp}\left[k_{\theta x}\ \theta_x^2 + k_{\theta y}\ \theta_y^2 + l\ \theta_x\ \theta_y\right]\ \mathrm{d}\theta_x\ \mathrm{d}\theta_y$$

The Δs term is easily integraged,

$$\int \rho_{s1}[\Delta s]\ \rho_{s2}[\Delta s]\ \mathrm{d}\Delta s = \int \frac{1}{\sqrt{2\ \pi}\ \sigma_{s1}}\ \mathrm{Exp}\left[-\frac{\Delta s^2}{2\ \sigma_{s1}^2}\right]\ \frac{1}{\sqrt{2\ \pi}\ \sigma_{s2}}\ \mathrm{Exp}\left[-\frac{\Delta s^2}{2\ \sigma_{s2}^2}\right]\ \mathrm{d}\Delta s$$

$$= \frac{1}{2\ \pi\ \sigma_{s1}\ \sigma_{s2}}\ \int \mathrm{Exp}\left[-\frac{\Delta s^2}{2\ \sigma_{s1}^2} - \frac{\Delta s^2}{2\ \sigma_{s2}^2}\right]\ \mathrm{d}\Delta s$$

$$= \frac{1}{2\ \pi\ \sigma_{s1}\ \sigma_{s2}}\ \frac{\sqrt{2\ \pi}}{\sqrt{\frac{1}{\sigma_{s1}^2} + \frac{1}{\sigma_{s2}^2}}}$$

$$= \frac{1}{\sqrt{2\ \pi\left(\sigma s1^2 + \sigma s2^2\right)}}$$

After evaluating the Δs term, the rate becomes,

$$R = \cfrac{1}{32\,\pi^5\,\epsilon x1\,\epsilon x2\,\epsilon y1\,\epsilon y2\,\text{p1}\,\sigma\text{p1}\,\text{p2}\,\sigma\text{p2}}$$

$$\sqrt{\cfrac{\pi^2\,\pi^2\,4\,\pi^2\,\text{p1}^2\,\text{p2}^2}{\text{Abs}\left[(ax)\,(dx)\,(ay)\,(dy)\,\left(4\,\text{gp1}\,\text{gp2}-i^2\right)\,2\,\pi\,\left(\sigma s1^2+\sigma s2^2\right)\right]}}$$

$$\iint \Delta v\left(\theta_x,\theta_y\right)\,\sigma\left(\theta_x,\theta_y\right)\,\text{Exp}\left[k_{\theta x}\,\theta_x{}^2+k_{\theta y}\,\theta_y{}^2+1\,\theta_x\,\theta_y\right]\,d\theta_x\,d\theta_y$$

We now assume that $\Delta v\left(\theta_x,\theta_y\right)$ and $\sigma\left(\theta_x,\theta_y\right)$ depend only on the total angle $\sqrt{\theta_x{}^2+\theta_y{}^2}$ and not on the θ_x and θ_y components separately. We introduce two new variables, ρ and v,

$$\theta_x = \sqrt{\rho}\,\cos v$$
$$\theta_y = \sqrt{\rho}\,\sin v$$

$$d\theta_x\,d\theta_y = \frac{d\rho\,dv}{2}$$

$$\chi = \sqrt{\theta_x{}^2+\theta_y{}^2} = \sqrt{\rho}$$

Giving,

$$R = \cfrac{1}{64\,\pi^5\,\epsilon x1\,\epsilon x2\,\epsilon y1\,\epsilon y2\,\text{p1}\,\sigma\text{p1}\,\text{p2}\,\sigma\text{p2}}$$

$$\sqrt{\cfrac{\pi^2\,\pi^2\,4\,\pi^2\,\text{p1}^2\,\text{p2}^2}{\text{Abs}\left[(ax)\,(dx)\,(ay)\,(dy)\,\left(4\,\text{gp1}\,\text{gp2}-i^2\right)\,2\,\pi\,\left(\sigma s1^2+\sigma s2^2\right)\right]}}$$

$$\int_0^\infty \int_0^{2\,\pi} \Delta v\left[\sqrt{\rho}\right]\,\sigma\left[\sqrt{\rho}\right]$$

$$\text{Exp}\left[\rho\left(k_{\theta x}(\cos v)^2+k_{\theta y}(\sin v)^2+1\,(\cos v\,\sin v)\right)\right]\,dv\,d\rho$$

The integral can be simplified,

$$\int_0^\infty \int_0^{2\,\pi} \Delta v\left[\sqrt{\rho}\right]\,\sigma\left[\sqrt{\rho}\right]\,\text{Exp}\left[\rho\left(k_{\theta x}(\cos v)^2-k_{\theta y}(\cos v)^2\right.\right.$$
$$\left.\left.+k_{\theta y}(\cos v)^2+k_{\theta y}(\sin v)^2+1\,(\cos v\,\sin v)\right)\right]\,dv\,d\rho$$

$$\int_0^\infty \int_0^{2\,\pi} \Delta v\left[\sqrt{\rho}\right]\,\sigma\left[\sqrt{\rho}\right]$$
$$\text{Exp}\left[\rho\left((k_{\theta x}-k_{\theta y})(\cos v)^2+k_{\theta y}+\frac{1}{2}(\sin 2\,v)\right)\right]\,dv\,d\rho$$

$$\int_0^\infty \int_0^{2\pi} \Delta v \left[\sqrt{\rho}\right] \sigma\left[\sqrt{\rho}\right]$$

$$\text{Exp}\left[\rho \left(k_{\theta y+} \left(\frac{k_{\theta x}-k_{\theta y}}{2}\right) (\cos 2v +1) + \frac{1}{2} (\sin 2 v)\right)\right] dv\, d\rho$$

$$\int_0^\infty \int_0^{2\pi} \Delta v \left[\sqrt{\rho}\right] \sigma\left[\sqrt{\rho}\right]$$

$$\text{Exp}\left[\frac{\rho}{2} ((k_{\theta x}+k_{\theta y}) + (k_{\theta x}-k_{\theta y}) \cos 2v + 1 \sin 2 v)\right] dv\, d\rho$$

$$\int_0^\infty \int_0^{2\pi} \Delta v \left[\sqrt{\rho}\right] \sigma\left[\sqrt{\rho}\right] \text{Exp}\left[\frac{\rho}{2} ((k_{\theta x}+k_{\theta y}))\right]$$

$$\text{Exp}\left[\frac{\rho}{2} (1 \sin 2 v + (k_{\theta x}-k_{\theta y}) \cos 2v)\right] dv\, d\rho$$

$$\int_0^\infty \int_0^{2\pi} \Delta v \left[\sqrt{\rho}\right] \sigma\left[\sqrt{\rho}\right] \text{Exp}\left[\frac{\rho}{2} ((k_{\theta x}+k_{\theta y}))\right]$$

$$\text{Exp}\left[\frac{\rho}{2} \left(\sqrt{1^2 + (k_{\theta x}-k_{\theta y})^2} \sin[2 v+\phi]\right)\right] dv\, d\rho$$

$$\int_0^\infty \Delta v \left[\sqrt{\rho}\right] \sigma\left[\sqrt{\rho}\right] \text{Exp}\left[\frac{\rho}{2} ((k_{\theta x}+k_{\theta y}))\right] \int_0^{2\pi}$$

$$\text{Exp}\left[\frac{\rho}{2} \sqrt{1^2 + (k_{\theta x}-k_{\theta y})^2} \cos[2 v+\phi]\right] dv\, d\rho$$

where

$$\phi = \text{arcsin}\left[\frac{k_{\theta x}-k_{\theta y}}{\sqrt{1^2 + (k_{\theta x}-k_{\theta y})^2}}\right] - \frac{\pi}{2}$$

The integration over v can be written as,

$$\int_0^{2\pi} \text{Exp}\left[\frac{\rho}{2} D1 \sin[2 v+\phi]\right] dv,$$

where

$$D1 = \sqrt{1^2 + (k_{\theta x}-k_{\theta y})^2} .$$

The following identity for the modified Bessel function becomes useful,

$$I_0\left(\frac{\rho}{2} D1\right) = \frac{1}{2\pi} \int_0^{2\pi} \text{Exp}\left[\frac{\rho}{2} D1 \cos[2v+\phi]\right] dv.$$

Usng this identity simplifies the integral to,

$$2\pi \int_0^\infty \Delta v \left[\sqrt{\rho}\right] \sigma\left[\sqrt{\rho}\right] \text{Exp}\left[\frac{\rho}{2} ((k_{\theta x}+k_{\theta y}))\right] I_0\left[\frac{\rho}{2} \sqrt{1^2 + (k_{\theta x}-k_{\theta y})^2}\right] d\rho$$

where $\sqrt{\rho} = \chi$ is the angle between the two colliding particles.

The equation for the rate becomes,

$$R = \cfrac{2\,\pi}{64\,\pi^5\;\epsilon x1\;\epsilon x2\;\epsilon y1\;\epsilon y2\;p1\;\sigma p1\;p2\;\sigma p2}$$

$$\sqrt{\cfrac{\pi^2\,\pi^2\;4\,\pi^2\;p1^2\;p2^2}{\mathrm{Abs}\big[\,(ax)\,(dx)\,(ay)\,(dy)\,\big(4\;gp1\;gp2-i^2\big)\,2\,\pi\,\big(\sigma s1^2+\sigma s2^2\big)\big]}}$$

$$\int_0^\infty \Delta v\left[\sqrt{\rho}\,\right]\sigma\left[\sqrt{\rho}\,\right]$$

$$\mathrm{Exp}\left[\tfrac{\rho}{2}\;(k_{\theta x}+k_{\theta y})\right]\;I_0\left[\tfrac{\rho}{2}\;\sqrt{1^2+(k_{\theta x}-k_{\theta y})^2}\,\right]\;d\!\!\!|\rho$$

Simplifying the factors yields,

$$R = \cfrac{1}{16\,\sqrt{2}\;\pi\,\sqrt{\pi}\;\epsilon x1\;\epsilon x2\;\epsilon y1\;\epsilon y2\;\sigma p1\;\sigma p2}$$

$$\sqrt{\cfrac{1}{\mathrm{Abs}\big[\,(ax)\,(dx)\,(ay)\,(dy)\,\big(4\;gp1\;gp2-i^2\big)\,\big(\sigma s1^2+\sigma s2^2\big)\big]}}$$

$$\int_0^\infty \Delta v\left[\sqrt{\rho}\,\right]\sigma\left[\sqrt{\rho}\,\right]$$

$$\mathrm{Exp}\left[\rho\;\tfrac{k_{\theta x}+k_{\theta y}}{2}\right]\;\mathrm{BesselI}\left[0,\rho\;\tfrac{\sqrt{1^2+(k_{\theta x}-k_{\theta y})^2}}{2}\right]\;d\!\!\!|\rho$$

Unless something is known about about the relative velocity Δv and cross-section σ, we are done. The above equation is exact. It gives the rate at which events whose cross-section is σ occur between particles in two overlapping beams at different energy. Generally, the integral must be evaluated numerically. First, we assume that Δv and σ are independent of ρ. This is done to aid double-checking the integration performed above. We pull Δv and σ out of the equation derived by Piwinski, and in the limit that the properties of beam 2 match those of beam 1, our equation should give the same number as Piwinski's equation.

214

We go back to the expression for the rate before ρ and ν were introduced,

$$R = \frac{1}{32 \pi^5 \; \epsilon x1 \; \epsilon x2 \; \epsilon y1 \; \epsilon y2 \; p1 \; \sigma p1 \; p2 \; \sigma p2}$$

$$\sqrt{\frac{\pi^2 \; \pi^2 \; 4 \pi^2 \; p1^2 \; p2^2}{\mathrm{Abs}\left[(ax)\,(dx)\,(ay)\,(dy)\left(4 \; gp1 \; gp2 - i^2\right) 2 \pi \left(\sigma s1^2 + \sigma s2^2\right)\right]}}$$

$$\iint \Delta v[\theta_x, \theta_y] \; \sigma[\theta_x, \theta_y] \; \mathrm{Exp}\left[k_{\theta x} \; \theta_x{}^2 + k_{\theta y} \; \theta_y{}^2 + l \; \theta_x \; \theta_y\right] d\theta_x \, d\theta_y$$

$$= \frac{1}{32 \pi^5 \; \epsilon x1 \; \epsilon x2 \; \epsilon y1 \; \epsilon y2 \; p1 \; \sigma p1 \; p2 \; \sigma p2}$$

$$\sqrt{\frac{\pi^2 \; \pi^2 \; 4 \pi^2 \; p1^2 \; p2^2}{\mathrm{Abs}\left[(ax)\,(dx)\,(ay)\,(dy)\left(4 \; gp1 \; gp2 - i^2\right) 2 \pi \left(\sigma s1^2 + \sigma s2^2\right)\right]}} \; \Delta v \; \sigma$$

$$\iint \mathrm{Exp}\left[k\theta x \; \theta x^2 + k\theta y \; \theta y^2 + l \; \theta x \; \theta y\right] d\theta x \, d\theta y$$

and solve the integral,

$$\iint \mathrm{Exp}\left[k_{\theta x} \; \theta_x{}^2 + k_{\theta y} \; \theta_y{}^2 + l \; \theta_x \; \theta_y\right] d\theta_x \, d\theta_y$$

The solution is,

$$\frac{2 \pi}{\sqrt{4 \; k\theta y \; k\theta x - l^2}}$$

Giving a rate,

$$R = \frac{1}{32 \pi^5 \; \epsilon x1 \; \epsilon x2 \; \epsilon y1 \; \epsilon y2 \; p1 \; \sigma p1 \; p2 \; \sigma p2}$$

$$\sqrt{\left(\frac{\pi^2 \; \pi^2 \; 4 \pi^2 \; p1^2 \; p2^2 \; 4 \pi^2}{\mathrm{Abs}\left[(ax)\,(dx)\,(ay)\,(dy)\left(4 \; gp1 \; gp2 - i^2\right) 2 \pi \left(\sigma s1^2 + \sigma s2^2\right)\left(4 \; k\theta y \; k\theta x - l^2\right)\right]}\right)} \; \Delta v \sigma$$

This can be simplified a bit to yield,

$$R = \left(\frac{1}{8 \sqrt{2} \; \pi \sqrt{\pi} \; \epsilon x1 \; \epsilon x2 \; \epsilon y1 \; \epsilon y2 \; \sigma p1 \; \sigma p2}\right.$$

$$\left.\sqrt{\frac{1}{\mathrm{Abs}\left[(ax)\,(dx)\,(ay)\,(dy)\left(4 \; gp1 \; gp2 - i^2\right)\left(\sigma s1^2 + \sigma s2^2\right)\left(4 \; k\theta y \; k\theta x - l^2\right)\right]}}\right) \; \Delta v \sigma$$

Numbers are plugged in notebook one_beam.nb. The
two equations do indeed agree.The equation for
the velocity is,

$$(*\chi=\sqrt{\theta_x{}^2+\theta_y{}^2}=\sqrt{\rho}\ *)$$

$$\Delta v\left[\sqrt{\rho}\right]:=\sqrt{vj\left[\sqrt{\rho}\right]^2+vl\left[\sqrt{\rho}\right]^2}$$

where

$$vj\left[\sqrt{\rho}\right]:=\frac{\beta1\ \beta2}{2\,p}\ (E1+E2)\ Sin\left[\sqrt{\rho}\right]$$
$$vl\left[\sqrt{\rho}\right]:=\frac{1}{2\,p}\left(\beta2^2\ E2-\beta1^2\ E1+\beta1\ \beta2\,(E1-E2)\ Cos\left[\sqrt{\rho}\right]\right)$$
$$p:=\frac{1}{2}\ Abs\left[\overrightarrow{p1}+\overrightarrow{p2}\right]$$

where E1 and E1 are the energies of beam 1 and beam 2,
and $\beta1$ and $\beta2$ are the relativistic β of beam 1 and beam 2.

The integrand decay's exponentially in ρ, so small angle
approximations on the formulas for the velocity are
justified. Approximating sin and cos yields,

$$vj\left[\sqrt{\rho}\right]:=\frac{\beta1\ \beta2}{2\,p}\ (E1+E2)\ \sqrt{\rho}$$
$$vl\left[\sqrt{\rho}\right]:=\frac{1}{2\,p}\left(\beta2^2\ E2-\beta1^2\ E1+\beta1\ \beta2\,(E1-E2)\right)$$
$$=\frac{1}{2\,p}\ (\beta2-\beta1)\ (\beta2\ E2+\beta1\ E1)$$
$$p:=\frac{1}{2}\ Abs\left[\overrightarrow{p1}+\overrightarrow{p2}\right]$$

Plugging these expressions into $\Delta v\left[\sqrt{\rho}\right]$ yields,

$$\Delta\mathbf{v}\left[\sqrt{\rho}\,\right] :=$$

$$\sqrt{\mathbf{vj}\left[\sqrt{\rho}\,\right]^2 + \mathbf{vl}\left[\sqrt{\rho}\,\right]^2} =$$

$$\sqrt{\left(\left(\frac{1}{2\,p}\,(\beta2 - \beta1)\,(\beta2\ E2 + \beta1\ E1)\right)^2 + \left(\frac{\beta1\ \beta2}{2\,p}\,(E1 + E2)\,\sqrt{\rho}\right)^2\right)}$$

$$= \frac{1}{2\,p}\,\sqrt{(\beta2 - \beta1)^2\,(\beta2\ E2 + \beta1\ E1)^2 + \beta2^2\ \beta1^2\,(E1 + E2)^2\,\rho}$$

$$= \frac{\beta2\ \beta1\ (E1 + E2)}{2\,p}\,\sqrt{\frac{(\beta2 - \beta1)^2\,(\beta2\ E2 + \beta1\ E1)^2}{\beta2^2\ \beta1^2\,(E1 + E2)^2} + \rho}$$

To simplify the expression, introduce two new definitions,

$$\mathbf{c1} = \frac{\beta2\ \beta1\ (E1 + E2)}{2\,p}$$

$$\mathbf{c2} = \frac{(\beta2 - \beta1)^2\,(\beta2\ E2 + \beta1\ E1)^2}{\beta2^2\ \beta1^2\,(E1 + E2)^2}$$

$$\Delta\mathbf{v}\left[\sqrt{\rho}\,\right] := \mathbf{c1}\,\sqrt{\mathbf{c2} + \rho}$$

**Note that in the limit E1 = E2 Piwinski's
expression for the relative velocity is obtained,**

$$\Delta\mathbf{v}\left[\sqrt{\rho}\,\right] := \frac{\beta1^2\ (2\,E1)}{2\left(\frac{1}{2}\,\mathbf{Abs}\left[\vec{p1} + \vec{p2}\right]\right)}\,\sqrt{0 + \rho}$$

$$= \frac{\beta1^2\ (2\,E1)}{\sqrt{\left(p1^2 + p1^2 + 2\,p1^2\ \cos\,\sqrt{\rho}\,\right)}}\,\sqrt{0 + \rho}$$

$$= \frac{2\,\beta1\ p1\ c}{\sqrt{4\ p1}}\,\sqrt{\rho}$$

$$= \beta1\ c\ \sqrt{\rho}$$

**Note that our expression $\sqrt{\rho}$ is the angle between the two
particles, whereas Piwinski's χ is half the angle.
Now plug the expression for the velocity into the
rate equation,**

$$R = \frac{1}{16 \sqrt{2}\ \pi \sqrt{\pi}\ \epsilon x1\ \epsilon x2\ \epsilon y1\ \epsilon y2\ \sigma p1\ \sigma p2}$$

$$\sqrt{\frac{1}{\text{Abs}\left[(ax)\ (dx)\ (ay)\ (dy)\ \left(4\ gp1\ gp2 - i^2\right)\left(\sigma s1^2 + \sigma s2^2\right)\right]}}\ c1$$

$$\int_0^\infty \sigma\left[\sqrt{\rho}\right]\ \sqrt{c2+\rho}\ \text{Exp}\left[\rho\ \frac{k\theta x + k\theta y}{2}\right]\ \text{BesselI}\left[0,\rho\ \frac{\sqrt{1^2 + (k\theta x - k\theta y)^2}}{2}\right] d\!\rho$$

Next we introduce two cross sections. The first, σ1, is the cross-section for scattering events that exchange longitudinal momentum between the two particles, resulting in one particle being kicked above an aperture ΔE₊ or below an aperture ΔE₋. σ1 is independent of ρ. The second, σ2, is the cross-section for scattering events that transfer transverse momentum to longitudinal momentum, kicking one particle above an aperture ΔE₊ or below an aperture ΔE₋. σ2 depends on ρ.

$$\sigma1 = \frac{\pi\ re^2}{\gamma^2}\left(\frac{1}{2}\left(3 - \frac{2}{\beta^2} - \frac{1}{\beta^4}\right)\text{Log}\left[\frac{2-D}{D}\right] - D + 1 + \left(1 + \frac{1}{\beta^2}\right)^2\left(\frac{2-2D}{D(2-D)}\right)\right)$$

$$D:=2\ \frac{\Delta E_+}{E2-E1}\quad \text{OR}\quad D:=2\ \frac{\Delta E_-}{E1-E2}$$

$$(\Delta E0\ \ 1) = E1 - \frac{E1+E2}{2} = \frac{E1-E2}{2} < 0$$

$$(\Delta E0\ \ 2) = E2 - \frac{E1+E2}{2} = \frac{E2-E1}{2} > 0$$

$$\sigma2 = \frac{\pi\ re^2}{\gamma^2}\left(\left(3 - \frac{2}{\beta^2} - \frac{1}{\beta^4}\right)\text{Log}\left[\frac{1}{B}\right] - B + 1 + \left(1 + \frac{1}{\beta^2}\right)^2\left(\frac{1}{B^2} - 1\right)\right)$$

$$B := \frac{\Delta E_- - (\Delta E0\ \ 1)}{2\ \gamma c\ \beta c\ c\ pperp}\quad\text{OR}\quad \frac{\Delta E_+ - (\Delta E0\ \ 1)}{2\ \gamma c\ \beta c\ c\ pperp}\quad\text{OR}\quad \frac{-\Delta E_- + (\Delta E0\ \ 2)}{2\ \gamma c\ \beta c\ c\ pperp}\quad\text{OR}\quad \frac{-\Delta E_+ + (\Delta E0\ \ 2)}{2\ \gamma c\ \beta c\ c\ pperp}$$

In both equations, γ and β are the relativistic factors of the particles in the center of momentum frame.
γc and βc are the relativistic factors of the center of momentum frame.

BIBLIOGRAPHY

[1] P. Bagley and D. Rubin. Correction of transverse coupling in a storage ring. In Proceedings of the 1998 Particle Accelerator Conference, pages 874–876, Chicago, 1998.

[2] K. L. F. Bane, H. Hayano, K. Kubo, T. Naito, T. Okugi, and J. Urakawa. Intrabeam scattering analysis of measurements at kek's accelerator test facility damping ring. Phys. Rev. ST Accel. Beams, 5, 2002.

[3] M. Bassetti and G. A. Erskine. Closed expression for the electrical field of a two-dimensional gaussian charge. Technical Report CERN-ISR-TH/80-06, CERN, 1980.

[4] Michael Billing. Bunch lengthening via vlassov theory. Technical Report CBN 80-02, LEPP, Cornell University, 1980.

[5] J. D. Bjorken and S. K. Mtingwa. Intrabeam scattering. Part. Accel., 13:115–143, 1983.

[6] A. W. Chao. Evaluation of beam distribution parameters in an electron storage ring. L. Appl. Phys., 50:595–598, 1979.

[7] Alex Chao and Enzo F. Haussecker. Influence of accelerator science on physics research. Phys. Perspect., 13:146–160, 2011.

[8] E. D. Courant and H. S. Snyder. Theory of the alternating-gradient synchrotron. Ann. Phys., 3:1–48, 1958.

[9] W. Decking and R. Brinkmann. Space charge problems in the tesla damping ring. In Proceedings of European Particle Accelerator Conference 2000, pages 1024–1026, Vienna, Austria, 2000.

[10] R. Durstenfeld. Algorithm 235: Random permutation. Communications of the ACM, 7, 1964.

[11] M.P. Ehrlichman, W. Hartung, M.A. Palmer, D.P. Peterson, D. Rider, Rubin, N., J.P. Shanks, C.R. Strohman, S. Wang, R. Campbell, R. Holtzapple, F. Antoniou, and Y. Papaphilippou. Intrabeam scattering studies at cesrta. In Proceedings International Particle Accelerator Conference 2012, pages 2970–2972, New Orleans, LA, 2012.

[12] L. Evans and B. Zotter. Intrabeam scattering in the sps. Technical Report CERN-SPS-80-15, CERN, 1980.

[13] A. V. Fedotov, M. Bai, D. Bruno, P. Cameron, R. Connolly, J. Cupolo, M. Della Penna, A. Drees, W. Fischer, G. Ganetis, L. Hoff, V. N. Litvinenko, W. Louie, Y. Luo, N. Malitsky, G. Marr, A. Marusic, C. Montag, V. Ptitsyn, T. Roser, T. Satogata, S. Tepikian, D. Trbojevic, and N. Tsoupas. Ibs suppression lattice in rhic: Theory and experimental verification. In Proceedings of Hadron Beams 2008, pages 148–152, Nashville, Tennessee, 2008.

[14] A. V. Fedotov, W. Fischer, S. Tepikian, and J. Wei. Experimental studies of ibs in rhic and comparison with theory. In Proceedings of Hadron Beams 2006, pages 259–261, Tsukuba, Japan, 2006.

[15] H. Goldstein. Classical Mechanics. Addison-Wesley, second edition, 1980.

[16] R. H. Helm, M. J. Lee, P. L. Morton, and M. Sands. Evaluation of synchrotron radiation integrals. IEEE Trans. Nucl. Sci., NS-20:900–901, 1973.

[17] R. Holtzapple, M. Billing, D. Hartill, M. Stedinger, and B. Podobedov. Single bunch longitudinal measurements at the cornell electron-positron storage ring. Phys. Rev. ST Accel. Beams, 3, 2000.

[18] H. S. Kang, J. Y. Huang, and S. H. Nam. Measurement of touschek lifetime in pls storage ring. In Proceedings of the Second Asian Particle Accelerator Conference, pages 314–316, Beijing, 2001.

[19] K. Kubo, S. K. Mtingwa, and A. Wolski. Intrabeam scattering formulas for high energy beams. Phys. Rev. ST Accel. Beams, 8(081001), 2005.

[20] Kiyoshi Kubo. Emittance growth due to intra beam scattering. In Proceedings of the 1st Strategic Accelerator Design Workshop, pages 125–126. KEK, 1999.

[21] Kiyoshi Kubo and Katsunobu Oide. Intrabeam scattering in electron storage rings. Phys. Rev. ST Accel. Beams, 4, 2001.

[22] J. Le Duff. Current and current density limitations in existing electron storage rings. Nucl. Instrum. Methods Phys. Res. A, 239(08/1985):83–101, 1985.

[23] J. Le Duff. Single and multiple touschek effects. In Proc. of CERN Accelerator School, pages 114–130, Berlin, 1989.

[24] Valeri Lebedev. Single and multiple intrabeam scattering in hadron colliders. In I. Hoffman, J. M. Lagniel, and R. W. Hasse, editors, High Intensity and High Brightness Hadron Beams: 33rd ICFA Advanced Beam Dynamics Workshop, volume 773, pages 440–442, 2005.

[25] M. Martini. Intrabeam scattering in the acol-aa machines. Technical Report CERN PS/84-9, CERN, 1984.

[26] Formal Education Group of the Space Telescope Science Institute's Office of Public Outreach. Q&a: Electromagnetic spectrum, 2013. [Online; accessed 24-March-2013].

[27] K. Ohmi, K. Hirata, and K. Oide. From the beam-envelop matrix to synchrotron-radiation integrals. Phys. Rev. E, 49(1), 1994.

[28] T. Okugi, H. Hayano, Kubo K., T. Naito, N. Terunuma, J. Urakawa, and F. Zimmermann. Lifetime measurement of atf damping ring. Technical Report SLAC-PUB-7859, SLAC, 1998.

[29] M.A. Palmer et al. The conversion and operation of the cornell electron storage ring as a test accelerator (cesrta) for damping rings research and development. In Proceedings Particle Accelerator Conference 2009, pages 4200–4204, Vancouver, Canada, 2009.

[30] A. Piwinski. Intra-beam scattering. In Proceedings of the 9th International Conference on High Energy Accelerators, pages 405–409, Stanford, 1974.

[31] A. Piwinski. Intra-beam scattering. In M. Month and S. Turner, editors, Frontiers of Particle Beams, pages 297–309. Springer, 1988.

[32] A. Piwinski. The touschek effect in strong focusing storage rings. Technical Report 98-179, DESY, 1998.

[33] Tor Raubenheimer. The core emittance with intrabeam scattering in e+/e- rings. Part. Accel., 45:111–118, 1994.

[34] J. R. Rees. Symplecticity in beam dynamics: An introduction. Technical Report SLAC-PUB-9939, SLAC, 2003.

[35] N. T. Rider, M. G. Billing, M. P. Ehrlichman, D. P. Peterson, D. Rubin, J. P. Shanks, K. G. Sonnad, M. A. Palmer, and J. W. Flanagan. Operation of a single pass,

bunch-by-bunch x-ray beam size monitor for the cesr test accelerator research program. In Proceedings of the International Beam Instrumentation Conference 2012, Tsukuba, 2012.

[36] D. Rubin. Sources of transverse coupling. In Maury Tigner and Alexander Wu Chao, editors, The Handbook of Accelerator Physics and Engineering 2nd, page 272. World Scientific, Singapore, 1999.

[37] D. Sagan. Bmad: A relativistic charged particle simulation library. Nucl. Instrum. Methods Phys. Res. A, 558:356–359, 2006.

[38] D. Sagan. The bmad reference manual. Technical report, CLASSE, 2013. http://www.lepp.cornell.edu/ dcs/bmad/manual.html.

[39] D. Sagan, J. A. Crittenden, D. Rubin, and E. Forest. A magnetic field model for wigglers and undulators. In Proceedings of the 2003 Particle Accelerator Conference, pages 1023–1025, Portland, 2003.

[40] D. Sagan, J. A. Crittenden, and E. Rubin, D. Forest. A magnetic field model for wigglers and undulators. In Proceedings of the 2003 Particle Accelerator Conference, pages 1023–1025, Portland, OR, 2003.

[41] David Sagan and David Rubin. Linear analysis of coupled lattices. PRST-AB, 2(074001), 1999.

[42] K. Schindl. Space charge. In Proceedings of CERN Accelerator School 2000, pages 285–300, Loutraki, 2000.

[43] Jochen R. Schneider. Photon science at accelerator-based light sources. Reviews of Accelerator Science and Technology, 3:13–37, 2010.

[44] Jim Shanks. Status of low emittance tuning at cesrta. In Proceedings of the 2011 Particle Accelerator Conference, pages 1540–1542, New York, 2011.

[45] Jim Shanks. Low Emittance Tuning in CesrTA. PhD thesis, Cornell University, 2013.

[46] K. Symon. Nonlinear dynamics. In Maury Tigner and Alexander Wu Chao, editors, The Handbook of Accelerator Physics and Engineering 3nd, page 83. World Scientific, Singapore, 2006.

[47] K. R. Symon. Derivation of hamiltonians for accelerators. Technical Report ANL/APS/TB-28, ANL, 1997.

[48] T. Takizuka and H. Abe. A binary collision model for plasma simulation with a particle code. Journal of Computational Physics, 25(3):205–219, 1977.

[49] T. Takizuka and H. Abe. A binary collision model for plasma simulation with a particle code. Journal of Computational Physics, 25:205–219, 1977.

[50] Andrzej Turos. Accelerators in materials research. Nukleonika, 50:S11–S15, 2005.

[51] M. Venturini. Direct space charge effects on the ilc damping rings: Task force report. Technical Report LBNL-59511, LBNL, 2006.

[52] S. Wang, D. Rubin, J. Conway, M. Palmer, D. Hartill, R. Campbell, and R. Holtzapple. Visible-light beam size monitors using synchrotron radiation at cesr. Nucl. Instrum. Methods Phys. Res. A, 703:80–90, 2013.

[53] H. Wiedemann. Synchrotron radiation in storage rings. In Maury Tigner and Alexander Wu Chao, editors, The Handbook of Accelerator Physics and Engineering 3nd, pages 209–212. World Scientific, Singapore, 2006.

[54] Wikipedia. Particle therapy, 2013. [Online; accessed 24-March-2013].

[55] Wikipedia. Positron emission tomography, 2013. [Online; accessed 24-March-2013].

[56] Wikipedia. Proton therapy, 2013. [Online; accessed 24-March-2013].

[57] Klaus Wille. The Physics of Particle Accelerators: An Introduction. Oxford University Press, 2001.

[58] Andrzej Wolski. Alternative approach to general coupled linear optics. Phys. Rev. ST Accel. Beams, 9(024001), 2006.

[59] A Xiao and M. Borland. Monte carlo simulation of touschek effect. Phys. Rev. ST Accel. Beams, 13(074201), 2010.

[60] A. Xiao, M. Borland, L. Emery, Y. Wang, and K. Y. Ng. Direct space-charge calculation in elegant and its application to the ilc damping ring. In Proceedings of Particle Accelerator Conference 2007, pages 3456–3458, 2007.